Report No.	2. Government Accession No.	3. PB83205559

Title and Subtitle nteraction and Load Transfer in Track Support tructures, Part 2: "Testing and Constitutive odelling of Materials and Interfaces"	5. Report Date September 1982
	6. Performing Organization Code University of Arizona, Tucson AZ
Author's) . S. Desai, H. J. Siriwardane and R. Janardhanam	8. Performing Organization Report No.
Performing Organization Name and Address epartment of Civil Engineering and Engineering Mechanics niversity of Arizona ucson, Arizona 85721	10. Work Unit No. (TRAIS)
	11. Contract or Grant No. DOT-OS-80013
2. Sponsoring Agency Name and Address I. S. Department of Transportation esearch and Special Programs Administration ffice of University Research ashington, D. C. 20590	13. Type of Report and Period Covered Final Report September 1981-September 1982
	14. Sponsoring Agency Code DPB-50

5. Supplementary Notes
echnical Monitor: John Putukian
U.S. Department of Transportation
Transportation Systems Center, Cambridge, MA 02142

6. Abstract

This final report is presented in two parts, and is in continuation of two pre-/ious reports prepared under this contract. Part 1 contains details of the develop-ment of finite element procedures for nonlinear analysis of track support structures. It provides the user options for using one-, two- or three-dimensional idealizations, and options for using various elasticity and plasticity based constitutive models. The numerical predictions are verified with respect to a number of closed-form solu-tions and field problems. The latter includes verifications for the field behavior of the UMTA Test Section, TTC, Pueblo, Colorado.

Part 2 contains comprehensive testing of 'solids' such as wood, ballast, sub-ballast and subgrade soil and interfaces; these materials were collected from the UMTA Test Section. The solid media were tested by using truly triaxial or multiaxial testing devices, whereas the interfaces between wood and ballast, concrete and ballast and ballast and subballast were tested by using a new cyclic multi-degree-of-freedom shear device. The laboratory test results were used to derive appropriate constitu-tive models for use in the finite element procedures.

The research results involve new and unique aspects such as general three-dimen-sional nonlinear procedures, three-dimensional testing of materials and cyclic testing of interfaces. They will be useful for design of track support structures, and for maintenance and safety analysis of existing tracks.

17. Key Words Track Support Structures, Nonlinear Analysis, Multi-dimensional Finite Elements Truly Triaxial Testing, Cyclic Shear Testing, Constitutive Modelling, Verifi-cations, Design, Maintenance	18. Distribution Statement Available to the Public through the National Technical Information Service Springfield, Virginia 22161.

| 19. Security Classif. (of this report) Unclassified	20. Security Classif. (of this page) Unclassified	21. No. of Pages	22. Price

Form DOT F 1700.7 (8-72)   Reproduction of completed page authorized
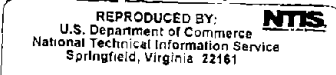
METRIC CONVERSION FACTORS

Approximate Conversions to Metric Measures

Symbol	When You Know	Multiply by	To Find	Symbol
		LENGTH		
in	inches	*2.5	centimeters	cm
ft	feet	30	centimeters	cm
yd	yards	0.9	meters	m
mi	miles	1.6	kilometers	km
		AREA		
in^2	square inches	6.5	square centimeters	cm^2
ft^2	square feet	0.09	square meters	m^2
yd^2	square yards	0.8	square meters	m^2
mi^2	square miles	2.6	square kilometers	km^2
	acres	0.4	hectares	ha
		MASS (weight)		
oz	ounces	28	grams	g
lb	pounds	0.45	kilograms	kg
	short tons (2000 lb)	0.9	tonnes	t
		VOLUME		
tsp	teaspoons	5	milliliters	ml
Tbsp	tablespoons	15	milliliters	ml
fl oz	fluid ounces	30	milliliters	ml
c	cups	0.24	liters	l
pt	pints	0.47	liters	l
qt	quarts	0.95	liters	l
gal	gallons	3.8	liters	l
ft^3	cubic feet	0.03	cubic meters	m^3
yd^3	cubic yards	0.76	cubic meters	m^3
		TEMPERATURE (exact)		
°F	Fahrenheit temperature	5/9 (after subtracting 32)	Celsius temperature	°C

*1 in = 2.54 (exactly). For other exact conversions and more detailed tables, see NBS Misc. Publ. 286, Units of Weights and Measures, Price $2.25, SD Catalog No. C13.10.286.
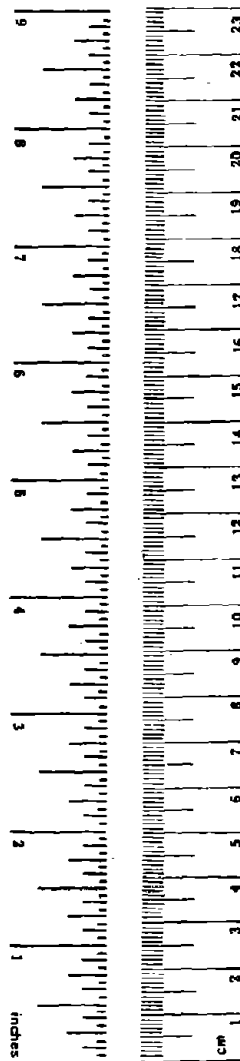
Approximate Conversions from Metric Measures

Symbol	When You Know	Multiply by	To Find	Symbol
		LENGTH		
mm	millimeters	0.04	inches	in
cm	centimeters	0.4	inches	in
m	meters	3.3	feet	ft
m	meters	1.1	yards	yd
km	kilometers	0.6	miles	mi
		AREA		
cm^2	square centimeters	0.16	square inches	in^2
m^2	square meters	1.2	square yards	yd^2
km^2	square kilometers	0.4	square miles	mi^2
ha	hectares (10,000 m^2)	2.5	acres	
		MASS (weight)		
g	grams	0.035	ounces	oz
kg	kilograms	2.2	pounds	lb
t	tonnes (1000 kg)	1.1	short tons	
		VOLUME		
ml	milliliters	0.03	fluid ounces	fl oz
l	liters	2.1	pints	pt
l	liters	1.06	quarts	qt
l	liters	0.26	gallons	gal
m^3	cubic meters	35	cubic feet	ft^3
m^3	cubic meters	1.3	cubic yards	yd^3
		TEMPERATURE (exact)		
°C	Celsius temperature	9/5 (then add 32)	Fahrenheit temperature	°F

°F   -40   0   32   40   80   98.6   120   160   200   212 °F
°C   -40   -20   0   20   37 40   60   80   100 °C
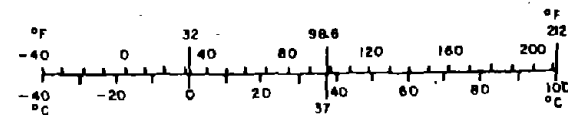
GENERAL DISCLAIMER

This document may have problems that one or more of the following disclaimer statements refer to:

- This document has been reproduced from the best copy furnished by the sponsoring agency. It is being released in the interest of making available as much information as possible.

- This document may contain data which exceeds the sheet parameters. It was furnished in this condition by the sponsoring agency and is the best copy available.

- This document may contain tone-on-tone or color graphs, charts and/or pictures which have been reproduced in black and white.

- The document is paginated as submitted by the original source.

- Portions of this document are not fully legible due to the historical nature of some of the material. However, it is the best reproduction available from the original submission.

EXECUTIVE SUMMARY

Introduction

This report describes investigations towards development of general finite element procedures for nonlinear analysis of multi-component track support systems idealized as one-, two- or three-dimensional problems. It also considers perhaps the most significant aspects of any solution procedure; namely, the stress-strain or constitutive behavior of materials in the structure. Here attention is given to both testing and modelling of improved and appropriate models; the testing is carried out by using new and advanced testing devices for 'solids' (wood, ballast, subballast and subgrade soil) and interfaces between these materials.

Problem Studied

A numerical finite element procedure has been developed that can account for complex factors such as three-dimensional geometry, non-linear behavior of materials, and interaction behavior at junctions or interfaces between various materials. In order to identify the interaction effects and relevant stress-strain behavior, a new cyclic multi-degree-of-freedom (CYMDOF) shear device has been developed and used. Truly triaxial (TT) or multiaxial testing devices with cubical specimens are used to characterize the behavior of ties, ballast, subballast and subgrade soil. The objective has been to develop a general procedure that permits evaluation of transfer of loads from moving vehicles through the track structure to the foundation.

Results Achieved

In addition to this report, two previous reports have been prepared. The topics covered in the two previous reports are: historical review of the problem; details of various components, their functions and role in the support structures; methods of determination of their properties; and available analytical and numerical procedures. These descriptions include advantages and limitations of the available methods, and identifies the need for a general model to account for various important and special factors that influence the track behavior and which are not included in previous works. Initial details of the numerical procedures developed, design and development of the CYMDOF device, and of laboratory testing and stress-strain modelling are also included in the previous reports.

Part 1 of this final report contains complete details of the one-, two- and three-dimensional finite element procedures and codes together with their verifications and applications. The latter involve comparison of predictions with a number of closed-form solutions, and observed results including field data from the UMTA Test Section, TTC, Pueblo, Colorado. The procedure includes development and use of four different constitutive models: linear elastic, nonlinear elastic (variable moduli),critical state and cap models; the latter allow for inelastic or plastic,hardening, stress path dependent and volume change behavior of the materials.

Part 2 of the report contains research accomplishment on the testing and modelling of the stress-strain behavior of materials by using the TT and CYMDOF devices. Comprehensive series of TT tests involving different initial confining pressures and a wide range of stress paths have been performed on wood (ties), ballast, subballast and subgrade (silty sand) collected from the UMTA Test Section. The CYMDOF device has been used to test interfaces between concrete and ballast, wood and ballast, and ballast-subballast under different normal loads and amplitudes of (repetitive) shear stress. These tests were conducted at the field density for the UMTA Test Section. Linear elastic, variable moduli, critical state and cap models have been developed for different materials depending upon the observed laboratory test behavior. These models were then used in the finite element codes for predicting the field behavior.

Utilization of Results

The research results will have significant potential in terms of both applications and further research. They can be used for stress-deformation analysis and design of track support structures for mass transport systems such as railroad tracks and for maintenance and safety analysis of existing tracks. Since the research has developed procedures for all the three-, one- two- and three-dimensional idealizations, they can provide options to the user depending upon his specific need. For instance, users interested in studying load-deflection behavior of the rail can use the one-dimensional option, while those interested in analyzing three-dimensional situations such as arbitrary geometry and loss or displacement of ties can use the three-dimensional option. Similarly, one can use simple linear elastic material model or advanced plasticity models.

The new CYMDOF device can permit study of behavior of interfaces as well as track materials under repetitive vertical and horizontal loads; the device will also be capable of testing under torsional and

ii

rocking modes of deformation. The test results can permit evaluation
of behavior under long repetitive loading useful for both design and
maintenance and safety analysis. With some modifications, the device
can allow repetitive and fatigue testing of interfaces and connections
such as between tie-plate and tie and spikes in the track support
structure. The device can also be used to study behavior of track
materials with modifications such as cementing and impermeable
membranes.

In the past, uniaxial or cylindrical triaxial tests have been
used to characterize behavior of track materials. Perhaps for the
first time, this study has considered detailed testing of track
materials under fully three-dimensional state of stress. Hardly any
previous works have considered the important question of the behavior
of interfaces. Development and use of the new CYMDOF device is
considered to open a new direction towards testing for behavior of
interfaces.

The general numerical procedures and the test device constructed
under this project are unique and new, and advances the state-of-the-
art and knowledge related to mechanism of load transfer in track
support structures.

Overall, the procedures and test device can provide improvements
in design, maintenance and safety procedures. As a result, they can
lead to savings in cost and enhancement of safety of track support
structures.

It is expected that various governmental and private agencies and
railroads involved in design and maintenance of track support struc-
tures can utilize the research results.

Conclusions

General and improved numerical procedures based on the finite
element method developed under this project will allow evaluation of
stresses, deformations and load transfer mechanism in track support
structures. The new cyclic interface testing device will permit
experimental determination of behavior of interfaces between various
track components. The results will enhance the state-of-the-art and
knowledge on analysis of track support structures, and can be applied
for design, and maintenance and safety analysis of these structures.

PREFACE

The research investigations presented in this final report were supported by Contract No. DOT-OS-80013 through the Office of University Research, U. S. Department of Transportation, Washington, D. C. The report is presented in two parts. Part 1 contains details of development and application of nonlinear finite element procedures and provides options for using one-, two- and three-dimensional idealizations and a number of nonlinear elastic and elastic-plastic stress-strain or constitutive models. Testing and constitutive modelling of materials such as (wood) tie, ballast, subballast and subsoil, and interfaces between these materials are the subject of Part 2 of the report. Here development and use of new cyclic multi-degree-of-freedom shear device for interfaces and use of truly triaxial or multiaxial devices for the track materials are discussed. The investigations were conducted by C. S. Desai, H. J. Siriwardane and R. Janardhanam. The latter two were doctoral students and contributed investigations in Part 1 and Part 2, respectively; A. Muqtadir assisted in conducting the laboratory testing for ballast-subballast interface. C. S. Desai acted as the principal investigator for the project.

The research was initiated in 1978 at Virginia Polytechnic Institute and State University, Blacksburg, VA (Va. Tech.). Portions of the research investigations have been included in two previous reports: (1) Interaction and Load Transfer Through Track Guideway Systems, No. DOT/RSPA/DPB-50/80/13, Office of University Research, U. S. Department of Transportation, Washington, D. C., prepared in 1978 and published in 1980 and (2)

iv

"Interaction and Load Transfer in Track Guideway Systems" prepared in June 1980 and is under publication. The previous two reports were prepared at Va. Tech. while this report was prepared at the University of Arizona, Tucson, AZ, as a continuation of the project, subcontracted through Va. Tech.

The project was monitored by J. Putukian, Transportation System Center (TSC), Cambridge, Mass.; previous monitors of the project were G. Butler, Urban Mass Transportation Administration (UMTA), Washington, D. C., and A. Sluz of TSC. G. Spons., UMTA Test Section at Transportation Test Center, Pueblo, Colorado, assisted in procuring various materials from the Test Section for testing in the laboratory, and Kaman Avidyne and Kaman Sciences, Inc. (E. Gadden, L. J. Mente, T. Stigliano) provided the report containing field observations at the UMTA Test Section at Pueblo, Colorado.

TABLE OF CONTENTS

TABLE OF CONTENTS (cont.)

LIST OF FIGURES

LIST OF FIGURES (cont.)

LIST OF FIGURES (cont.)

LIST OF FIGURES (cont.)

LIST OF FIGURES (cont.)

LIST OF TABLES

Chapter 1

INTRODUCTION

1.1 General

The need for the development of mass transportation is felt
acutely in the recent times partly due to the spiraling rise in oil
prices. Considerable attention is being given to improve the existing
rail road system and to plan and rationalize the design of new track
beds to suit the needs of high speed passenger systems. For complete
understanding of the behavior of track support structures, it is
necessary to determine the characteristics of various components of
the track beds and their behavior under repeated load.

In the present state of affairs, it is often seen that the
potential waste due to geotechnical problems related to track beds is
very large. About 40 percent of the money spent to upkeep the track
bed is being spent on the procurement, distribution and rehabilitation
of ballast [41,53]. About 15 to 20 percent is spent to replace de-
cayed ties and repair spike torn ties [1,11]. For a complete assess-
ment of the economic importance of geotechnical problems, the cost of
derailments, need of restricted speed and other delays caused by
deteriorated track support, should also be included.

Numerical schemes such as the finite element method can be used
for rational analysis of track beds and to attain a high degree of
precision and reliability. The potential of the finite element
method as an analytical tool is well recognized in the area of

1

geotechnical engineering. This is due to the fact that the method can be applied to a variety of problems with complex boundary conditions that may even change during construction and operation, and to nonhomogeneous, inelastic materials which may undergo large deformations.

But the ultimate effectiveness of this modern analysis procedure is restricted by the validity of constitutive relations for the materials under consideration. The accuracy and precision of these relations are governed by the applicability of the constitutive law and the ability to measure true material response in the laboratory. Conventional laboratory test equipment is not capable of providing the material parameters accounting for the effects of three-dimensional stress fields.

In this investigation, advanced techniques have been used for testing the materials in track beds. A highly sophisticated dynamic multi-degree of freedom shear device [22,23] has been used to study the interface behavior between those materials constituting the layered track bed. A high capacity truly triaxial device [18] of 20000 psi (1.4×10^5 Kpa) capacity with a very sensitive electrical inductance type deformation detection system has been used for multi-axial testing of wood and ballast. Soil and subballast have been tested in a 200 psi (13.8×10^2 Kpa) capacity multiaxial testing device [69]. This fluid cushion truly triaxial device uses 18 LVDTs in its deformation measuring system. High degree of accuracy and reproducibility in test results have been ovserved in these devices.

1.2. Aim of the Research

The aims of this research are

1. To develop constitutive laws for soils, subballast, ballast and wood based on comprehensive laboratory tests,

2. to study the interface behavior between tie-ballast interface in the newly developed Dynamic Multi-Degree of Freedom Shear Device,

3. to study the grain size effect of ballast on strength and deformation properties, and

4. to compare the materials response with relavent existing data.

This study is divided into five phases. The four chapters after introduction describe the development of constitutive laws of subballast, wood, ballast and soils. Each chapter by itself includes a brief preamble, the theory based on which the constitutive law is developed for that material, testing procedure, test results and the constitutive model.

Chapter 6 describes the salient features of the Dynamic Multi-Degree of Freedom Shear Device and presents the results of a test series on tie-ballast interface in that device.

Finally, in Chapter 7, a summary of the work in the current research is given, and suggestions are made for further research.

Chapter 2

CONSTITUTIVE CHARACTERIZATION OF SUBBALLAST

2.1 INTRODUCTION

The growing demand for the mass transportation system together with technological rapid progress in the development of high speed mass transport vehicles requires the development of improved procedures for new designs and for maintenance of support structures for mass transportation such as rail-track beds. Although the question of ballast and subgrade support design has been extensively studied in the highway and airfield disciplines, little attention has been paid to a rational design methods for rail-road track support systems. More sophisticated engineering analysis of track system response involves consideration of the interrelated and coupled behavior of the components of the track system.

The identification of failure and other useful criteria of the materials in the track beds, the relationships between loading environment and foundation material behavior, and factors influencing the total track structure performances will make the analysis of track bed more reational and realistic.

The road bed Fig. (2.1) is intended to facilitate free drainage, to provide smooth, regular surface on which the ballast section and the track structure can be laid on the established grade and to carry the weight of the track, ballast as well as superimposed loadings as uniformly as possible. Magnitude of gross vertical load,
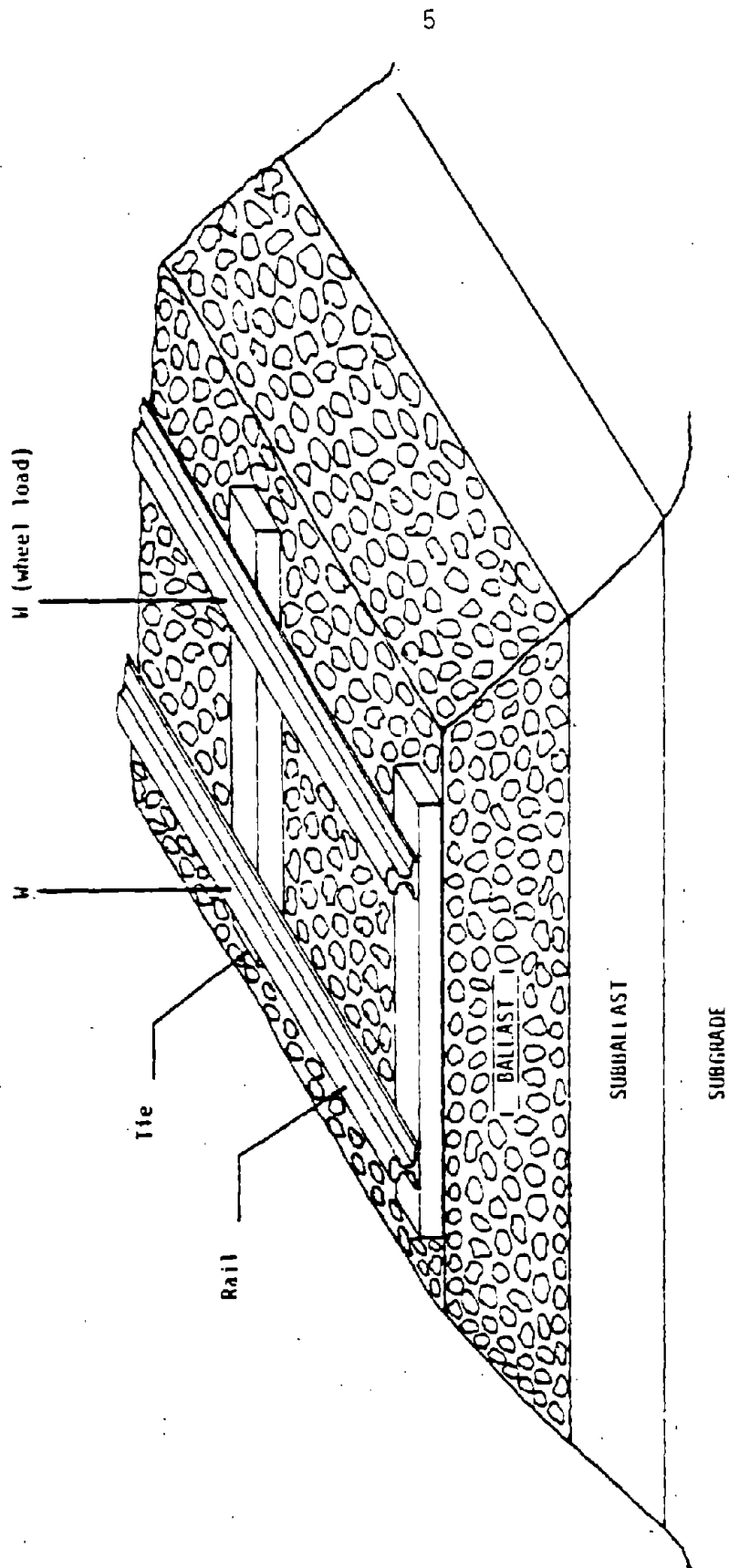
Figure 2.1 Rail Track Picture

axle load and wheel load, dynamic loading, and number and frequency
of load applications influence the behavior of the track bed. Pre-
dominantly freight oriented North American vehicles maximum wheel
load is 41 tons (360 KN) [4]. But the average load intensity in the
ballast/subballast interface can be less than 20 psi (140 Kpa). This
stress should be increased for high speed; it is often doubled for
equivalent static design.

2.2 STATEMENT OF THE PROBLEM

The material is called a subballast when it is used as a tran-
sition layer between the upper layer of large particle size, good
quality ballast and the fine graded subgrade. The subballast, in
addition to fulfilling some of the functions of the ballast, is
intended to prevent the mutual penetration or intermixing of the sub-
grade and ballast, to reduce frost penetration in the subgrade and to
avoid the pumping of ballast (6,12). The types of materials used as
subballast are generally any free draining material such as crushed
stone, sand gravel and stabilized soil. In addition to filtering of
layers above and below, subballast also dampens the vibration and
distributes the superimposed load to the subgrade. It can thus be
the source of the accumulative permanent deformations associated with
deterioration of surface and traffic line. The behavior of subballast
under repeated loading has not been studied so extensively as for
ballast.

2.3 OUTLINE OF THE OBJECTIVE

The potential of the finite element method as an analytical tool to analyse the rail track is restricted due to lack of realistic material models. The multi-phase and granular nature of subballast makes it more difficult to characterize its behavior. Extensive testing of the materials for precise prediction of their response will enable development of a realistic constitutive law. Also it is highly desirable to evaluate their response under laboratory conditions which simulate the inservice conditions. In order to develop rational constitutive laws, the conglomerated granular mass is tested for its strength properties and its stress-strain responses under various stress paths by using the truly triaxial testing.

2.4 REVIEW OF PAST WORK

During the service life of a rail track, permanent strains accumulate in the substructure causing permanent deformations. This leads to degradation of track geometry, eventually to decreased safety and increased potential for derailment. This permanent deformation of track structure results from four basic mechanisms of ballast, subballast and subgrade mechanical behavior. First is the volume reduction or densification from particle rearrangement under cyclic shear strain produced by repeated train loads. Second is inelastic recovery on unloading or stress removal, which is a function of both stress history and stress state. Third is volume reduction caused by particle breakdown from train loading or environmental factors.

Fourth is subgrade penetration into ballast voids allowing ballast to sink into the subgrade.

Many investigations have been carried out by various investigators, Selig [66], Robnett [58,59], Thompson [3,42] and Raymond [53.57] to study the mechanical behavior of ballast and subballast with regards to the foregoing third and fourth factors. New means for measuring insitu density have been developed [64], but the basic mechanism responsible for densification has not been yet fully investigated. Insitu plate-load tests [65] proposed by Selig can assess the deformation characteristics of subballast. They are essentially intended for immediate settlement [65], but not the permanent deformations the subballast may undergo. Details of the work done in the repeated load behavior of granular material is reported in this report in section 4.4. Their qualitative conclusions can be extended to subballast also. However, study of the exact response of the material under consideration to the repeated load and under different stress paths will require techniques that can allow improved simulation of the field conditions. Hence, a comprehensive test series was performed under this research by using the truly triaxial device that permits three-dimensional testing under different stress paths.

2.5 TESTING PROGRAM

2.5.1 Details of Sample Tested

The subballast collected from the UMTA test-track at Peublo, Colorado [39] is a dry mixture of granular materials such as broken

stone, round pebbles, coarse sand, fine sand and silt. The subballast was spread in steel trays and airdried. The moisture content was found to be varying between 2 to 3 percent. This may be the hygroscopic moisture content present in the subballast, as it is freely exposed to the atmosphere. The grain size distribution curve is shown in Fig. (2.2). It shows that the mixture is a well grade, its uniformity coefficient was 4.76. The field density of subballast at test site was about 144 pcf.

2.5.2 Test Apparatus

Introduction

The details of design, development and construction of the truly triaxial device of capacity 200.00 psi (13.80×10^2 Kpa) are given by Sture and Desai [69]; salient features are reproduced herein for the sake of completeness. The device uses fluid cushions to apply uniform independently controlled principal stresses to the six faces of a cubical specimen of 4.00 inches (10.16 cms). It has a very sensitive deformation detecting system capable of measuring both shear and normal deformations.

Linear Variable Differential Transformer (LVDT) Probes are used for the measurement of displacements. By independently varying the fluid (compressed air) pressures in the three orthogonal directions, a known general and purely compressive three-dimensional stress state can be achieved.
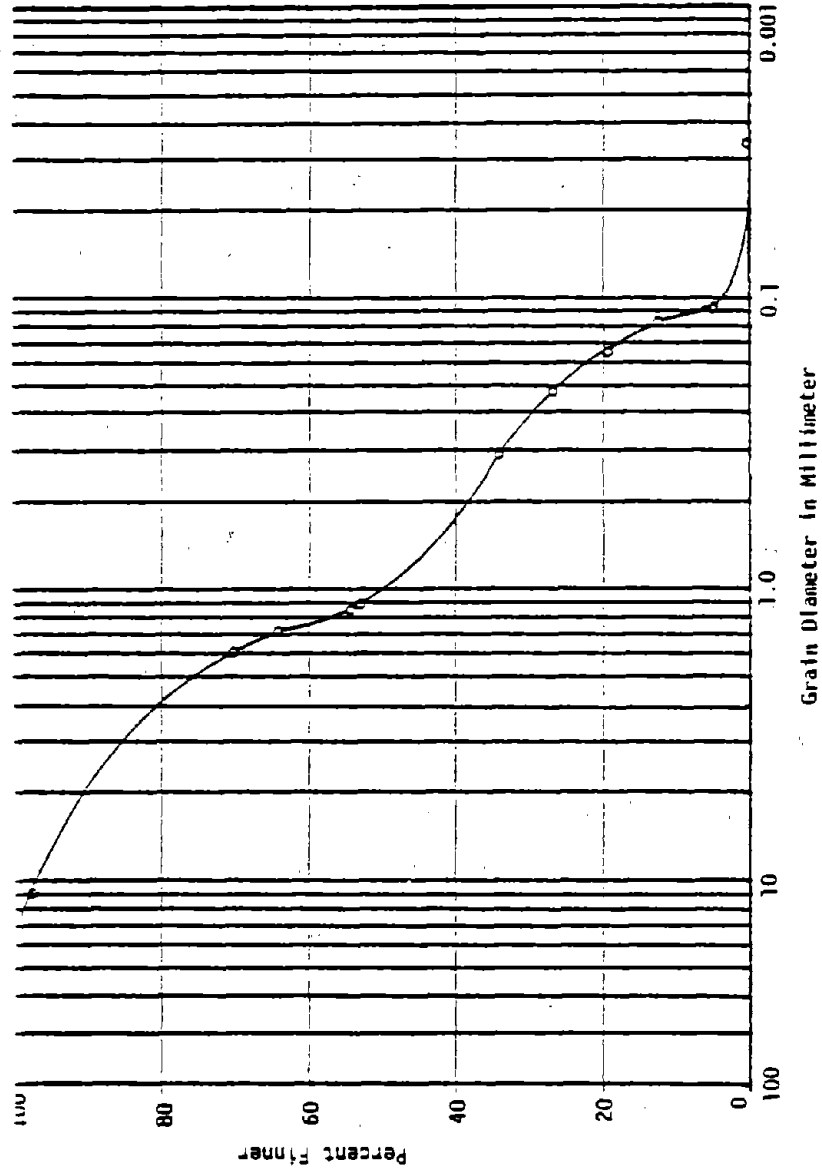
Figure 2.2 Grain Size Distribution Curve for Subballast

The apparatus is ideally suited for exploring the constitutive behavior along arbitary paths in stress space. Simultaneous operation of three precision pressure regulators controlling the applied principal compressive stresses enable the operator to follow such arbitrary paths in loading or unloading according to a predetermined scheme. This apparatus can be operated at the stress levels ranging from 0-200 psi (0 to 1.38 x 10^3 kpa). The cubical specimen is located in the center of the cubical cavity of a high strength aluminum space frame. The flexible membranes are pressurized pneumatically here. Figure (2.3) shows an "exploded view" of one face assembly of the apparatus.

Frame

The reaction frame Fig. (2.4) of this cubical apparatus is made of hard annealed aluminum. The external and interval dimensions of the frame are 7.5 inch (19.05 cm) and 4.5 inch (11.43 cm) respectively. A narrow recess is machined into each face of the frame in order to accommodate the membrane flanges. The edges between faces and the interior cavities are given a large curvature in order to prevent the tearing of a fully stretched membrane and to facilitate membrane expansion and contraction. Holes are threaded into each face of the frame to provide connection between the back-up walls and the frame.

Wall

Each wall assembly essentially consists of a main cover plate which serves as the back-up seal for the interior pressure cavity
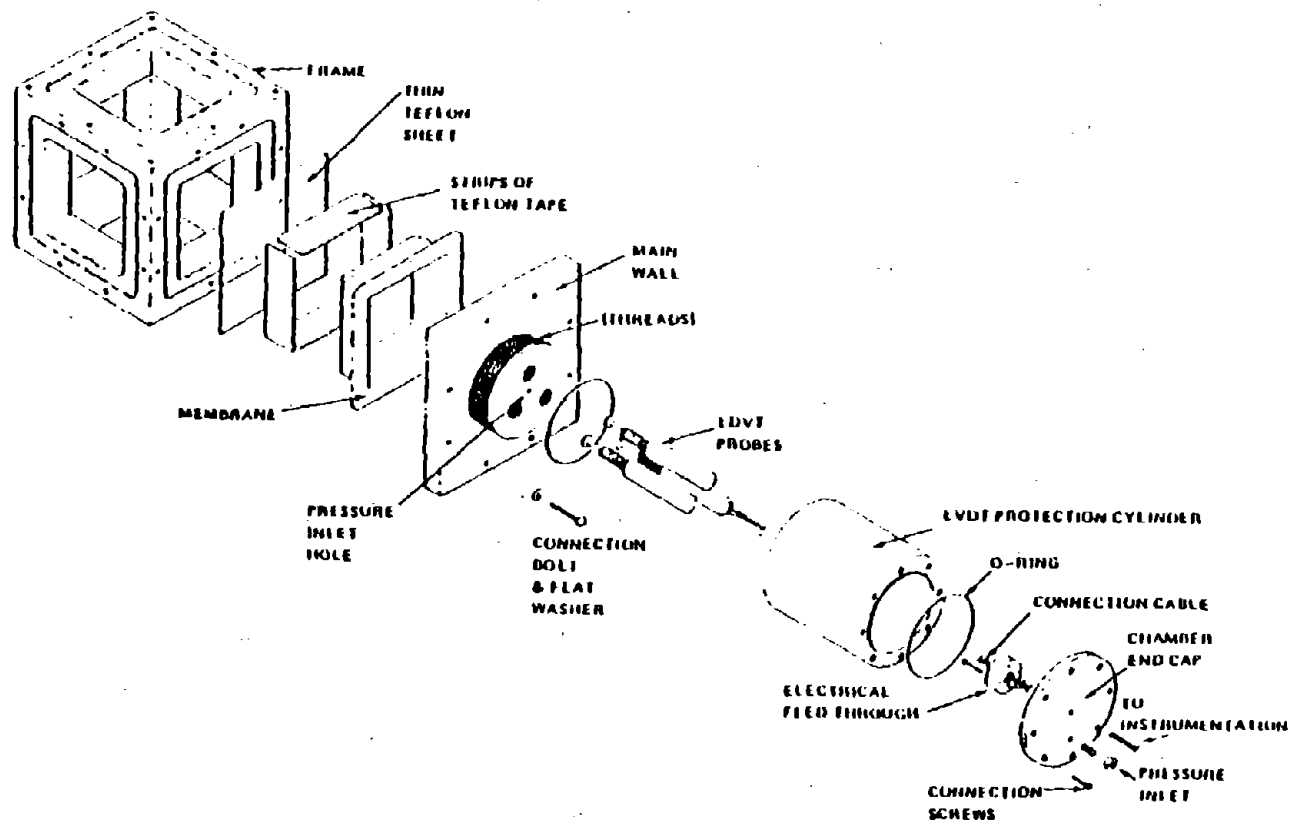
Figure 2.3 Exploded View Showing One Face of the Multiaxial Cubical Apparatus
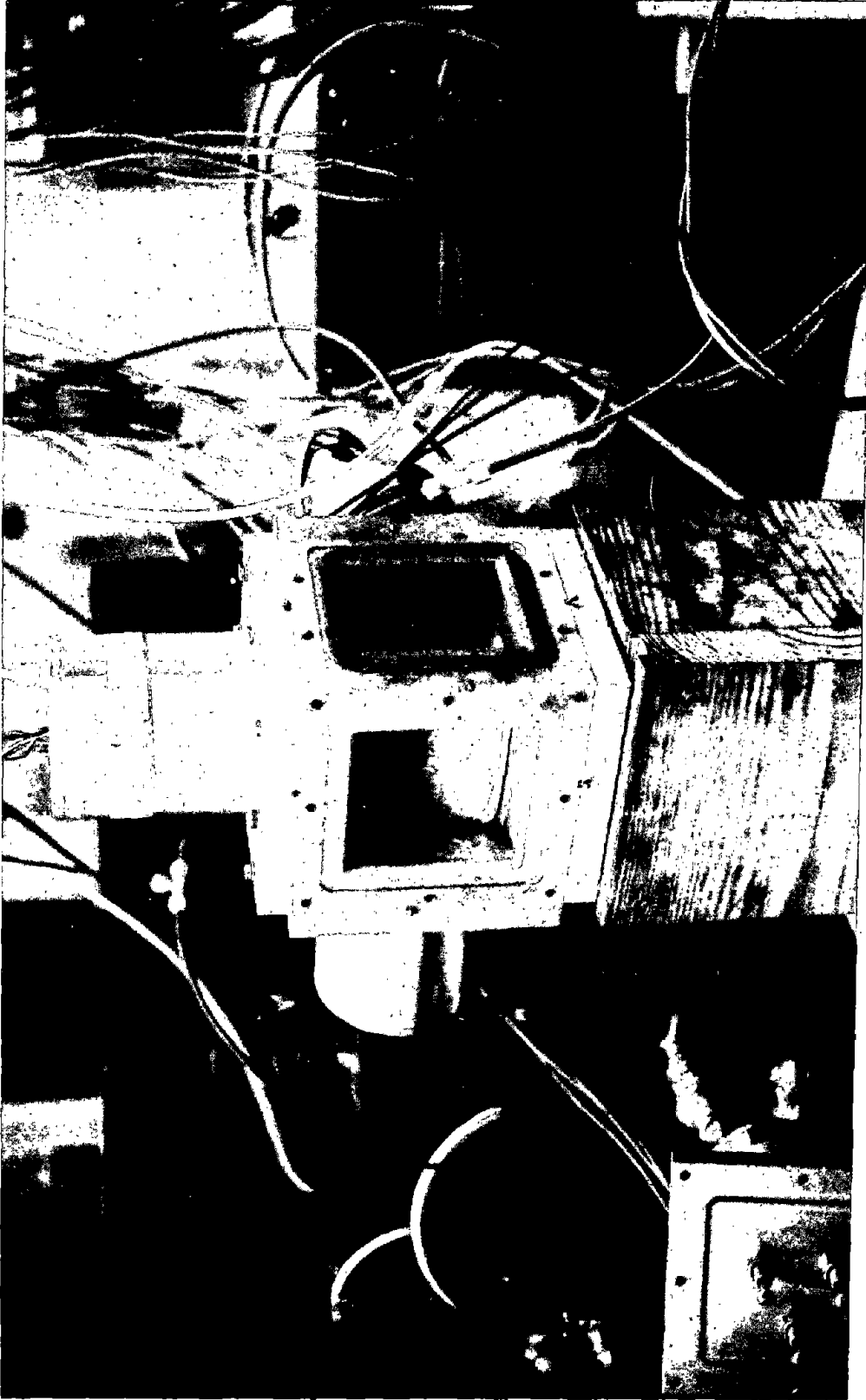
Figure 2.4 Truly Triaxial Cell – Reaction Frame and Assembly

as shown in Fig. (2.5). Three LVDTs are spaced 120° apart on a circle

of 6.35 cm diameter as they are fitted to the cover plate with locking

nuts. The longitudinal position of the LVDTs can be adjusted, prior

to testing. A square groove is machined into the front face of each

cover plate to contain an "O" ring. Its function is to assist in

holding the stretched membrane. The LVDTs are housed in a contain-

ment vessel which acts as a protective shield. The transducers are

designed to operate in a hydrostatically pressurized fluid or gas

medium. They are initially calibrated in a special calibrating

device namely a hand operated micro-screw calibration rig.

Pressure Chamber

The flexible membrane on front face, the cover plate with LVDTs

on the rear side and the four sides of one face of the frame form the

pressure chamber. The flexible membranes are made from PVC processing

high tearing strength and low stiffness in shear (Sture/Desai). The

membranes transmit the pressure from the regulated pressurizing fluid

or gas to the soil specimen faces. These membranes allow for large

specimen strains without boundary interferences resulting in sample

disturbance. Also they maintain uniform stress over the specimen

surfaces even at large strains. The mutual contact influence during

interference is reduced by using lubricated teflon sheets. These

membranes are made specifically comparitively thicker in the edge

regions so that bulging of membranes will not occur at the edges as

there could be a difference in internal membrane pressure between

adjacent membranes.
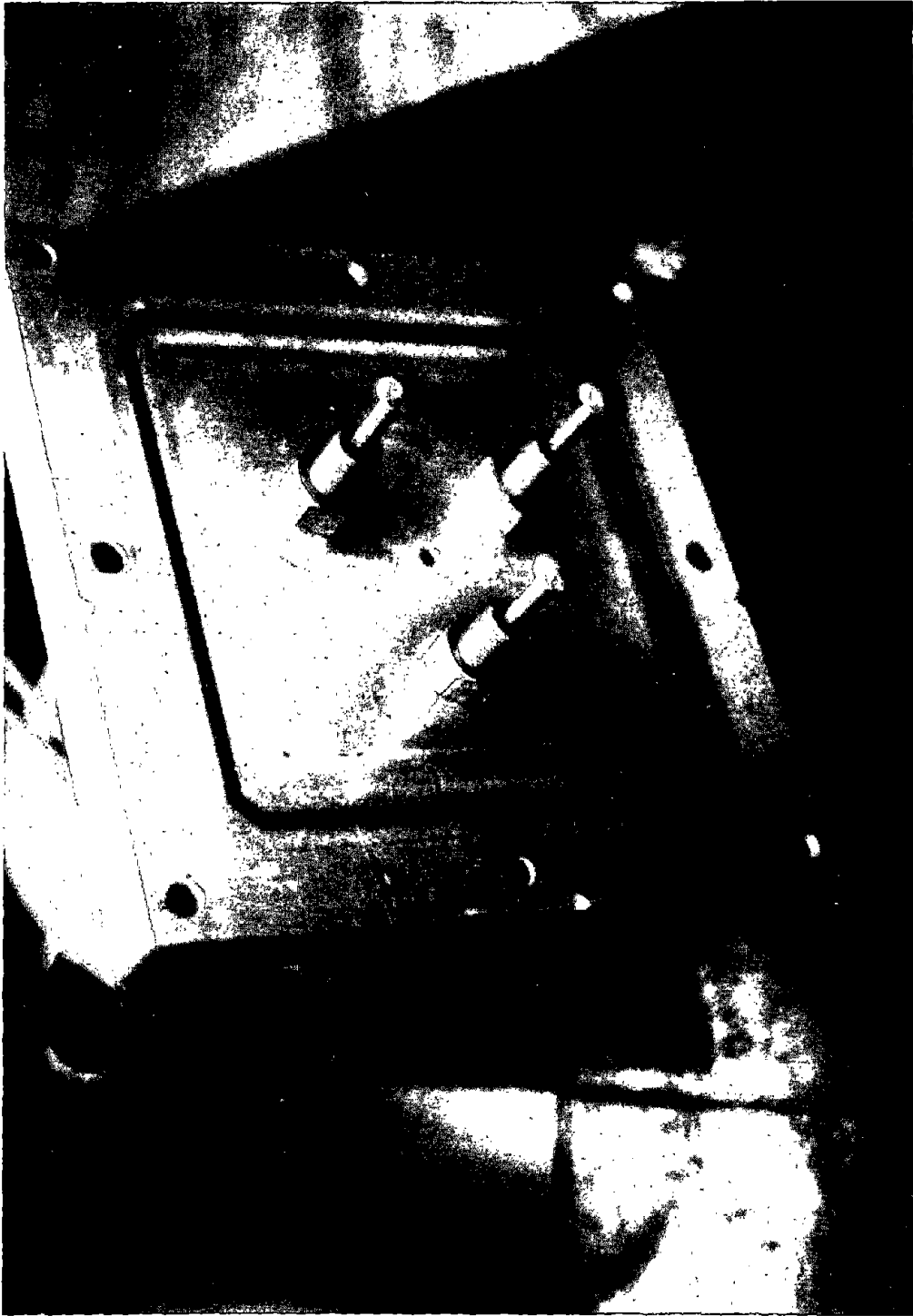
Figure 2.5 Wall with LVDTs and "O" Ring

Pressure Regulator System

Compressed air is used to apply stress on the sample under test. The compressed air is regulated by hand operated precision regulators, valves and Bourdon tube pressure gages, Fig. (2.6). The valve connections are made as such any two or all three channels can be arranged for common control featured in conventional triaxial compression ($\sigma_2 = \sigma_3$), extension ($\sigma_2 = \sigma_3$) or isotropic compression ($\sigma_1 = \sigma_2 = \sigma_3$). Thus this load application units enable to follow any complex stress paths and also enable to center the sample in the cell prior to an experiment. An air compressor supplies the required pneumatic pressure.

Deformation Measurement System

The specimen deformations are monitored on all the six faces of the specimen, with three LVDTs on each face. The LVDTs used are of special type with a vented casing and protective coated internal wiring. The sensing element of the LVDT is a thin spring loaded rod, whose end has the shape of a circular disc with a hemisherical surface. The probes have a total stroke length of 0.70 inch (2.47 cm). The probes are situated behind the pressurized membranes. The probes are completely submerged in the pressurizing medium. These special type probes are designed to function upto 300.00 psi (2×10^3 kpa). In addition to 18 LVDTs, the deformation detection system consists of an oscillator, amplifiers and demodulators. Oscillators are adjusted for a frequency of 2.5 KHz. The signals in form of output voltages from the deformation detection system are processed by a Hewlett Packard data acquisition unit.
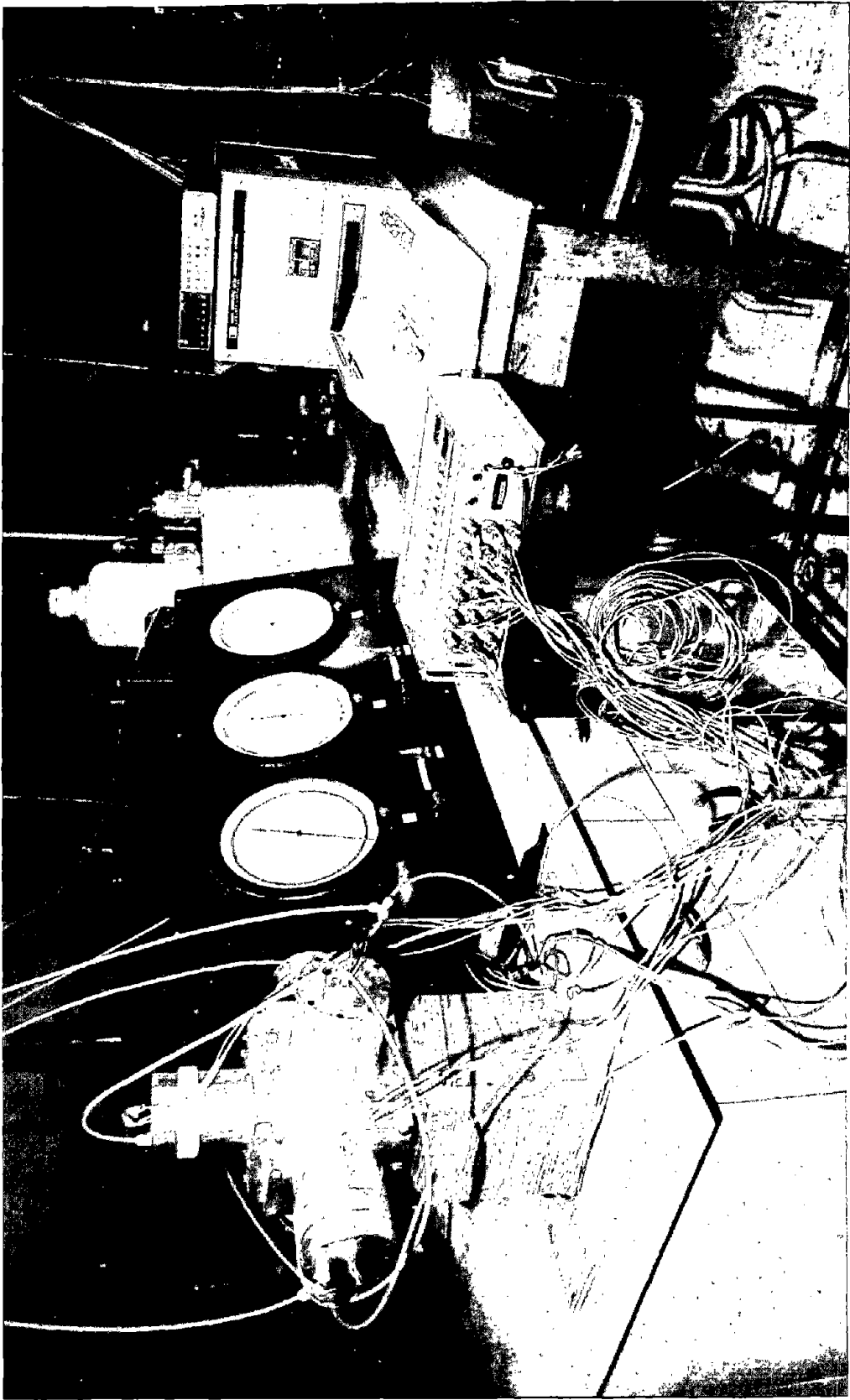
Figure 2.6 Cell Assembly, Pressure Regulator System and Data Acquisition System

2.5.3 Sample Preparation

The sequence of operations in preparing a specimen of subballast is as follows:

A special sample preparation mold is used for this purpose. The mold is made of four thin wall aluminum plates, 4.00 x 4.00 x 0.25 inch (10.16 x 10.16 x 0.64 cm). These plates are screwed together to form a hollow 4.00 inch (10.16 cm). Two aluminum plates of 6.00 inches (15.00 cm) square and 0.25 inch (0.64 cm) thick, one as the base plate and another as the cover plate to the mold are used. This mold not only serves to contain the sample compacted to the desired density, but also serves as a sample sheath (inner membrane) expander.

Pure latex dental dam is used as the sheath material. It has very low stiffness and insignificant (0.06 inch/0.15 cm) thickenss. So it will not influence the specimen response during test. A 16.00 inch (30.00 cm) length of dental dam is cut, and the ends of the sheet are glued together such that they overlap about 0.5 inch (1.27 cm) and form a hoop of 15.5 inch (28.75 cm) circumference. This hoop is then placed inside the mold. The excess sheath material over the ends of mold are folded and securely fixed with the mold by using rubber bands. A vacuum is applied through the side ports of the mold to hold the membrane in place and wrinkles, if any, are smoothed out.

The base and cover plates of the mold are greased. Then 4.00 inch (10.16 cm) square teflon sheets are placed centrally in both

plates, they are then covered by sheets of dental dam of 6.00 inch (15.00 cm) square.

A teflon tube of 0.0025 inch (0.156 cm) diameter is used for vacuum line. One tip of the teflon tube vacuum line is sealed in a filter paper so that no particles will enter the tube during vacuum suction. Glue is applied to the sheath on the bottom of the sample mold and the mold is placed on the base plate so that vacuum line falls under a groove cut in the side wall.

A collar extension is now attached to the mold. The mold and bottom plate are clamped together and tied by binding wire. Subballast is now filled into the mold by spooning. It is tamped by using a special hand compactor and then vibrated for 2 minutes at a frequency of 20 Hz. Then the next layer is filled and the process is repeated. The sample is compacted in three layers. The collar is then removed and the top surface is levelled. Only by trial and error, it is decided how much compaction energy (in form of tamping and vibrating) is necessary to achieve the desired initial density of the sample (equal to field density) and is then followed uniformly for all sample preparation. For the test herein, each layer is tamped 25 times dropping the weight of 1.00 lb (453 gm) through a drop of 6.00 inches (15.00 cm) and vibrated for 2 minutes at a frequency of 20 Hz.

Glue is applied to the sheath on the top of the mold and the cover plate is placed on the mold. The external vacuum is now released. A vacuum commensurate with the initial confining pressure

2.00 psi (14.00 kpa) is applied through the vacuum lines. Any leaks in the sheath are sealed. The mold is carefully removed and excess sheath material is trimmed. Finally, the sample is loaded into the apparatus through the side of the frame by using a thin lubricated plexiglass sheet as a ramp, and it is pushed with a wooden plunger that distributes the driving stresses evenly over the sample face.

2.5.4 Equipment Preparation

All six membranes are liberally coated with Dow Corning stop-cock grease. The four sides of each face where the membrane flanges are also lubricated by stopcock grease. Teflon sheets are greased and positioned on each side. Three walls are fixed to the frame, one in each direction (say X,+Y,-Z). The screws used for fixing the walls to the reaction frame are tightened by using a torque wrench with a torque of about 5 ft-lbs (69.27 cmKg).

Square teflon sheets should be greased and positioned on each sample face taking care to avoid any wrinkles and folds. The sample is then placed on a well lubricated plexiglass, which is used as a ramp to slide the sample through one of the side openings into the cubical cavity. The vacuum line is gently fed through the diagonal ports when the sample is slided into the cavity. A wooden plunger of 3.9 x 3.9 inch (9.91 x 9.91 cm) is used to push the sample. The sample is visually centered in the cubical cavity. The other three walls are then fixed and air pressure lines are connected to the respective side ports. The inlet vents are at the end cap on each

LVDT protection cyclinder. The nylon poly-flo connectors are tightened until they are snug. An initial hydrostatic confining pressure is applied on the sample, equal to that of initial vacuum pressure. The vacuum pressure is then discontinued. Now the sample is ready for test for a desired stress path.

2.5.5 Testing

The electronics of the deformation measurement system of this device is switched on and allowed to warm up for at least a half hour. The eighteen channels are checked to verify that the sample is centered and that all LVDTs are functioning well. Then the test is initiated by initial scanning of these 18 channels. The initial output voltages are recorded and stored in a tape.

The pressure control board contains three regulators corresponding to three pressure gages. The desired pressure in each direction is applied simultaneously by operating the regulators. The sample undergoes deformation and the output voltages are verified at frequent intervals. The pressure applied remains constant and is maintained at the same level until the deformations get stabilized. The verification of stabilization of voltages (indirectly the deformations) is facilitated by a plotter arrangement, which also forms a part of the deformation measurement system. Once the deformations are stabilized, the channels are scanned and the output voltages and the pressure levels in the three directions are recorded and stored. The testing is continued along the

predetermined stress path including primary loading, unloading and reloading. The recorder voltages and pressures are converted into stresses and strains and the stress-strain response curves are then plotted.

2.6 STRESS PATH DEPENDENCY

Various straight line stress paths in stress space are modelled in this study. Figure (2.7) shows the abbreviation for various stress paths and their trajectories in principal stress space. Hydrostatic or Isotropic Compression (HC/IC), Conventional Triaxial Compression (CTC), conventional Triaxial Extension (CTE), Reduced Triaxial Compression (RTC) and Reduced Triaxial Extension (RTE) paths lie in the triaxial plane. $(\sqrt{2}\sigma_2 = \sqrt{2}\sigma_3)$. Triaxial Compression (TC), Triaxial Extension (TE) and Simple Shear (SS) paths lie in the octahedral plane. All these stress paths can be simulated in the truly triaxial device.

2.6.1 Hydrostatic Compression (HC or IC)

The specimen is compacted to an initial density of 1.81 gm/cm^3. The initial hydrostatic confinement is held to be 2.00 psi (14.00 kpa). Increments of load (stresses) of same magnitude are applied on all six faces of the specimen. The pressure is applied by compressed air and the deformation readings are recorded. Loading is continued upto a stress level, when the sample is unloaded completely. The sample is reloaded to a higher stress level and then the load is reversed. Strains in three principal directions are plotted against
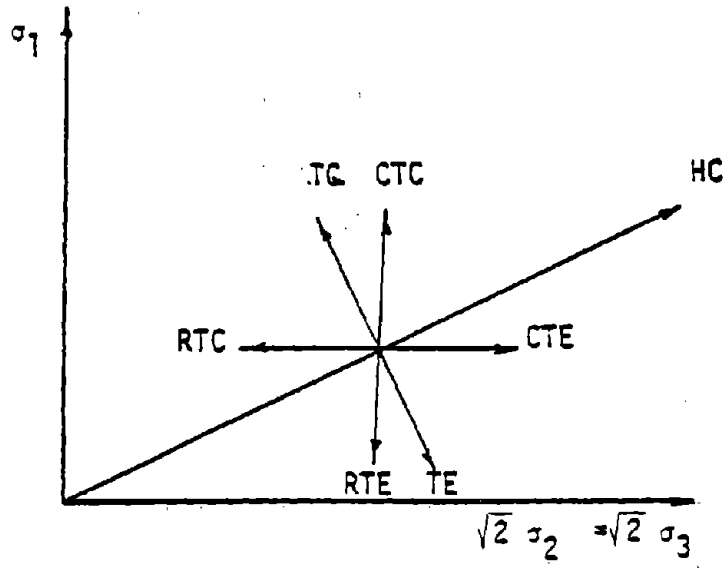
Stress Paths on Triaxial Plane
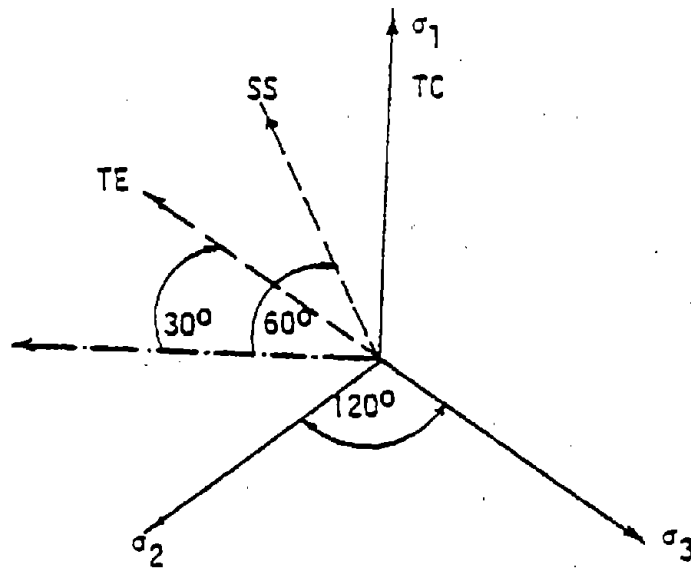
Figure 2.7 Stress Paths on Octahedral Plane

the hydrostatic stress in Fig. (2.8). It is noticed that the material stiffens as it gets compressed. The elastic (unloading/reloading) bulk modulus appears to remain almost constant throughout the test 2.23×10^4 psi (15.6×10^4 kpa). The subballast exhibits a pronounced memory with respect to hydrostatic loading history as evidenced by the sharp breaks between reloading and virgin loading curves.

The truly triaxial device is sufficiently sensitive so to indicate the samples inherent anisotropy due to its flexible boundary construction. The inherent anisotropy, because of subballast being a mixture of soil, gravel and pebbles is evidenced by the different stress-strains responses in the three directions. The trend of the curve resembles that of a dense granular material under hydrostatic state of stress.

2.6.2 <u>Conventional Triaxial compression</u> (CTC)

In the conventional triaxial compression stress path, σ_2 and σ_3 are held constant while σ_1 is increased. This increases the shear stresses $\Delta\tau_{oct}$ by $\Delta\sigma_1 \sqrt{2}/3$ and also the hydrostatic confining pressure $\Delta\sigma_{oct}$ by $\Delta\sigma_1/3$. The stress-strain response curves for three separate CTC tests at different confining pressures but similar densities are plotted in Figs. (2.9) and (2.11). It is noticed that the stiffness increase with confining pressure as expected for a frictional material. None of the CTC tests reached an ultimate strength plateau indicating failure. The tests are
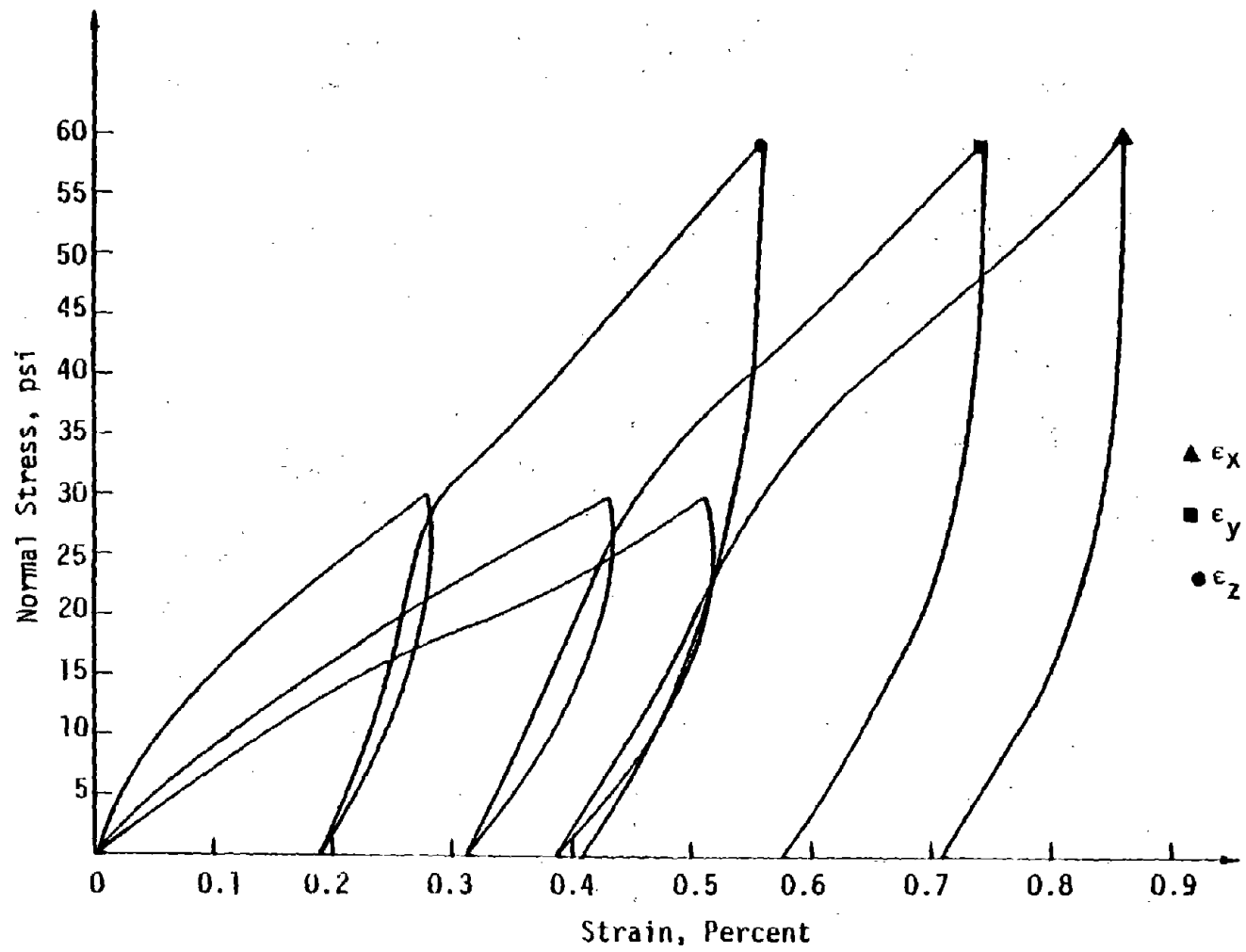
Figure 2.8   Stress-Strain Response Curves for Hydrostatic
Compression Test.
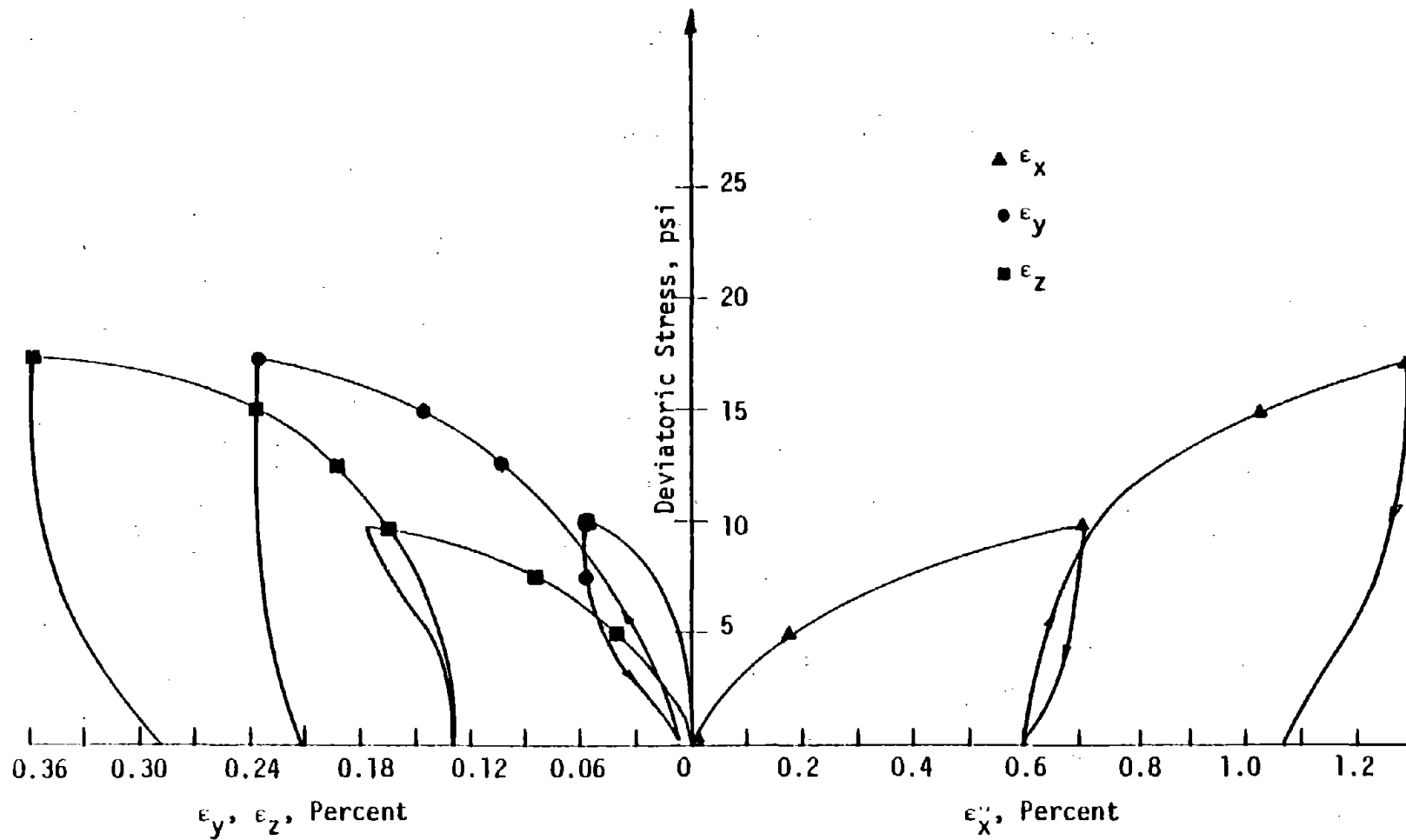
Figure 2.9   Stress-Strain Response Curves for Conventional Triaxial
Compression Test.   (σ_3 = 9 psi)
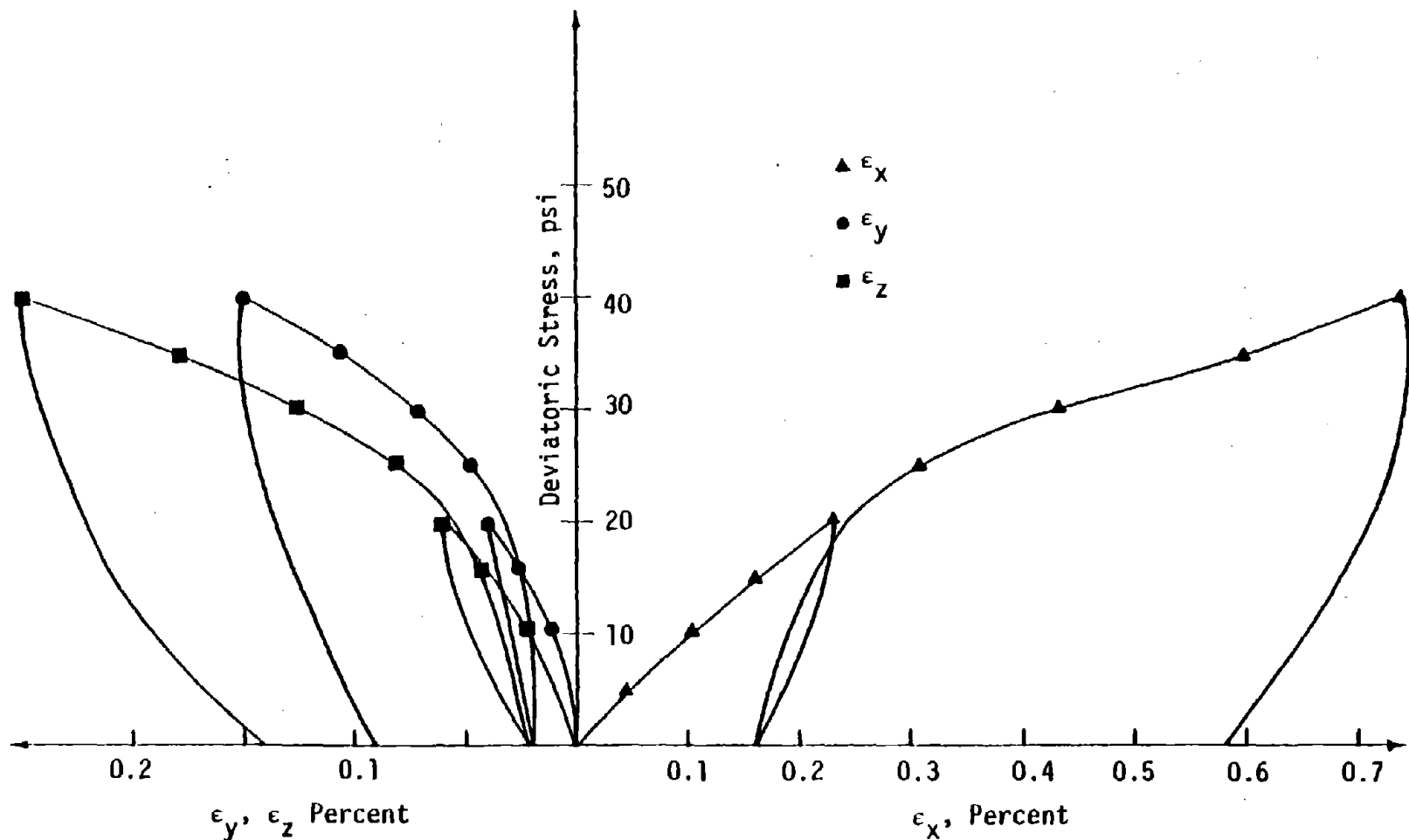
Figure 2.10   Stress-Strain Response Curves for Conventional Triaxial
Compression Test   (σ_3 = 25.00 psi)

28
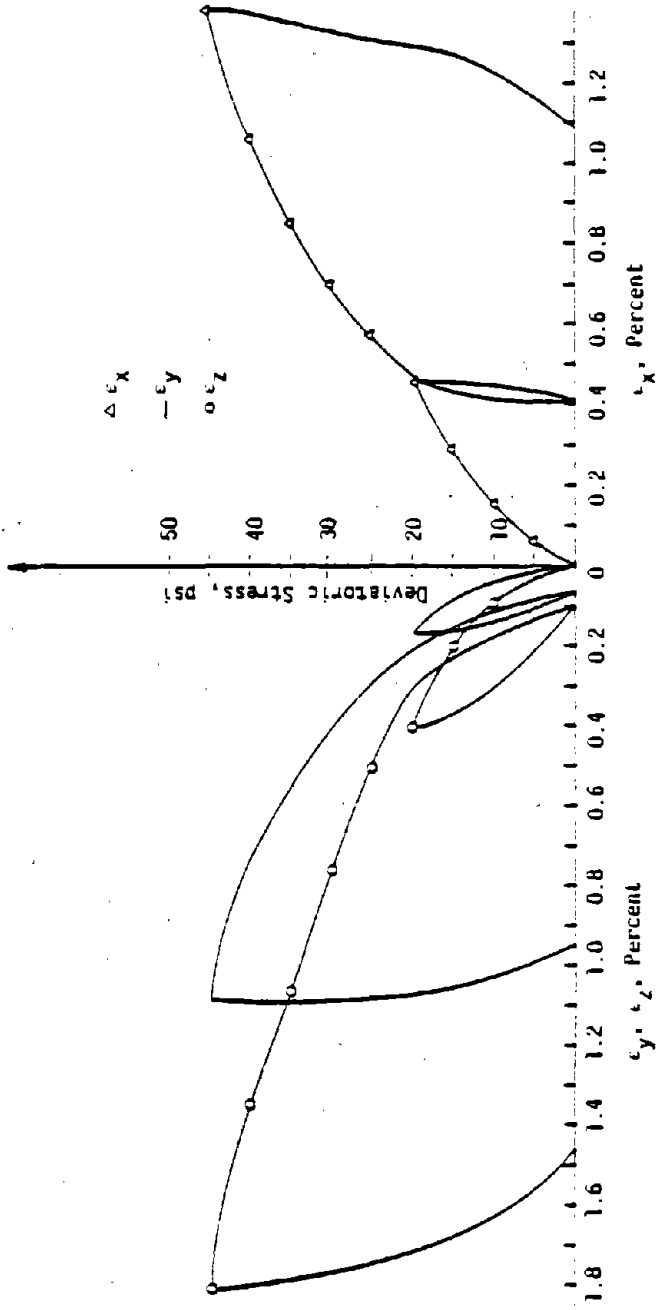
Figure 2.11 Stress-Strain Response Curves for Conventional Triaxial
Compression Test ($\sigma_3 = 35$ psi)

terminated when the strains are large and reach measuring capabilities
of the apparatus.

2.6.3 Reduced Triaxial Compression (RTC)

The subballast sample is loaded to a desired hydrostatic stress
level by increasing the pressure in steps, each increment applied
after the stabilization of load at that level. Strains are measured
in all the three direction. In a Reduced triaxial compression test,
σ_1 is held constant while σ_2 and σ_3 are reduced in stages with decre-
ment $\Delta\sigma_2$ equal to the decrement $\Delta\sigma_3$. Thus the confining pressure drops
$(\Delta\sigma_{oct} = \frac{-2\Delta\sigma_2}{3})$ as the specimen is sheared $(\Delta\tau_{oct} = (\sqrt{2}/3)\Delta\sigma_2)$. This
produces a well defined ultimate strength level at relatively small
strains of about 1.5 percent, Fig. (2.12).

The strains in the extension side of the sample seems to get
stabilized to a maximum after a certain load level, whereas the
compressive strains are increasing at a higher rate thereafter.
Several factors may contribute to this. Difference in elastic rebound
during unloading between adjacent particles due to either material
or geometric factors may leave gaps into which particles may fall.
Also sharp features in the case of broken ballast or coarse grain soil
at particle contacts may be crushed during the initial loading so that
slip occurs as the load is released.

2.6.4 Simple Shear (SS)

The state of stress of a specimen under simple shear refers to
an octahedral plane normal to the space diagonal at a given
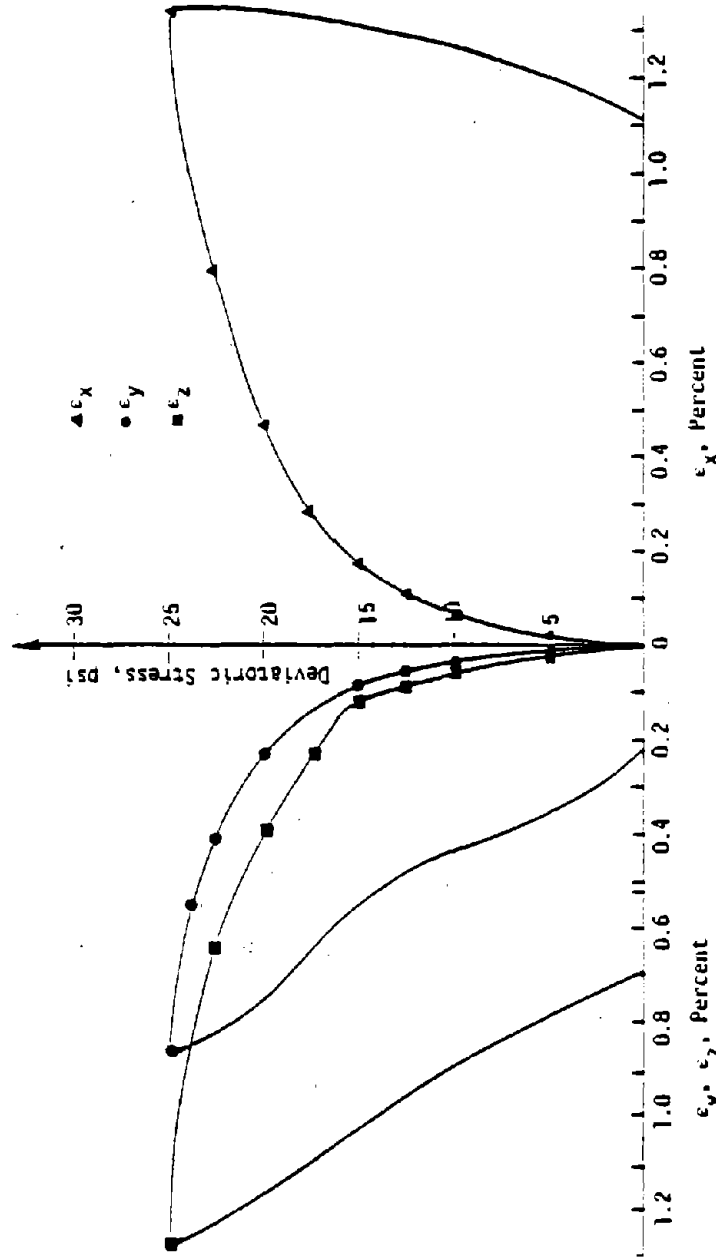
Figure 2.12 Stress-Strain Response Curves for Reduced Triaxial Compression Test

hydrostatic stress level, $\sigma_{oct} = \frac{1}{3}(\sigma_1 + \sigma_2 + \sigma_3)$. Intermediate principal stress, σ_2 is kept constant, but the major and minor principal stress, σ_1 and σ_3 are increased and decreased respectively by the same amount so that σ_{oct} remains constant. The type of decomposition of simple shear stress path is shown in Fig. (2.13). Figure (2.14) shows the results from simple shear test. The sample was compacted to an initial density of 1.92 gm/cm^3 and tested at σ_{oct} = 30.00 psi (140.00 kpa). It is significant to note that the intermediate strain is slightly compressive. A plot of octahedral shear stress τ_{oct} versus octahedral shear strain γ_{oct} is shown in Fig. (2.15). The initial slope of the curve is steep giving rise to a high value of initial shear modulus. Large shear strain increase is noticed at ultimate strength level.

2.6.5 Triaxial Compression (TC)

State of stress of a specimen under triaxial compression test also refers to an octahedral plane. In the TC stress path, major principal stress σ_1 is increased while the minor principal stresses σ_2 and σ_3 are decreased. The increment of major principal stress, $\Delta\sigma_1$ is double that of the decrement $\Delta\sigma_2 = \Delta\sigma_3$ of minor principal stress. Thus σ_{oct} remains constant because $\Delta\sigma_1 = 2\Delta\sigma_2$. As with other stress paths in the octahedral plane, this separates the effects of hydrostatic and deviatoric stress components. The sample tested in triaxial compression stress path was compacted to an initial density of 1.93 gm/cm^3 and tested at σ_{oct} = 20.00 psi (140.00 kpa). The stress-strain responses for this test are plotted in Fig. (2.16).
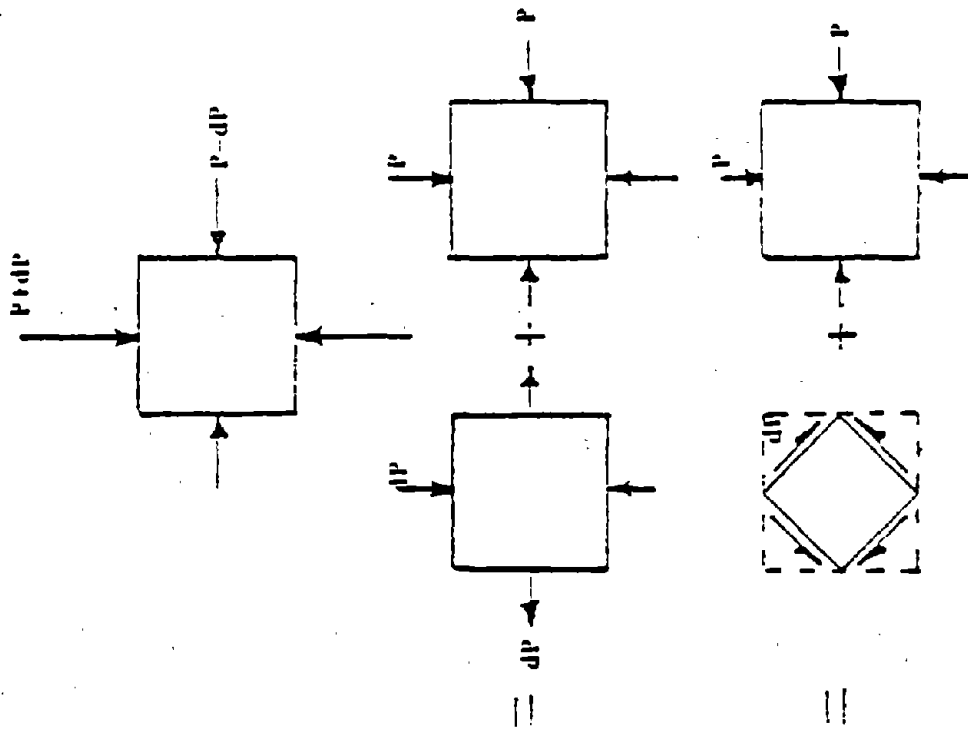
Figure 2.13   Decomposition of Simple Shear Stress Path
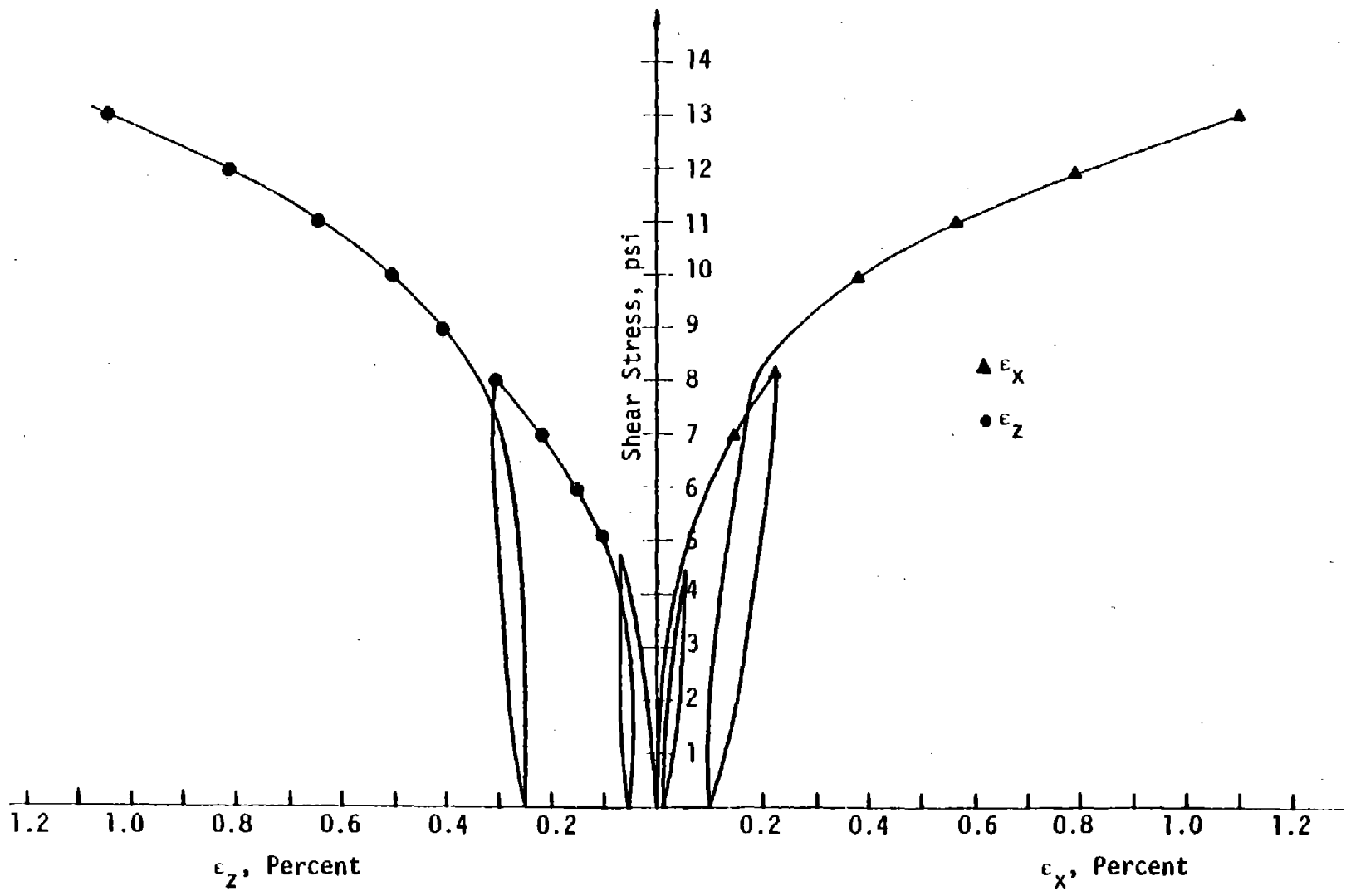
Figure 2.14 Stress-Strain Response Curves for Simple Shear Test
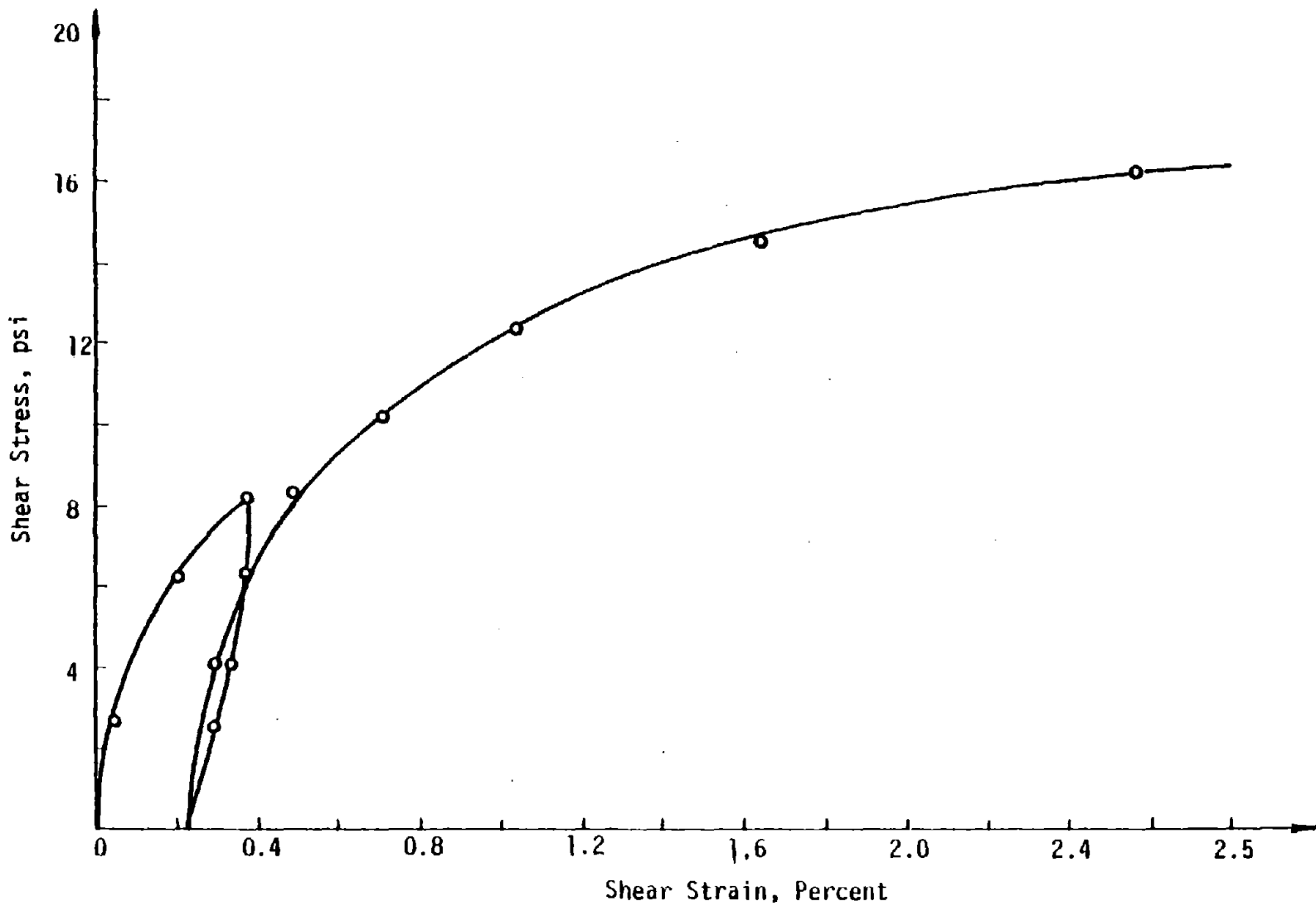
Figure 2.15 Stress-Strain (Shear Response Curves in Simple Shear Test
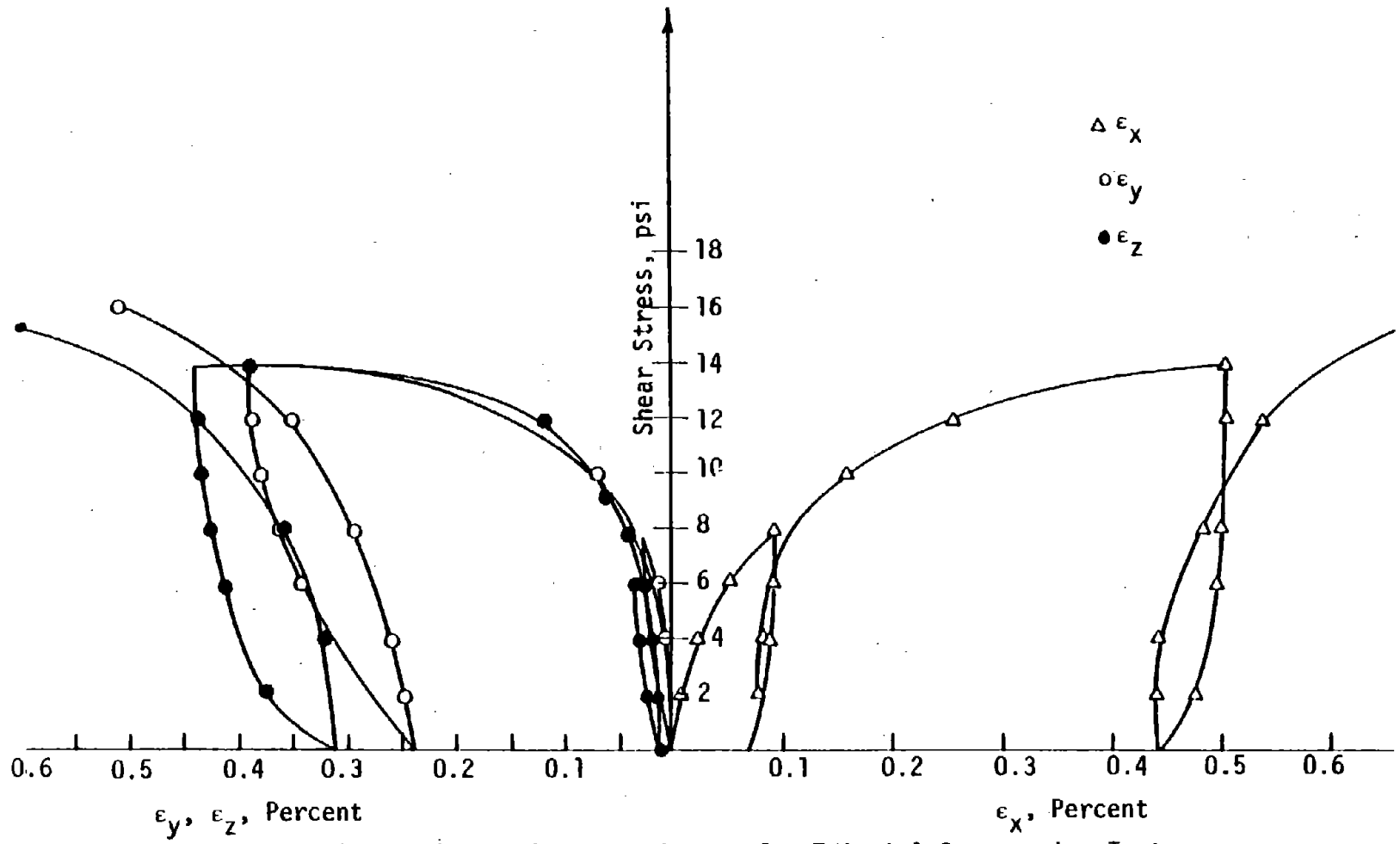
Figure 2.16 Stress-Strain Response Curves for Triaxial Compression Test

These curves exhibit a definable ultimate strength level, asymptotic to the curve. The trend of responses in the two principal directions Y and Z are almost alike; except that increased strains are observed in direction Y at low stress levels than compared to those in direction Z.

2.6.6 Triaxial Extension (TE)

In the TE test, σ_1 is reduced but σ_2 and σ_3 are increased to maintain a constant level of σ_{oct}. The decrement $\Delta\sigma_1$ is double that of increment $\Delta\sigma_2$ or $\Delta\sigma_3$, both being equal. The sample is compacted to an initial density of 1.91 gm/cm^3 and with an initial hydrostatic confining pressure of 2.00 psi (14.00 kpa). The test is conducted with σ_{oct} = 20 psi (140.00 kpa).

The response curves are plotted in Fig. (2.17). They show a well defined ultimate strength level. The responses are not the same in directions X and Y. The strain is greater in direction Y than that in direction X for the same stress level. The magnitude of ultimate shearing stress here is almost the same as that of the ultimate value in the TC test.

Note: The initial density of samples almost the same σ_{oct} = 20.00 psi (140.00 kpa) same in both cases and also initial hydrostatic confining pressure of 2.00 psi (14.00 kpa) is the same in either case.
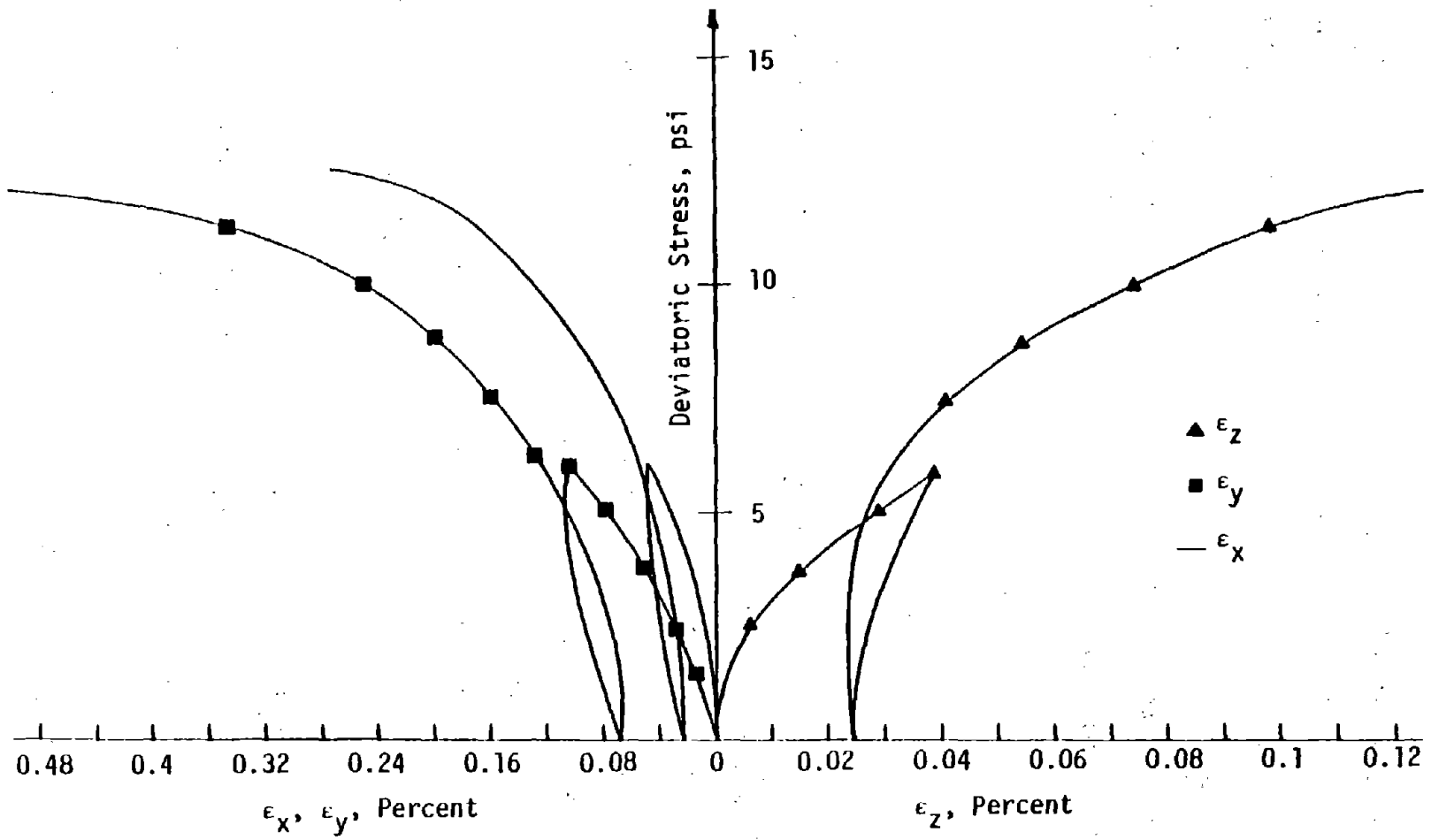
Figure 2.17   Stress-Strain Response Curves for Triaxial Extension Test

2.6.7 Effects of Stress Paths

The dependence of the shear moduli on stress paths is shown in Fig. (2.18). The shear moduli, calculated from the test results CTC, TC, and RTC are plotted against the gradients, g, of the stress paths for the three tests. The gradients g_i can be computed during an incremental loading as [24]

$$g_i = \frac{\partial(\sqrt{J_{2D}})}{\partial P}$$

or

$$g_i = \frac{\partial(\sigma_1 - \sigma_3)}{\partial \sigma_3}$$

The gradients for CTC, TC and RTC are 3.0, 0.0 and -1.50 respectively in $J_1 - \sqrt{J_{2D}}$ space.

2.7.1 CONSTITUTIVE MODELLING

Development of a viable constitutive law for a given medium is considered to involve the following steps: [14]

1. mathematical formulation,

2. identification of significant parameters,

3. determination of parameters from appropriate tests, and

4. verification with respect to laboratory test data under various stress paths.

A good material model should also satisfy the theoretical requirements needed to prove existence, uniqueness and stability conditions.

A variety of models are currently used for geologic media. The simplest of these is the elastic model, most often linear elastic.
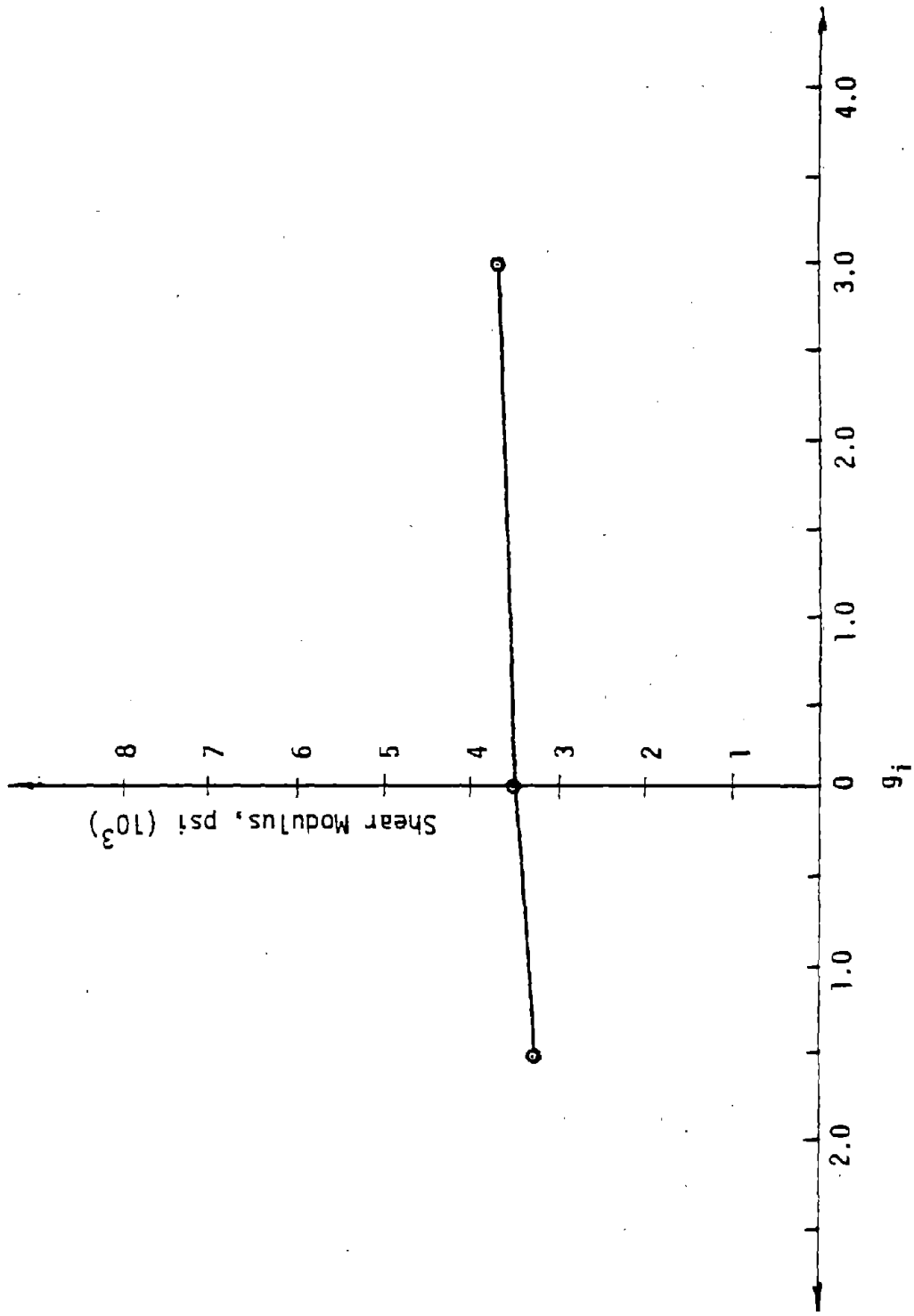
Figure 2.18   Influence of Stress Path on Shear Modulus

A brief description of the basic relationship in stress space and some discussion about elastic-plasticity are given here before the development of the material model is described.

2.7.2 Basic Relationship in the stress space

The principal stress space is defined by an orthogonal coordinate system with one of the principal stresses for each of the coordinates. A space axis is a line passing through the origin and is equally inclined to the three coordinate axes.

A state of stress can be represented by the vector $\sigma = OZ$, Fig. (2.19) originating from the origin point 0, and ending at the stress point Z. The magnitude of the stress vector

$$OZ = \sqrt{\sigma_1^2 + \sigma_2^2 + \sigma_3^2}$$

The stress tensor is represented as follows

$$\sigma_{ij} = \begin{bmatrix} \sigma_{xx} & \sigma_{xy} & \sigma_{xz} \\ & \sigma_{yy} & \sigma_{yz} \\ \text{sym} & & \sigma_{zz} \end{bmatrix} \tag{2.1}$$

In the principal stress space, the tensor components are obtained from the equation

$$\left| \sigma_{ij} - \sigma\delta_{ij} \right| = 0 \tag{2.2}$$

Which is a cubic equation in σ whose roots are the principal stress σ_1, σ_2 and σ_3
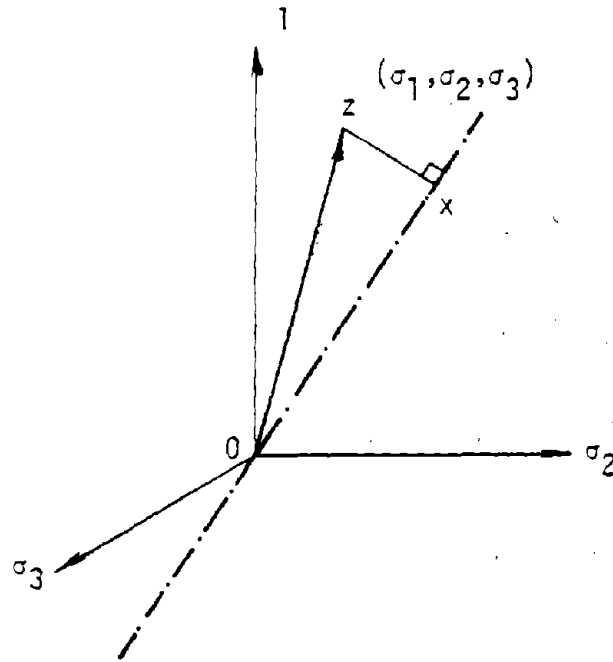
Figure 2.19   Representation of a Stress Tensor
             in the Principal Stress Space.

$$|\sigma_{ij} - \sigma\delta_{ij}| = -\sigma^3 + J_1\sigma^2 - J_2\sigma + J_3 = 0 \tag{2.3}$$

where J_1, J_2, and J_3 are the stress invariants defined as follows:

$$J_1 = \sigma_{ii} = \sigma_{xx} + \sigma_{yy} + \sigma_{zz} = \sigma_1 + \sigma_2 + \sigma_3 \tag{2.4}$$

$$J_2 = \frac{1}{2}(\sigma_{ii}\sigma_{jj} - \sigma_{ij}\sigma_{ij}) \tag{2.5}$$

$$J_2 = \begin{vmatrix} \sigma_{yy} & \sigma_{yz} \\ \sigma_{zy} & \sigma_{zz} \end{vmatrix} + \begin{vmatrix} \sigma_{xx} & \sigma_{xz} \\ \sigma_{zx} & \sigma_{zz} \end{vmatrix} + \begin{vmatrix} \sigma_{xx} & \sigma_{xy} \\ \sigma_{yx} & \sigma_{yy} \end{vmatrix} \tag{2.6}$$

$$J_2 = \sigma_1\sigma_2 + \sigma_2\sigma_3 + \sigma_3\sigma_1 \tag{2.7}$$

$$J_3 = \frac{1}{3}\sigma_{ij}\sigma_{jk}\sigma_{ki} \tag{2.8}$$

$$J_3 = \text{Det } (\sigma_{ij}) \tag{2.9}$$

$$J_3 = \sigma_1 \sigma_2 \sigma_3 \tag{2.10}$$

Then mean or octahedral or hydrostatic stress σ_m of a stress tensor is defined as follows:

$$\sigma_m = \frac{1}{3}(\sigma_{xx} + \sigma_{yy} + \sigma_{zz}) = \frac{1}{3}(\sigma_1 + \sigma_2 + \sigma_3) \tag{2.11}$$

The deviatoric stress tensor is defined as

$$S_{ij} = \sigma_{ij} - \sigma_m\delta_{ij} \tag{2.12}$$

The principal stresses of the deviatoric stress tensor are obtained from the relation

$$|S_{ij} - \sigma\delta_{ij}| = 0 \tag{2.13}$$

which is a cubic equation whose roots are the values of σ for the deviatoric stress tensor

$$\sigma^3 - J_{2D}\sigma - J_{3D} = 0 \tag{2.14}$$

where J_{2D} and J_{3D} are the deviatoric stress invariants and are defined as follows:

$$J_{2D} = \frac{1}{2} S_{ij}S_{ij}$$
$$= \frac{1}{6} [(\sigma_1 - \sigma_2)^2 + (\sigma_2 - \sigma_3)^2 + (\sigma_3 - \sigma_1)^2] \tag{2.15}$$

$$J_{3D} = \frac{1}{3} S_{ij}S_{jk}S_{ki}$$
$$= J_3 - \frac{2}{3} J_1 J_2 + \frac{2}{27} J_1^3 \tag{2.16}$$

The octahedral plane is perpendicular to the space axis, the state of stress can be conveniently represented by the projection of the stress tensor on the stress space axis and its projection on the octahedral plane can be determined if orientation angle on the octahedral plane is known.

Since the space axes are equally inclined to the coordinate axes, their direction cosines have equal magnitudes of $1/\sqrt{3}$. The projection of the stress tensor on the space axis equals $1/\sqrt{3}$ $(\sigma_1+\sigma_2+\sigma_3)$.

These relationships described above will be used for determining the state of stress for a specific stress tensor in the constitutive relationship used here.

2.7.3 Theoretical Considerations for Continuum Models

Constitutive models based on continuum theories should satisfy certain theoretical requirements [28]. These requirements insure that the initial and boundary value problems involving the constitutive model, together with the equations of continuum mechanics, be properly posed.

A major contribution to the theoretical aspects of continuum models is the introduction of Drucker's (156) stability postulate, which implies that positive work is done by an external agent in any excursion from equilibrium, which can be expressed as

$$\oint (\sigma_{ij} - \sigma_{ij}^0) \, d\varepsilon_{ij} \geq 0 \qquad (2.17)$$

The equal sign applies to only elastic or reversible paths. Satisfaction of Drucker's postulate is sufficient but not necessary to insure unique solutions and continuous dependence on the data.

A geometric interpretation of Drucker's postulates is shown in Fig. (2.20). A loading scheme in which stresses and strains vary is represented. Consider a small stress increment, $d\sigma_{ij}$ applied from a given stress state, σ_{ij} on the yield surface. The corresponding plastic strain increment, $d\varepsilon_{ij}^p$ will in general depend on the previous loading history and the stress increment.
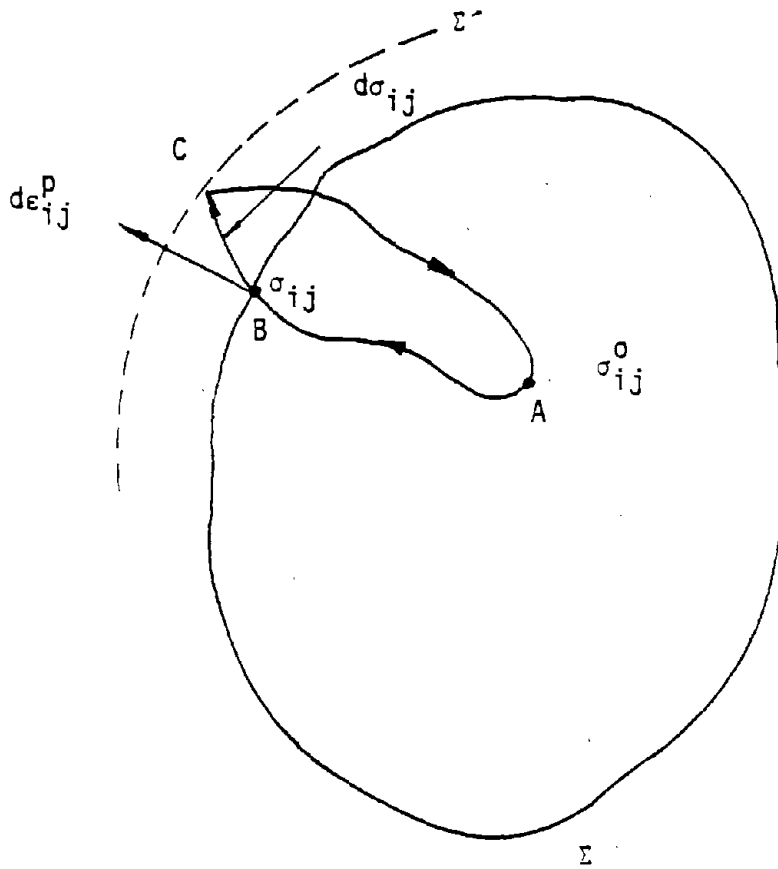
Figure 2.20 Schematic Representation of Drucker's
Stability Criterion

According to Prager [51], four conditions need to be satisfied to establish a relationship between the plastic strain increment and the corresponding state of stress. 1) continuity, 2) consistency, 3) uniqueness and 4) the irreversibility. The continuity condition states that the tangential component of a stress increment at a point on the yield surfaces constitutes a neutral loading and does not produce any plastic strains, that is, the plastic strain increment $d\varepsilon_{ij}^p$ associated with the stress increment $d\sigma_{ij}$ is entirely dependent on the normal component. In other words, a stress increment produces strains only in its own direction, in a direction normal to the yield surface.

In the plasticity theory, the strain increment $d\varepsilon_{ij}$ due to a stress increment $d\sigma_{ij}$ is to decomposed into elastic and plastic components; here it is assured that the strains are small. Then

$$d\varepsilon_{ij} = d\varepsilon_{ij}^e + d\varepsilon_{ij}^p \tag{2.18}$$

The consistancy condition requires these plastic strain increment vectors to act in the direction outward from the yield surface, whereas the uniqueness condition requires that for a given set of final boundary values, a unique solution for stress and strain must exist in the interior of the body. This uniqueness condition can be related to the concept of work hardening and perfect plasticity. A material is said to work-harden if in a stress-strain diagram, stress is a monotonically increasing function of strain [29, 51]. In other words, if the product of an increment of stress and its corresponding increment of

strain, Fig. (2.21), is positive, the material is said to be work-hardening. Work-hardening indicates that the deformations are stable, but work softening leads to instability. Work-hardening thus implies that (1) positive work is done by an external agent during the application of the set of stresses, and 2) the net work performed by it over the cycle of application and removal is zero or positive. These two conditions, when put into mathematical form, yield the Drucker's stability postulate.

$$d\sigma_{ij} \; d\varepsilon_{ij} \geq 0 \qquad\qquad (2.19)$$

By using the condition of continuity, this equation is modified as

$$d\sigma_{ij} \; (d\varepsilon_{ij} - d\varepsilon_{ij}^e) > 0 \qquad\qquad (2.20)$$

Since

$$d\varepsilon_{ij} = d\varepsilon_{ij}^e + d\varepsilon_{ij}^p \qquad\qquad (2.21)$$

The Drucker's stability postulate can be written as

$$d\sigma_{ij} \; d\varepsilon_{ij}^p \geq 0 \qquad\qquad (2.22)$$

This is a mathematical definition of work hardening and also this condition implies that the yield surface should be convex and the plastic strain increment vectors orthogonal to the yield surface. In summary, uniqueness and stability follow if normality is satisfied on a convex yield surface.
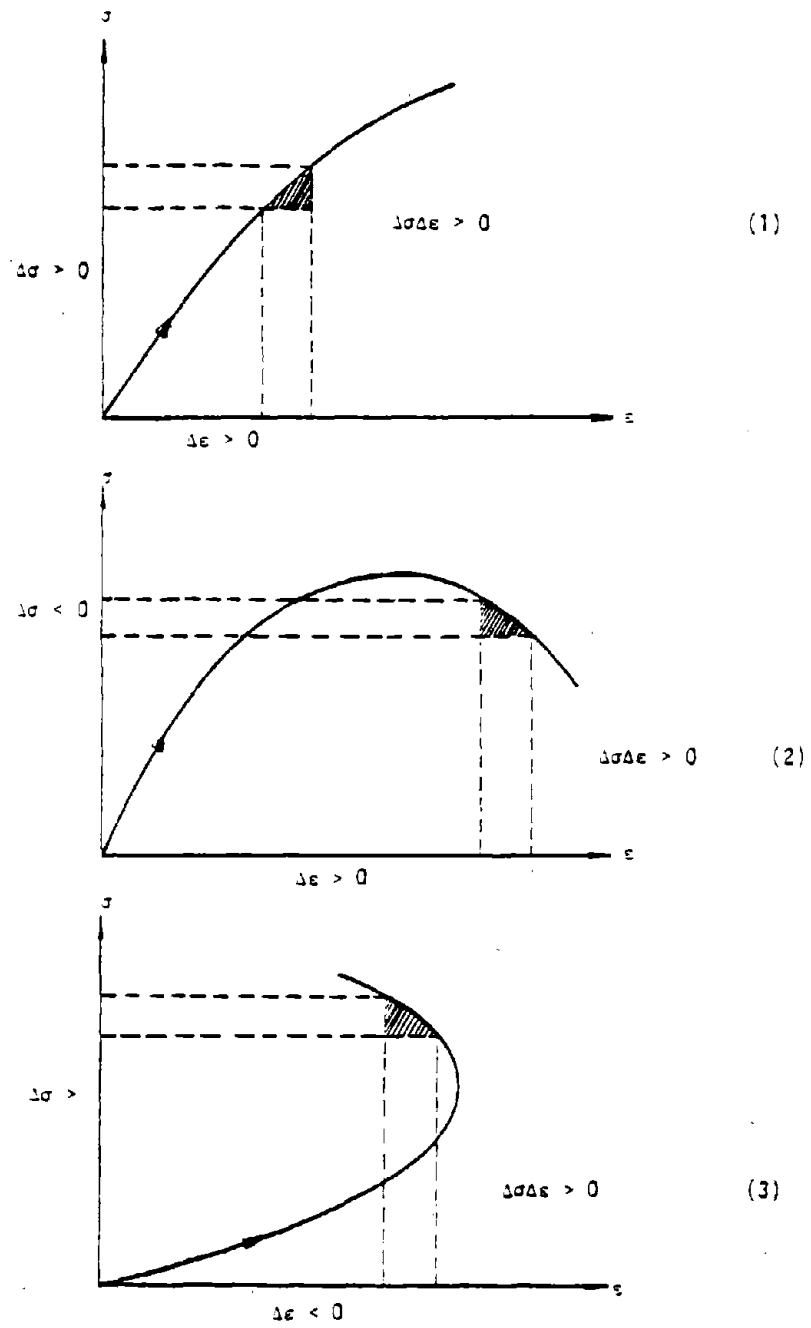
Figure 2.21 Stress-Strain Curve for Work-Hardening Material

For an ideally plastic material, the Drucker's postulate can be written as

$$d\sigma_{ij}\, d\epsilon^p_{ij} = 0 \tag{2.23}$$

It means that work done by the external agent, which applies slowly and then removes, a set of stresses is zero over an equilibrium cycle.

A further assumption in the yield surface is function of stress alone, $F(\sigma_{ij})$. The material is elastic for $F(\sigma_{ij}) < 0$ and when $F(\sigma_{ij}) = 0$, plastic deformation takes place.

It is the nature of plastic or elasto-plastic materials to flow to whenever they are subjected to stresses that bring them to yield. If Q is the potential function, the velocity components of such a flow must be directly proportional to the partial derivatives of the potential function

$$d\epsilon^p_{ij} = \lambda\, \frac{\partial Q}{\partial \sigma_{ij}} \tag{2.24}$$

where λ is a scalar factor of proportionality. In this case, the plastic strain increment $d\epsilon^p_{ij}$ are the velocity components and further the potential function Q is a function of the components stress.

If the yield function $F(\sigma_{ij})$ also serves as the potential function for the flow, it can be written

$$d\epsilon^p_{ij} = \lambda\, \frac{\partial F}{\partial \sigma_{ij}} \tag{2.25}$$

which is the equation of normality and the material is said to follow the associated flow rule [37,51].

If yield function $F(\sigma_{ij})$ is not the same as the potential function, then the material is said to follow non-associated flow laws in which normality is associated to a plastic potential function rather than to a yield function.

From the observed stress-strain response of subballast, it is concluded to be a work-hardening material and the foregoing relations are used in deriving the material model for it.

2.7.4 Review of Models

Conventional Plasticity Models

In elastic-ideally plastic model, there is fixed yield condition given by

$$F(\sigma_{ij}) = 0 \qquad (2.26)$$

which restricts the magnitude of the stress. If the material is isotropic, the yield condition can depend only on the principal stresses or alternatively the stress invariants.

$$F(J_1, J_2, J_3) = 0 \qquad (2.27)$$

Before yield, within the yield surface the material is elastic.

$$d\varepsilon_{ij}^e = \frac{1}{2G} dS_{ij} + \frac{1}{9K} \delta_{ij} dJ_1 \qquad (2.28)$$

where $d\varepsilon_{ij}^e$ is the elastic strain increment, dS_{ij} the increment of

the deviatoric stress tensor. Linear elastic model is usually not suitable for geologic materials.

The simplest form of the yield condition is the vonMises condition.

$$F = \sqrt{J_{2D}} - k_1 = 0 \qquad (2.29)$$

where J_{2D} is the second invariant of the deviatoric stress tensor given by $J_{2D} = \frac{1}{2} S_{ij} S_{ij}$ and k_1 is a constant. The von Mises criterion plots as a cylinder in the principal stress space, Fig. (2.22), and can be used for saturated clays.

A more realistic yield condition for granular material is

$$\sqrt{J_{2D}} = k + \alpha J_1 \qquad (2.30)$$

as was suggested by Drucker and Prager (1952). This yield surface is a cone, opening towards the positive (compressive) J_1 axes, Fig. (2.23). This criterion is independent of the third stress invariant. When used with the associated flow rule, this model satisfies Drucker's postulates, insuring unique solution, but has the following short comings [26].

(1) The amount of dilatancy (plastic volume increase under shear loading) predicted is much greater than observed experimentally.

(2) Tests indicate a considerable hysteresis in a hydrostatic loading-unloading path, which cannot be predicted by using the same

VON MISES FAILURE SURFACE
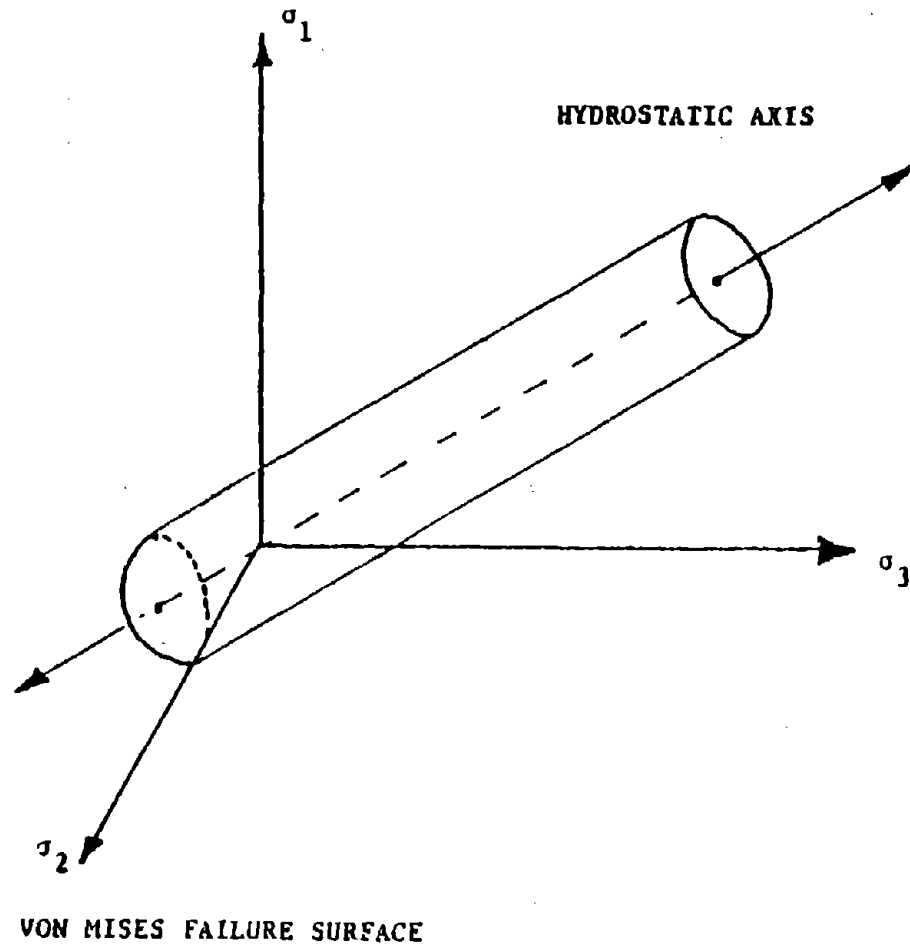
Figure 2.22 Failure Surface in Principal Stress Space
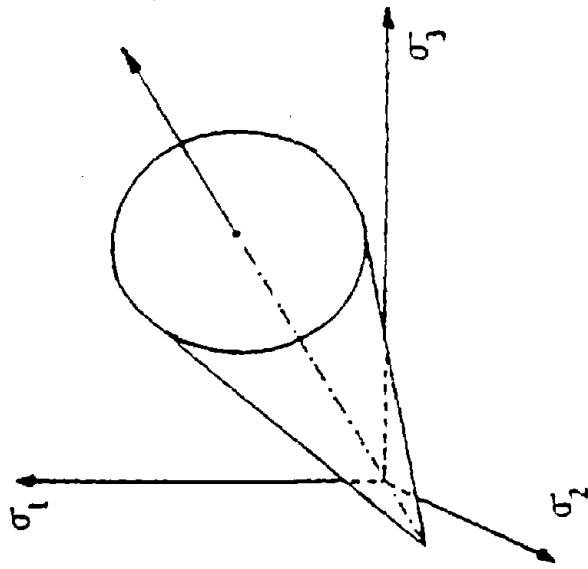
Figure 2.23 Drucker-Prager Failure Surface

elastic modulus of loading and unloading and a yield surface which does not cross the hydrostatic loading J_1 axis, and

(3) at high pressure levels, as the material passes to a fluid state, shear strength should not vary with hdrostatic pressure, namely the yield condition should be essentially independent of J_1 for large J_1.

Variable Moduli Model

Nelson and Baron [47] have proposed two models which do not have the physical shortcomings of that proposed by Drucker and Prager, but are not mathematically convenient with respect to continuity or uniqueness conditions or both. One model uses a modified Drucker-Prager yield condition.

$$F = \sqrt{J_{2D}} - k + \alpha J_1 \left(1 + \frac{J_1}{2C}\right) = 0, \quad \text{when } J_1 + C \geq 0 \qquad (2.31)$$

$$= \sqrt{J_{2D}} - k - \frac{\alpha C}{2} = 0, \quad \text{when } J_1 + C \leq 0 \qquad (2.32)$$

in which c corresponds to a transition pressure, a non-associated flow rule using the Mises yield function as plastic potential, that is

$$Q = \sqrt{J_{2D}} - k \qquad (2.33)$$

and different bulk moduli $K_1(J_1)$ and $K_2(J_1)$ on loading and unloading respectively. The yield function of Eq. (2.31), which approximates the Drucker-Prager relation for $J_1 \ll C$ gives the constant shear strength of a Mises material for $J_1 \geq C$. Use of the plastic potential

of Eq. (2.33) precludes dilatancy, while adoption of different bulk moduli for loading and unloading permits hysteresis.

In the second model, no yield condition is explicitly specified and the strain is not decomposed into an elastic and plastic part. By letting S_{ij} and ε_{ij} to be the deviatoric stress and strain tensors, respectively and ε_v be the volumetric strain (dialation), this model stipulates that

$$S_{ij} = 2G_L \, \varepsilon_{ij} \qquad \text{if } J_{2D} > 0 \qquad\qquad (2.34)$$

$$= 2G_U \, \varepsilon_{ij} \qquad \text{if } J_{2D} \leq 0 \qquad\qquad (2.35)$$

and

$$J_1 = 3K_L \, \varepsilon_v \qquad \text{if } J_1 < 0 \qquad\qquad (2.36)$$

$$= 3K_U \, \varepsilon_v \qquad \text{if } J_1 \geq 0 \qquad\qquad (2.37)$$

Equation (2.34) does not satisfy the continuity requirements that there should be a finite difference in response for loading and unloading paths infinitesimally close to neutral loading ($J_{2D} = 0$).

Cap Model

In order to reproduce the hysteresis which materials display when loaded and unloaded hydrostatically, Drucker, Givson and Henkel proposed modification to the Drucker-Prager yield condition of Eq. (2.30), by adding a work-hardening cap to it which crosses the hydrostatic loading axis.

Sandler and DiMaggio (1971) developed a model Fig. (2.24) combining ideal plasticity and strain hardening. An ideally plastic modified Drucker-Prager yield condition is denoted by

$$F(J_1, \sqrt{J_{2D}}) = 0 \tag{2.38}$$

and the strain-hardening cap, which expands or contracts as the plastic volumetric strain decreases or increases respectively, is

$$F(J_1, \sqrt{J_{2D}}, \varepsilon^p) = 0 \tag{2.39}$$

These are used with the associated flow rule. At the intersection of the yield curves of Eqs. (2.38) and (2.39), there is a corner, where the plastic strain rate vector is normal to the intersecting surfaces. The elastic behavior in loading and unloading is assumed to be governed by constant shear and bulk moduli. Because the movement of the cap is controlled by the increase or decrease of plastic volumetric strain, strain hardening is reversible in this method for some loading paths.

The (isotropic) cap model has theyield surface, which is composed of two parts, a fixed failure envelop (Drucker-Prager) of the form

$$\sqrt{J_{2D}} = \alpha + \beta J_1 \tag{2.40}$$

at low pressures, and

$$\sqrt{J_{2D}} - K_2 = 0 \tag{2.41}$$
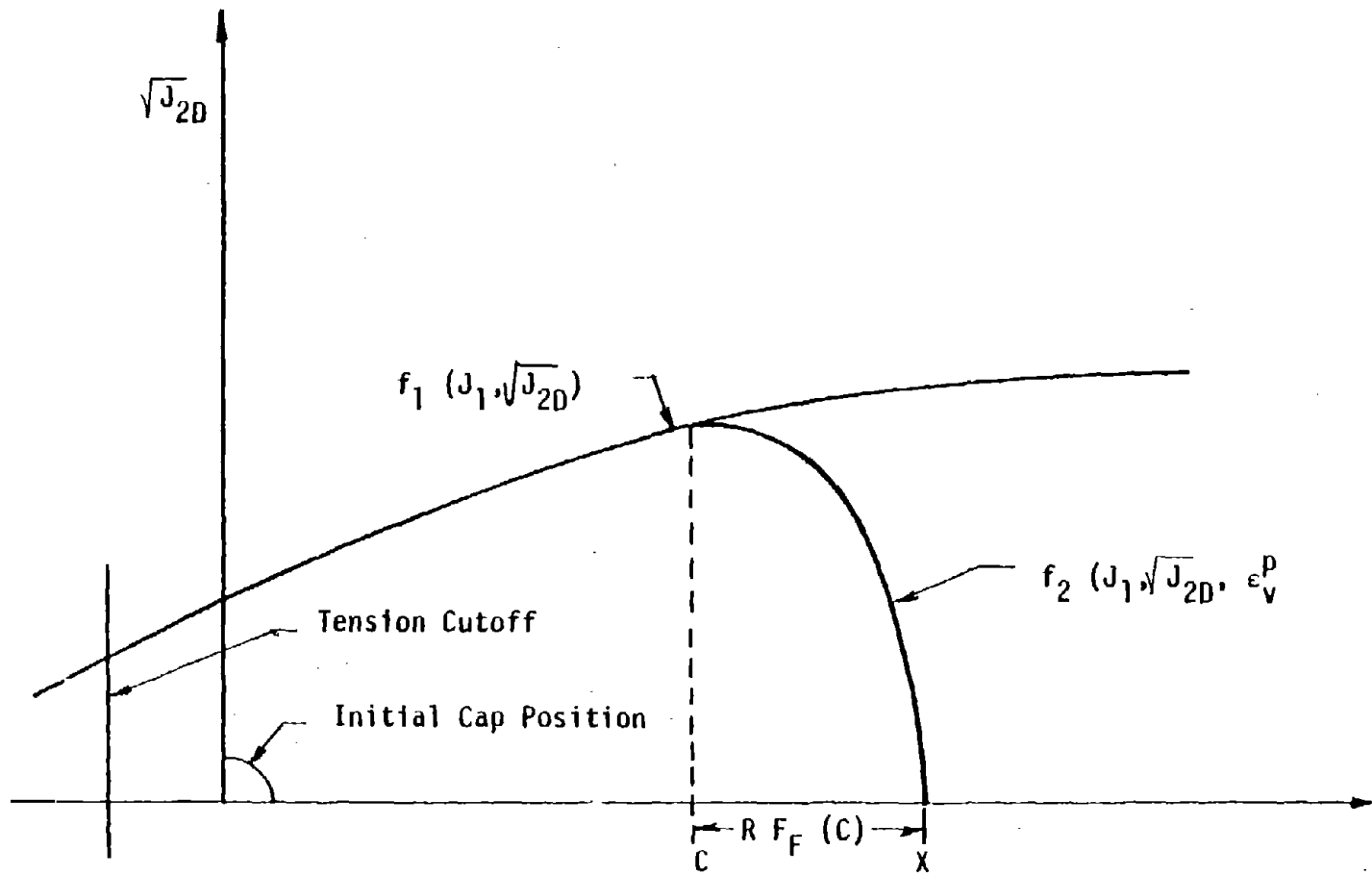
Figure 2.24 Representation of Cap Parameters in $J_1 - \sqrt{J_{2D}}$ Space

(vonMises condition) at high pressures, and a movable cap which crosses the J_1 axis. The combined yield surface is every where convex, Fig. (2.24).

The motion of the cap is related to the plastic strain by means of a hardening rule. An elliptical surface is of the form

$$R^2 J_{2D} + (J_1 - L)^2 = R^2 b^2 \qquad (2.42)$$

where $Rb = (X-L)$ and R is the ratio between the principal axes in the ellipse, X is J_1 value at the intersection between the ellipse and J_1 axis, L is J_1 value at the center of the ellipse and b is $\sqrt{J_{2D}}$ value when $J_1 = L$. The cap consists of a family of similar ellipses, each of which corresponds to a value of ε_v^p, whose axes are parallel to the J_1 and $\sqrt{J_{2D}}$ axes and whose center lies on $\sqrt{J_{2D}} = 0$ directly below the intersection point of each ellipse with the failure envelop. The tangent to the elliptical cap at its intersection with failure envelop will be horizontal. If it is not so, the plastic strain vector would suddenly become vertical, when the failure surface is reached rather than approach this position gradually. This would lead to discontinuity in slope in stress-strain diagram of a tri-axial stress test. X is related to the mean stress level and it is a function of the volumetric plastic strain as

$$3\sigma_{oct} = X = \frac{1}{D} \ln \left(1 + \frac{\varepsilon_v^p}{W}\right) + Z \qquad (2.43)$$

where W characterizes the maximum volumetric strain, D the total volumetric strain rate and Z the initial elastic portion of the
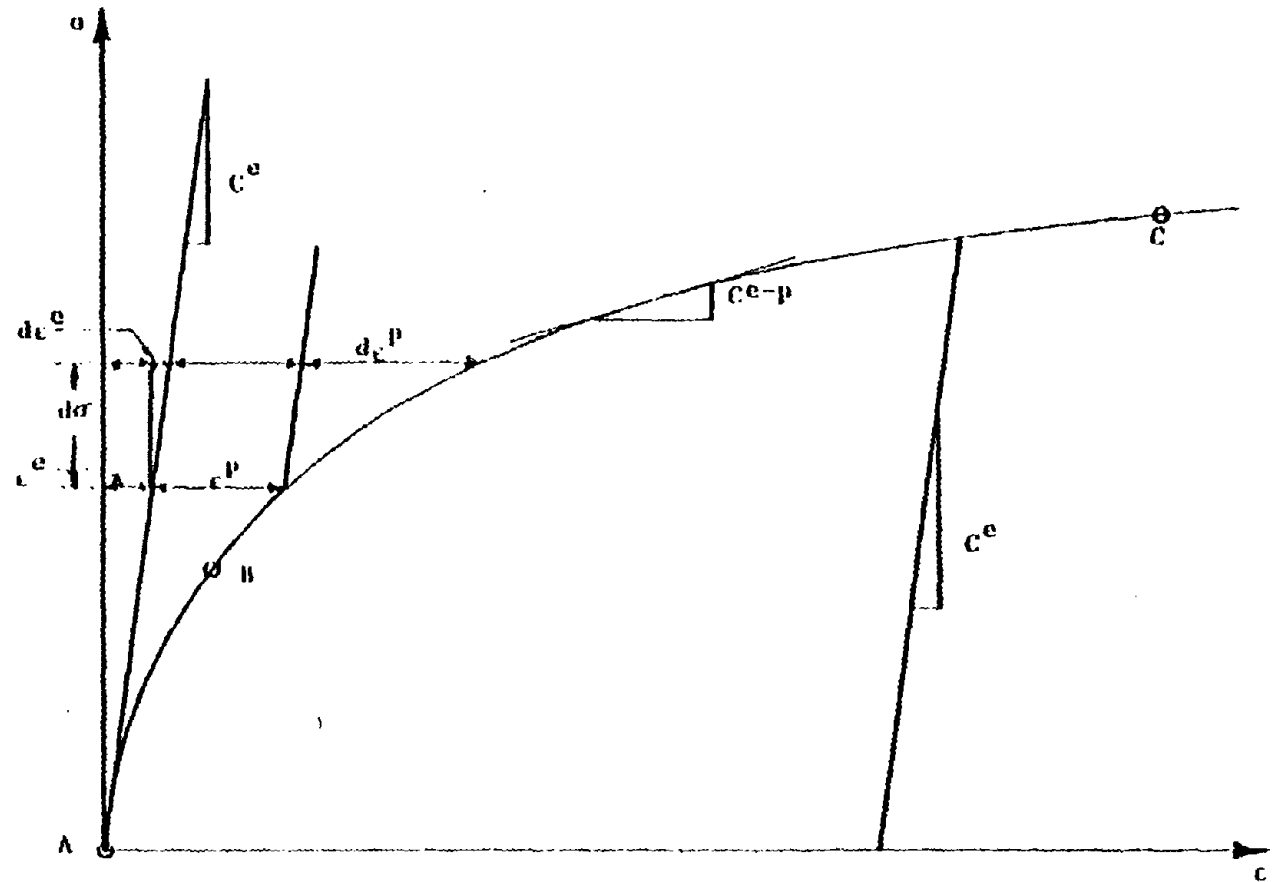
Figure 2.25   Stress-Strain Response Curve for Elastic-Hardening Material

volumetric stress-total strain curve. The role of parameters in simple cap model is given in the Table 2.1.

2.8 Details of Cap Model

Some classical plasticity relations and associated terminology are discussed below. These are used to make the derivation of an isotropic cap model for the subballast. Although it is seen that the material exhibits anisotropy, it is proposed to use this model as an approximation by using average of the responses.

The principles of continuity and consistancy in Drucker's postulate enable to decompose an incremental strain tensor into elastic part and plastic part as

$$d\epsilon_{ij} = d\epsilon_{ij}^e + d\epsilon_{ij}^p \qquad (2.44)$$

These relations are shown schematically in the stress-strain response curve, Fig. (2.25), for a hardening material. Hook's law for a linear elastic isotropic material can be written in the incremental form as [17]

$$d\epsilon_{ij}^e = \frac{1-2\nu}{E} \delta_{ij} (d\sigma_{kk}) + \frac{dS_{ij}}{2G} \qquad (2.45a)$$

or

$$d\sigma_{ij} = C_{ijkl} d\epsilon_{kl}^e \qquad (2.45b)$$

where δ_{ij} is Kronecker delta dnd C_{ijkl} is the constitutive tensor of the material.

Table 2.1

Role of Parameters in Simple Cap Model

Parameter	Role in Model	Effect on Behavior
K	Elastic Bulk Modulus	Controls Volumetric Behavior During Unloading
G	Elastic Shear Modulus	Controls Shear Behavior During Unloading
A	Mises Failure Limit	Maximum Shear Stress Which can be Supported by Material
B	Rate at which Failure Envelope Approaches Max.	Controls Angle of Friction Low Pressures
C	Shear Strength at Zero Pressure	Cohesion
W	Maximum Plastic Volumetric Strain	Locking Strain-Unfilled Voids
D	Rate at which Compaction Occurs with Pressure	Controls Initial Loading Moduli
R	Shape Factor for Cap	Controls Loading Stress Path in Hydrostatic Strain

Substituting for $d\varepsilon_{kl}^{e}$ in this equation gives

$$d\sigma_{ij} = C_{ijkl} (d\varepsilon_{kl} - d\varepsilon_{kl}^{p}) \qquad (2.46)$$

If $F(\sigma_{ij}) < 0$, $d\varepsilon_{ij}^{p} = 0$ indicates loading in the elastic range. In classical metal plasticity $d\varepsilon_{kk}^{p} = 0$ and in case of geologic materials $d\varepsilon_{kk}^{p} \geq 0$ to accommodate dilatancy. So the yield function can now be written as

$$F = F(\sigma_{ij}, d\varepsilon_{ij}^{p}) \leq 0 \qquad (2.47)$$

The yield function is equal to zero during loading and expansion of the strain hardening yield surface,

$$F(\sigma_{ij}, d\varepsilon_{ij}^{p}) = 0 \qquad (2.48)$$

The elastic strains can be eliminated from the normality rule

$$d\varepsilon_{ij}^{p} = d\lambda \frac{\partial F}{\partial \sigma_{ij}} \qquad (2.49)$$

and then strain decomposition equation by differentiating the above equation

$$\frac{\partial F}{\partial \sigma_{ij}} d\sigma_{ij} + \frac{\partial F}{\partial \varepsilon_{ij}^{p}} d\varepsilon_{ij}^{p} = 0 \qquad (2.50)$$

After rearranging, it can be written as

$$\frac{\partial F}{\partial \sigma_{ij}} d\sigma_{ij} = - \frac{\partial F}{\partial \varepsilon_{ij}^{p}} d\varepsilon_{ij}^{p} \qquad (2.51)$$

Substituting the Eq. (2.46) and (2.49) in (2.51)

$$\frac{\partial F}{\partial \sigma_{ij}} C_{ijkl}(d\varepsilon_{kl} - d\varepsilon_{kl}^p) = - \frac{\partial F}{\partial \varepsilon_{ij}^p} d\lambda \frac{\partial F}{\partial \sigma_{ij}} \tag{2.52}$$

$$d\lambda([- \frac{\partial F}{\partial \varepsilon_{ij}^p} \frac{\partial F}{\partial \sigma_{ij}}] + \frac{\partial F}{\partial \sigma_{ij}} \frac{\partial F}{\partial \sigma_{kl}} C_{ijkl}) = \frac{\partial F}{\partial \sigma_{ij}} C_{ijkl} d\varepsilon_{kl} \tag{2.53}$$

So the scalar parameter of proportionality can be written as

$$d\lambda = \frac{\frac{\partial F}{\partial \sigma_{ij}} C_{ijkl} d\varepsilon_{kl}}{(\frac{\partial F}{\partial \sigma_{ij}} \frac{\partial F}{\partial \sigma_{kl}} C_{ijkl} - \frac{\partial F}{\partial \sigma_{ij}} \frac{\partial F}{\partial \varepsilon_{ij}^p})} \tag{2.54}$$

Equation (2.54) when substituted back in Eqs. (2.45) and (2.49) yields

$$d\sigma_{ij} = C_{ijkl} (d\varepsilon_{kl} - d\lambda \frac{\partial F}{\partial \sigma_{ij}}) \tag{2.55}$$

$$d\sigma_{ij} = (C_{ijkl} - \frac{C_{rskl} \frac{\partial F}{\partial \sigma_{kl}} \frac{\partial F}{\partial \sigma_{ij}} C_{ijkl}}{\frac{\partial F}{\partial \sigma_{ij}} C_{ijkl} \frac{\partial F}{\partial \sigma_{kl}} - \frac{\partial F}{\partial \varepsilon_{ij}^p} \frac{\partial F}{\partial \sigma_{ij}}}) d\varepsilon_{kl} \tag{2.56}$$

or

$$d\sigma_{ij} = (C_{ijkl}^e - C_{ijkl}^p) d\varepsilon_{kl} \tag{2.57}$$

This can be rewritten as

$$d\sigma_{ij} = C_{ijkl}^{e-p} d\varepsilon_{kl} \tag{2.58}$$

where C_{ijkl}^{e-p} is known as the elasto-plastic constitutive tensor.

$\frac{\partial F}{\partial \sigma_{ij}}$ and $\frac{\partial F}{\partial \epsilon_{ij}^p}$ must be evaluated from a given yield function. $\frac{\partial F}{\partial \sigma_{ij}}$

in the Eqs. (2.54) and 2.55) can be expanded by the chain rule.

$$\frac{\partial F}{\partial \sigma_{ij}} = (\frac{\partial F}{\partial J_1} \frac{\partial J_1}{\partial \sigma_{ij}}) + (\frac{\partial F}{\partial J_{2D}} \frac{\partial J_{2D}}{\partial \sigma_{ij}}) + (\frac{\partial F}{\partial J_3} \frac{\partial J_3}{\partial \sigma_{ij}}) \qquad (2.59)$$

The stress-strain response of some geologic materials may not be influenced by the third stress invariant J_3. So the last term in Eq. (2.59) can be dropped. The other terms can be evaluated. F corresponds to the corresponding yield function or ultimate strength function depending upon the stress point considered.

When the potential surfaces are plotted in space J_1 vs $\sqrt{J_{2D}}$, Fig. (2.27), with the plastic strain increment vectors, the coefficients of the two strain invariants α and β for I_1^p and I_{2D}^p are to be established from the work relations principle in plasticity. I_1^p is the first invariant of the plastic strain tensor and I_{2D}^p is the second invariant of the plastic strain deviator tensor.

2.8.1 Evaluation of α and β from Work Relation

Usually the yield and potential surfaces are plotted in J_1 vs $\sqrt{J_{2D}}$ space. Increments of plastic strain vectors and total plastic volumetric strain are plotted in the same space. In order that they are consistant with the work relation in plasticity, the plot of plastic strain invariants such as I_1^p and I_{2D}^p should have appropriate factors α and β respectively. In other words, the plastic strain

vectors should be plotted with respect to αI_1^p and βI_{2D}^p. In the following, the values of α and β are evaluated for various stress paths. The plastic work increment in three dimensions can be written as

$$dW^p = \sigma_1 d\varepsilon_1^p + \sigma_2 d\varepsilon_2^p + \sigma_3 d\varepsilon_3^p \qquad (2.60)$$

where σ_1, σ_2, and σ_3 are arbitrary total stress states and $d\varepsilon_1^p$, $d\varepsilon_2^p$ and $d\varepsilon_3^p$ the associated plastic strain increments, when the plastic work increment is written in terms of stress and strain invariants, it is

$$dW^p = J_{2D}^{1/2} (\alpha dI_{2D}^{p\ 1/2}) + J_1 (\beta dI_1^p) \qquad (2.61)$$

The coefficients α and β are to be determined in order to establish equivalence between Eqs. (2.60) and (2.61).

$$dI_1^p = d\varepsilon_1^p + d\varepsilon_2^p + d\varepsilon_3^p \qquad (2.62)$$

$$(dI_{2D}^p)^{1/2} = \frac{1}{\sqrt{6}} [(d\varepsilon_1^p - d\varepsilon_2^p)^2 + (d\varepsilon_2^p - d\varepsilon_3^p)^2 + (d\varepsilon_3^p - d\varepsilon_1^p)^2] \qquad (2.63)$$

The coefficients α and β are determined for the three straight line stress paths.

CTC, RTC, TC, Stress Paths

For these stress paths $\sigma_1 \geq \sigma_2 = \sigma_3$ and thus

$$J_1 = \sigma_1 + 2\sigma_3 \qquad (2.64)$$

$$J_{2D}^{1/2} = \frac{1}{\sqrt{3}} (\sigma_1 - \sigma_3) \tag{2.65}$$

$$dI_1^p = d\varepsilon_1^p + 2d\varepsilon_3^p \tag{2.66}$$

and

$$(dI_{2D}^p)^{1/2} = \frac{1}{\sqrt{3}} (d\varepsilon_1^p - 2d\varepsilon_3^p) \tag{2.67}$$

Substitution of these values in Eq. (2.61), gives

$$dW^p = \frac{1}{\sqrt{3}} (\sigma_1 - \sigma_3) \frac{\alpha}{\sqrt{3}} (d\varepsilon_1^p - d\varepsilon_3^p) + \\ (\sigma_1 + 2\sigma_3) (d\varepsilon_1^p + 2d\varepsilon_3^p) \tag{2.68}$$

Rearranging this equation gives

$$dW^p = \sigma_1 d\varepsilon_1^p (\frac{\alpha}{3} + \beta) + \sigma_3 d\varepsilon_3^p (\frac{\alpha}{3} + 4\beta) \\ + (\sigma_3 d\varepsilon_1^p + \sigma_3 d\varepsilon_3^p) (-\frac{\alpha}{3} + 2\beta) \tag{2.69}$$

Rewriting the Eq. (2.60) for these stress paths as

$$dW^p = \sigma_1 d\varepsilon_1^p + 2\sigma_3 d\varepsilon_3^p \tag{2.70}$$

Equation (2.70) can be equivalent to (2.69) only if $\alpha = 2$ and $\beta = 1/3$.

CTE, RTE, TE Stress Paths

For these stress paths $\sigma_1 = \sigma_2 \geq \sigma_3$ and so the invariants are

$$J_1 = 2\sigma_1 + \sigma_3 \tag{2.71}$$

$$J_{2D}^{1/2} = \frac{1}{\sqrt{3}} (\sigma_1 - \sigma_3) \tag{2.72}$$

$$dI_1^p = 2d\epsilon_1^p + d\epsilon_3^p \tag{2.73}$$

$$(dI_{2D}^p)^{1/2} = \frac{1}{\sqrt{3}} (d\epsilon_1^p - d\epsilon_3^p) \tag{2.74}$$

Substituting these values in Eq. (2.61), it gives

$$dW^p = \frac{1}{\sqrt{3}} (\sigma_1 - \sigma_3) \frac{\alpha}{\sqrt{3}} (d\epsilon_1^p - d\epsilon_3^p) +$$

$$(2\sigma_1 + \sigma_3) \beta(2d\epsilon_1^p + d\epsilon_3^p) \tag{2.75}$$

Rearranging this equation gives

$$dW^p = \sigma_1 d\epsilon_1^p (\frac{\alpha}{3} + 4\beta) + \sigma_3 d\epsilon_3^p (\frac{\alpha}{3} + \beta) +$$

$$(\sigma_3 d\epsilon_1^p + \sigma_1 d\epsilon_3^p) (- \frac{\alpha}{3} + 2\beta) \tag{2.76}$$

The Eq. (2.60) for these stress paths is rewritten as

$$dW^p = 2\sigma_1 d\epsilon_1^p + \sigma_3 d\epsilon_3^p \tag{2.77}$$

and this Eq. (2.77) will be equivalent to (2.76) only if $\alpha = 2$ and $\beta = 1/3$.

S.S. Stress Path

In this stress path, the state of stress is $\sigma_1 \geq \sigma_2 \geq \sigma_3$ whereas σ_{oct} is a constant. The stress increments have equal magnitude but opposite sign, as

$$\sigma_1 + \Delta\sigma_1 > \sigma_2 > \sigma_3 + \Delta\sigma_3 \tag{2.78}$$

$$\Delta\sigma_1 = -\Delta\sigma_3 \qquad (2.79)$$

The intermediate principal stress σ_2 remains constant. The octahedral normal stress increment is zero.

In the case of HC path,

$$\sigma_1 = \sigma_2 = \sigma_3 = \sigma_{oct} \qquad (2.80)$$

$$\varepsilon_1^p = \varepsilon_2^p = \varepsilon_3^p = \varepsilon_{oct}^p \qquad (2.81)$$

In the case of simple shear loading the σ_{oct} remains constant, Eq. (2.60) can be rewirtten as

$$dW^p = (\sigma_{oct} + \Delta\sigma)\,(\varepsilon_{oct}^p + \Delta\varepsilon^p) + \sigma_{oct}\,\varepsilon_{oct}^p$$
$$+ (\sigma_{oct} - \Delta\sigma)\,(\varepsilon_{oct}^p - \Delta\varepsilon^p) \qquad (2.82)$$

or

$$dW^p = 3\sigma_{oct}\,\varepsilon_{oct}^p + 2\Delta\sigma\,\Delta\varepsilon^p \qquad (2.83)$$

and

$$J_{2D}^{1/2} = \frac{1}{\sqrt{6}}\,[(\sigma_{oct} + \Delta\sigma - \sigma_{oct})^2 + (\sigma_{oct} - \sigma_{oct} + \Delta\sigma)^2$$
$$+ (\sigma_{oct} - \Delta\sigma - \Delta\sigma_{oct} - \Delta\sigma)^2]^{1/2} \qquad (2.84)$$

Simplifying Eq. (2.84) yields

$$J_{2D}^{1/2} = \Delta\sigma \qquad (2.85)$$

Similarly it can be shown

$$(dI_{2D}^p)^{1/2} = \Delta\varepsilon^p \tag{2.86}$$

Substituting the values for $J_1 = 3\sigma_{oct}$ and $dI_1^p = 3\Delta\varepsilon_{oct}^p$ in Eq. (2.61), it gives

$$dW^p = \alpha\Delta\sigma\ \Delta\varepsilon^p + 9\beta\ \sigma_{oct}\ \varepsilon_{oct}^p \tag{2.87}$$

Equations (2.83) and (2.87) are equivalent to each other only if $\alpha = 2$ and $\beta = 1/3$.

2.9.2 Curve Fitting Procedure for Cap Model

The procedure for obtaining the functional forms and parameters used in cap model is based on the representative material data obtained from laboratory tests.

The first step in the fitting procedure is to employ the unloading portion of the tests to determine appropriate elastic behavior of the model. Unloading behavior indicates the bulk modulus, K, in hydrostatic tests, the shear modulus, G, in triaxial tests and the combination K + (4/3) G in uniaxial tests.

The next step is to establish the failure envelop, namely the portion of the yield surface which limits the shearing stresses that the material can withstand. The failure envelop is generally obtained by using failure data from triaxial tests and proportional loading tests. These test data are fitted by using a function of stresses and are usually seen to involve only the first stress invariant J_1 and the second invariant of the stress deviator J_{2D}.

The third step is to obtain the cap portion of the model. It is obtained by a trial and error procedure in which a cap shape and hardening rule are assumed and the behavior of this assumed model is computed and compared to the material data. If the fit requires improvement, a new set of parameters are tried and the procedure is repeated. The computation of model behavior is based on the equations describing the relations between the stress and strain increments during the common laboratory loading paths.

2.10 Details of Material Model Developed

The bulk modulus, K and the shear modulus, G are determined to be 2.23×10^4 psi (15.61×10^4 kpa) and 7.643×10^2 psi (54.50×10^2 kpa). They are determined from the slopes of unloading portions of the HC and SS (TC, TE) test data.

2.10.1 Failure Surface

The straight line stress paths described in section 2.6 are plotted in the J_1 vs $\sqrt{J_{2D}}$ space. Several tests have been conducted along each path and the upper and lower strengths are noted by dots. The analytical representation of the failure envelop suggests a combi·nationof Drucker-Prager failure surface at low stress levels, vonMises failure surface at high stress levels, both connected by an exponentia transition surface. The surface of the following form is sought.

$$\sqrt{J_{2D}} = \alpha + \beta J_1 - \nu e^{-J_1 \theta} \qquad (2.88)$$
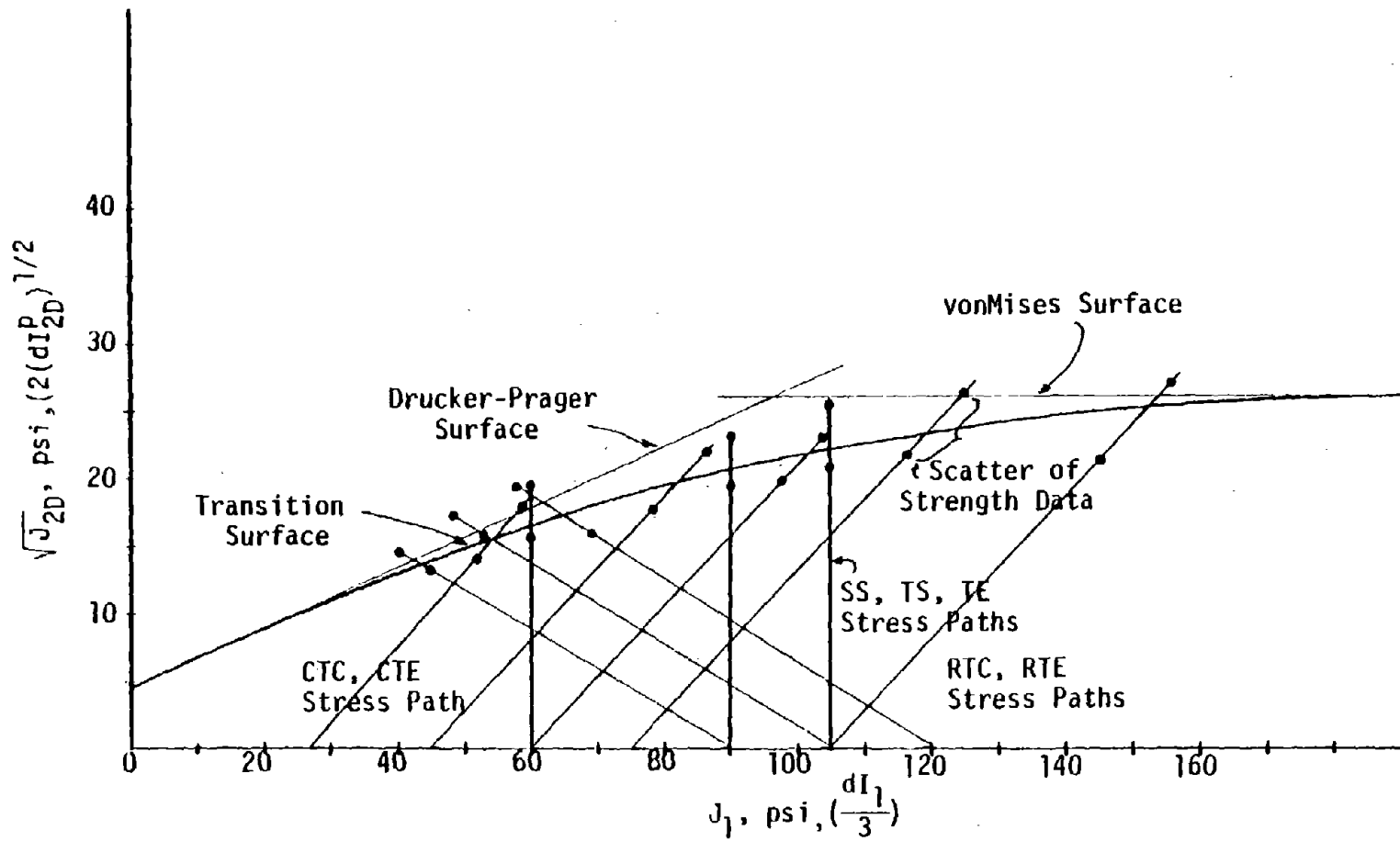
Figure 2.26   Stress Paths and Failure Surface

The parameters for $F = F(J_1, \sqrt{J_{2D}})$ surface are indicated in Fig. (2.26) are given below. From the Fig. (2.26),

$$(\alpha - \nu) = 4.5 \text{ psi} = 31.5 \text{ kpa}$$

$$\alpha = 26.00 \text{ psi} = 182.00 \text{ kpa} \qquad (2.89)$$

$$\nu = 26 - 4.5 = 21.5 \text{ psi} = 150.5 \text{ kpa}$$

The slope angle of Drucker-Prager surface β is tan β = 10/46 and β = 0.1785.

One point on the transition curve is chosen and values of J_1 and $\sqrt{J_{2D}}$ are substituted in Eq. (2.88) to obtain the values of θ

$$J_1 = 100.00 \text{ psi} = 700.00 \text{ kpa};$$
$$\qquad (2.90)$$
$$\sqrt{J_{2D}} = 21.5 \text{ psi} = 149.5 \text{ kpa}$$

$$21.5 = 26 + (0.1785 \times 100) - 21.5e - (\theta \times 100)$$
$$\qquad (2.91)$$
$$\theta = -0.00031 \text{ (kpa}^{-1})$$

The resulting failure surface is

$$F = \sqrt{J_{2D}} - 182 - 0.1785 \, J_1 + 150.5e - 0.00031 \, J_1 = 0 \qquad (2.92)$$

and when the failure surface becomes vonMises

$$F = \sqrt{J_{2D}} - k_1 = 0 \qquad \sqrt{J_{2D}} = k_1 = 26.4 \text{ psi}$$
$$\qquad (2.93)$$
$$= \sqrt{J_{2D}} - 144.8 = 0 \text{ (kpa)}$$

2.10.2 Moving Cap or Yield Surface

The yielding cap intersects the J_1 axis at right angles but intersects the failure surface at a slope parallel to the J_1 axis. The accumulated volumetric plastic strain, ϵ_v^p is calculated at number of points along the J_1 axis and along the other stress paths, and the points are marked along the paths. Then contours of equal ϵ_v^p are drawn, Fig. (2.28). These contour are obtained by joining the points so that ϵ_v^p is constant along the surface.

2.10.3 Potential Surface

Plastic strain increment vectors are computed at several selected points along the various stress paths from the available stress-strain curves. The plastic strain increments correspond to J_1 and J_{2D} are $1/3$ dI_1^p and $2(dI_{2D}^p)^{1/2}$ respectively, where I_1 and I_{2D} are the first invariant of the strain tensor and the second invariant of the deviatoric stress tensor, respectively.

The sets of plastic strain increment vectors represent discrete segments of a continuous plastic flow field. This flow field is intersected by a plastic potential field $(I_1^p,\ I_{2D}^p)$. The shape of plastic potential surfaces are established such that the strain increment vectors are orthogonal to them, Fig. (2.27).

The drawn plastic yield and plastic potential surfaces do not coincide. Thus the material exhibits non-associative properties. The two functions are not equal, that is, $Q \neq F$. A new approach to incorporate non-associative behavior [21] is used. The approach
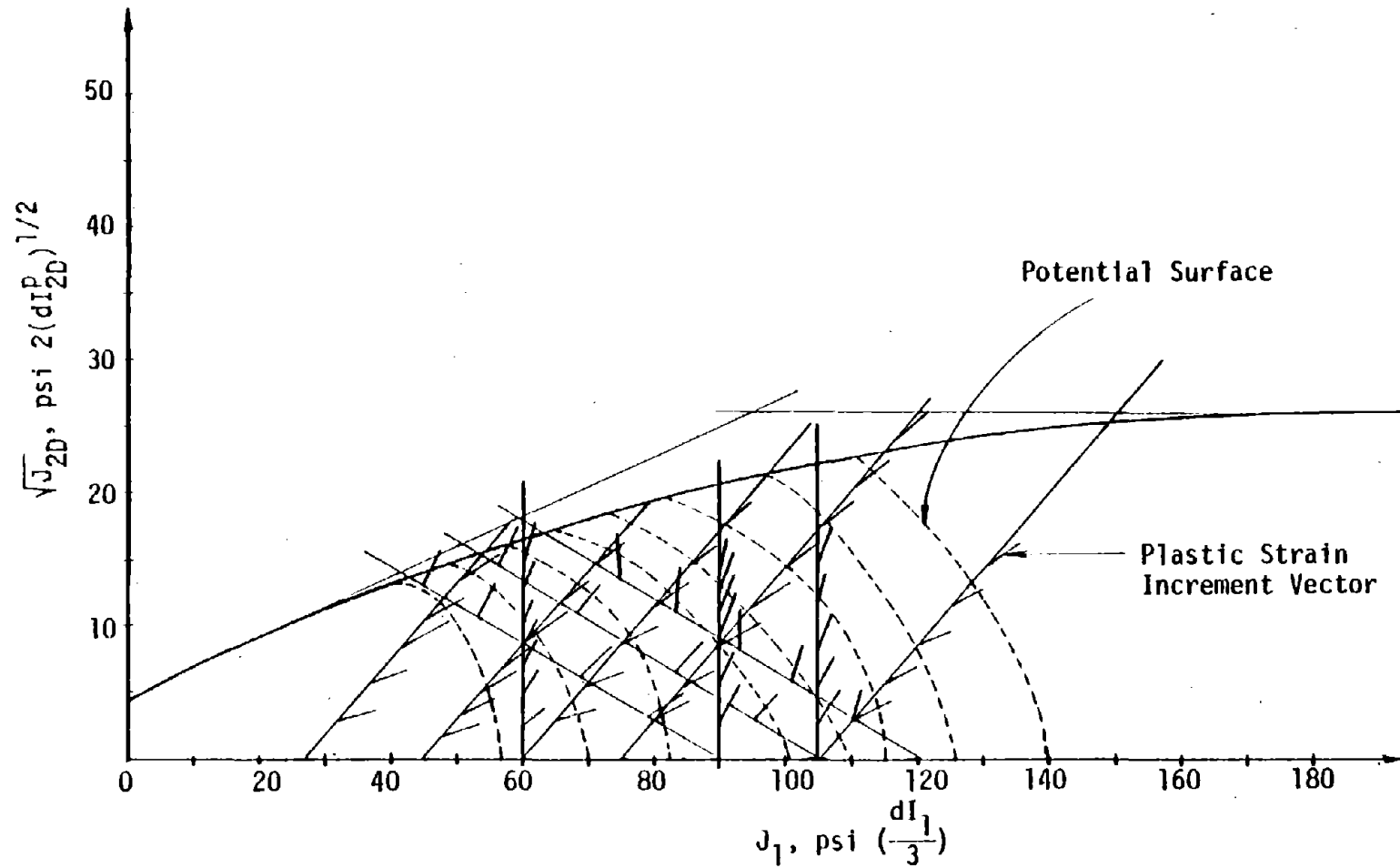
Figure 2.27 Plastic Strain Increment Vectors and Potential Surfaces
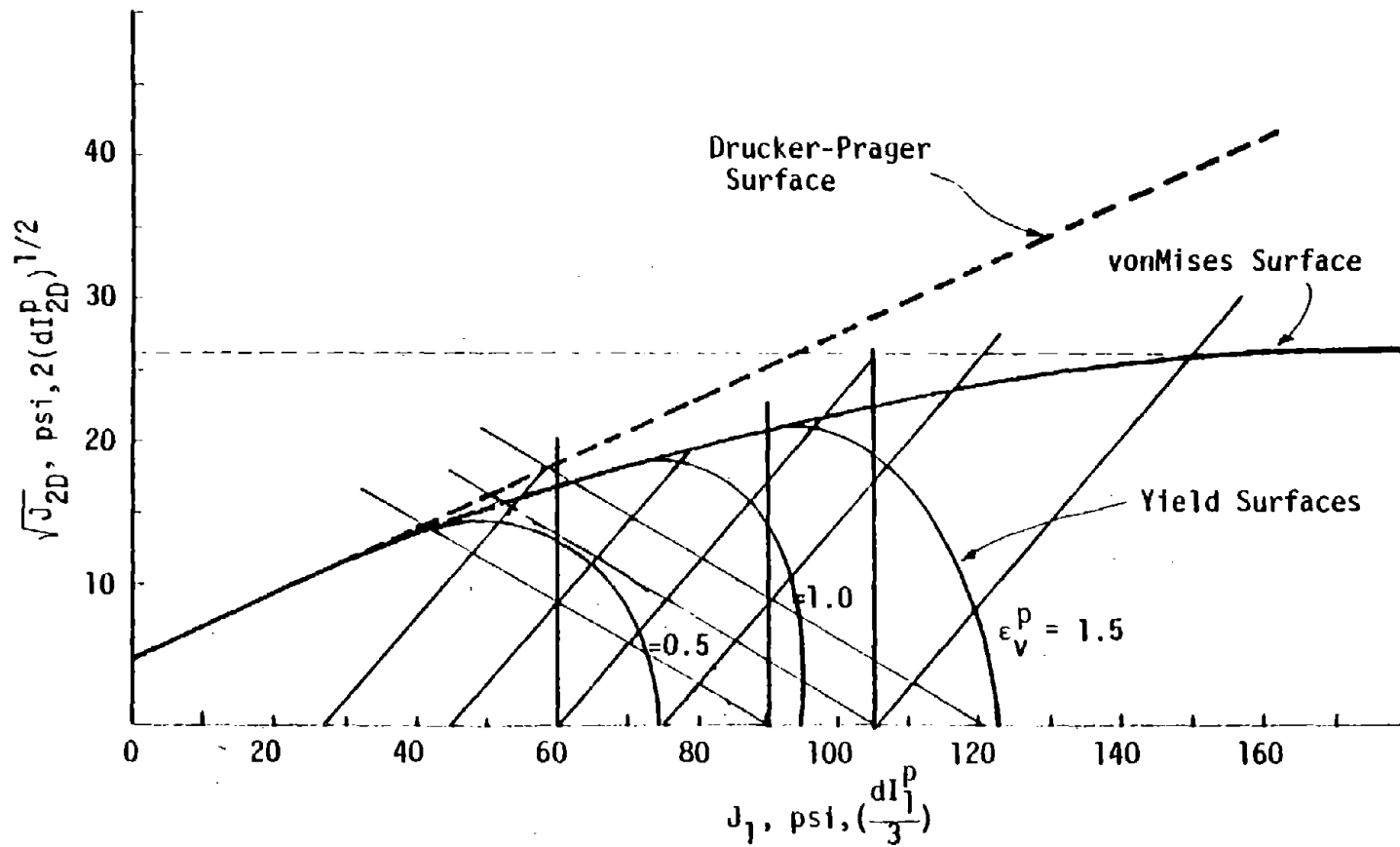
Figure 2.28   Stress Paths and Yield Srfaces

involves a modification or correction to account the behavior in form of a correction factor A, where A can be expressed as

$$A(J_1, J_{2D}, I_1^p) = \frac{Q(J_1, J_{2D}, I_1^p)}{F(J_1, J_{2D})} \qquad (2.94)$$

This approach can permit the use of available and existing formulations and codes and can avoid evaluation of plastic potential, Q, and the non-symmetric constitutive matrix that arises if a rigorous formulation were used. The correction function A is determined from the functions Q and F obtained from laboratory tests and presented here.

If the non-associative property is ignored, namely if Q is regarded the same as F for simplicity and convenience, the surfaces become near elliptical. The parameters from these elliptical caps are also determined and presented.

In this case, where the two functions Q and F are regarded the same, the elliptical surfaces are defined by the Eq. (2.42), namely

$$F = R^2 J_{2D} + (J_1 - L)^2 - R^2 b^2 = 0 \qquad (2.95)$$

The total volumetric strain can be written as

$$\varepsilon_v = \varepsilon_v^e + \varepsilon_v^p \qquad (2.96)$$

$$= \frac{\sigma_{oct}}{K} + W [e^{D(3\sigma_{oct} - Z)} - 1] \qquad (2.97)$$

Here Z is found to be negligible. R is measured from the plotted surface and is found to be 1.24. The constants D and W are found by trial and error fitting as $D = 0.308 \times 10^{-4}$ and $W = 3.505$ percent.

For the case when $Q \neq F$, the correction factor A denotes a function obtained by dividing Q by F

$$Q = AF \tag{2.98}$$

The correction function A, now can be expressed as a polynomial

$$A = 1.0 + (A_1 + A_2 J_1 + A_3 J_{2D}^{1/2}) \tag{2.99}$$

The Eq. (2.98) then becomes

$$Q = A_o + A_1 F + A_2 J_1 F + A_3 J_{2D}^{1/2} F \tag{2.100}$$

The constants A_o, A_1 and A_2 are obtained by trial and error fitting the two functions Q and F obtained from laboratory test results.

$$F = 1.96 J_{2D} + (J_1 - L)^2 - 1.96 b^2 = 0$$

$$Q = 0.36 J_{2D} + (J_1 - L)^2 - 0.36 b^2 = 0$$

$$A_o = 1.00 \quad A_1 = 0.3825 \quad A_2 = 0.6735 \tag{2.101}$$

$$A_3 = 0.9845$$

2.11.1 RESILIENT MODULUS

The resilient modulus, E_r, is defined as the deviator stress divided by the recoverable axial strain. The resilent modulus for a granular material is not constant but varies with the state of stress. E_r values at various deviator stress levels are plotted in Fig. (2.29) depicting its stress dependent behavior.

2.11.2 Computation of Resilient Modulus

The resilent modulus can be expressed as

$$E = K\sigma_3^n \qquad (2.102)$$

where K and n are material parameters and σ_3 is the deviator stress. Taking logarithm, the Eq. (2.102) is

$$\log E_r = \log K + n \log \sigma_3 \qquad (2.103)$$

when $\sigma_3 = 1$, in the Fig. (2.29), $E_r = K = 400.00$ psi (2.76×10^3 kpa).

The slope of the line n is 1.4 and the resilient modulus can now be expressed as

$$E_r = 400 \ \sigma_3^{1.4} \ \text{psi} \qquad (2.104)$$

This relationship can be used if it is considered sufficient to include only the elastic response of the material.

2.11.3 Influence of Anisotropy

The stress-strain response curves obtained in this investigation show that subballast exhibits anisotropy. A qualitative assessment
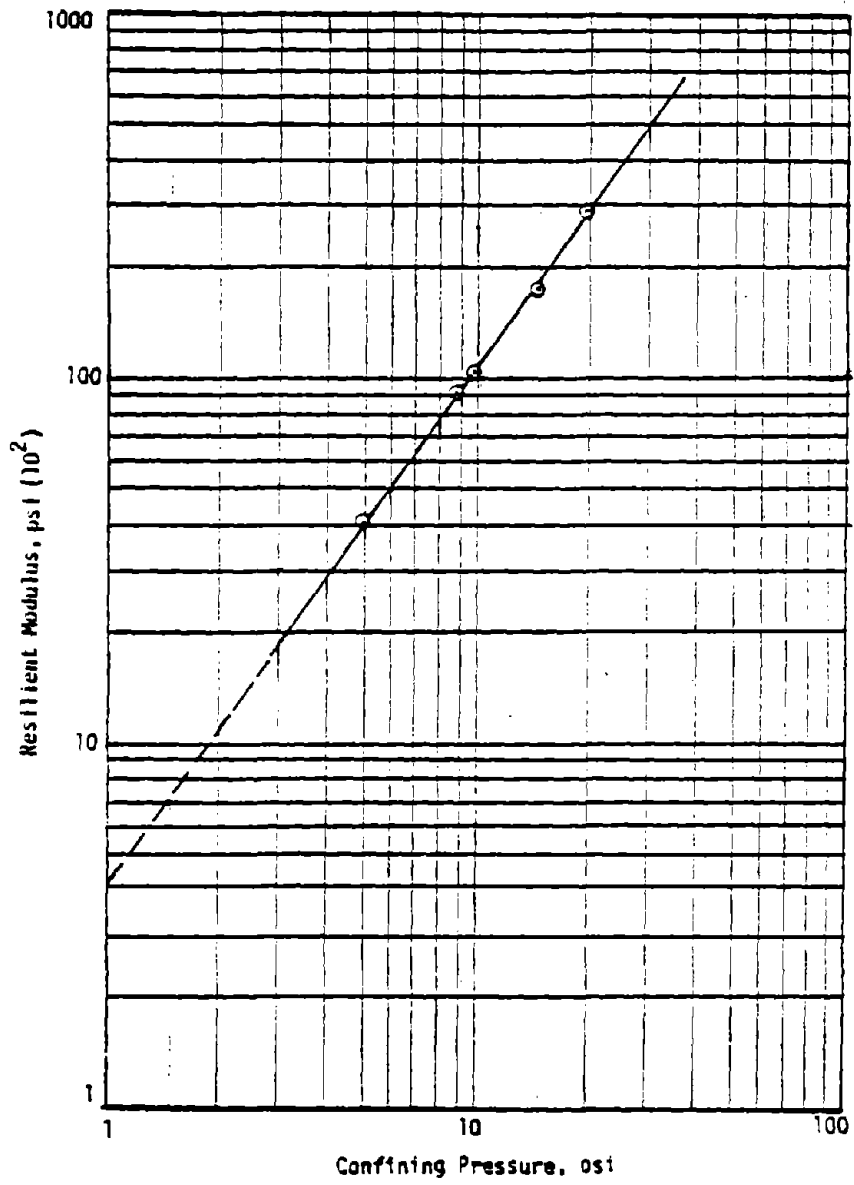
Figure 2.29 Variation of Resilient Modulus
with Confining Pressure

of anisotropy can be made by comparing the values of $E_{z(x)}$ and $E_{y(x)}$. $E_{z(x)}$ is defined as the deviator stress in X direction divided by recoverable strain in Z direction. $E_{y(x)}$ is the deviator stress in X direction divided by recoverable strain in Y direction. These two values are plotted against confining pressure σ_3 in Fig. (2.30). These two lines are parallel to each other and have same slope, n = 1. The variation is in the intercept and thus

$$E_{z(x)} = 2800 \, \sigma_3 \, (psi) \tag{2.105}$$

$$E_{y(x)} = 2200 \, \sigma_3 \, (psi) \tag{2.106}$$

From this analysis, it is felt, the material can be approximated as isotropic by using average of the responses in Y and Z directions.
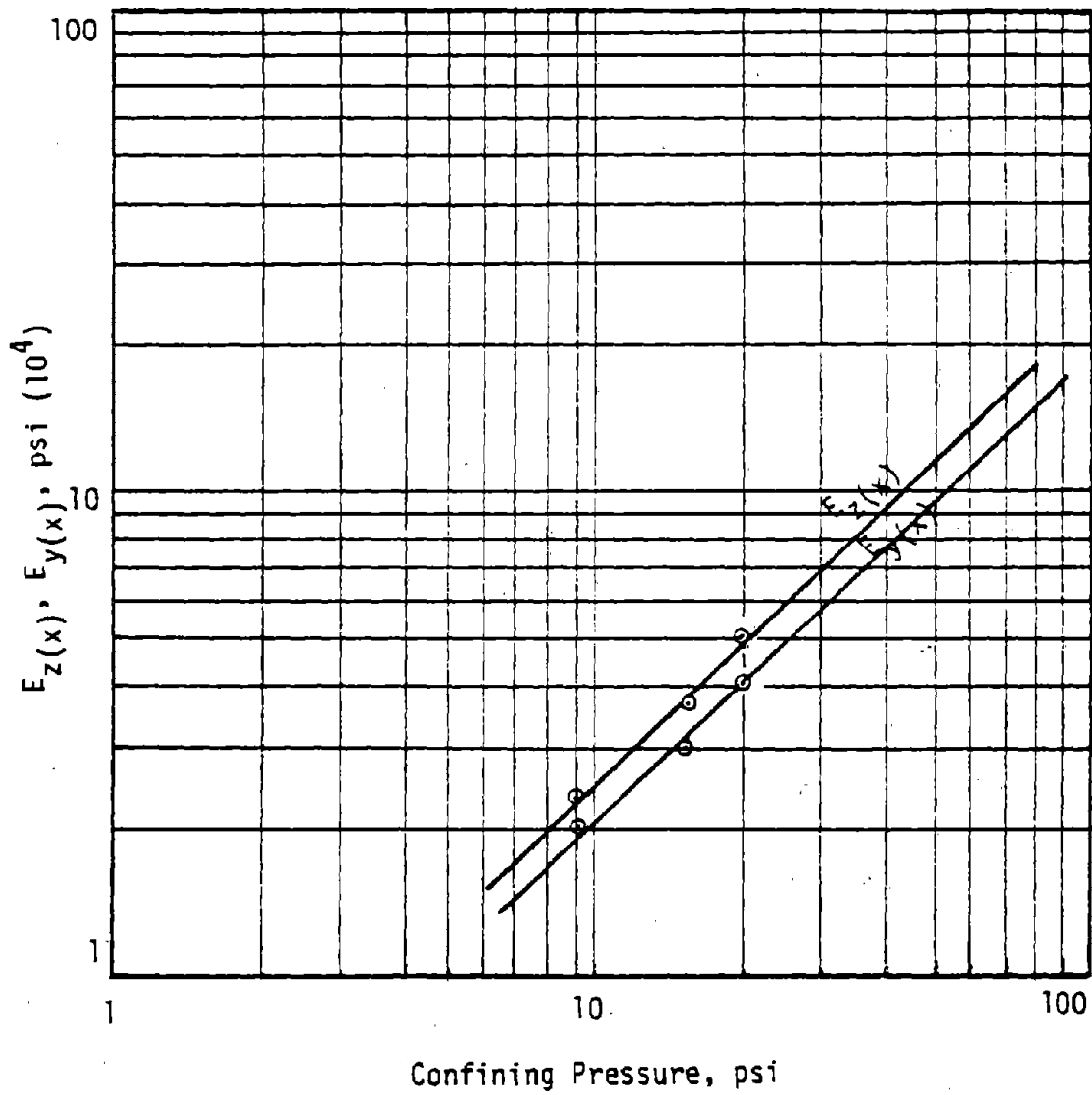
Figure 2.30   Variation of $E_{z(x)}$ and $E_{y(x)}$ with Confining Pressure

Chapter 3

CONSTITUTIVE MODELLING FOR WOOD

3.1 INTRODUCTION

Timber is perhaps the most abundant construction material used in this country. Its use for housing and other structural purposes like rail-ties has continuously grown. The fast growing housing industry and upcoming modern structures may probably make the resource out of phase with the demand. So the need for best use of the available wood is being badly felt. Good understanding of the behavior of wood under all significant loading configurations will enable to judge and make best use of the material.

Wood-ties used in the railroad bed are subjected to repetitive loading. This is caused by the moving vehicles. It has been reported [11] that about 20 percent of maintenance cost of the track bed is being spent in repairing and replacing wood-ties in the existing track-bed. In this investigation, cubical samples of wood-ties are tested under all possible stress paths and the stress-strain responses are used to make a three-dimensional characterization of wood. The results can be useful for an improved analysis of track structures.

3.2 PROBLEM STATEMENT

Modern structures involve complicated geometries and loading conditions. As a consequence, the materials in the structures are called upon to withstand and sustain a variety of complex stress

82

distributions and stress paths. For example, woodties used in railroad industry are subjected to moving loads which are repetitive and dynamic in nature. So successful and efficient use of the material (wood) can be achieved only if its strength characteristics are well defined and its stress-strain relations are precisely known under different possible loading conditions.

3.3 OUTLINE OF THE OBJECTIVE

The influence of various factors such as anisotropy, inherent local variations in properties, state of stress and stress paths on the behavior of wood are worth investigating. Hardly any work appears to have been done in the direction of development of three-dimensional characterization of wood by including the foregoing significant factors.

So the main objective is to develop general constitutive laws for wood on the basis of comprehensive series of three-dimensional tests on cubical specimens in a high capacity truly triaxial device. Here the main attention is given to the state of stress, plastic behavior, stress paths and anisotropy. However, conventional tests have also been run on samples of wood and reported.

3.4.1 REVIEW OF PAST WORK

Numerous research works have been carried out on both the structure and strength of wood [7,44,48]. But most of them, toward development of constitutive laws for wood, have been based on highly simplified models and testing configurations [7]. Very

often uniaxial tests have been utilized to determine the bending, compression and tension strength of wood.

Conventionally, to find the Young's modulus of elasticity, bending test is conducted on a simply supported wooden beam. Plate twist test, according to ASTM D 805 -(2), is conducted on wood to determine the shear modulus. Here the longitudinal fibers are normal to the plane of twisting. From the determined shear (G) and elastic (E) moduli, the Poisson's ratio (ν) is determined using the relationship

$$E = 2G (1 + \nu). \tag{3.1}$$

Uniaxial compression test is conducted according to ASTM D 143-52 (1), keeping the longitudinal grains parallel to direction of loading till failure, for determination of compressive strength of wood. Compression test keeping longitudinal grains perpendicular to the direction of loading are conducted till failure to determine the compressive strength perpendicular to grains.

In conventional tests like bending, uniaxial compression and tension, it is assumed wood to be a linear, elastic and isotropic material. In reality, it is an orthotropic material [37]. How far it is a linear elastic material depends mostly upon the load level. At high stress levels, it exhibits a good amount of nonlinear behavior. Furthermore, some types of wood exhibit hysteresis and plasticity. At high stress levels, in case of many woods, it has been observed that on removal of load, recovery of strain is not total. Behavior of wood can be influenced by number of factors

such as state of stress, initial and induced anisotropy, nonhomo-
geneities and stress paths with temperature and moisture content
constant conditions.

Testing of wood sample is complicated by the structure of the
wood itself. A transverse section cut from a tree may be observed
to have an interesting pattern of radial rings eminating from the
center, while a longitudinal section shows a longitudinally striated
fiber arrangements. Wood can be regarded as a material exhibiting
three mutually perpendicular axes of symmetry [34], ignoring the
growth ring curvature. The axes of symmetry for wood, Fig. (3.1),
are selected to correspond with the longitudinal axis of the tree
(L), the direction of rays (R) and the tangent to the growth rings
(T).

One of the early works on anisotropy of wood has been by
Herman [48]. It has further been developed by many investigators,
including Goodman, Freas and Werren and Norris [48]. Uniaxial com-
pression tests are employed to find the orthotropic elastic
constants. Load is applied uniaxially and deformations are measured
in all three directions, either by dial gages or strain gages [35].
A minimum of three different orientations of loading are necessary
to be tested. Difficulties are faced very much with deformation
measurements, particularly in lateral directions. In addition,
plate twist tests have to be conducted to determine the Shear
Moduli. These tests can be laborious and lack reproducibility
[34].
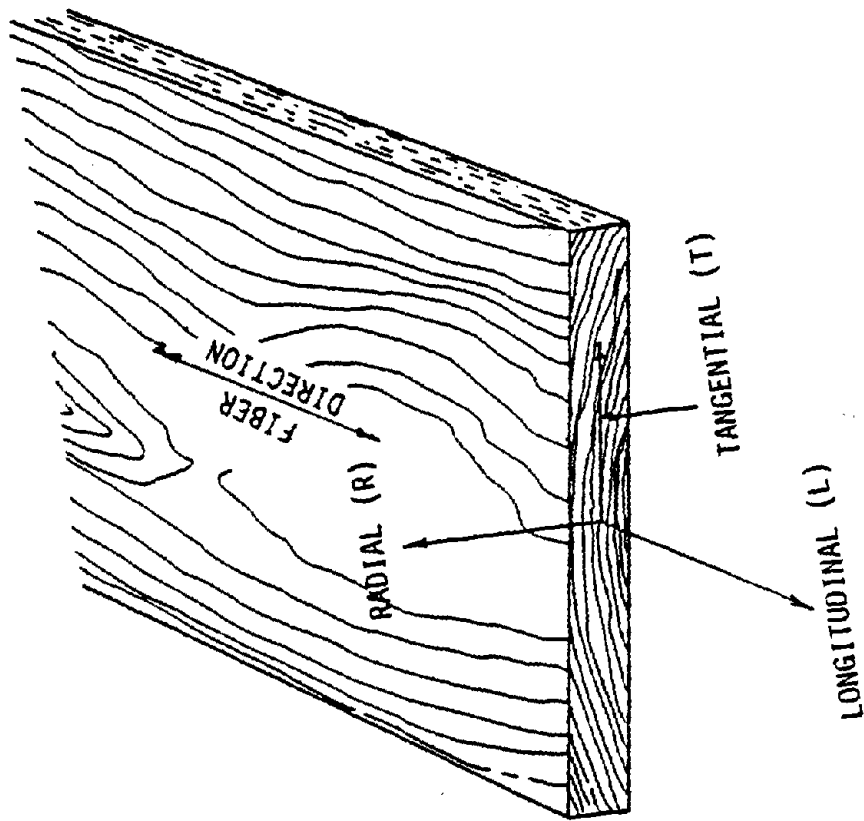
Figure 3.1 Anisotropic Wood

In general, response of wood can consist of three components, namely (1) elastic response, (2) visco-elastic response and (3) plastic or flow response. Hence, an increment of strain, $d\epsilon_{ij}$ can be decomposed as

$$d\epsilon_{ij} = d\epsilon_{ij}^e + d\epsilon_{ij}^{ve} + d\epsilon_{ij}^p \qquad (3.2)$$

where $d\epsilon_{ij}^e$ and $d\epsilon_{ij}^{ve}$ are increments of elastic, visco elastic and plastic components of strain tensor respectively. Both the elastic strains and viscoelastic strains can be recovered upon complete removal of the load. The plastic strains are irrecoverable. Material modelling has been done accounting for viscoelastic strains by some investigators [44], but seldom including plastic strains, probably the chief reason being inadequate testing technique and sophisticated highly sensitive device. The truly triaxial device [18,19] enables to conduct tests on wood in any desired stress path.

A brief outline of the principle of determination of elastic material constants are given here. These principles are later used to determine the orthotropic elastic constants from the test results.

3.4.2 Determination of Elastic Material Constants

Methods to determine the material constants for a linear, elastic, orthotropic material are developed. These methods are applicable for determination of the material constants of wood. The determination of the material constants using mechanical testing methods requires that known external stresses be applied to a specimen and the resulting deformations be measured. The relation of the material

symmetry axes to the direction of the applied stresses must be clearly known.

Equations of Linear Elasticity

Consider an elemental cube within a body which is loaded externally. The change in the relative positions within the body is a deformation. In a rectangular co-ordinate system, the displacement of a point can be resolved into three components along the axis directions as u_1, u_2 and u_3. With those quantities a strain tensor can be defined [37,67] as

$$\varepsilon_{ij} = \frac{1}{2} (u_{i,j} + u_{j,i}) \qquad (i,j = 1,2,3) \qquad (3.3)$$

Einstein's tensor notations are employed here, in which partial differentiation is indicated by a comma in the subscript and two equal subscripts indicates a sum. It has been shown that $\varepsilon_{ij} = \varepsilon_{ji}$, so 6 of 9 components in the strain tensor are independent. Three of the strains are known as normal strains ($i=j$), and the other three are called shear strains ($i \neq j$). The strains are related to each other through the displacements, and the displacements must be consistant with the geometrical constraints. This mutual dependence is formulated in the equations of compatability and can be written as

$$\varepsilon_{ij,kl} + \varepsilon_{kl,ij} - \varepsilon_{ik,jl} - \varepsilon_{jl,ik} = 0 \qquad (3.4)$$

This equation expands into 81 equations, but many of these are identically satisfied, because of symmetry conditions in strain tensor [67].

When a body is deformed, shear and normal stresses will be developed on each of the six faces of the elemental cube of the body. The stress components constitute a stress tensor σ_{ij}. If the body is in static equilibrium, the resultant force acting on it must vanish.

$$\sigma_{ij,j} - X_i = 0 \qquad (i = 1,2,3) \qquad (3.5)$$

This equation is known as the equation of equilibrium and must always be satisfied. Moment equilibrium conditions require $\sigma_{ij} = \sigma_{ji}$ [17]. Therefore, only 6 independent stress components exist. The second order strain and stress tensors are related to each other through a fourth order tensor as

$$\sigma_{ij} = C_{ijkl} \, \varepsilon_{kl} \qquad (3.6)$$

This is the generalized Hooke's law for linear elastic materials. C_{ijkl} is known as the stiffness tensor of the material. If the equation is inverted,

$$\varepsilon_{ij} = D_{ijkl} \, \sigma_{kl} \qquad (3.7)$$

D_{ijkl} is termed the elastic compliance tensor of the material.

$$C_{ijkl} = C_{jikl} \text{ and } C_{ijkl} = C_{ijlk} \qquad (3.8)$$

If the material is linearly elastic then,

$$C_{ijkl} = C_{klij} \qquad (3.9)$$

thus reducing the number of independent constants from 36 to 21.

Because of this symmetry, it is appropriate to introduce the single subscript notion $\{\varepsilon_i\}$ and $\{\sigma_i\}$, where

$$\{\varepsilon_{ij}\} = \begin{Bmatrix} \varepsilon_{11} \\ \varepsilon_{22} \\ \varepsilon_{33} \\ 2\varepsilon_{23} \\ 2\varepsilon_{13} \\ 2\varepsilon_{12} \end{Bmatrix} = \begin{Bmatrix} \varepsilon_1 \\ \varepsilon_2 \\ \varepsilon_3 \\ \varepsilon_4 \\ \varepsilon_5 \\ \varepsilon_6 \end{Bmatrix} \tag{3.10}$$

and

$$\{\sigma_{ij}\} = \begin{Bmatrix} \sigma_{11} \\ \sigma_{22} \\ \sigma_{33} \\ \sigma_{23} \\ \sigma_{13} \\ \sigma_{12} \end{Bmatrix} = \begin{Bmatrix} \sigma_1 \\ \sigma_2 \\ \sigma_3 \\ \sigma_4 \\ \sigma_5 \\ \sigma_6 \end{Bmatrix} \tag{3.11}$$

this enables the generalized Hooke's law be represented as

$$\{\varepsilon_i\} = [D_{ij}] \{\sigma_j\} \tag{3.12}$$

Transformation Rules

Some materials possess certain planes or axes about which material properties are symmetrical. This symmetry can be expressed by transformation of coordinates that correspond either to (a) rotation about an axis, or (b) reflection in a plane. Certain of the D_{ij} terms can be shown to be equal to zero for a particular transformation. A material that is symmetric about three orthogonal planes is termed orthotropic or orthorhombic. A total of 9 constants remain in this case. Thus with respect to the material principal axes 1, 2, and 3, D_{ij} is given in the following form

$$[D_{ij}] = \begin{bmatrix} D_{11} & D_{12} & D_{13} & 0 & 0 & 0 \\ & D_{22} & D_{23} & 0 & 0 & 0 \\ & & D_{33} & 0 & 0 & 0 \\ & & & D_{44} & 0 & 0 \\ & \text{Sym} & & & D_{55} & 0 \\ & & & & & D_{66} \end{bmatrix} \qquad (3.13)$$

A material may also be symmetric about an axis. For a material symmetric about the X_3 axis, the resulting D_{ij} matrix becomes,

$$[D_{ij}] = \begin{bmatrix} D_{11} & D_{12} & D_{12} & 0 & 0 & 0 \\ & D_{11} & D_{13} & 0 & 0 & 0 \\ & & D_{33} & 0 & 0 & 0 \\ & & & D_{44} & 0 & 0 \\ & \text{Sym} & & & D_{44} & 0 \\ & & & & & D_{66} \end{bmatrix} \qquad (3.14)$$

in which $D_{66} = \frac{1}{2} [D_{11} - D_{12}]$.

Here only five independent material constants are necessary to represent this material which is of hexagonal symmetry.

An isotropic material is one which is symmetric with respect to rotation about all axes and with respect to reflection in all planes. Then the material matrix can be expressed with only two independent constants.

$$[D_{ij}) = \begin{bmatrix} D_{11} & D_{12} & D_{12} & 0 & 0 & 0 \\ & D_{11} & D_{12} & 0 & 0 & 0 \\ & & D_{11} & 0 & 0 & 0 \\ & & & D_{44} & 0 & 0 \\ & \text{Sym} & & & D_{44} & 0 \\ & & & & & D_{44} \end{bmatrix} \qquad (3.15)$$

where $D_{44} = \frac{1}{2} [D_{11} - D_{12}]$.

For the determination of material constants, consider, for an example, an axially symmetric material with five independent material constants, whose stress-strain relationship is

$$
\begin{Bmatrix} \epsilon_1 \\ \epsilon_2 \\ \epsilon_3 \\ \epsilon_4 \\ \epsilon_5 \\ \epsilon_6 \end{Bmatrix} = \begin{bmatrix} D_{11} & D_{12} & D_{13} & 0 & 0 & 0 \\ D_{12} & D_{11} & D_{13} & 0 & 0 & 0 \\ D_{13} & D_{13} & D_{33} & 0 & 0 & 0 \\ 0 & 0 & 0 & D_{44} & 0 & 0 \\ 0 & 0 & 0 & 0 & D_{44} & 0 \\ 0 & 0 & 0 & 0 & 0 & D_{44} \end{bmatrix} \begin{Bmatrix} \sigma_1 \\ \sigma_2 \\ \sigma_3 \\ \sigma_4 \\ \sigma_5 \\ \sigma_6 \end{Bmatrix} \qquad (3.16)
$$

This relation is valid for a material whose axis of symmetry is parallel to the "3" axis. Such a material having axially symmetric anisotropy might be a geologic material that is layered or bedded in a plane perpendicular to the vertical axis which is taken to be the "3" direction. The material properties in any direction perpendicular to the "3" axis will be equal. From this material, cubical specimens are cut with the bedding plane parallel to one side of the cube. The unprimed axes in Fig. (3.2) thus refer to the material principal directions.

If a cube cut in the above manner, a uniaxial compressive stress increment, $\Delta\sigma_3$, is super-imposed on an existing stress state, then
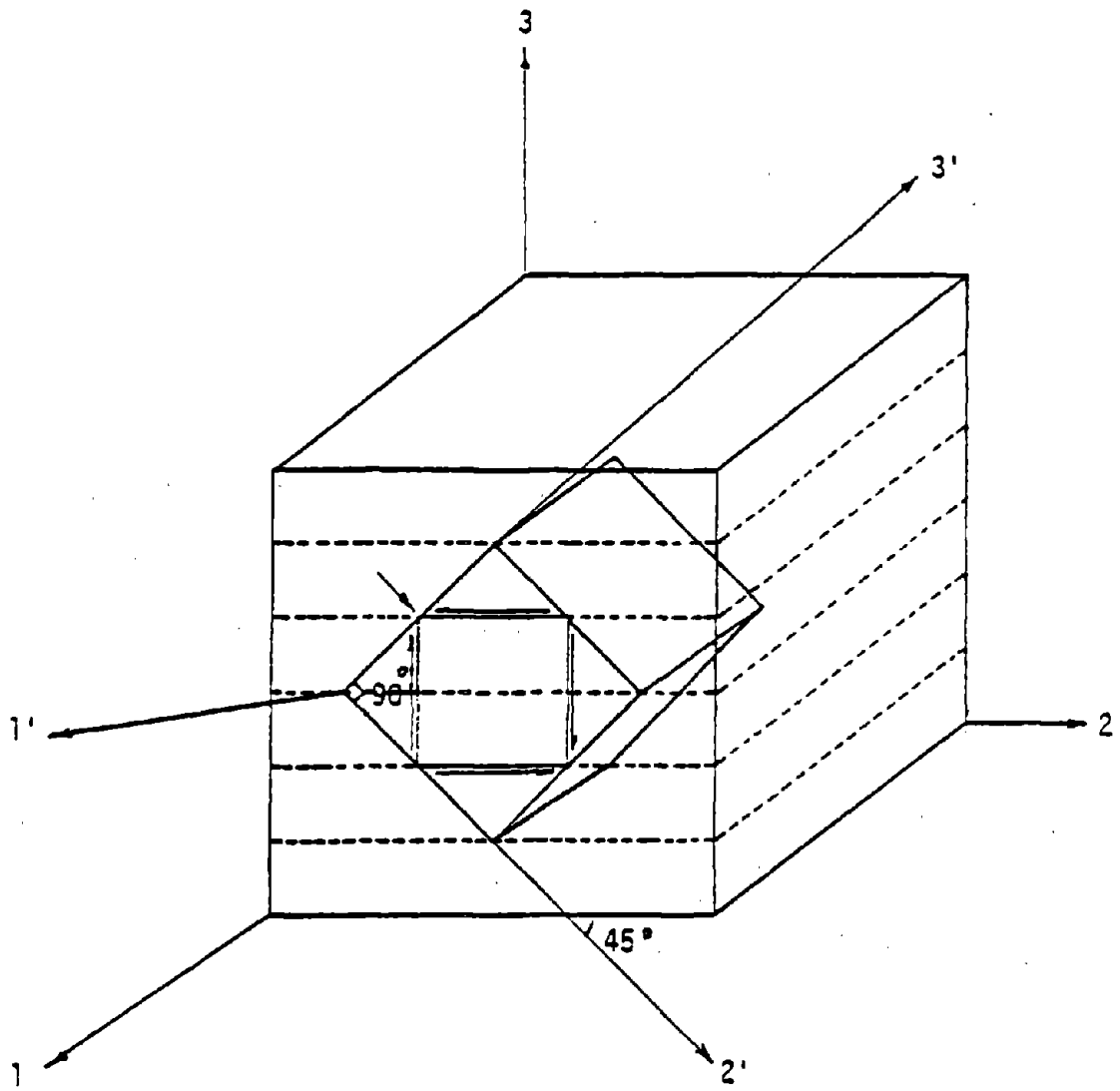
Figure 3.2 Principal Material Planes

$$\Delta\varepsilon_1 = D_{13}\,\Delta\sigma_3 \qquad\qquad D_{13} = \frac{\Delta\varepsilon_1}{\Delta\sigma_3}$$

$$\Delta\varepsilon_2 = D_{13}\,\Delta\sigma_3 \qquad \text{(or)} \qquad D_{13} = \frac{\Delta\varepsilon_2}{\Delta\sigma_3} \qquad\qquad (3.17)$$

$$\Delta\varepsilon_3 = D_{33}\,\Delta\sigma_3 \qquad\qquad D_{33} = \frac{\Delta\varepsilon_3}{\Delta\sigma_3}$$

If a uniaxial compressive stress increment, $\Delta\sigma_1$ is applied in the 1 - 1 direction, then

$$\Delta\varepsilon_1 = D_{11}\,\Delta\sigma_1 \qquad\qquad D_{11} = \frac{\Delta\varepsilon_1}{\Delta\sigma_1}$$

$$\Delta\varepsilon_2 = D_{12}\,\Delta\sigma_1 \qquad \text{(or)} \qquad D_{12} = \frac{\Delta\varepsilon_2}{\Delta\sigma_1} \qquad\qquad (3.18)$$

$$\Delta\varepsilon_3 = D_{13}\,\Delta\sigma_1 \qquad\qquad D_{13} = \frac{\Delta\varepsilon_3}{\Delta\sigma_1}$$

Thus four of the five material constants are determined. A uniform shear stress state is to be created in the cubical specimen in order to determine the only shear compliance constant, D_{44}. This is extremely difficult to achieve experimentally. A procedure can be developed in which a cube cut at an angle of 45° to the bedding plane, Fig. (3.2) is subjected to uniform pressure loading. In the figure, the primed coordinates refer to those of the rotated cubical specimen whereas the unprimed coordinates refer to the axes along the principal material directions. The stress-strain relation of an element in the rotated position is

$$\epsilon_{i'j'} = D_{i'j'k'l'} \; \sigma_{k'l'} \tag{3.19}$$

It is now desired to transform the measured properties in the primed coordinate system to the unprimed system where the 3 - 3 axis is perpendicular to the bedding plane. For the specific case of rotation about the 1 - 1 axis, the coordinates transform as

$$X_1 = X_1$$

$$X_2 = X_2 \cos\theta + X_3 \sin\theta \tag{3.20}$$

$$X_3 = -X_2 \sin\theta + X_3 \cos\theta$$

where θ is the angle of rotation.

For $\theta = -45°$ (negative because the transformation is from the primed to the unprimed system). $-\sin\theta = \cos\theta = \dfrac{1}{\sqrt{2}}$ and the table of direction cosines is given as

	X_1	X_2	X_3
X_1	1	0	0
X_2	0	$\dfrac{1}{\sqrt{2}}$	$\dfrac{1}{\sqrt{2}}$
X_3	0	$-\dfrac{1}{\sqrt{2}}$	$\dfrac{1}{\sqrt{2}}$

$$(3.21)$$

The five non-zero material constants in the principal material axis system when expressed in the four subscript system for an elastic material are as

$$D_{11} = D_{1111} = D_{2222}$$

$$D_{12} = D_{1122} = D_{2211}$$

$$D_{13} = D_{1133} = D_{3311} = D_{2233} = D_{3322} \qquad (3.22)$$

$$D_{33} = D_{3333}$$

$$D_{44} = 4\, D_{2323} = 4\, D_{3131}$$

The symmetry of the stress and strain tensors required that D_{ijkl} be invarient with respect to interchange of the i's and j's and with respect to interchange of the k's and l's. Hence $D_{2332} = D_{3232}$. For a linear elastic material D_{ijkl} is invarient with respect to interchange of ij for kl. Hence $D_{2332} = D_{3223}$ and $D_{1122} = D_{2211}$.

Writing $D_{ijkl} = D_{i'j'k'l'}$, the transformation for the five material constants can be written as

$$D_{11} = D_{1111} = D'_{1111}$$

$$D_{12} = D_{1122} = \frac{1}{2} D'_{1122} - D'_{1123} + \frac{1}{2} D'_{1133}$$

$$D_{13} = D_{1133} = \frac{1}{2} D'_{1122} + D'_{1123} + \frac{1}{2} D'_{1133} \qquad (3.23)$$

$$D_{33} = D_{3333} = \frac{1}{4} D'_{2222} + \frac{1}{2} D'_{2233} + \frac{1}{4} D'_{3333} - D'_{2323}$$

$$\frac{1}{4} D_{44} = D_{2323} = \frac{1}{4} D'_{2222} - \frac{1}{2} D'_{2233} + \frac{1}{4} D'_{3333}$$

In an uniaxial compression test on the obliquely oriented cube, if a uniaxial compressive stress increment is applied in the 3' - 3' direction to the cube, Fig. (3.3) then
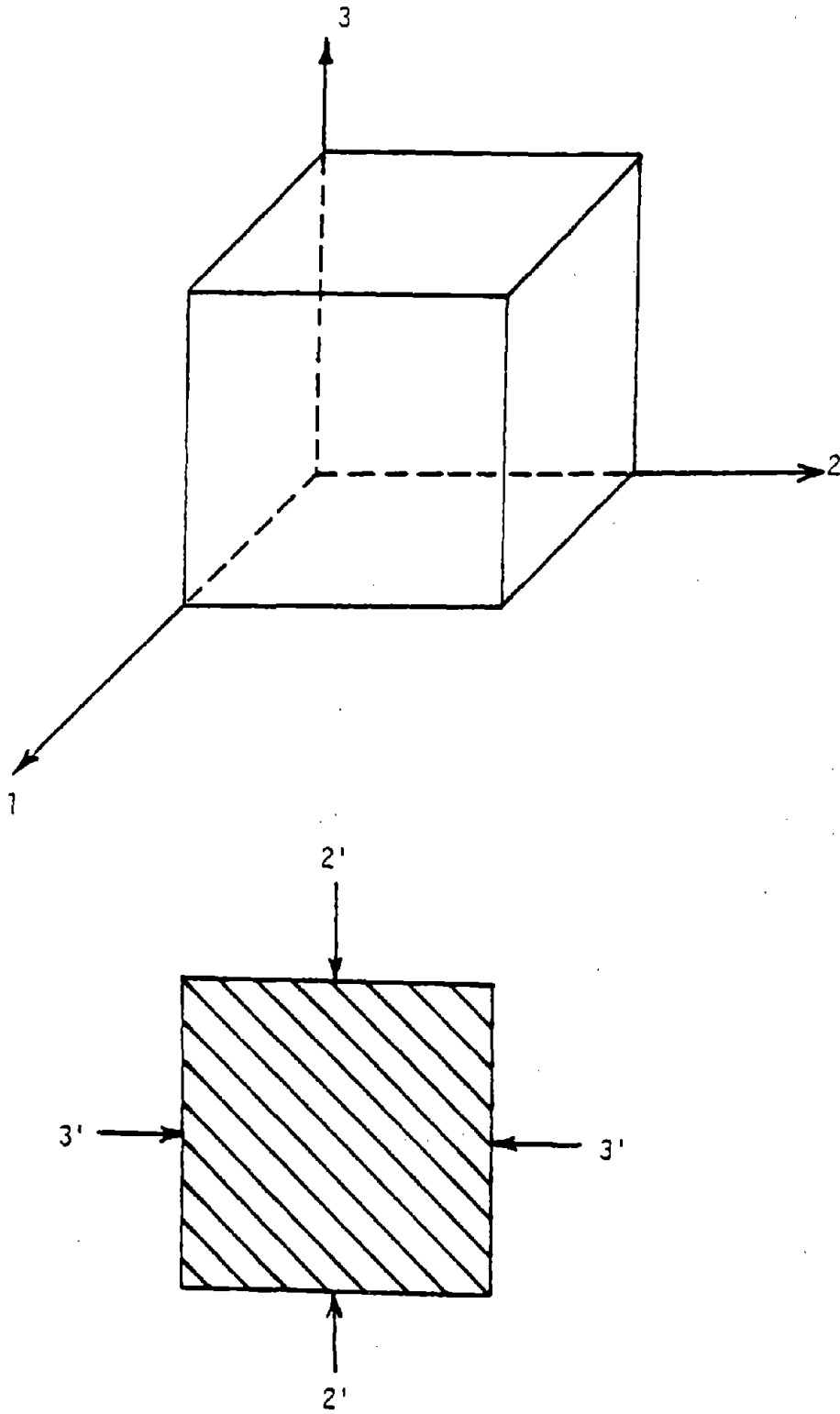
Figure 3.3 Loading Directions

$$D'_{3333} = \frac{\Delta\varepsilon'_{33}}{\Delta\sigma'_{33}} \quad \text{and} \quad D'_{2233} = \frac{\Delta\varepsilon'_{22}}{\Delta\sigma'_{33}} \quad\quad (3.24)$$

Similarly by applying a uniaxial compressive stress increment in the 2' - 2' direction,

$$D'_{2222} = \frac{\Delta\varepsilon'_{22}}{\Delta\sigma'_{22}} \quad \text{and} \quad D'_{2233} = \frac{\Delta\varepsilon'_{33}}{\Delta\sigma'_{22}} \quad\quad (3.25)$$

For a 45 degree rotation, it can be shown that $D'_{3333} = D'_{2222}$ and so the value of D_{44} is given by

$$D_{44} = 4 D_{2323} = 2 D'_{3333} - 2 D'_{2233} \quad\quad (3.26)$$

In case of an orthotropic material like wood, there are three independent shearing compliance constants, namely D_{44}, D_{55} and D_{66}. To determine these values, cubes are to be cut rotated at 45 degree angle to the 1, 2 and 3 axes respectively, the three axes in case of wood being longitudinal, radial and tangential directions. The values of D_{55} would be

$$D_{55} = 2 D'_{3333} - 2 D'_{1133} \quad\quad (3.27)$$

and that of D_{66} would be

$$D_{66} = 2 D'_{2222} - 2 D'_{1122} \quad\quad (3.28)$$

Using these values of compliance parameters the constitutive equation for orthotropic material (wood) can be written as

$$
\begin{Bmatrix} \varepsilon_1 \\ \varepsilon_2 \\ \varepsilon_3 \\ \varepsilon_4 \\ \varepsilon_5 \\ \varepsilon_6 \end{Bmatrix} =
\begin{bmatrix}
\dfrac{1}{E_{11}} & \dfrac{-\nu_{21}}{E_{22}} & \dfrac{-\nu_{31}}{E_{33}} & & & \\[2mm]
\dfrac{-\nu_{12}}{E_{11}} & \dfrac{1}{E_{22}} & \dfrac{-\nu_{32}}{E_{33}} & & 0 & \\[2mm]
\dfrac{-\nu_{13}}{E_{11}} & \dfrac{-\nu_{23}}{E_{22}} & \dfrac{1}{E_{33}} & & & \\[2mm]
& & & \dfrac{1}{G_{23}} & & \\[2mm]
& 0 & & & \dfrac{1}{G_{13}} & \\[2mm]
& & & & & \dfrac{1}{G_{12}}
\end{bmatrix}
\begin{Bmatrix} \sigma_1 \\ \sigma_2 \\ \sigma_3 \\ \sigma_4 \\ \sigma_5 \\ \sigma_6 \end{Bmatrix}
\qquad (3.29)
$$

where E_{ii} is Young's modulus in i direction, ν_{ij} is Poisson's ratio, strain in j direction due to stress in i direction and G_{ij} is shear modulus in the ij plane.

3.5 TESTING PROGRAM

3.5.1 Details of Wood Tested

Samples tested are cut from wood-ties used at all Railtrack test bed by D.O.T. at Pueblo, Colorado. They are creosote treated, well seasoned timber logs. Ties selected for cutting samples are free from splits, decay, plate-cut spike-killed or shattered. As the moisture content is a significant contributing factor in the behavior of wood, care has been taken to keep that variable namely the moisture content, a constant. Cut specimens are wrapped in polythene sheets and stored in humidity chamber. The overall

average moisture content of the samples tested is 5.7 percent and the density 53.00 lbs/cu ft. (0.84 g/cc). Conventional type of testing of wood like bending test, compression test parallel to grains and perpendicular grains are conducted and reported here.

3.5.2 Bending test on Wood

A beam of wood with longitudinal fibers (grains) running along the length of beam is cut out from the wood-tie. The cross-section of the beam is 2.0 x 2.0 inch (5.08 x 5.08 cm). Moment of Inertia of the section is 1.34 inch^4 (3.46 cm^4). The beam is simply supported on roller ends, Fig. (3.4). The span of the beam is 20.00 inches (50.80 cm). This roller arrangement specially made for this purpose has the facility of varying the span length, if desired. A loading yoke of known weight is hung at the mid-point of span. The deflection of the wooden beam is then measured with a dial gage. The central load is increased in steps, and corresponding deflections are measured and recorded. After reaching a magnitude of 50.00 lbs (22.72 kg), the central load is decreased in steps and the respective deflections are measured and noted. Average of deflection during loading and unloading processes for same central loading are calculated and plotted against the central load in Fig. (3.5). The slope of this load-deflection curve obtained from this flexure test of wood is the Young's modulus of Elasticity of wood E_R, and is found to be 2.46 x 10^5 psi (1.69 x 10^6 kpa).

Figure 3.4 Bending Test on Wood
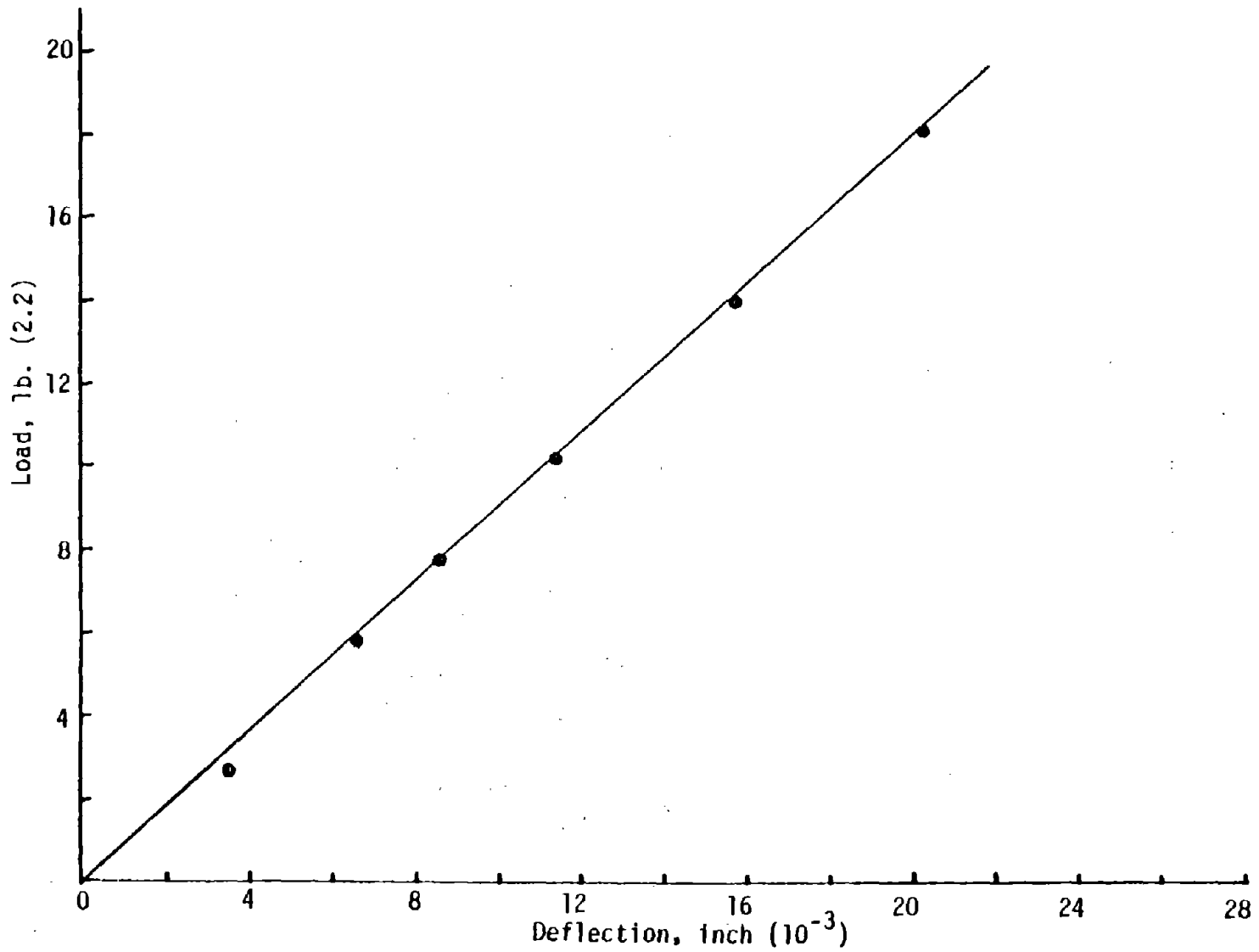
Figure 3.5 Load Deflection Curve for Bending Test

3.5.3 <u>Compression Test on Wood</u> (Parallel to Grains)

Specimens of wood-ties to the standard size of 8.00 x 2.00 x 2.00 inches (20.00 x 5.00 x 5.00 cm) are cut with their longitudinal grains running along the length of the sample. The sample is tested in the Universal Testing Machine, the loading being in the direction parallel to the grains of the sample. The deformation (longitudinal) of the sample is measured with the help of a dial gage, Fig. (3.6). The load is increased in a slow rate and the deformations at various load levels are measured and recorded. The sample is loaded upto failure. The failure of the sample is due to complete crushing of the grains. This is the possible difficulty encountered in measuring the lateral strains in other two directions during uniaxial compression [35]. This confined uniaxial compression test results exhibits a linear stress-strain relation upto certain level and then it becomes nonlinear, Fig. (3.7). The tangent modulus of this stress-strain diagram is the Young's modulus of Elasticity of wood E_L and is found to be 2.2 x 10^6 psi (1.52 x 10^7 kpa). It is adopted in practice that E_L is ten times E_T or E_R [33]. It is also proven here. The ultimate compressive strength is found to be 8050.00 psi (5.5 x 10^4 kpa).

3.5.4 <u>Compression Test on Wood</u> (Perpendicular to Grains)

The size of the specimen prepared according to ASTM [5] specifications is 6.0 x 2.0 x 2.0 inches (30.24 x 5.08 x 5.08 cm), with the longitudinal grains running along the length of the specimen. The
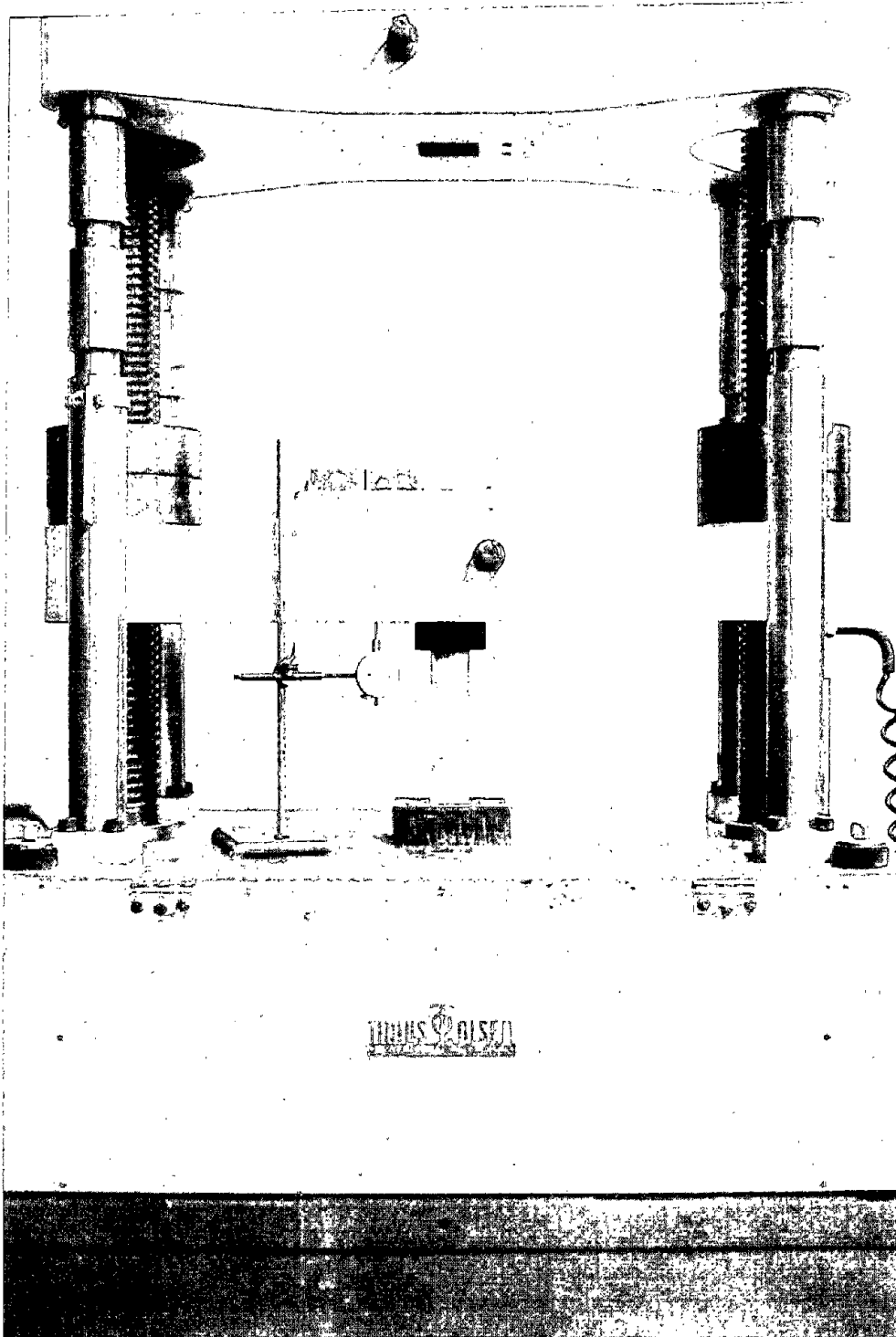
Figure 3.6 Compression Test on Wood
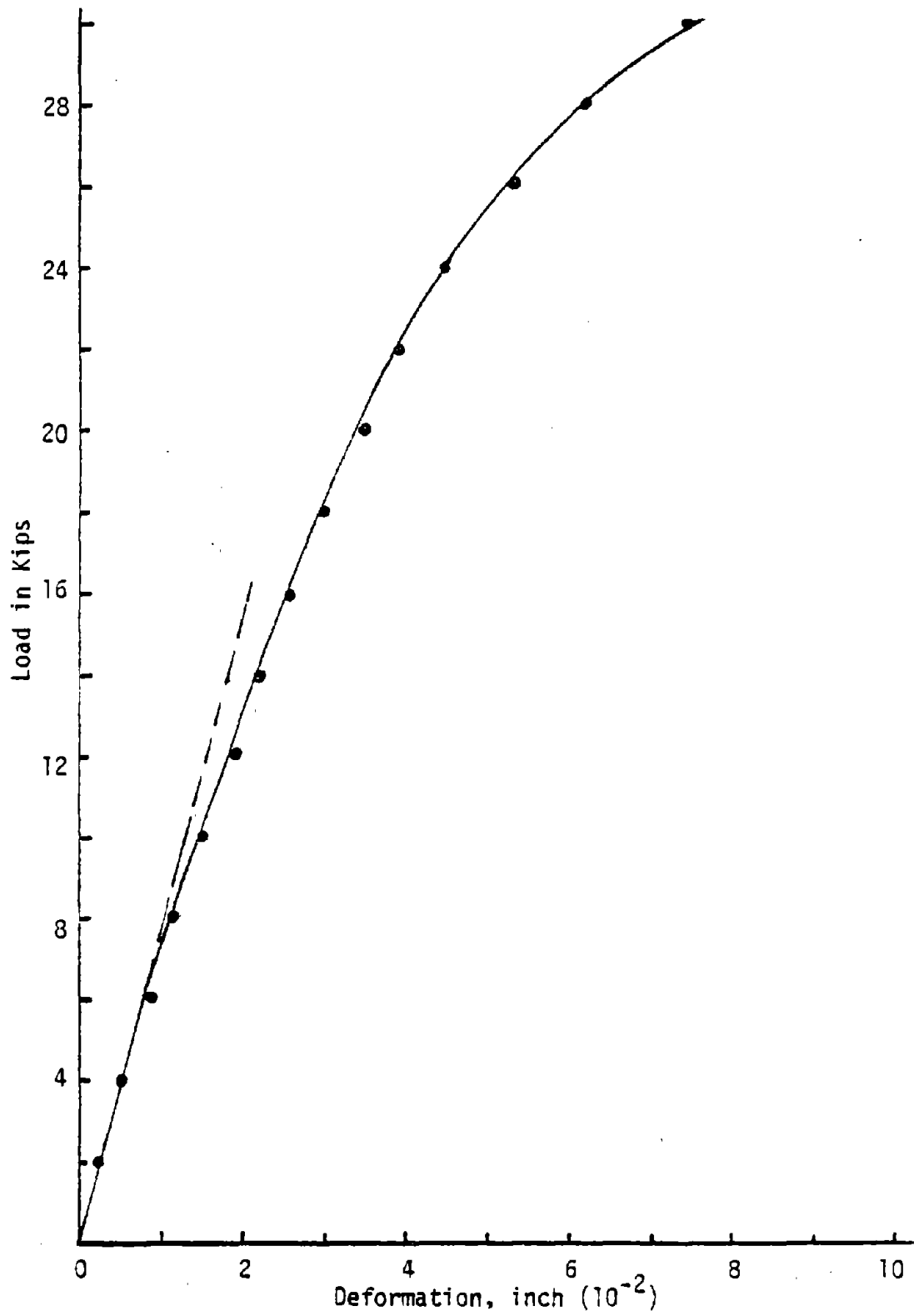
Figure 3.7 Load Deformation Curve for Compression Test

specimen is placed in universal testing machine with the length of specimen lying horizontal. A steel bearing plate of 2.00 inch (5.08 cm) wide is placed exactly at the center of the length. The load is applied on the bearing plate, in turn to the wood specimen, the direction of loading being normal to the direction of longitudinal grains. The specimen is loaded up to failure. The failure has been observed due to the splitting of the grains and the ultimate compressive strength perpendicular to grains is 2425.00 psi (1.67 x 10^4 kpa). It can be observed that this compressive strength is less than one third of that when the loading direction is parallel to the grains. Even in the rail-track bed it happens so. The loading , direction is perpendicular to the grains.

3.5.5 Multiaxial Testing

Orthotropic elastic properties of wood are determined experimentally by testing cubical 4.00 x 4.00 x 4.00 inch (10.6 x 10.16 x 10.16 cm) samples of wood in multiaxial cubical test apparatus. The details of construction of the truly triaxial device are given in references 18 and 19; salient features are reproduced herein for the same of completeness.

Truly Triaxial Device

The new truly triaxial test apparatus used in this investigation consists of a rigid cubical space frame, Fig. (3.8) to which is attached the six walls. The frame serves two functions: (1) it forms the sides of the six pressure chambers that apply the load to
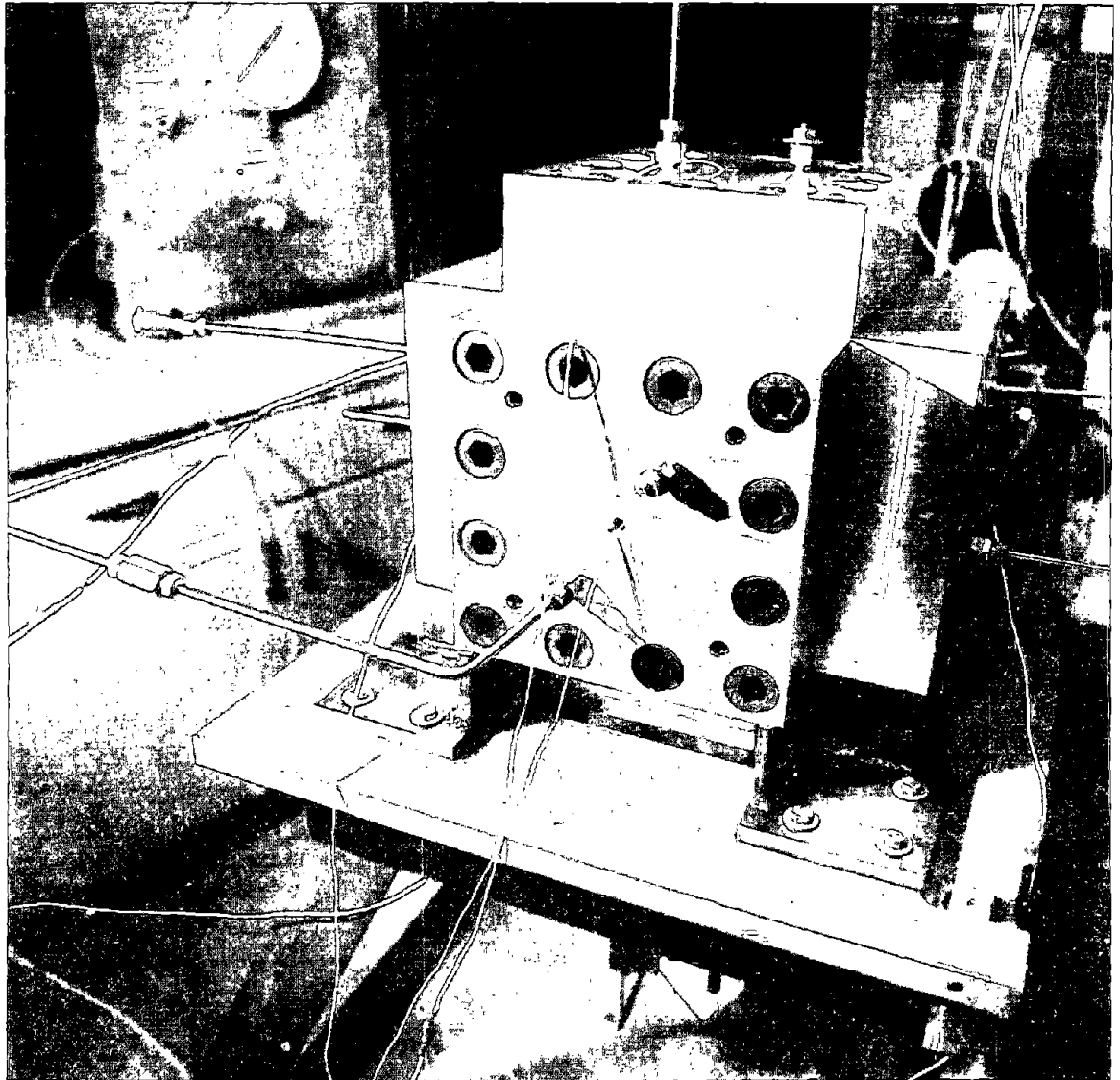
Figure 3.8 Truly Triaxial - Reaction Frame

the specimen, and (2) it serves as the reaction structure for the
loads applied to the specimen. The instrumented aluminum walls
attached to the frame serve as lids. They form the rear of the
pressure chambers and contain the deformation measuring transducers.
The openings in the frame form six similar cavities. Each of these
cavities together with adjoining walls and a proper seal arrange-
ment, acts as a pressure vessel. The wood specimen to be tested
is first placed in the center of the frame and then sealed off from
the six cavities by flexible pads. The pressure generated in the
pressure chambers are resisted by the test specimen and exterior
walls. By means of suitable hydraulic system, two oppositing faces
are connected to a common pressure generator and thus the sample is
in equilibrium.

Frame

The cubical frame is made from hard nickel steel. The exterior
of the frame is machined to a dimension of 9.900 inch (25.14 cm)
cube. The interior cubical cavity is machined to 4.070 inch
(10.33 cm). Each face of the cube has a circular, 6.075 inch
(15.43 cm) diameter, 0.720 inch (1.82 cm) deep cavity. A square
of 4.070 inch (10.33 cm) and depth of 2.193 inch (5.57 cm) opening
is centered in the center of circular cavity. This square cavity
is referred to as "pressure vessels".

The Walls

The walls serve as covers for the six pressure vessels and as a base for the displacement measuring proximitors. The walls are made from 4.00 inch (10.16 cm) thick aluminum plates. The wall essentially contains the pressure seal device and the hydraulic fluid inlet ports. Displacement measuring proximity probe is mounted at the center of the inner face of the wall. The port located at the lower side of the wall is meant for the entry of the fluid and the port at the upper side for the escape of entrapped air. The walls are securely fastened to the frame by 1.00 inch (2.54 cm) diameter Allen bolts. Because of the nature of the tightfitting wall-seal, disassembling requires a push out technique provided by 4 bolts mounted at the corners on each face. The exploded view of the wall is shown in the Fig. (3.9).

Seals

Vinyl membranes are used to contain the silicon liquid in the pressure chamber. "0" ring seal holds on to the outer sleeve of the vinyl membrane. A polyurethane pad with sleeves rests on the sample face and transmits the fluid pressure from the membrane to the specimen. It is flexible enough to follow minor differential distortions on the specimen surface. The hydrostatic pressure inside the membrane squeezes the pad sleeves towards the steel walls inside the cavity Fig. (3.10). With a smooth uniform contact between the pad and the sidewalls of the pressure cells, a proper seal is maintained.
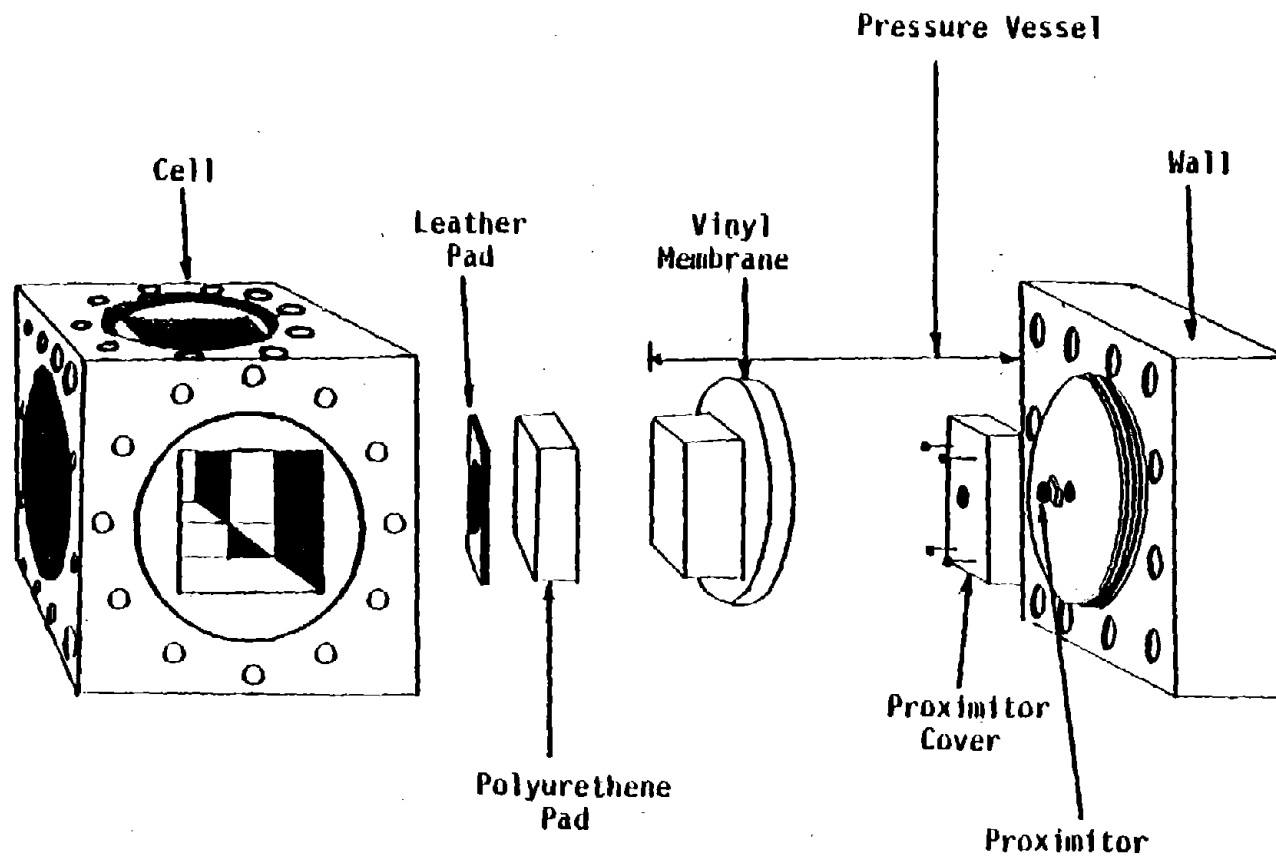
Figure 3.9 Details of Multiaxial Cell and One Wall

Cell

Leather Pad

Vinyl Membrane

Pressure Vessel

Wall

Polyurethene Pad

Proximitor Cover

Proximitor

111
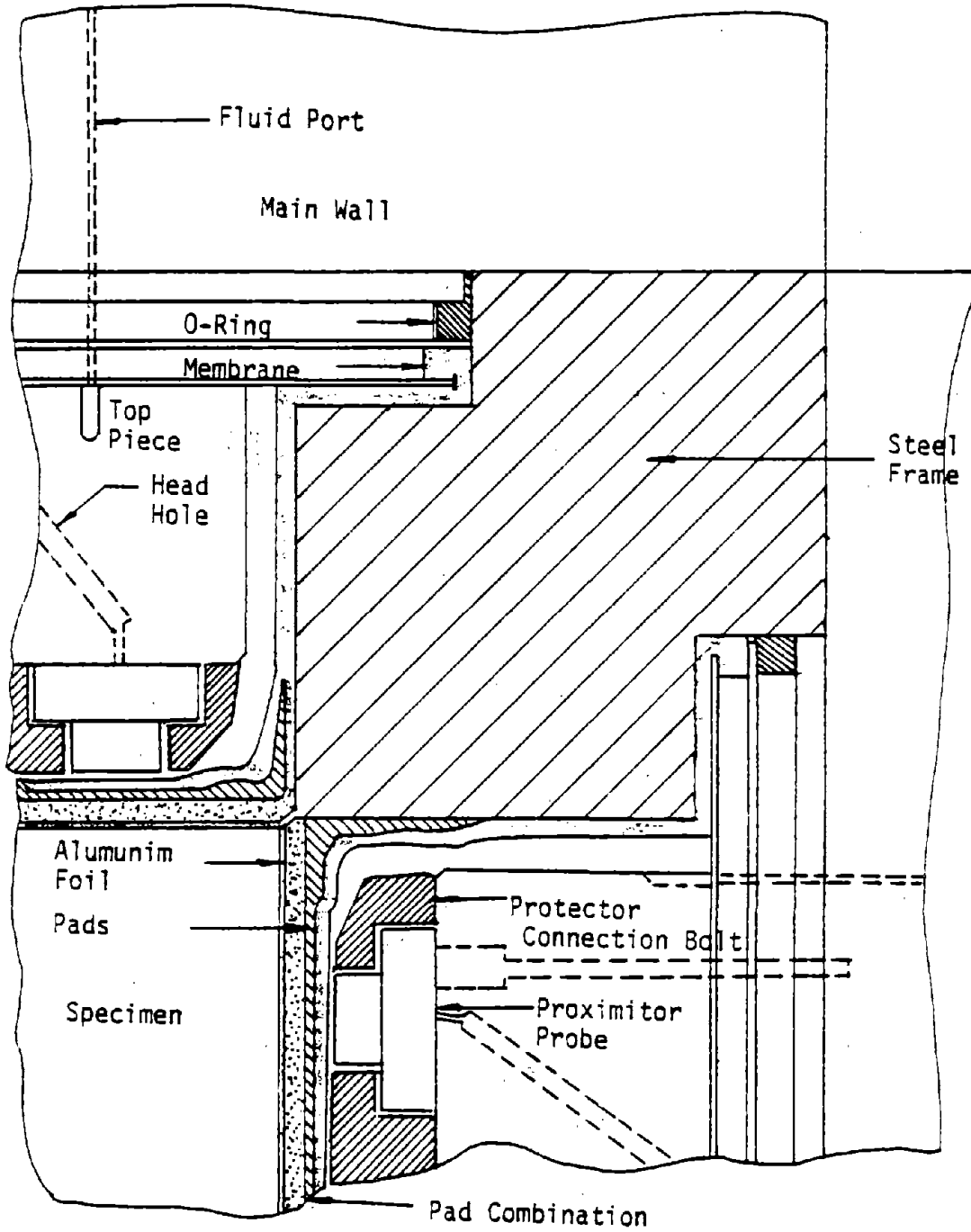
Figure 3.10 Pressure Seal Arrangement

Pumping System

The hydraulic pressure that is applied to each of the six sides of the cubical specimen is generated and controlled by a hydraulic system constructed for this experiment. Silicon liquid is pumped by positive displacement pumps. These three independently operated pumps, by suitable valving, can be used to produce any combination of the stresses in the three principal axes. Pressures are measured by Bourdon pressure gages 0-20,000 psi (0-1.38 x 10^5 kpa) range, fitted to each pump, Fig. (3.11). The pumps themselves with thier drain valves act as pressure regulators. Valves are installed in the lines leading to the wall. A rapid filling arrangement is used to fill the membranes before the start of the experiment. Silicon liquid is forced into the membranes from a reservoir of liquid by compressed air. The same arrangement works backward in draining the liquid from the membranes, when vacuum is applied instead of compressed air.

Deformation Measurement System

Surface displacements on the specimen are measured by a Bently Proximitor probe system. The system is composed of two basic units; the probe, which is the sensing element, and the proximitor driver, which provides the excitation to the probe. The system works on inductive proximity principles and so does not have any physical contact with the specimen under test. The probe Fig. (3.12) measures the distance between the specimen and a detector coil embedded in
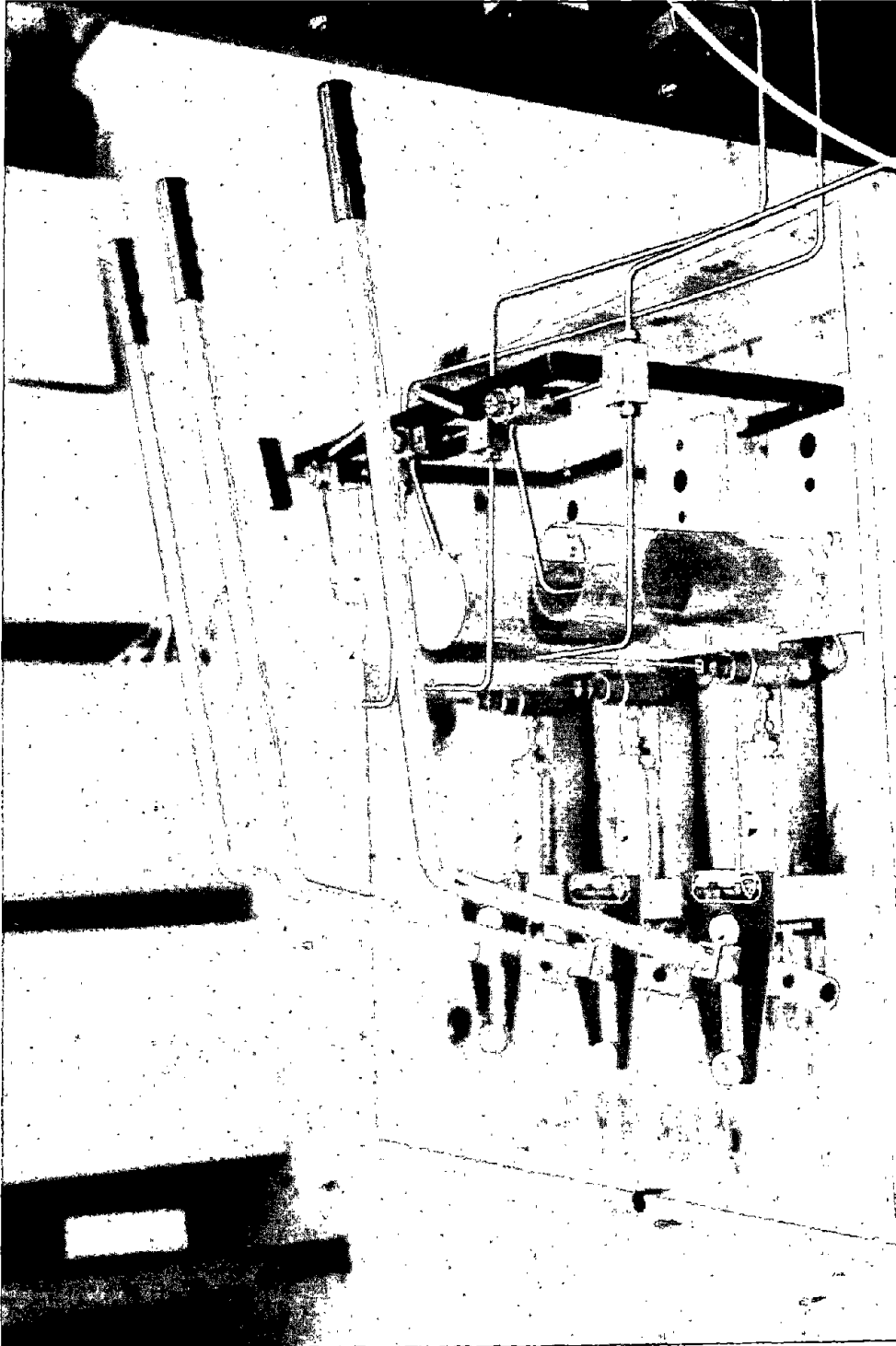
Figure 3.11 Pumping Unit for Truly Triaxial Device

Figure 3.12 Proximity Probe - Exploded View of the Valve

the tip of the probe. The test specimen is covered with a con-
ducting aluminum foil. The probes now have the foil as a well
defined target to aim at. The vinyl membrane, silicon fluid
and pad system occupies the space between the target and the
probe tip. Presumably these are all non-conductive and
dielectric.

The proximitor probes are calibrated in a special calibration
set up, Fig. (3.13) before use in an experiment. The calibration
set up is so designed that it simulates the action inside the
pressure vessels. Readings are taken with the help of a dial gage
connected to a target through a solid threaded aluminum rod. These
calibration values are used to extrapolate the measured displacements
in form of voltages during the experiment.

Data Acquisition System

The pressures (stresses) in the three principal directions of
the device are recorded and stored in a calculator. The proximitor
readings are monitored by means of scanner, voltmeter and then
recorded and stored in the memory of the calculator. The recording
sequence consists of the readings of six proximitors, one control
proximitor to record electronic drift, preceeded by three pressure
readings. The recorded pressure and voltage readings are printed out
on a paper tape. A constant scanner recording frequency is "set",
so that each channel has equal time to "set" to a steady voltage.
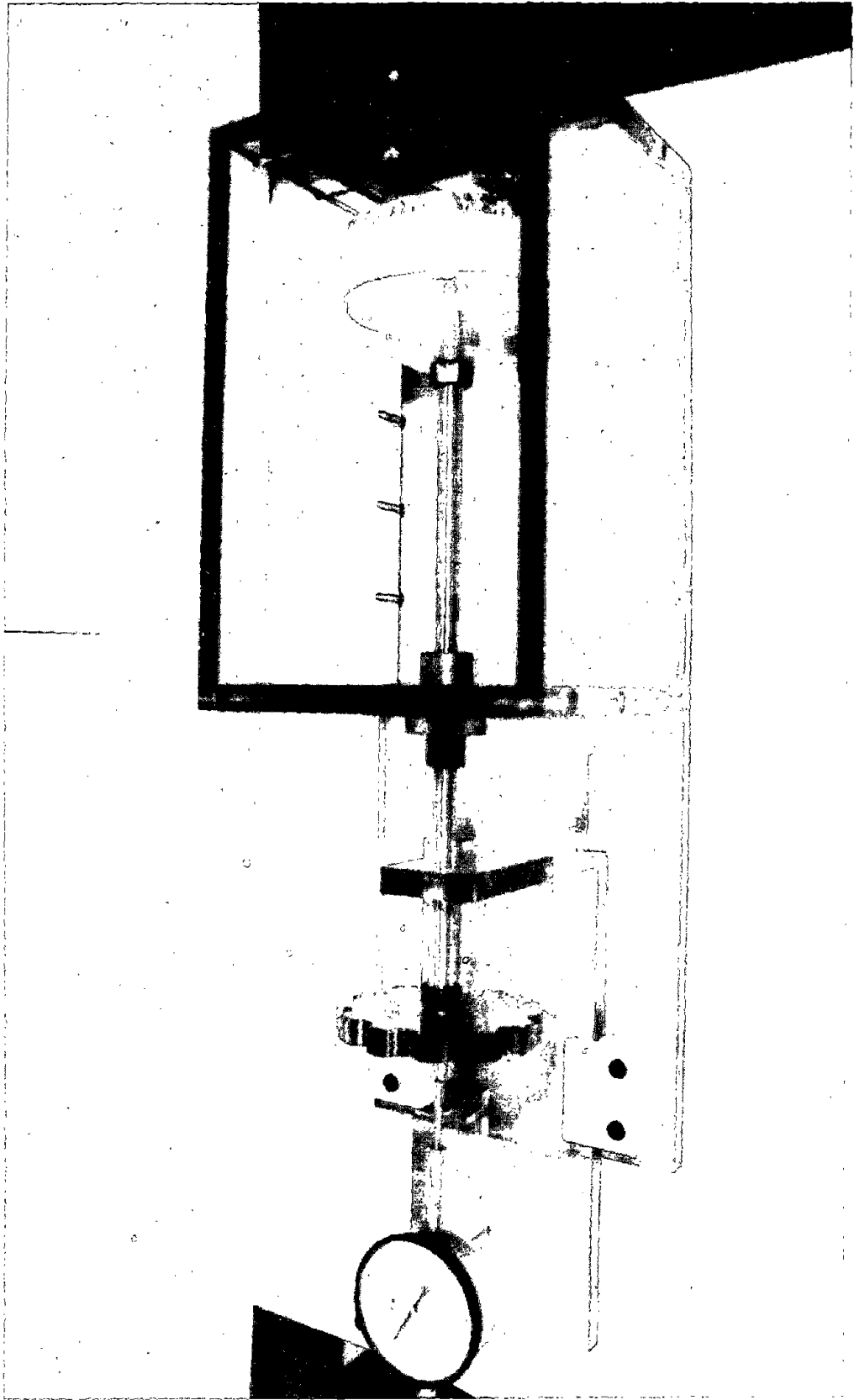
Figure 3.13 Proximity Probe Calibration Unit

3.5.6. Procedure for Testing

Sample Preparation

A 4.00 inch (10.16 cm) cubical sample of wood must be cut and finished to within a tolerance of 0.01 inch (0.25 cm) with smooth surfaces. Samples from wood ties from the test bed Pueblo, Colorado are cut so that the longitudinal grains are truly horizontal. The grain angle is zero in that case. Samples are finely finished in lathes for smooth surfaces and correct dimensions. Too large a sample will not fit into the cavity, and too small a sample will result in large gap widths between the aluminum foils covering the sample and the proximitors. This gives decreased accuracy in measurement of the deformations. Also a large gap will give bad boundary conditions because the pads will be exposed to each other to a larger degree. Cracks and cavities on the surfaces of the sample if any are filled with plastic wood putty.

Equipment Preparation

The proximitor coaxial cable after its calibration against the same material is fixed to the aluminum wall. A protective cap is inseted over the proximitor head. Vinyl membrane is fitted over the proximitor and its rim slipped over the 'O' ring. In this manner, all six walls are prepared. The sides of square cavity in the frame are greased with silicon grease. The sleeves of the pads are coated with "stop cork grease" and a thin teflon sheet is laid over the coating of the grease. All these lubricating efforts are to

minimize any friction between the sleeves of the pad and the cavity. The bottom wall is bolted on to the frame first. The pads are inserted in their cavities.

Testing

Now the sample, with six sides covered with aluminum foil is placed carefully into the mid cavity to rest on top of the bottom pad. Care is exercised to see the longitudinal grains to remain horizontal. The top wall is then bolted on. The specimen is centered before the walls are bolted on. The other faces are then bolted to the frame with high strength steel Allen bolts. These bolts are tightened in a systamatic pattern to a torque of 250.00 ft.lbs (34.43 m-kg) with a torque-wrench. The probes are then connected through coaxial cables to the appropriate channels in the data acquisition system. The membranes are filled with silicon liquid by the rapid filling system, with the entrapped air bled through the drain holes. The pressure vessels are connected to the pumps. The test is then initiated with an initial scanning of proximitor readings, with the hydrostatic pressure to be zero. The fluid is pumped to get desired stress intensities in the three principal directions of the device. The pumping is continued till the load gets stabilized. Then the proximitor readings are scanned and recorded. The scanning process is repeated at every increment of the load history.

Orthotropic elastic constants for wood are determined by conducting uniaxial compression test on the specimen. The load is applied, incrementally, in one direction, but the deformations are measured in all the three directions. The stresses applied and the strains measured are plotted.

The truly triaxial test cell is only capable of applying normal stresses. So to find the shear compliances, the technique used is to apply normal stresses to non-principal material planes, monitor the resulting normal and shear strains in these directions, and transform the measured strains to refer to the principal directions. By cutting a specimen with an oblique orientation with respect to its principal material planes, the applied normal stresses can be resolved into components of shear stresses and normal stresses on these planes.

Cubical samples with the longitudinal grains inclined at 45 degrees to the horizontal are cut from the wood-ties. They are trimmed to the size and shape and tested. Uniaxial compression test on the same sample has been conducted in two directions, $3'-3'$ direction and $2'-2'$ directions, Fig. (3.3), but the deformations are monitored in all the three directions. The ability to apply three independently variable principal stresses in this device, makes it possible to perform three separate tests on one cubical specimen without retrieving the sample from the machine and reorienting it. To determine the shear compliance values D_{55} and D_{66} in Eq. (3.13) specimens are cut with an obliquity of 45 degrees to the other

two axes, radial and tangential directions respectively and tested. The stresses applied in each case and the respective strains measured are plotted. Samples have been so selected that they do not contain knots and cavities inside the specimen. From the values of compliance parameters determined from the experimental results, the moduli and Poisson's ratios are determined.

Test Results

The stress-strain responses obtained from uniaxial tests on cubical samples are presented in Figs. (3.14), (3.15) and (3.16). In all the three cases, the longitudinal grains are kept horizontal during testing, that is, α equals to zero.

The sensitivity of the deformation measuring system is so high that very minute changes in strain are recorded accurately. The uniaxial loading is once in direction normal to the longitudinal grains, namely loading in (Z) radial direction and in other two times once along the tangential (Y) direction and the other along longitudinal (X) direction. The loading is applied incrementally and at each increment, the deformations are measured in all three directions.

The stress-strain responses plotted for these three tests show a near linear relationship. The compliance parameters E_{ii} and ν_{ij} in Eq. (3.29) are determined from these test results. Different scales are used in the strain axis depending upon their magnitudes so that they can be well presented.
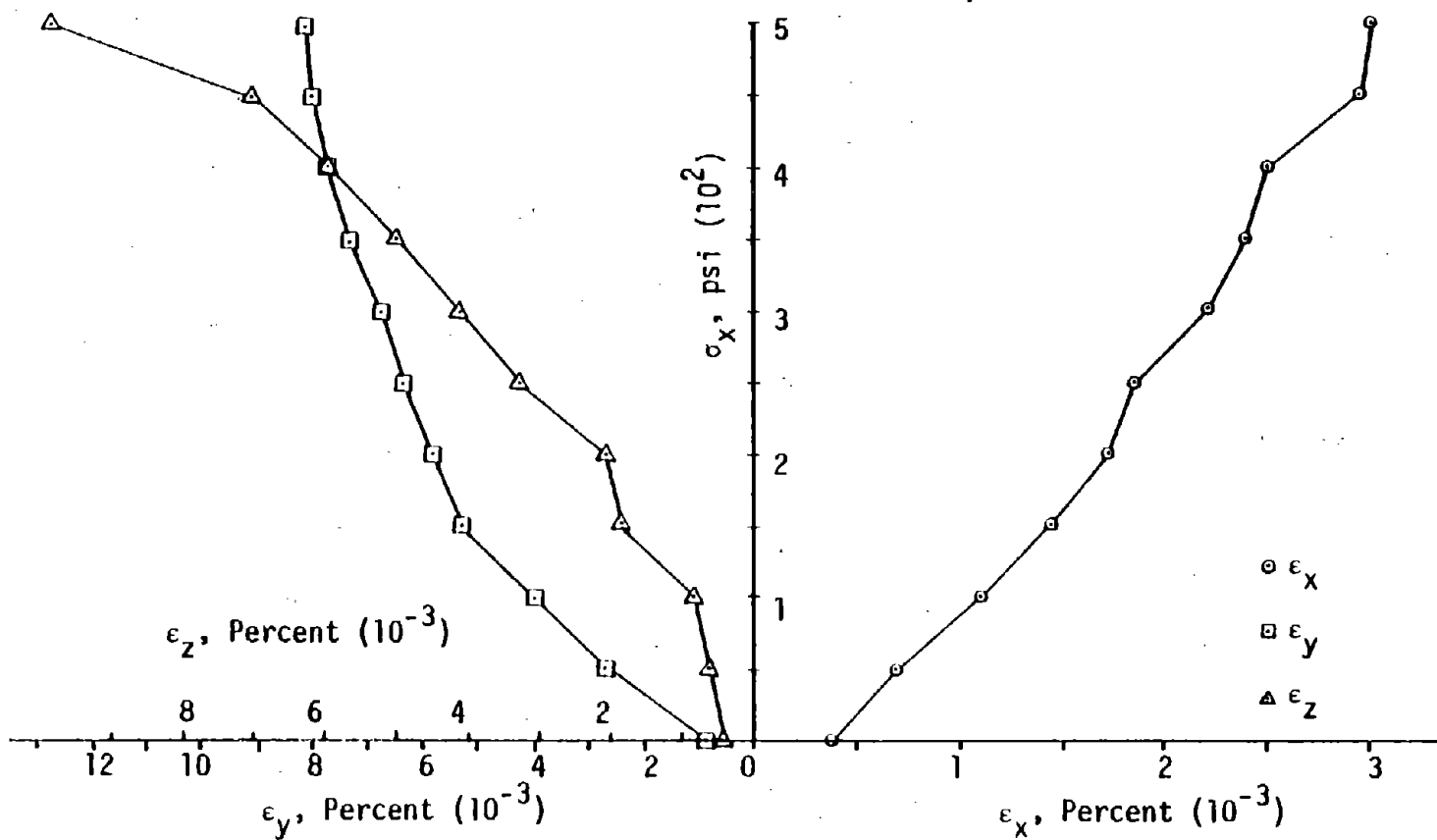
Figure 3.14 Stress-Strain Response Curves for Uniaxial Compression Test (α = 0°)
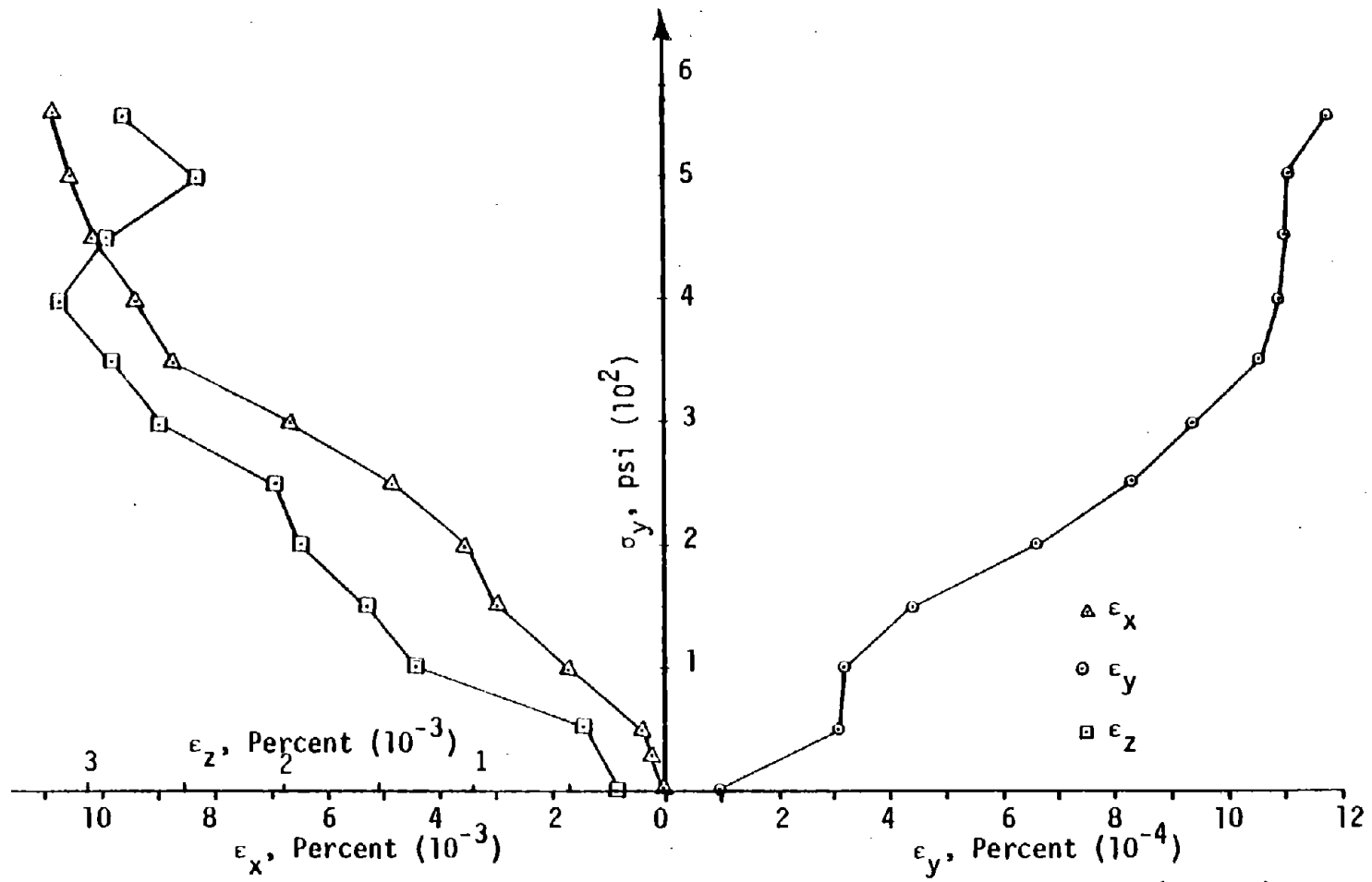
Figure 3.15   Stress-Strain Response Curves for Uniaxial Compression Test ($\alpha = 0°$)
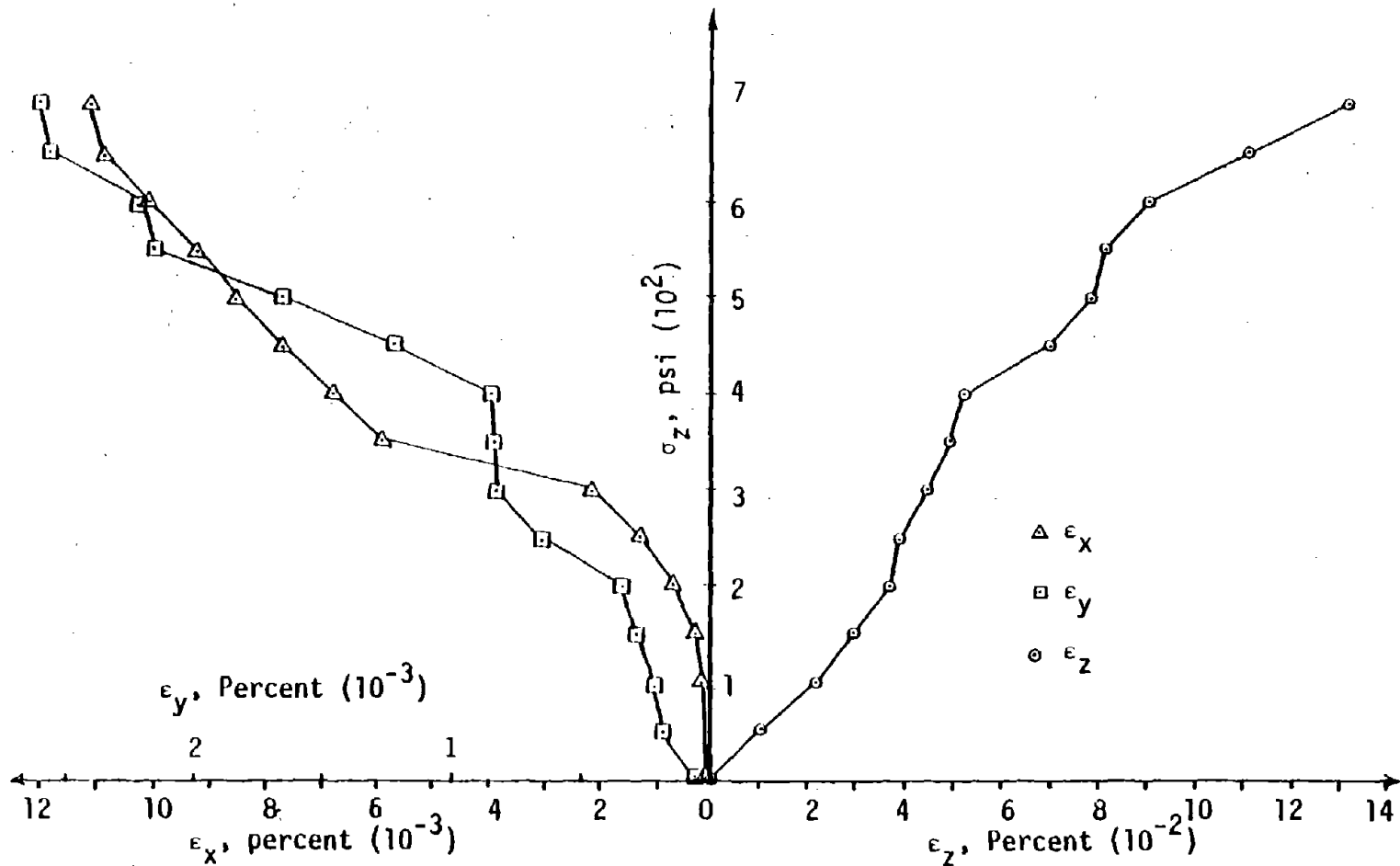
Figure 3.16 Stress-Strain Response Curves for Uniaxial Compression Test (α = 0°)

The shear compliances are determined by testing cubical samples with their grains cut at 45 degrees orientations to the material principal planes. The sample is loaded uniaxially in different directions like 3′-3′, 2′-2′ and 1′-1′ as shown in Fig. (3.3). The stress-strain responses are shown in Figs. (3.17), (3.18) and (3.19).

The variations of strain when tested with direction of loading either in x direction (2′-2′) or in z direction (3′-3′) are very non-uniform. The scatter may be due to the slipping of the grains along the slipping planes and also probably due to collapse of the structure and then regrouping upon subsequent loading. However, when the loading is in the y direction 1′-1′, the stress-strain response curves do not meander as they do in other two cases. This may be because the direction of the loading coincides with the slipping planes and that the structure does not get disrupted as it does when loaded either in direction 3′-3′ or 2′-2′.

Many samples cut at 45 degree orientation some to longitudinal direction, some to radial direction and others to tangential direction are tested. Results from experiments considered well conducted are presented. The shear compliances in the Eq. (3.29) are then determined from the stress-strain responses obtained from such tests and are presented in Table 3.1.

3.5.7 MODELING AS NONLINEAR MEDIUM

Wood as a structural member is likely to get often loaded beyond its elastic limit. Wood-ties in particular are subjected to heavy

Table 3.1

Elastic Constants for Wood

| Youngs Modulus in KN/m^2	E_{11}	E_{22}	E_{33}
	151.8×10^5	140.1×10^4	128.7×10^4
Shear Modulus in KN/m^2	G_{13}	G_{12}	G_{23}
	135.1×10^4	92.6×10^4	318.0×10^3
Poissons Ratio	ν_{12} ν_{13}	ν_{21} ν_{23}	ν_{32} ν_{31}
	0.215 0.347	0.241 0.221	0.324 0.302

Figure 3.17 Stress-Strain Response Curves for Uniaxial Compression Test (α = 45°)
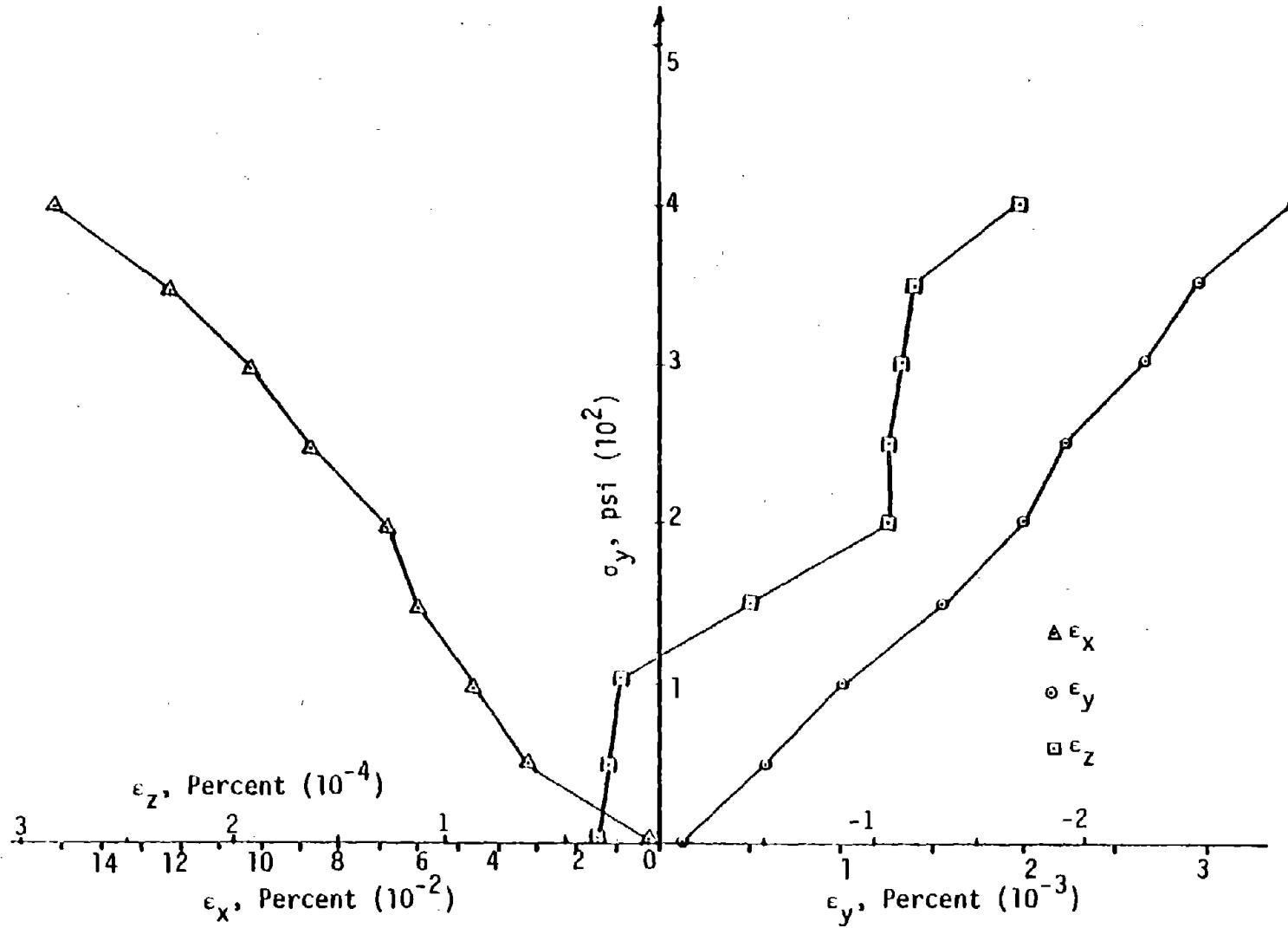
Figure 3.18   Stress-Strain Response Curves for Uniaxial Compression Test
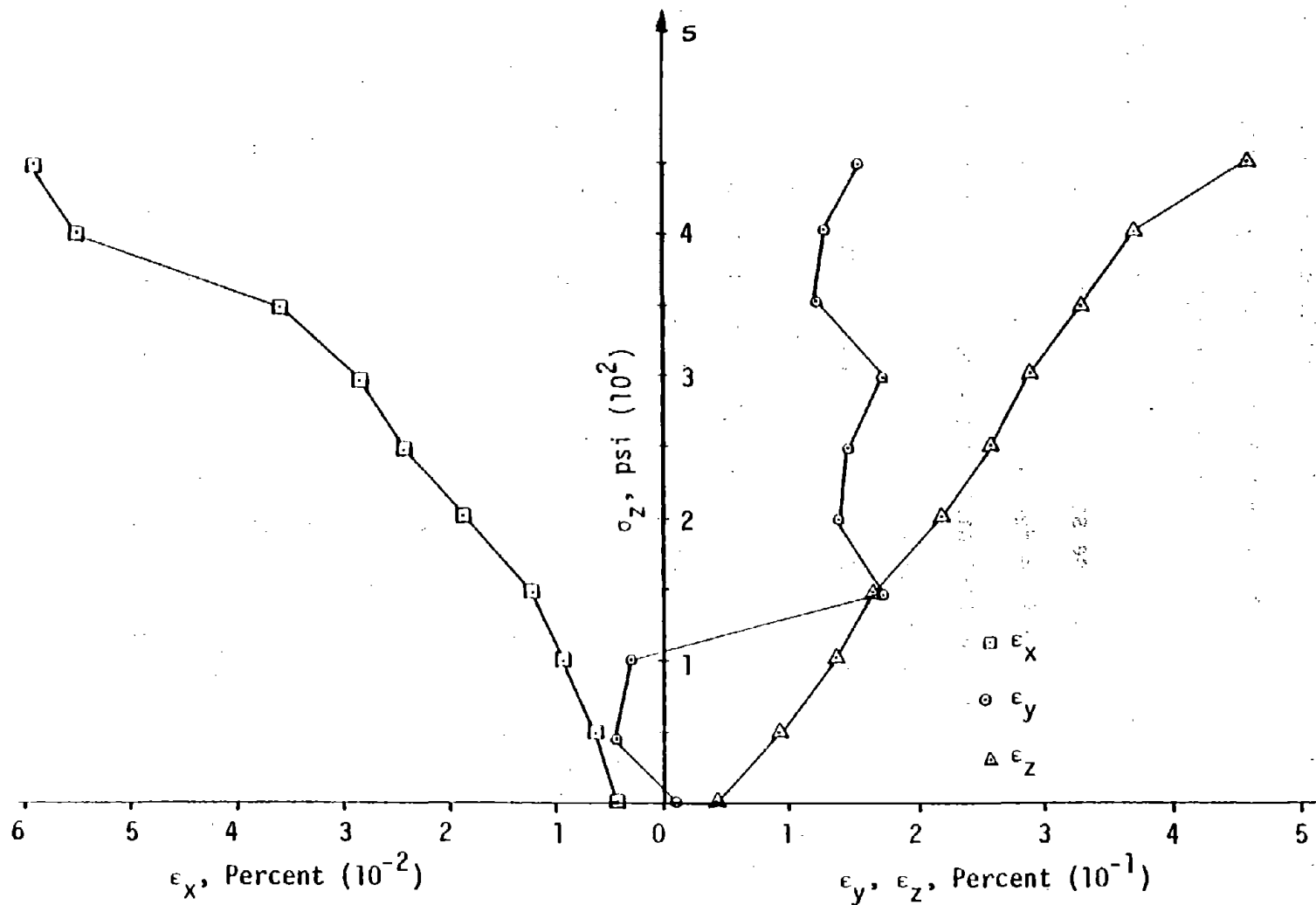
Figure 3.19. Stress-Strain Response Curves for Uniaxial Compresssion Test

moving loads, which are repetitive in kind and dynamic in nature. The stress-strain relationship of wood at high stress levels is observed to be nonlinear and upon unloading the recovery of strain is not total. Timber-ties in rail-track bed are subjected to various types of stresses. The stresses depend upon many factors such as wheel loads, dynamic effect of wheel loads, elasticity of the rail, effeciency of the fastening, track modulus and traction force due to suddenly applied breaks.

Further, due to yielding property of the ballast, the bearing pressure under different points of the tie varies. It deflects like an inverted over hanging beam with hogging in the middle and sagging at the ends [62]. Idealising wood as a linear elastic material in such conditions, no longer gets justified. A meaningful three-dimensional characterization of the wood can be achieved by testing in all possible stress paths and stress levels.

3.5.8 Stress Path Dependency

In order to investigate stress path dependency, tests are con ducted by following significant stress paths, Fig. (2.7). The specimens cut with α equals to zero, α being the inclination of longitudinal grains with horizontal plane, are tested. They are positioned in the cubical cell (reaction frame) with the longitudinal grains remain horizontal.

3.5.9 Hydrostatic Compression (HC or IC)

Increments of Load (stresses) of same magnitude are applied on all six faces of the specimen. Silicon fluid is pumped to develop the pressure. The valve positions are arranged such that one pump can be used to pump fluid to all six pressure vessels to develop a hydrostatic compression state. Pumping is stopped once the load level is reached. If the pressure drops, fluid is pumped again till the load gets stabilized. The deformation readings are then recorded. Loading is continued upto a stress level, when the sample is unloaded completely. The sample is reloaded to a higher stress level and then the load is reversed.

Strains in three principal directions are plotted against the hydrostatic stress in Fig. (3.20). The strain in the z direction, namely normal to the longitudinal grains is greater than that of those observed in the other two directions. The magnitude of strains in the x and y directions do not vary significantly from each other. This probably suggests that transverse isotropy (isotropy along the plane normal to longitudinal grains) can be assumed for a better approximation.

3.5.10 Conventional Triaxial Compression (CTC)

Wood sample is tested in CTC stress path with its longitudinal grains remain horizontal. The deviator stress is applied in a direction normal to the longitudinal grains. The stress strain responses for CTC tests at different confining pressures are
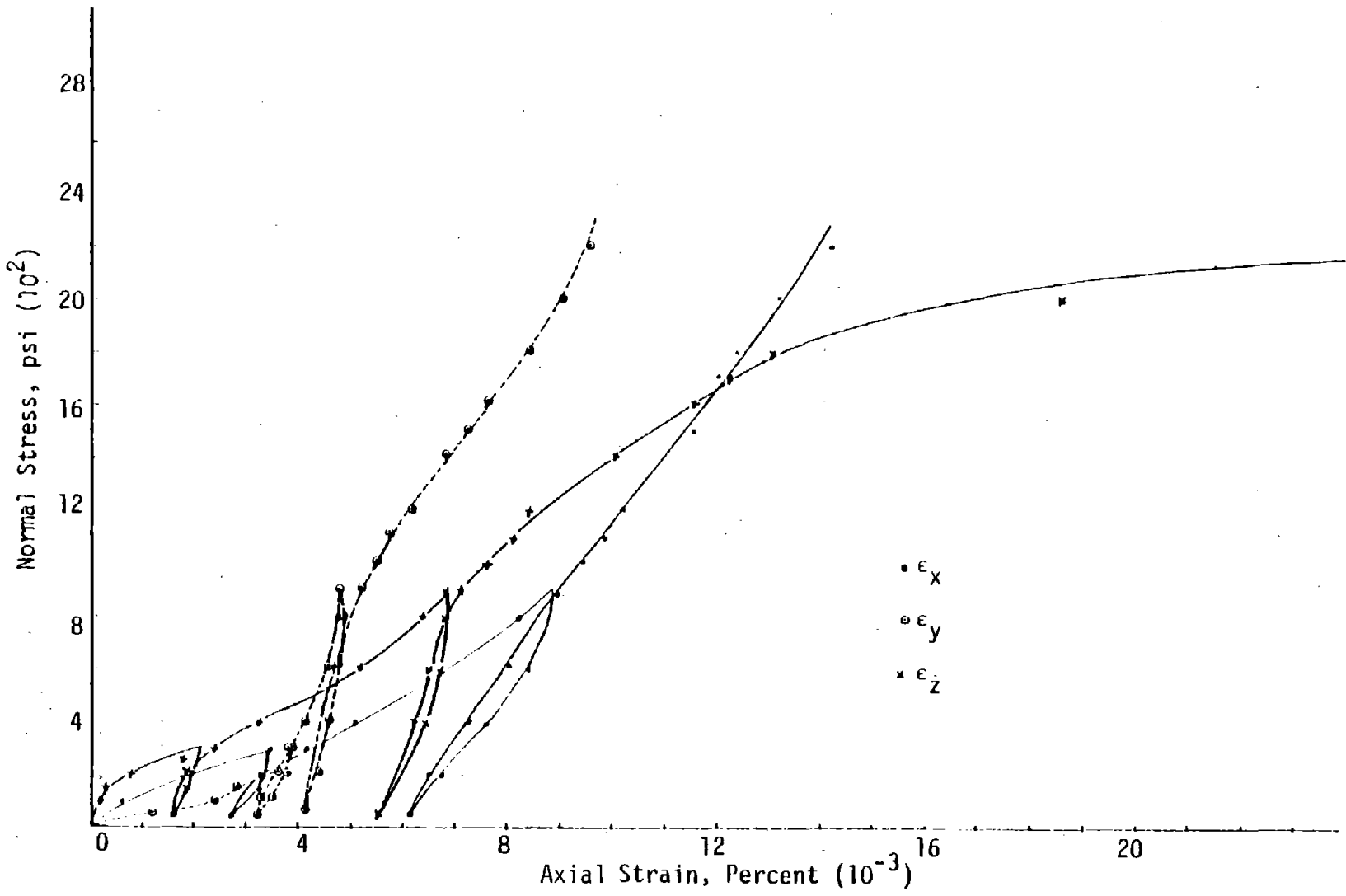
Figure 3.20   Stress-Strain Response Curves for Hydrostatic Compression Test

plotted in Figs. (3.21) and (3.22). The strain in direction of deviator stress is seen nearly ten times that noticed in the lateral directions. However, the recovery of strain is more in the deviator stress direction upon unloading. No well defined ultimate strength plateau indicating failure is noticed. Details of conducting a CTC test is given in section 2.6.2.

3.5.11 Reduced Triaxial Compression (RTC)

The sample is loaded to a desired hydrostatic stress level of 1000.00 psi (6.9 x 10^3 kpa). The pressure is increased in steps, each increment applied after the stabilization of load at that level. σ_1 is then held constant while σ_2 and σ_3 are reduced in stages with decrement $\Delta\sigma_2$ equal to $\Delta\sigma_3$. The confining pressure drops as the specimen is sheared. The magnitude of decrement is 100.00 psi (6.9 x 10^2 kpa). The stress-strain responses for this test are shown in Fig. (3.23). A well defined ultimate strength level is reached in this test. At a deviator stress of 900.00 psi (6.21 x 10^3 kpa) the specimen fails to shear.

3.5.12 Simple Shear (SS)

Intermediate principal stress, σ_2 is kept constant, equal to σ_{oct} = 500.00 psi (3.45 x 10^3 kpa). The major and minor principal stresses σ_1 and σ_3 are increased and decreased respectively by the same amount so that σ_{oct} remains constant. The stress-strain response curves are shown in Fig. (3.24).
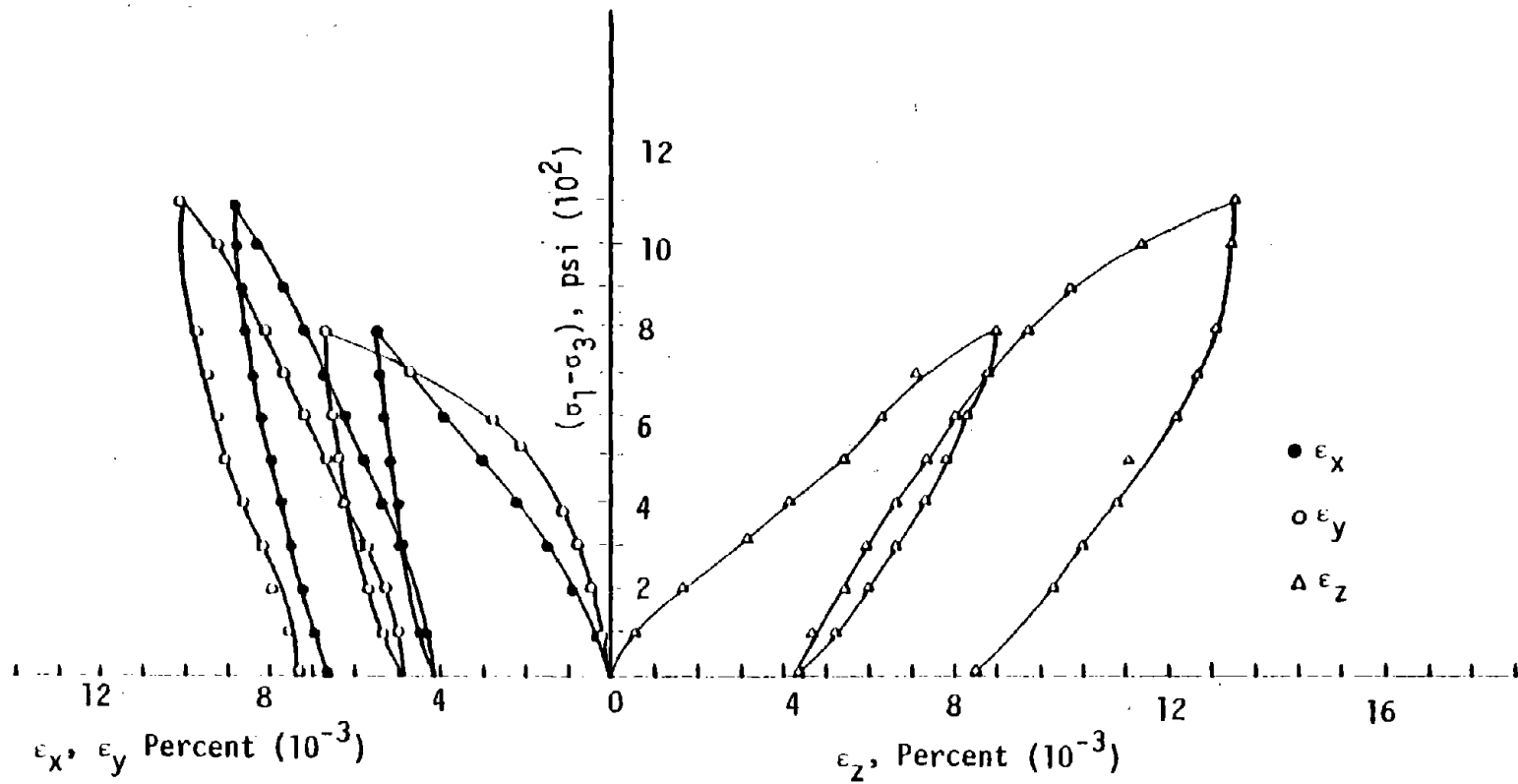
Figure 3.21   Stress-Strain Response Curves for Conventional Triaxial Compression Test ($\sigma_2 = \sigma_3 = 100$ psi)
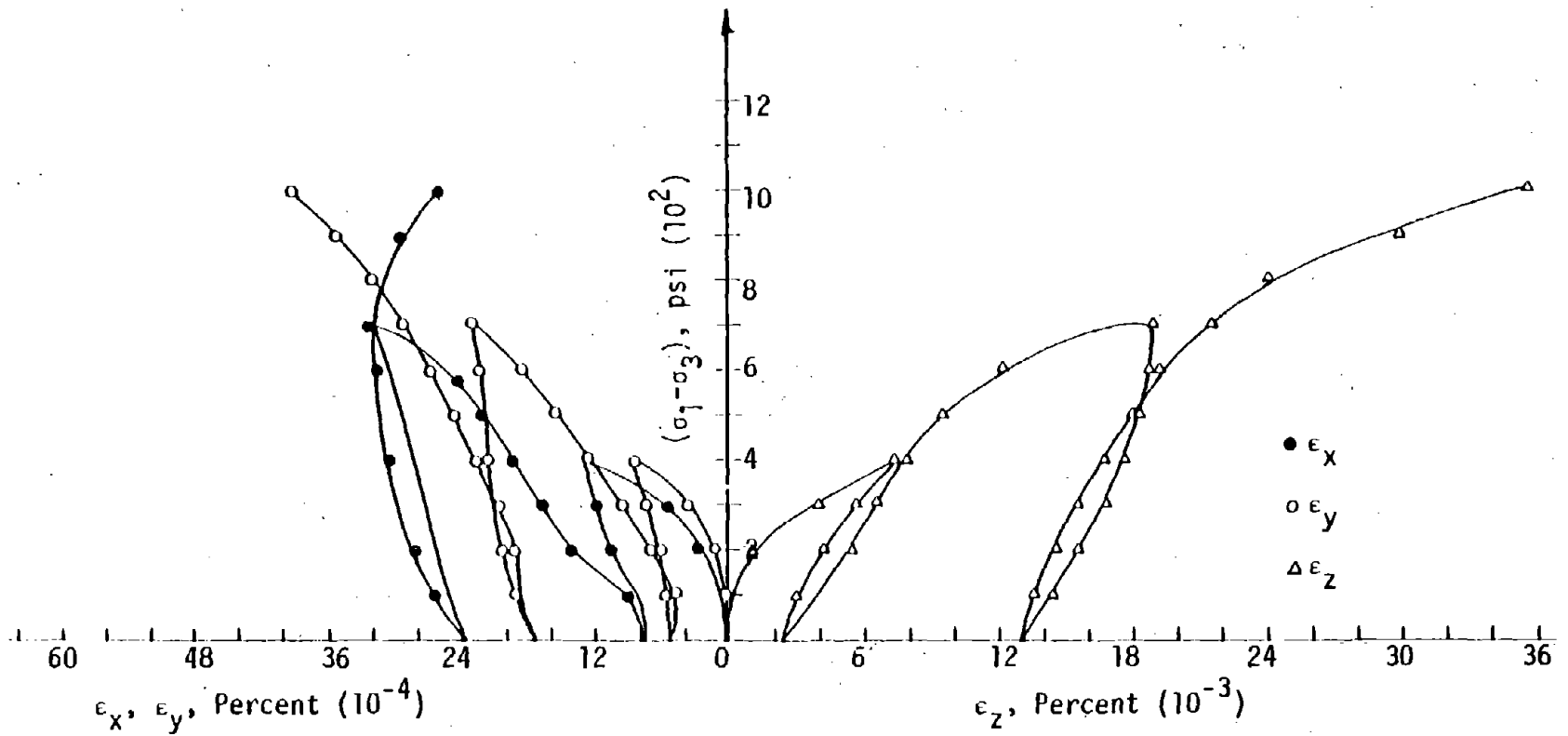
Figure 3.22   Stress-Strain Response Curves for Conventional Triaxial
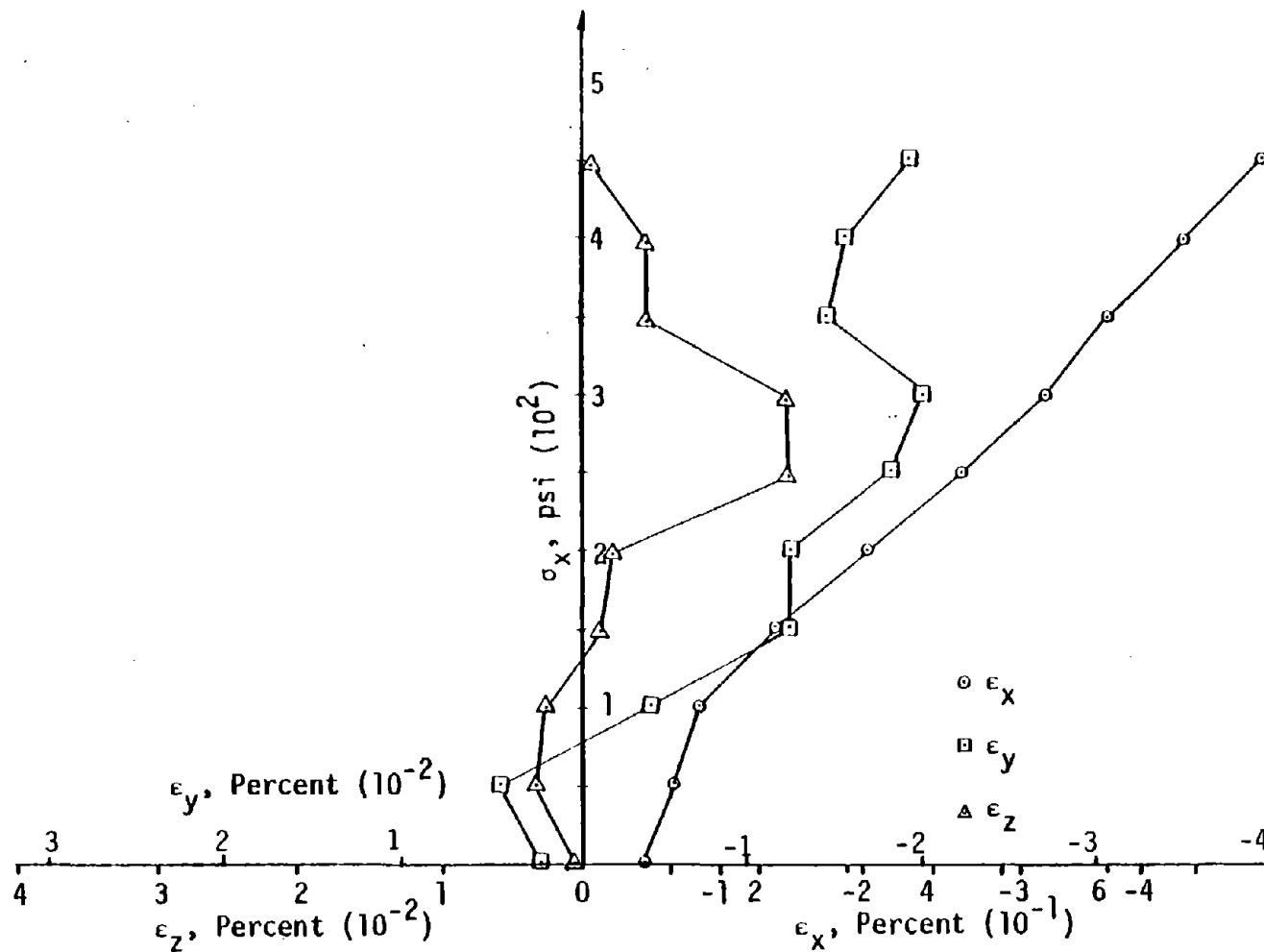Compression Test ($\sigma_2 = \sigma_3 = 200$ psi)
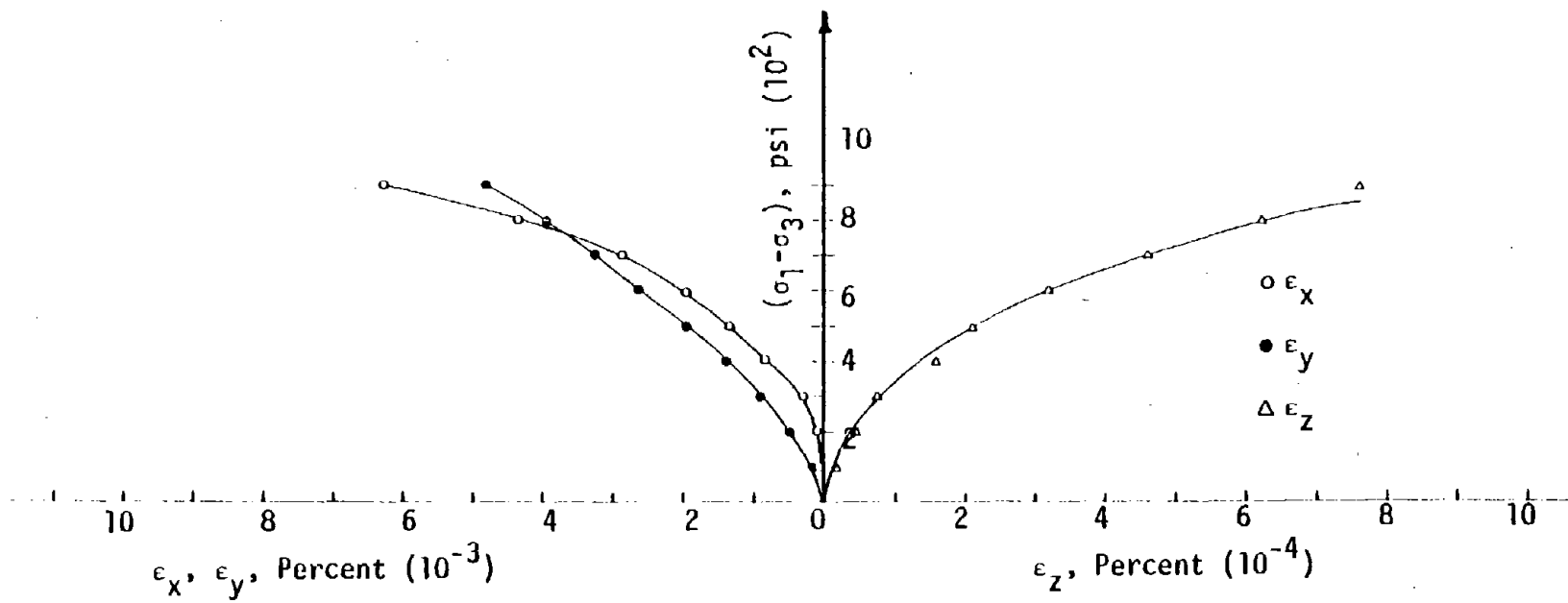
Figure 3.23 Stress-Strain Response Curves for Reduced Triaxial Compression Test ($\alpha = 0°$)
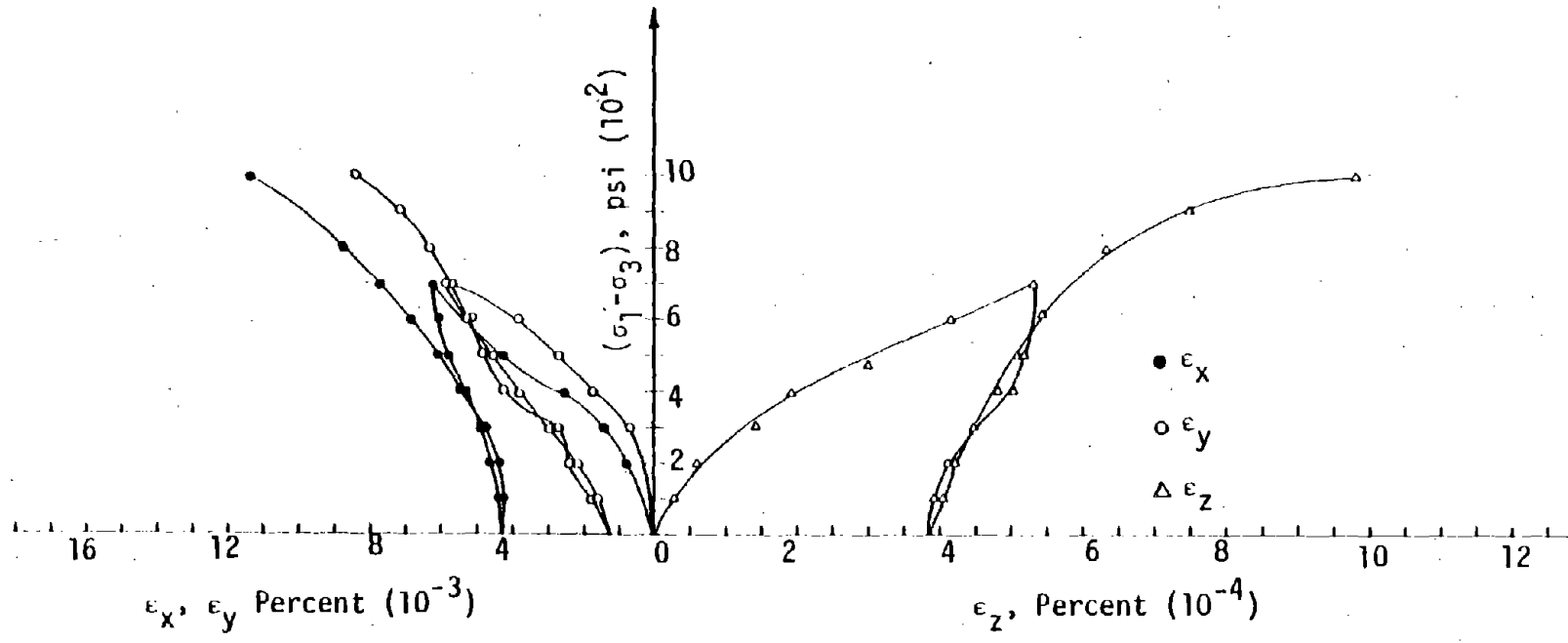
Figure 3.24   Stress-Strain Response Curves for Simple Shear Test

137

The strains along the major principal stress σ_1 increases as σ_1 increases. The strains in σ_3 direction (x direction) increases comparitively more as σ_3 decreases. If a material is isotropic, the intermediate principal strain will be very insignificant. Here the intermediate principal strain increases as $(\sigma_1-\sigma_3)$ increases. This is probably because of the anisotropy nature of the material. Furthermore, ε_y does not differ very much with ε_x at different load levels. It gives an insight into the behavior of the cross-anisotropic wood in which shearing takes place in both x and y directions. Strains in y directions are little less than those in x probably because of the application constant intermediate stress in y direction.

3.5.13 Triaxial Compression (TC)

The major principal stress σ_1 is increased while σ_2 and σ_3 are decreased. The sample is loaded upto 400.00 psi (3.96 x 10^3 kpa) of hydrostatic state and then σ_1 is increased. The increment of major principal stress, $\Delta\sigma_1$, is double that of decrement $\Delta\sigma_2 = \Delta\sigma_3$. σ_{oct} remains constant. The stress strain responses for this test are plotted in Fig. (3.25). The major principal stress σ_1 direction is normal to longitudinal grains.

3.5.14 Conventional Triaxial Extension (CTE)

The hydrostatic stress is increased upto 300.00 psi (2.07 x 10^3 kpa). σ_1 is kept constant to be 300.00 psi (2.07 x 10^3 kpa), σ_2 and σ_3 are increased and the strains are measured in all the three
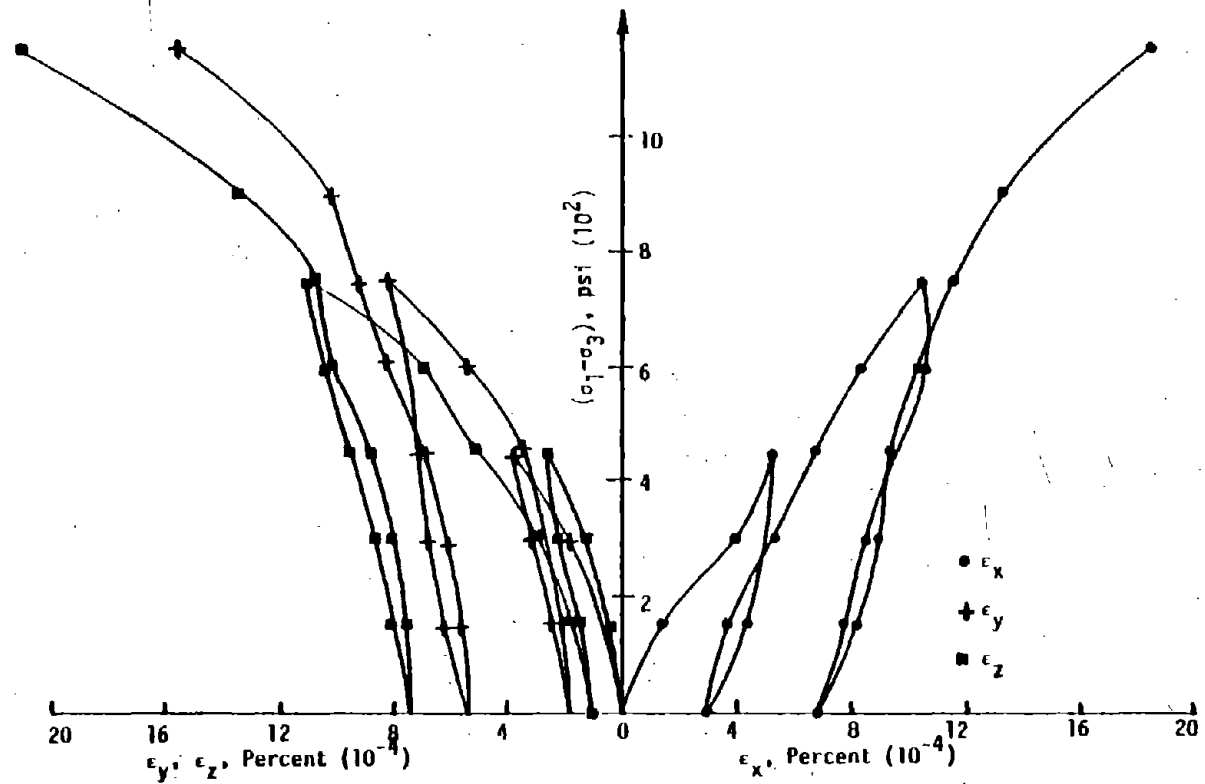
Figure 3.25 Stress-Strain Response Curves for Triaxial Compression Test

directions. The stress-strain responses of this test are plotted in Fig. (3.26).

3.5.15 Triaxial Extension (TE)

In the TE test, σ_1 is reduced and σ_2 and σ_3 are increased such that σ_{oct} is constant. From the hydrostatic stress level of 600.00 psi (4.14 x 10^3 kpa), σ_1 is decreased, the decrement is double that of the increment $\Delta\sigma_2$ or $\Delta\sigma_3$, both $\Delta\sigma_2$ and $\Delta\sigma_3$ being equal. The stress-strain curves are plotted in Fig. (3.27). They show a well defined ultimate strength level.

3.5.16 Reduced Triaxial Extension (RTE)

Figure (3.28) shows the stress-strain response curves for the RTE test on wood. The stresses σ_2 and σ_3 are kept constant at 600.00 psi (4.14 x 10^3 kpa), the stress level up to which the sample is loaded hydrostatically. The stress is decreased in steps.

As the magnitude of $(\sigma_3 - \sigma_1)$ increases, namely as the shearing stress increases, the sample shears and shear distortions in x and y (tangential and radial directions) are more than the strain in the direction of σ_1, normal to longitudinal grains. These curves reach a well defined ultimate strength plateau.

3.6.1 MATERIAL MODELING

The test results presented in section 3.5 clearly document the fact that the material (wood) upon loading undergoes both elastic and plastic deformations. In an attempt to develop an elasto-plastic
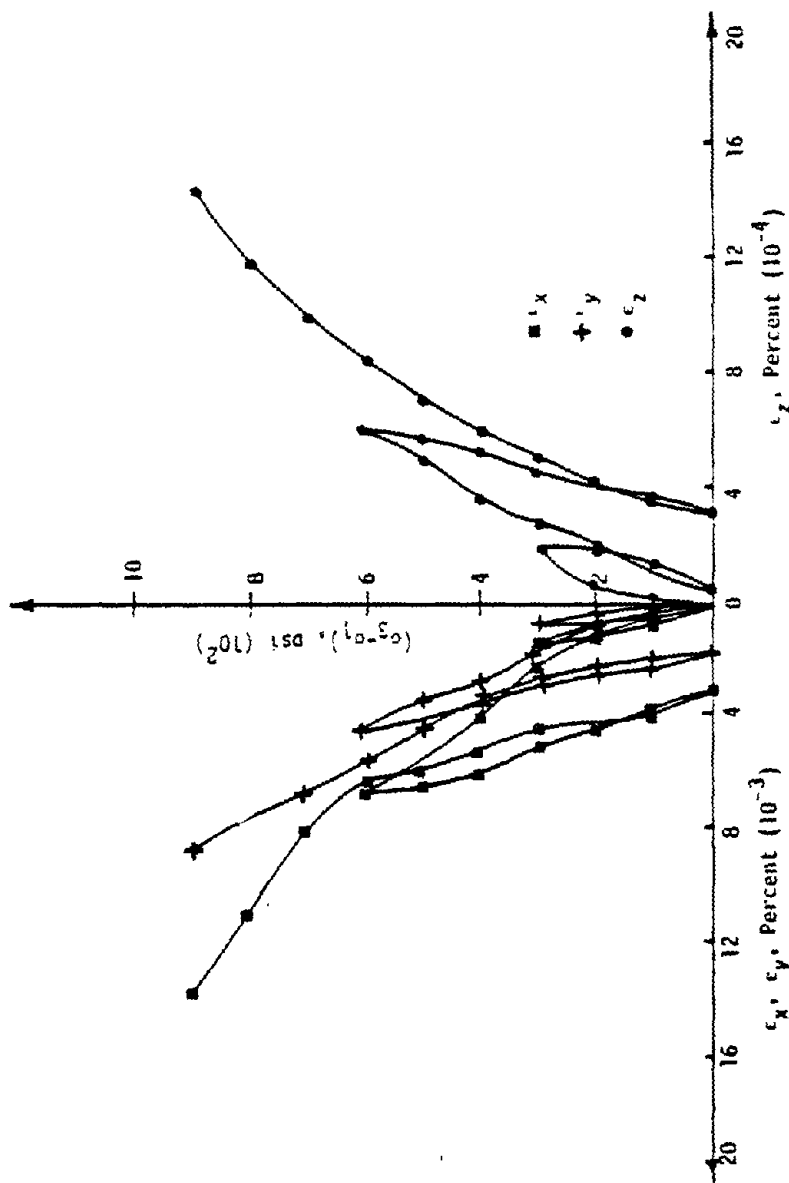
Figure 3.26 Stress-Strain Response Curves for Conventional Triaxial Extension Test.
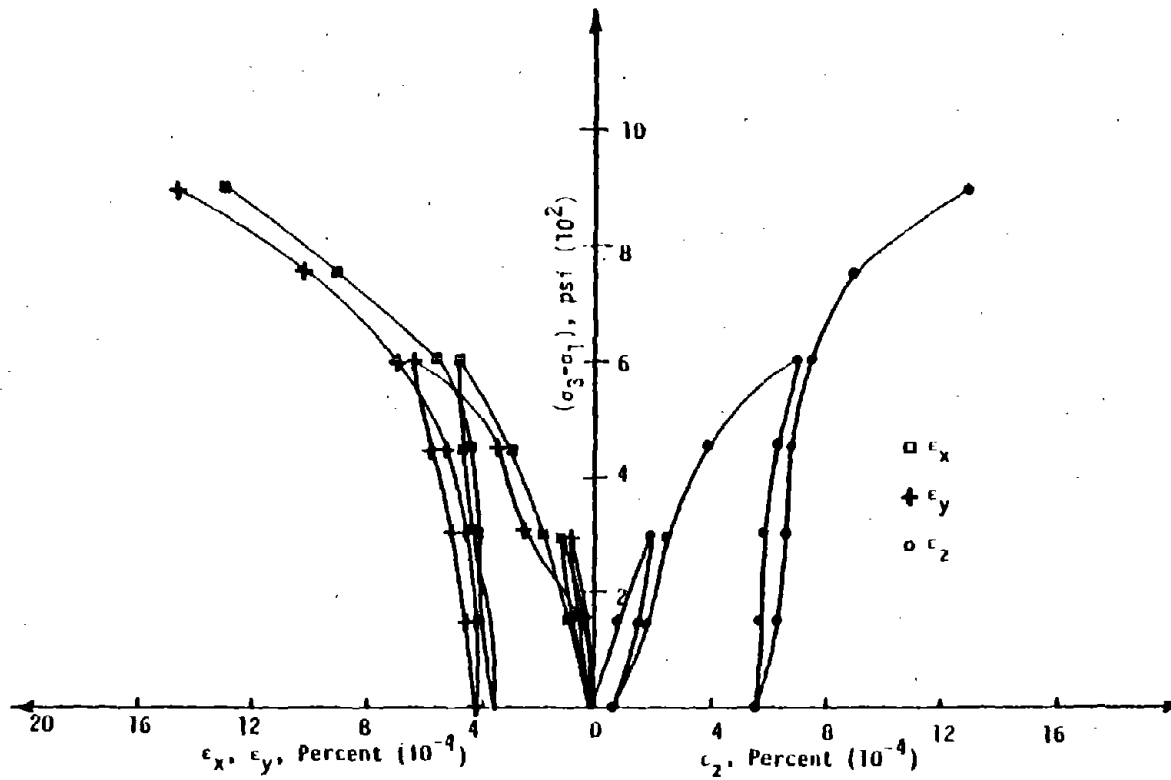
Figure 3.27 Stress-Strain Response Curves for Triaxial Extension Test
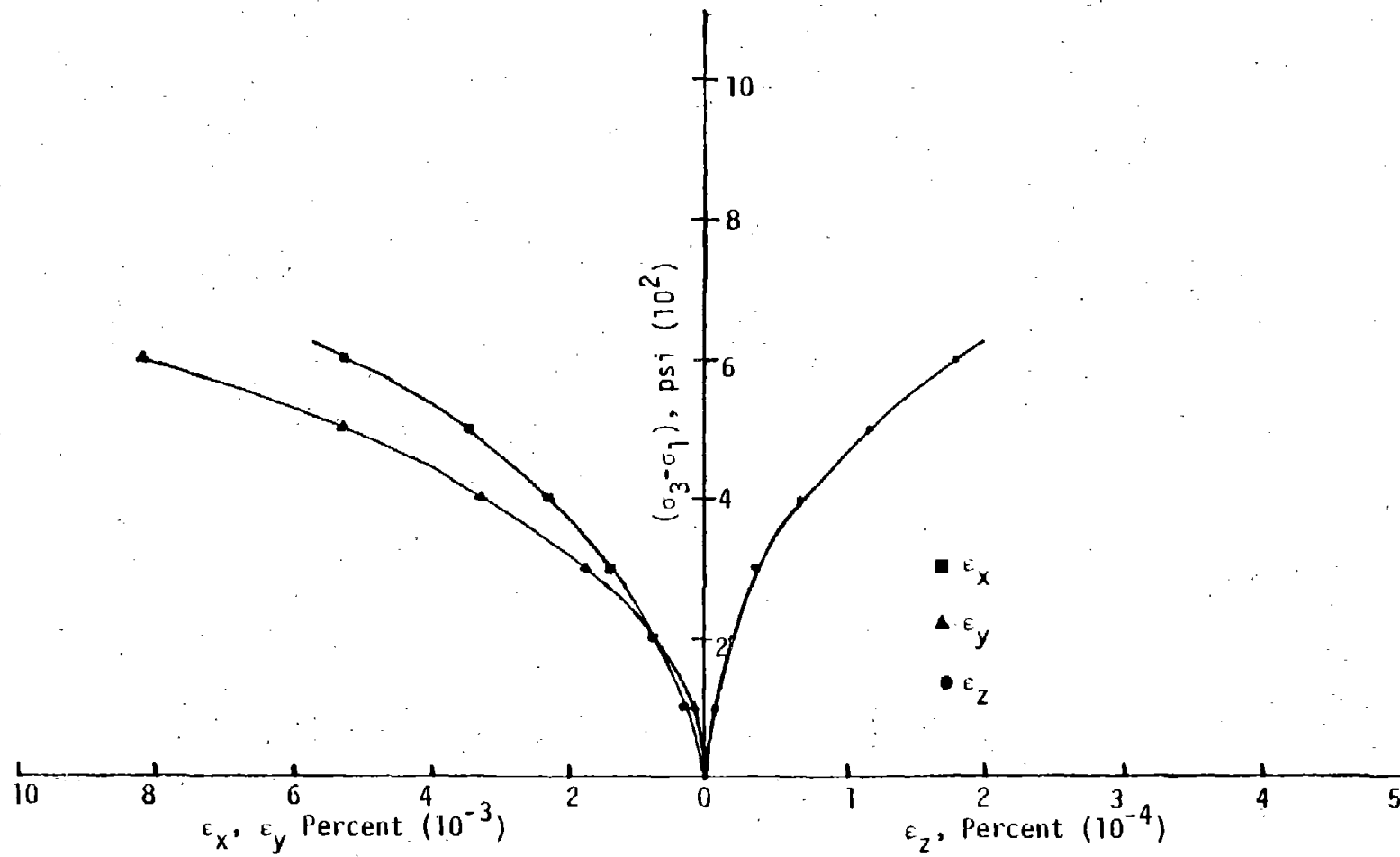
Figure 3.28 Stress-Strain Response Curves for Reduced Triaxial Extension Test.

143

material model, the increments of strains at different load levels are decomposed into elastic and plastic strains as explained in section 2.3.3 and Fig. (2.25). The volumetric and deviatoric components of plastic strain are then plotted along the respective stress paths in a space of J_1 and $\sqrt{J_{2D}}$ for isotropic materials as described in section 2.3.4. Wood is not an isotropic material. In such a case, the modifications to be made and the justification for the modifications are given in the next section.

3.6.2 Elasto-Plastic Model

In many cases of practical interest like wood, where anisotropy appears to be important, it may be appropraite to assume horizontal planes of isotropy on cross-anisotropy. In other words, a vertical axis of symmetry (longitudinal axis) exists and all directions in any horizontal plane (planes defined by radial-tangential axes) are equivalent with respect to elastic-plastic properties. It is also justified by the fact the Young's Modulus in the radial and tangential directions are almost the same and that in longitudinal direction, E_L is nearly ten times that of E_R ($=E_T$). Such a material is said to be transversely isotropic. The elastic and plastic constitutive equations for transversely isotropic materials, which satisfy the requirements and continuity are discussed in the next section.

Linear elastic, stress-strain relations are first established by a transversely isotropic material and then extended to elasto-

plastic stress-strain relations. The most general linear relation between the elastic stress σ_{ij} and strain ε_{ij} is

$$\{\varepsilon_{ij}\} = [D_{ijkl}] \{\sigma_{kl}\} \tag{3.30}$$

where D_{ijkl} is known as the compliance matrix. When this compliance matrix is reduced to a two subscript form, it gives Eq. (3.13).

If the axis of symmetry is taken to be a vertical z axis and cylindrical coordinates r, θ, z are used, then r, θ, z replace 1,2,3 respectively. It gives [67]

$$\varepsilon_{rr} = \frac{1}{E} \sigma_{rr} - \frac{\nu}{E} \sigma_{\theta\theta} - \frac{\nu'}{E'} \sigma_{zz}$$

$$\varepsilon_{\theta\theta} = \frac{-\nu}{E} \sigma_{rr} + \frac{1}{E} \sigma_{\theta\theta} - \frac{\nu'}{E'} \sigma_{zz}$$

$$\varepsilon_{zz} = \frac{-\nu'}{E'} \sigma_{rr} - \frac{\nu'}{E'} \sigma_{\theta\theta} + \frac{1}{E'} \sigma_{zz}$$

$$\tag{3.31}$$

$$\varepsilon_{\theta z} = \frac{1}{2G} \sigma_{\theta z}$$

$$\varepsilon_{rz} = \frac{1}{2G'} \sigma_{rz}$$

$$\varepsilon_r = \frac{1+\nu}{E} \sigma_{r\theta} = \frac{1}{2G} \sigma_{r\theta}$$

and the compliance matrix can be rewritten as

$$[D_{ij}] = \begin{bmatrix} \frac{1}{E} & \frac{-\nu}{E} & -\frac{\nu'}{E} & & & \\ \frac{-\nu}{E} & \frac{1}{E} & -\frac{\nu'}{E'} & & 0 & \\ -\frac{\nu'}{E'} & -\frac{\nu'}{E'} & \frac{1}{E'} & & & \\ & & & \frac{1}{G'} & & \\ & 0 & & & \frac{1}{G'} & \\ & & & & & \frac{1}{G} \end{bmatrix} \quad (3.32)$$

where ν is poisson's ratio for horizontal strain due to horizontal stress, ν' is Poisson's ratio for horizontal strain due to vertical stress, E is Young's modulus in the horizontal plane, G is shear modulus in the horizontal plane, E' is young's modulus in the vertical plane and G' is shear modulus in the vertical plane.

For a linear isotropic material the complementary energy can be written as

$$W = \frac{1}{18K} J_1^2 + \frac{1}{2G} J_{2D} \quad (3.33)$$

in which

$$J_1 = \sigma_1 + \sigma_2 + \sigma_3$$

$$J_{2D} = \frac{1}{6} [(\sigma_1 - \sigma_2)^2 + (\sigma_2 - \sigma_3)^2 + (\sigma_3 - \sigma_1)^2]$$

$$+ \sigma_4^2 + \sigma_5^2 + \sigma_6^2$$

$$(3.34)$$

$$K = \frac{1}{3[D_{11} + 2D_{12}]}$$

and

$$G = \frac{1}{2[D_{11} - D_{12}]}$$

For a transversely isotropic body, the complementary energy function (3.33) in terms of compliances, becomes

$$W = \frac{1}{2} D_{11} \sigma_1^2 + D_{12} \sigma_1 \sigma_2 + D_{13} \sigma_1 \sigma_3 + \frac{1}{2} D_{11} \sigma_2^2$$

$$+ D_{13} \sigma_2 \sigma_3 + \frac{1}{2} D_{33} \sigma_3^2 + \frac{1}{2} D_{44} \sigma_4^2 + \frac{1}{2} D_{44} \sigma_5^2 \qquad (3.35)$$

$$+ (D_{11} - D_{12}) \sigma_6^2$$

when written in a form analogus to Eq. (3.33), it is

$$W = \frac{1}{18K^e} (Q_1^e)^2 + \frac{1}{2G^e} (Q_2^3) \qquad (3.36)$$

where

$$q_1^e = \alpha^e (\sigma_1 + \sigma_2) + \sigma_3$$

$$Q_2^e = \frac{1}{6} (\sigma_1 - \sigma_2)^2 + \frac{\beta^e}{6} (\sigma_2 - \sigma_3)^2$$

$$+ \frac{\beta^e}{6} (\sigma_3 - \sigma_1)^2 + \nu^3 (\sigma_4^2 + \sigma_5^2)$$

$$+ \frac{1}{3} (2 + \beta^e) \sigma_6^2$$

(3.37)

These five elastic constants K, G, α, β, and ν with super script 'e', are related to the five independent compliances of Eq. (3.14).

For linear elastic isotropic material, these constants become

$$K^e = K; \quad G^e = G; \quad \alpha^e = \beta^e = \nu^e = 1$$

(3.38)

Similarly it can be shown that the complementary energy due to plastic work done is

$$W = \frac{1}{18K^p} (Q_1^p)^2 + \frac{1}{2G^p} (Q_2^p)$$

(3.39)

in which

$$Q_1^p = \frac{p}{\alpha} (\sigma_1 + \sigma_2) + \sigma_3$$

and

$$Q_2^p = \frac{1}{6}(\sigma_1 - \sigma_2)^2 + \frac{\beta^p}{6}(\sigma_2 - \sigma_3)^2 + \frac{\beta^p}{6}(\sigma_3 - \sigma_1)^2$$

$$+ \nu^p(\sigma_4^2 + \sigma_5^2) + \frac{1}{3}(2 + \beta^p)\sigma_6^2 \qquad (3.40)$$

In the model (2.3.4), the loading function is assumed to be isotropic and to consist of two parts; a yield condition

$$F_1(J_1, \sqrt{J_{2D}}) = 0 \qquad (3.41)$$

and a hardening CAP

$$F_2(J_1, \sqrt{J_{2D}}, k) = 0 \qquad (3.42)$$

which may expand or contract as the hardening parameter k increases or decreases.

For transversely isotropic material in which anisotropy is rotationally symmetric about vertical axis z, Eqs. (3.36) and (3.37) may be generalized by replacing J_1 and J_{2D} by Q_1 and Q_2 defined as in Eqs. (3.39) and (3.40) with new constants α^p, β^p, ν^p replacing α^e, β^e and ν^e.

Elasto-plastic constitutive relations will therefore be obtained by using the associated flow rule

$$d\varepsilon_{kl}^p = \lambda \frac{\partial F_{1,2}}{\partial \sigma_{kl}} \qquad (3.43)$$

with convex yield and loading functions

$$F_1(Q_1, Q_2) = 0 \qquad (3.44)$$

$$F_2 \ (Q_1, \ Q_2, \ \varepsilon_v^p) = 0 \qquad\qquad (3.45)$$

In this investigation, when the wood samples are tested in the truly triaxial device, only principal stresses and principal strains are measured. The terms Q_1 and Q_2 in Eq. (3.40) eventually thus get reduced to J_1 and $\sqrt{J_{2D}}$ only. Therefore the yield, failure and potential surfaces are constructed in J_1 verses $\sqrt{J_{2D}}$ space only.

3.6.3 Yield, Failure and Potential Surfaces

The foregoing test results for various stress paths are used to obtain the failure envelope, f_f, Fig. (3.29). It is obtained on the basis of stresses at failure, defined as the state asymptotic to the stress-strain curves. It consists of two parts; (1) Drucker-Prager surface at low stress levels and (2) van Mises surface at high stress levels.

Since the wood exhibits continuously yielding behavior, the yield surfaces, f_c are constructed by drawing contours of equal volumetric strain, I_1^p along various stress paths, Fig. (3.29). No definite mathematical shape can be attributed to the yield surfaces drawn; they can be possibly approximated elliptical in shape.

Vectors of increments of plastic strains, $d\varepsilon_{ij}^p$, at various points, along a given stress path is shown in Fig. (3.30). Curves drawn orthogonal to the strain increment vectors will give the plastic potential surface, Q_s. It is seen, in the case of this wood, it is difficult to draw such curves in a consistent manner. Even if
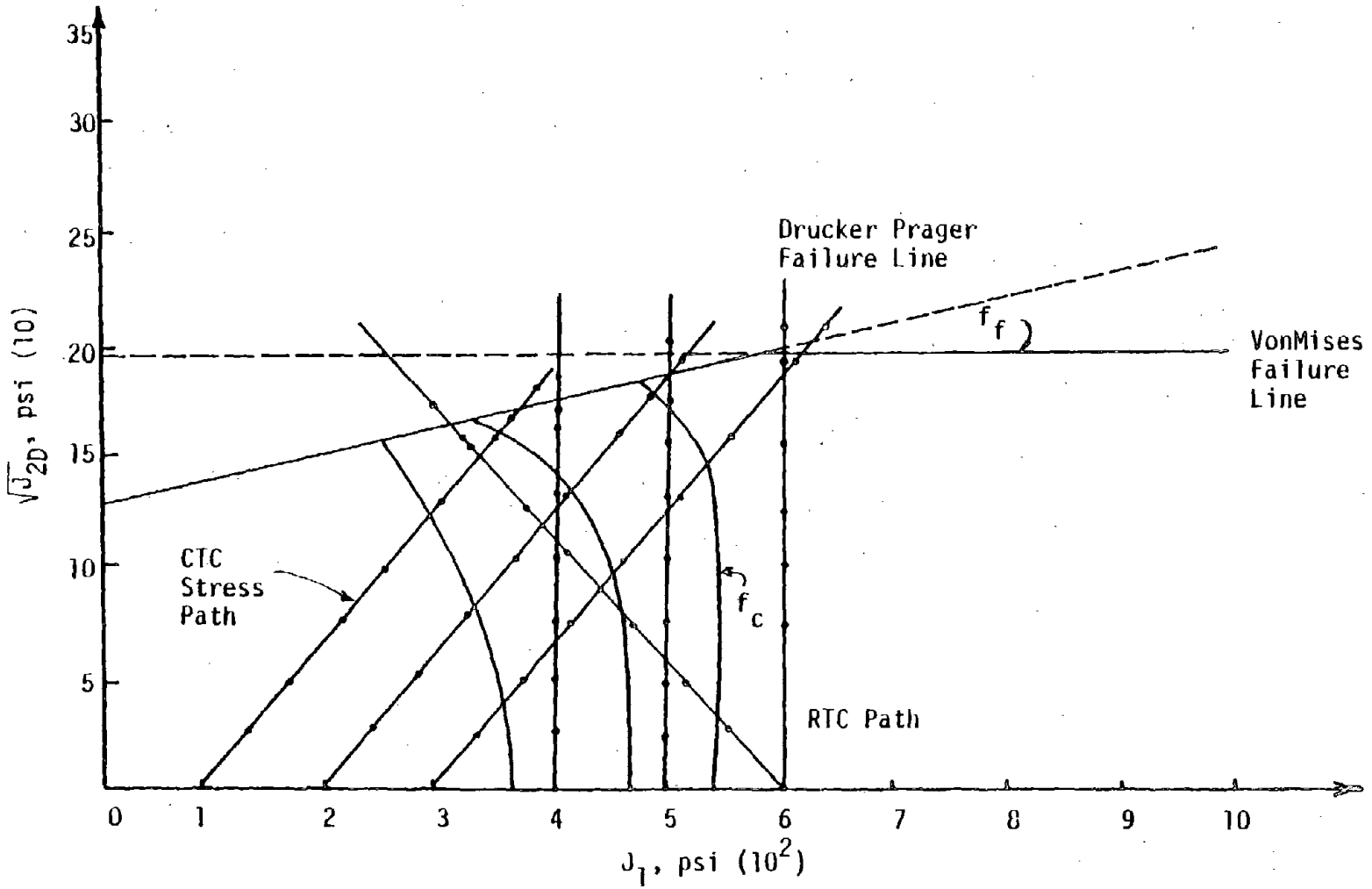
Figure 3.29 Failre and Yield Surfaces
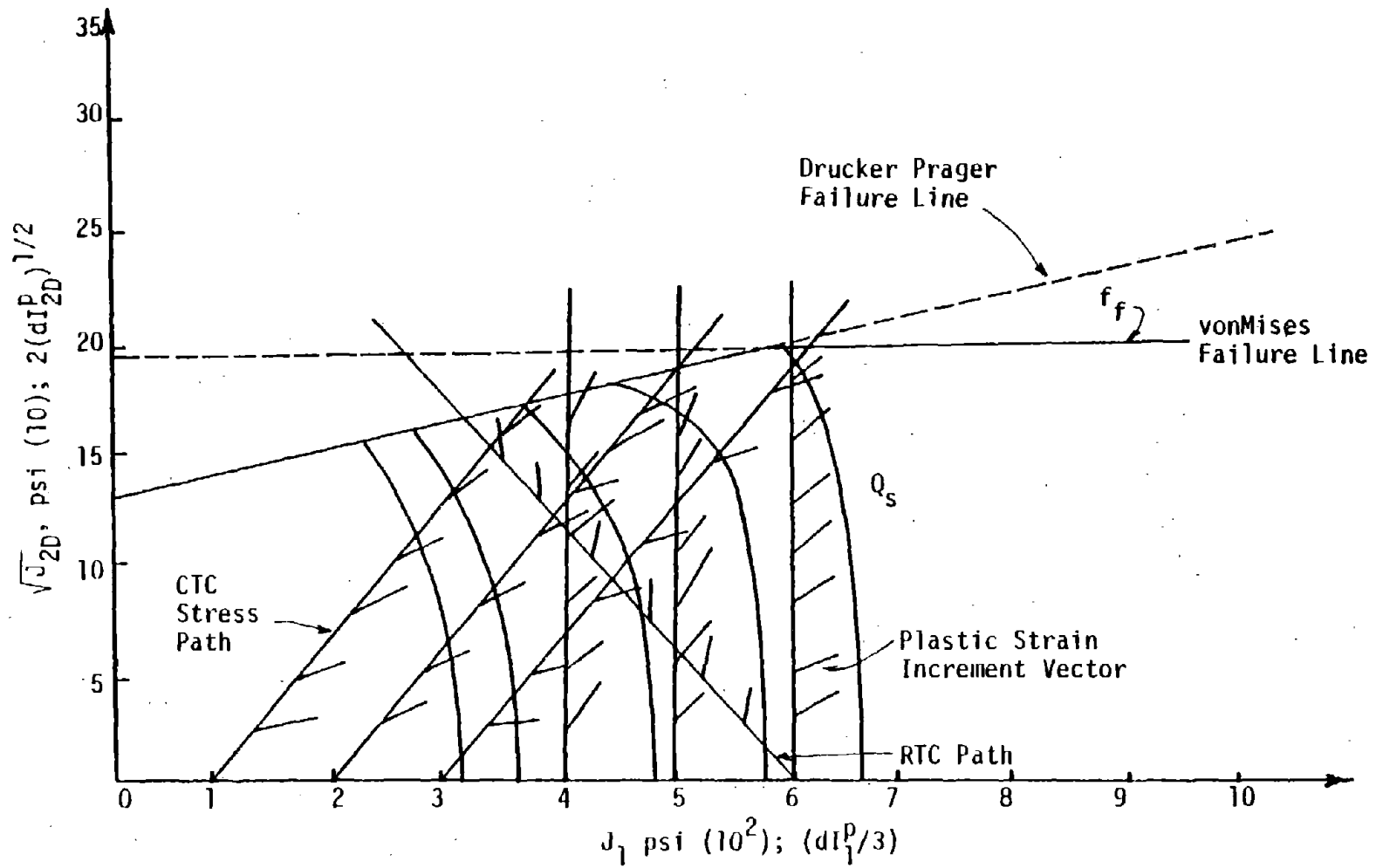
Figure 3.30 Plastic Strain Increment Vectors and Potential Surfaces

a set of such surfaces are drawn as shown in Fig. (3.30), they do not show any geometrically similar shapes in the stress space.

This may be due to the fact that the wood, although it exhibits plastic behavior, it may not exhibit the flow behavior as defined in classical plasticity. This may be attributed to the nonhomogeneities, anisotropy, and local collapse and then hardening exhibited by wood. Such local collapses are seen from the test results by abrupt changes in the curvature of the stress-strain curves. Then, during subsequent loading, the material again exhibits regrouping and hardening behavior.

Therefore, it is felt better to investigate a general function form as suggested by Desai [20]

$$F = f (J_i, I_i^p, \beta_j) \tag{3.46}$$

where F = general function that can provide yield, failure and potential functions, J_i (i = 1,2,3) = invarients of the stress tensor, σ_{ij}, I_i^p (i = 1,2,3) = invarients of the plastic strain tensor, ε_{ij}^p and β_j (j = 1,2,...) denote parameters such as initial density, anisotropy and local collapse.

The general form of the function f, expressed as a complete polynomial in terms of the three invarients J_1, J_2 and J_3 of the stress tensor, σ_{ij} [20]

$$f (J_1, J_2, J_3) = \alpha_0 + \alpha_1 J_1 + \alpha_2 J_2^{1/2} + \alpha_3 J_3^{1/3} + \alpha_4 J_1^2$$

$$\tag{3.47}$$

$$+ \alpha_5 J_1 J_2^{1/2} + \alpha_6 (J_2^{1/2})^2 + \ldots$$

α_0, α_1, ... are parameters and can be functions of state of stress and physical state of the body. It is possible to express f as a complete polynomial by using other parameters, strain as independent of coordinates in addition to J_1, J_2 and J_3. It is assumed at this time, the dependence of 'f' on strains can be included in the functional representation for the α's.

The general function can be truncated by retaining certain terms and many resulting expressions can be used as yield, failure and potential functions. Physically, such truncations would imply an assumption that the material behavior is influenced only by the invarients of particular order retained in the truncated forms. It has been shown in the reference 20 that von Mises, Drucker-Prager and Lade-Duncan failure functions are special cases of this functional form. The decision on the appropriate choice can be made on the basis of available laboratory test data. Of the many arbitrarily chosen truncated forms of the basic equation the one given below is considered for the behavior of wood.

$$F = f(J_1, J_2, J_3) = \alpha_1 (J_2^{1/2})^2 + \alpha_2 J_1 J_3^{1/3} = 0 \qquad (3.48)$$

This equation when written in a modified form gives

$$g = \frac{(J_2^{1/2})^2}{J_1 J_3^{1/3}} = - \frac{\alpha_2}{\alpha_1} \qquad (3.49)$$

where α_1 and α_2 are material parameters.

As a material is loaded and yields plastically, the value of g will vary. Thus before failure, it defines progressive yielding and at failure g is seen to have some invarient values.

Similarly plastic potential functions, Q can also be expressed as

$$Q = f(J_1, J_2, J_3) = (J_2^{1/2})^2 + k_1 J_1 J_3^{1/3} \tag{3.50}$$

where k_1 is a material parameter.

The mathematical interpretation and physical meaning of this analysis are given in detail in the reference 20.

Table 3.2 shows the computed values of the function $J_2/J_1 J_3^{1/3}$, at failure for the tests conducted on wood. The function seems to be the most appropriate from the viewpoint of its invarience at failure. So the failure function can be expressed as

$$F = \alpha_1 J_2 + \alpha_2 J_1 J_3^{1/3} = 0 \tag{3.51}$$

Only a limited number of tests indicated well-defined ultimate conditions, hence only those tests are considered herein.

Table 3.2

Values of g at failure, Eq. (3.49)

Stress Path	$\dfrac{(J_2^{1/2})^2}{J_1 J_3^{1/3}}$
RTC $(\sigma_1 = 1000.00 \text{ psi})$	0.615
CTC $(\sigma_3 = 200.00 \text{ psi})$	0.569
TE $(\sigma_{oct} = 600.00 \text{ psi})$	0.572
SS $(\sigma_{oct} = 500.00 \text{ psi})$	0.617
RTE $(\sigma_3 = 600.00 \text{ psi})$	0.573

Chapter 4

CONSTITUTIVE MODELLING OF BALLAST

4.1 INTRODUCTION

Railroads have long used ballast to provide support for the rail-tie system and to provide a free draining medium. For ballasted track, an elastic, noncemented, stable, and weather resistant ballast bed, well laid and compacted on a stable, compact sub-ballast and subgrade, is the first condition for low expenditure for maintenance. Ballast materials are subjected to excessive elastic deformations caused by the rapid application and removal of the wheel loads and the accumulation of large plastic deformations resulting from many repetitions of individual wheel loads. So ballast must be capable of withstanding many combinations of forces. Extremely large repetitive loadings, vibrations of varying frequencies and intensities, repeated freezing and thawing, plus other factors, all cause deterioration of the ballast.

4.2 PROBLEM STATEMENT

Excessive elastic deformations in the ballast can result in shortening the life of the rail-track support system because of fatigue resulting from increased (bending) stresses. The plastic deformations necessitate continual realignment of the track system by addition of ballast and tamp it. This is being done on the ballast near the rail leaving the center undisturbed, resulting ballast pockets. The pockets serve as traps for water, resulting

157

almost in continual saturation of the subgrade. So even continued
maintenance may not prove to be a satisfactory solution. It is
found that about 40 percent of the track maintenance funds is spent
on the procurement, distribution and rehabilitation of ballast [4,53].
Amounts of ballast used in North America by material type [4] are
given in Table 4.1.

Improved design of the rail-track support system is one of the
answers for an efficient and economical track bed. So modern
analytical models can be tried to improve the present day experience
oriented design of rail-tie support systems. However, before modern
techniques can be applied, adequate input in the form of material
response parameters must be obtained. The response of granular
materials has been seen to be stress dependent, namely, the response
of the material depends upon the applied state of stress. So in
order to accurately predict the behavior, the test method should
simulate the insitu and in service stress conditions.

4.3 OUTLINE OF THE OBJECTIVE

Several investigations of the repeated load behavior of
granular material have been made. Triaxial equipment has been used
to study dense graded aggregates. Repeated deviator stress and
either constant or pulsed confining pressure have been used.
However, most of the research has been directed towards studies
of the elastic (resilient) properties of the material, but little
attention has been paid to the plastic behavior of the ballast

Table 4.1

Amounts of Ballast used by Material

Type in North America [4]

Material	Amount in Tons
Lime Stone	7.25×10^6
Granite	6.15×10^6
Slag (Air Cooled Blast-Furnace)	3.68×10^6
Gravel	2.23×10^6
Trap Rock	2.23×10^6
Steel Slag	1.33×10^6
Sand Stone and Quartzite	1.02×10^6

subjected to repeated load conditions. Accumulated plastic strains are important because they can be principally responsible for differential settlements.

Cyclic triaxial testing of ballast have been performed [6,9,36, 41,53-59,64]. The limitations of the tests due to rigid end platens, and also the inability of the cylindrical triaxial device to conduct tests under all significant stress paths necessiates the use of truly triaxial device.

It is possible to investigate the effects of material type and aggregate sizes on both the elastic and plastic behavior of ballast. The influence of the stress path, stress level and the degree of compaction on the material response can be well studied by conducting tests in this device. At the same time, in view of the limitations on the size of the cubical samples, full size ballast cannot be tested in this device. So ballast is scaled down to smaller size and tested, and size effects are investigated. Experimentally it is proved that scaled down ballast deformation and strength character-istics are mostly similar to original ballast if the uniformity coefficient of the two graded materials is the same.

4.4.1 REVIEW OF PAST WORK

Ballast in track-bed is subjected to repeated load. The behavior of ballast under repetitive load has been studied by many investigators [41,50,56]. However, it is desirable to evaluate the response of granular materials under laboratory conditions which

simulate the in-service conditions. Several investigators [41,50,56] have used the conventional triaxial cell with a repeated deviator stress, and either constant or pulsed confining pressure. Early works [31,53,57] include some tests on rigidly confined materials, more like one-dimensional compression, but are with varying degrees of success.

4.4.2 Resilient Modulus

The concept of resilient modulus has been used to describe the behavior of the ballast subjected to repeated loading conditions [41]. In order to account for the stress dependency of the materials, several predictive equations have been developed. They are verified and justified by the results obtained from laboratory testing of material, at several stress states. The most widely used equation is

$$E_r = K J_1^n \qquad (4.1)$$

where E_r is the resilient modulus, K and n are material constants determined from analysis of the laboratory data and J_1 represents the first invariant of the stress tensor, σ_{ij}.

A conclusion arrived has been that for evaluating the resilient response of ballast, repeated load triaxial testing is perhaps the most suitable method.

Ties are generally 8.00 inch (20.00 cm) wide and spaced at every 20.00 inch (50.00 cm). Thus the compacted ballast forms

rectangular columns under the ties about 8.00 x 12.00 inch (20.00 x 30.00 cm) surrounded by losse compacted ballast. Even the addition of ballast and shoulder compaction tends to compact only the ballast near the top of the ballast bed. Under such conditions, among the available testing devices in the past, compressive triaxial testing is believed to be more representative of field conditions than other devices such as plane strain testing. Of course, three-dimensional stress state would be the most representative, desirable and this investigation considers testing of ballast in three-dimensional state of stress by using the truly triaxial test device.

Some of the factors influencing the results of triaxial testing of ballast are discussed in the following section.

4.4.3 Factors Influencing Resilient Modulus

Various factors such as stress history, frequency and duration of load application, geometric characteristics of aggregate, gradation, degree of compaction, degree of saturation and the stress levels, can influence the magnitude of the resilient modulus. Particularly ballast in track bed is subjected to a complex stress history. From extensive laboratory investigations, many investigators [2,6,41] have condluced that the resilent modulus is insensitive to magnitude in frequency or the values of pulse duration, that is duration of load application.

Another factor, the gradation and its meaningful influence on resilent modulus have been studied by Hudson and others. Gradation

is estimated through the use of the gradation parameter, A. The gradation parameter is defined as the logarithm to the base 2 of the ratio of 54.8 to the effective mean diameter in millimeters of a particular size fraction. The gradation parameter of the aggregate system is the weighed mean of the values of the individual size fractions. The value of A for a size fraction can be computed from

$$2^{\overline{A}} = \frac{54.8}{\overline{d}} \tag{4.2}$$

where $\overline{d} = \dfrac{0.443 \, (d_1 - d_2)}{\log \, (d_1/d_2)}$, d_1 is the size of larger sieve in millimeters and d_2 is the size of smaller sieve in millimeters.

The effect of the degree of compaction on resilent modulus is not well understood [41]. Several studies have included density as a variable, but the conclusions are inconclusive. Ballast is placed in the track and tamped to increase the density of the compacted mass. It is generally acknowledged that the ballast underneath the tie undergoes increase in density due to the repeated loading of traffic. Selig [65] has evolved a field density determination technique of ballast in the track bed. The service density of ballast is generally 90.0 pcf (1.44 g/cm^3) and that density is kept as the initial density of ballast samples tested in this investigation.

Many investigators such as Thompson [42] have observed that for dense graded granular materials like ballast, increased levels of saturation generally resulted in decreased modulus values. Ballast

layer serves as an elastic bed and a free draining medium in the layered track bed. This investigation is aimed to obtain more fundamental stress-strain relationship of ballast than hitherto. This involves the application of a wider range of stresses to fully characterise the non-linearity of the material, and the use of dry material so that the results could be expressed in terms of effective stress.

4.4.4 Factors Influencing Permanent Deformation

Various factors affecting resilient behavior of granular materials probably influence the plastic strain behavior. The manner and magnitude may be different.

Many methods have been evolved for predicting permanent axial strain caused by repeated loading. The expression suggested by Barksdale [6] is given by

$$\varepsilon^p = \frac{(\sigma_1 - \sigma_3)/E_i}{1 - \dfrac{(\sigma_1 - \sigma_3)(1 - \sin\phi) R_F}{2(c \cos\phi + \sigma_3 \sin\phi)}} \tag{4.3}$$

where ε^p is permanent axial strain, E_i is a relationship defining the initial tangent modulus, c is cohesion, ϕ is angle of internal friction in degrees and R_F is a ratio relating the stress difference at failure to the stress difference which the stress-strain curve approaches at infinite strain.

From repeated load triaxial testing of ballast, the Office of Research and Experiments, ORE [49,50] suggest an equation to find the plastic strain as

$$\varepsilon^p = 0.082 \ (100n - 38.2) \ (\sigma_1 - \sigma_3)^2 \ (1 + 0.2 \ \text{logN}) \qquad (4.4)$$

where ε^p is permanent axial strain after N cycles, n is the initial porosity, $(\sigma_1 - \sigma_3)$ is deviator stress, and N is number of repeated loading cycles.

The qualitative conclusions from different investigations can be summarized as follows:

1. The angle of internal friction is not an important factor in determining the plastic strain behavior [40,41],

2. Increase in density of material results in decrease in accumulated repeated load deformation, [2,3], and

3. Maximum size of aggregate increases its resistance better to permanent deformation [36].

4.5.1 <u>Influence of Gradation on Strength and Deformation Properties</u>

Testing of triaxial specimens of the prototype ballast material is not possible in the truly triaxial device. The size of the field material is scaled down to smaller size. The technique followed is that proposed by Lowe [45] which involves modelling of the grain-size distribution of the field material and forming laboratory specimens with a grain-size distribution curve exactly parallel to that of the field material. Described briefly herein are the theoretical and experimental basis for the modelling technique and the results of investigations on properties of ballast materials performed.

Table 4.2 shows a summary of previous investigation of particle size effect. On the basis of the summary, it appears that frictional

Table 4.2

Summary of Previous Investigation on Particle Size Effect [13]

Source (1)	Maximum Particle Size Type of Test (2)	Conclusion (3)
Bishop	1-1/4 in	Particle size does not affect angle of internal friction
Lewis	1/4 in Direct shear	Angle of internal friction increases as particle size increases
Vallerga, et al	0.2 in Triaxial shear	Particle size does not affect angle of internal friction
Rowe	1 mm Sliding friction	Friction increases as particle size decreases
Leslie	3 in Triaxial shear	Angle of internal friction increases as particle size decreases
Kirkpatrick	2 mm Triaxial shear	Angle of internal friction increases as particle size decreases
Marsal	9 in Triaxial shear	Angle of internal friction increases as particle size decreases
Lee, et al	3/4 in Triaxial compression	Deformation increases as the particle size increases
Fumagalli	260 mm Triaxial compression	Deformation increases as the particle size increases

and deformational characteristics of assemlage of particles do not depend significantly on size. On the other hand, based on adhesion theory and plastic deformation of contacts, it has been shown [13,27,59] that all contacts deform plastically until the true contact area is equal to the load divided by the yield strength of the material, and in case of such materials the coefficient of friction is a material property and independent of all other dimensional parameters.

So the one of the aims of the tests performed herein is to provide further experimental data showing the effects of modelling of the gradation curves on the strength and deformation character- istics of ballast material.

4.5.2 TEST PROGRAM

Material

The ballast material tested is from the test-track site at Pueblo, Colorado. The grain size distribution of the parent material is shown in Fig. (4.1), as can be seen, it is a uniformly graded material. When uniformly graded ballast is placed on sand subballast containing little or no gravel sizes, fouling of ballast by subballast occurs. This is not generally preferred. From the grading curve, uniformity coefficient of ballast is found to be about 1.2. The prototype ballast is scaled down by passing through a pulvarizer, which is adjusted to break the ballast to the desired size. Fines present are removed by sieving. The grain size distribution curves of the two scaled down sizes are shown in Figures (4.2) and (4.3).
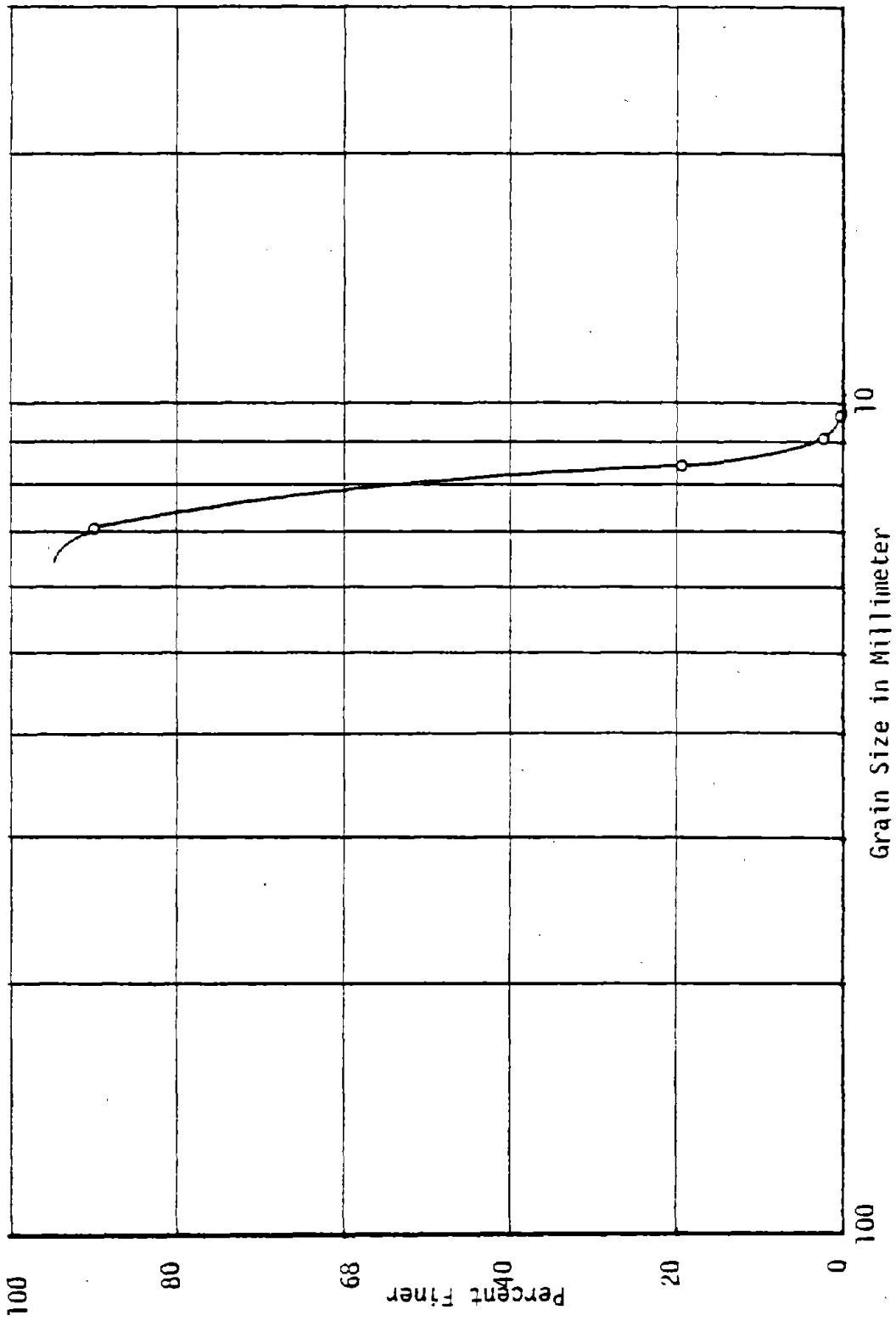
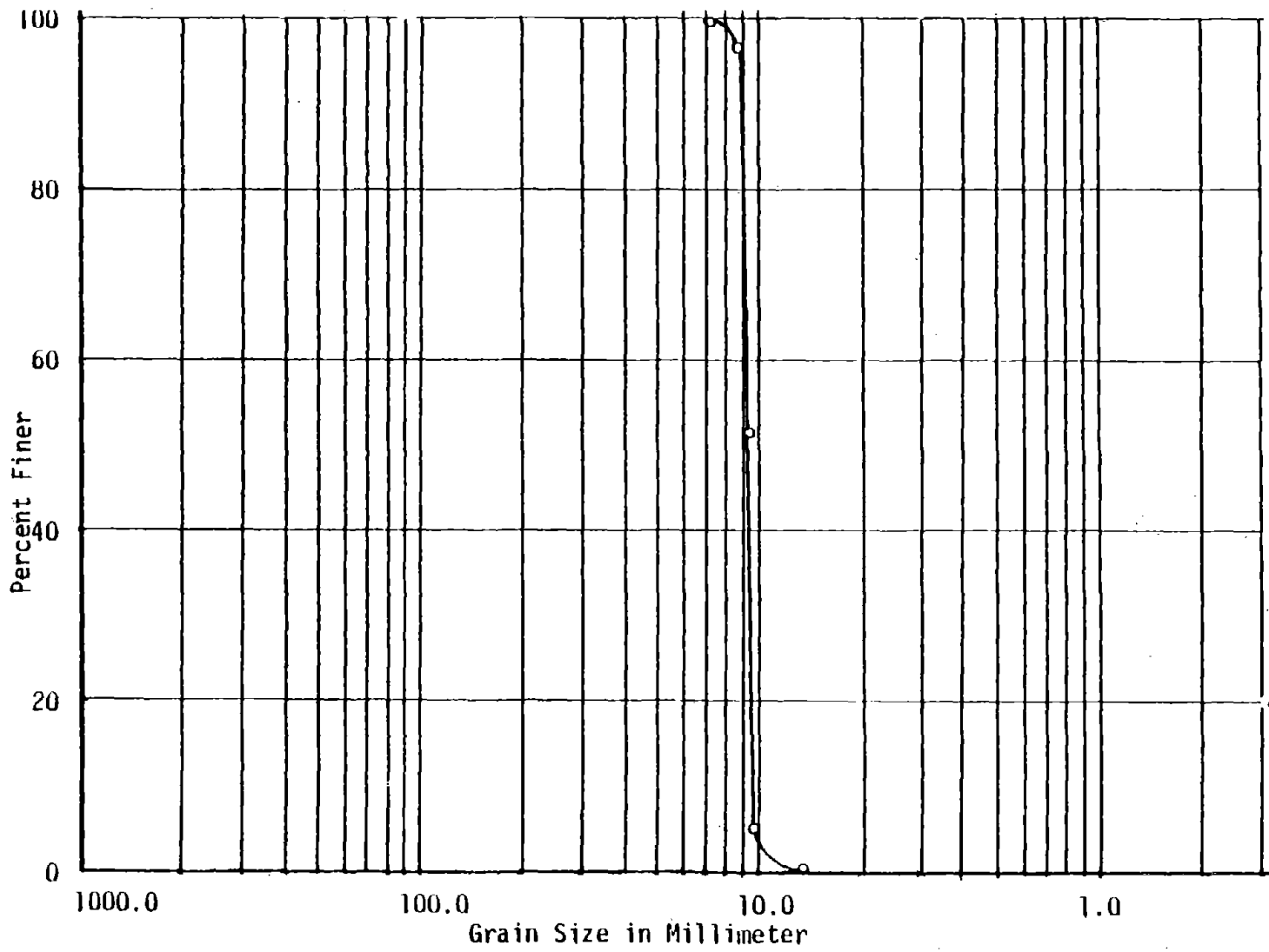Figure 4.1 Grain Size Distribution Curve for Ballast I (C_u = 1.19)

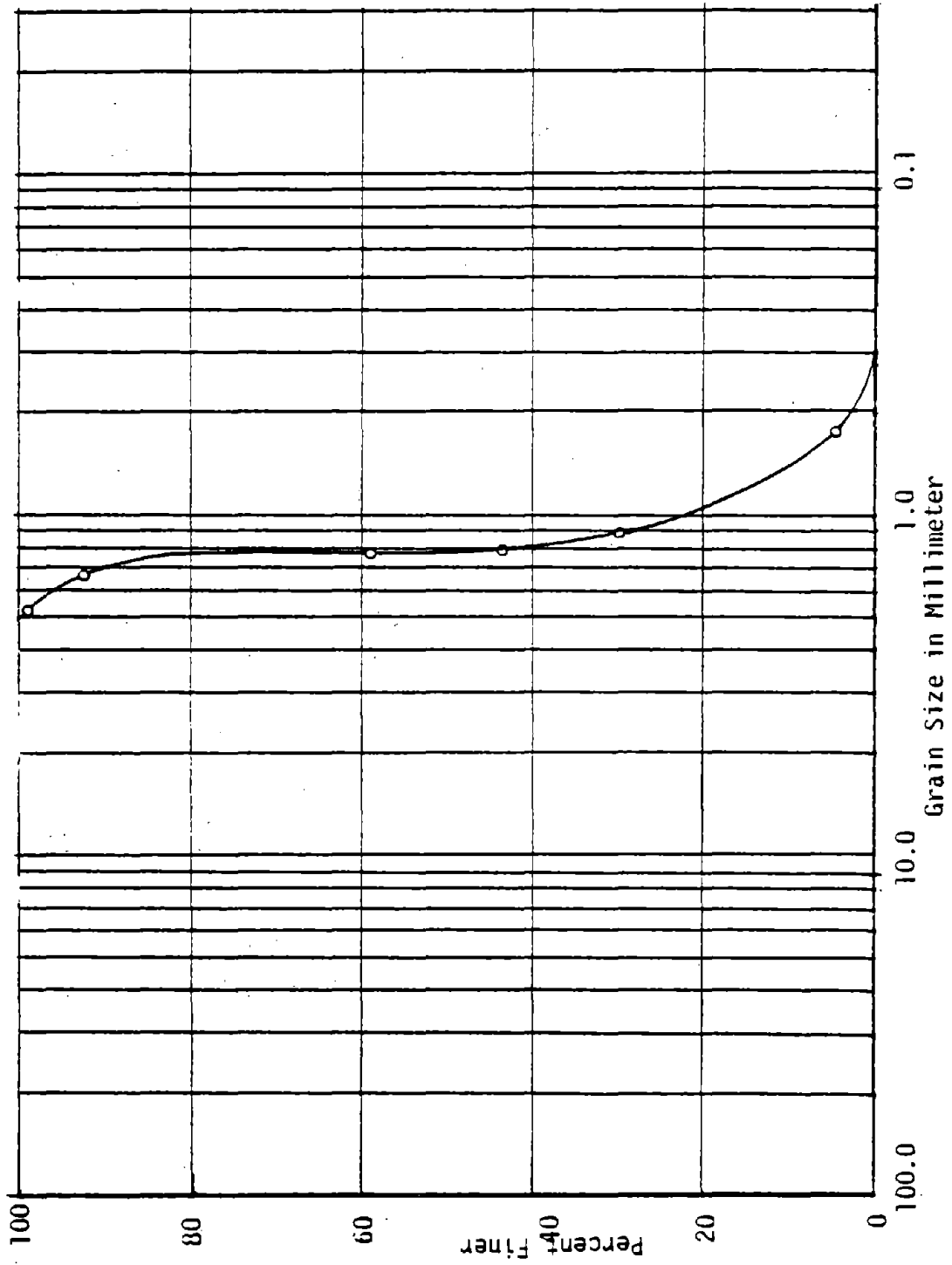Figure 4.2 Grain Size Distribution Curve for Ballast II (C_u = 1.22)

Figure 4.3 Grain Size Distribution Curve for Ballast III (C_u = 1.19)

It is verified that the uniformity coefficient of the two samples are

nearly equal to 1.2, equal to that of the parent material, that is,

Ballast I. The scaled-down sizes are referred as Ballast II and

III hereafter.

The scaled down material (Ballast II) is tested in the truly

triaxial device and the stress-strain response curves under

HC and CTC tests are shown in Figs. (4.13), (4.14), (4.15) and

(4.16). The sample is compacted to the field density of 90.0 pcf

(1.44 g/m^3) and is prepared as explained in section 2.5.3.

Compacted density of each sample is measured and noted. Like-

wise, Ballast III is tested, with the same initial compacted density,

in truly triaxial device. The stress-strain responses under HC and

CTC tests are plotted in Figs. (4.4) (4.5), (4.6) and (4.7).

4.5.3 Test Results

The test results on ballast III are furnished in this section

for the sake of completeness and comparison. The mean strains at

different mean pressure levels in hydrostatic compression, ballast

II and III, have undergone are tabulated in Table 4.3. They do not

differ very much as can be seen from the table. However, as the

pressure increases, the strain ballast III undergoes becomes slightly

greater than that of ballast II.

Whereas, in case of conventional triaxial compression state,

as seen in Table 4.4, as the deviator stress increases, the little

difference in strain existing at low deviator stress levels gets
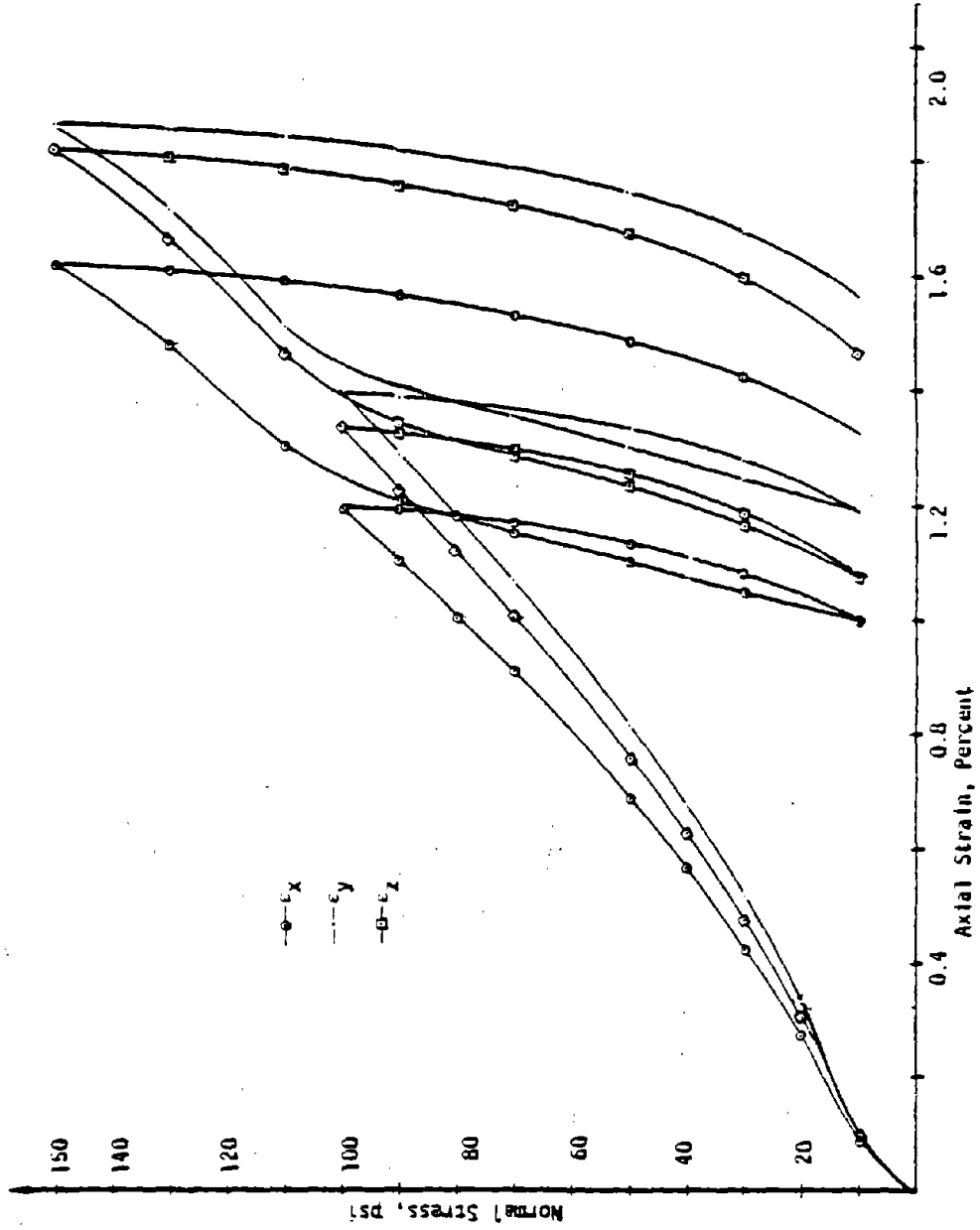
Figure 4.4   Stress-Strain Curves for Hydrostatic Compression
Test. Ballast III
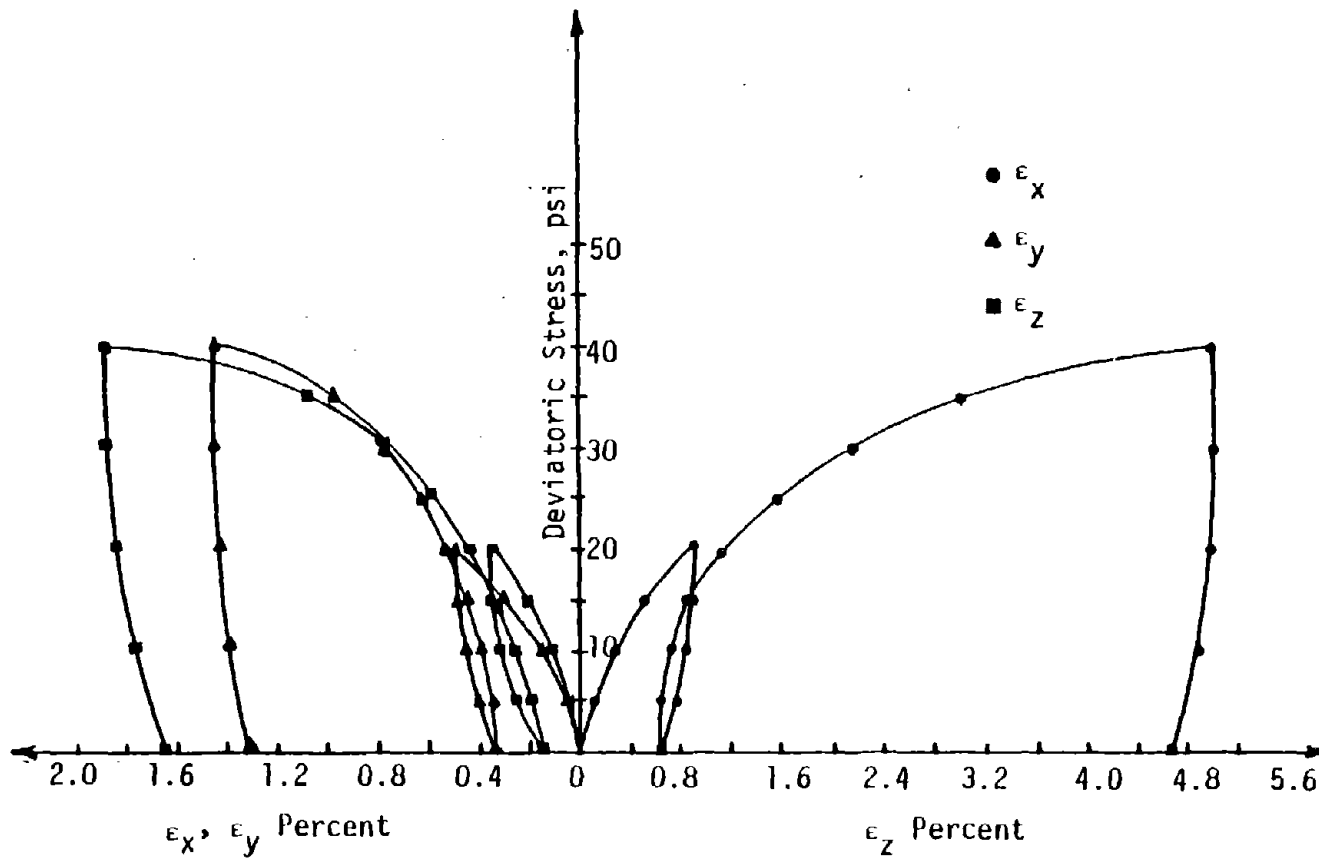
Figure 4.5 Stress-Strain Response Curves for Conventional Triaxial
Compression Test (σ_3 = 10.00 psi) Ballast III
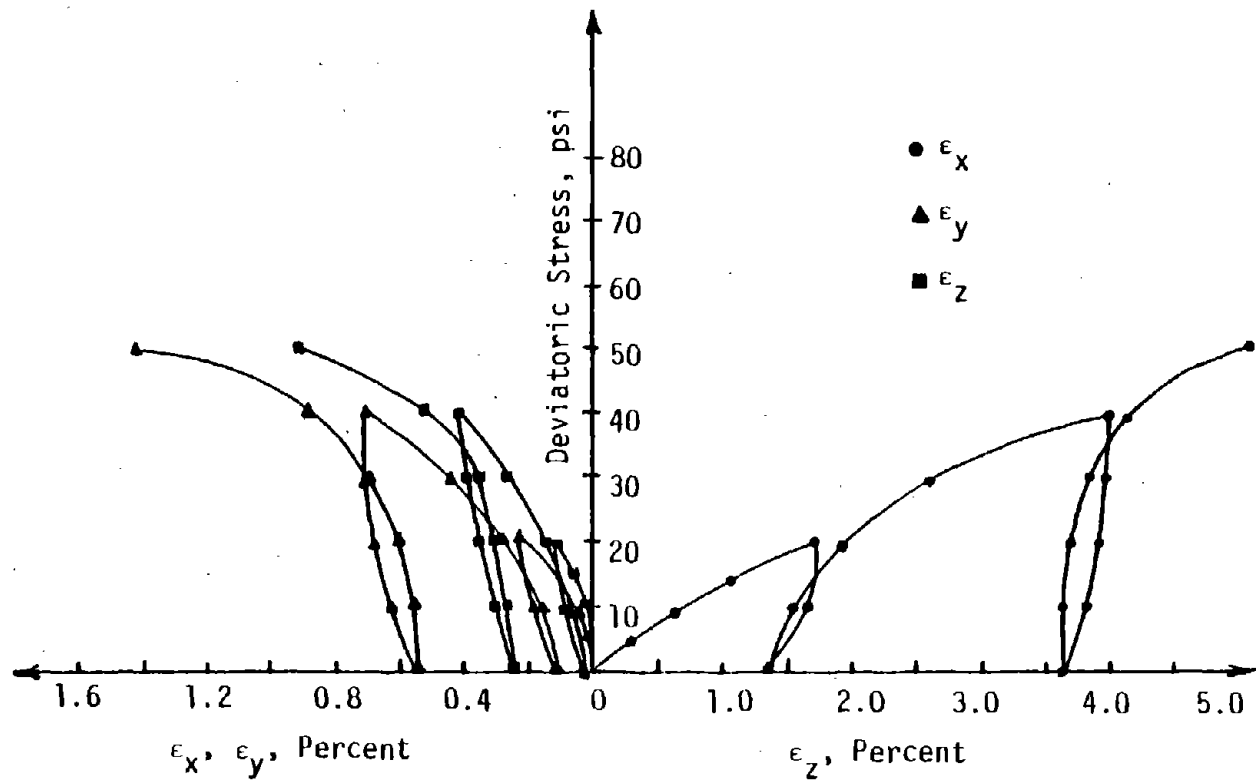
Figure 4.6 Stress-Strain Response Curves for Conventional Triaxial Compression
Test. (σ_3 = 15.00 psi)   Ballast III
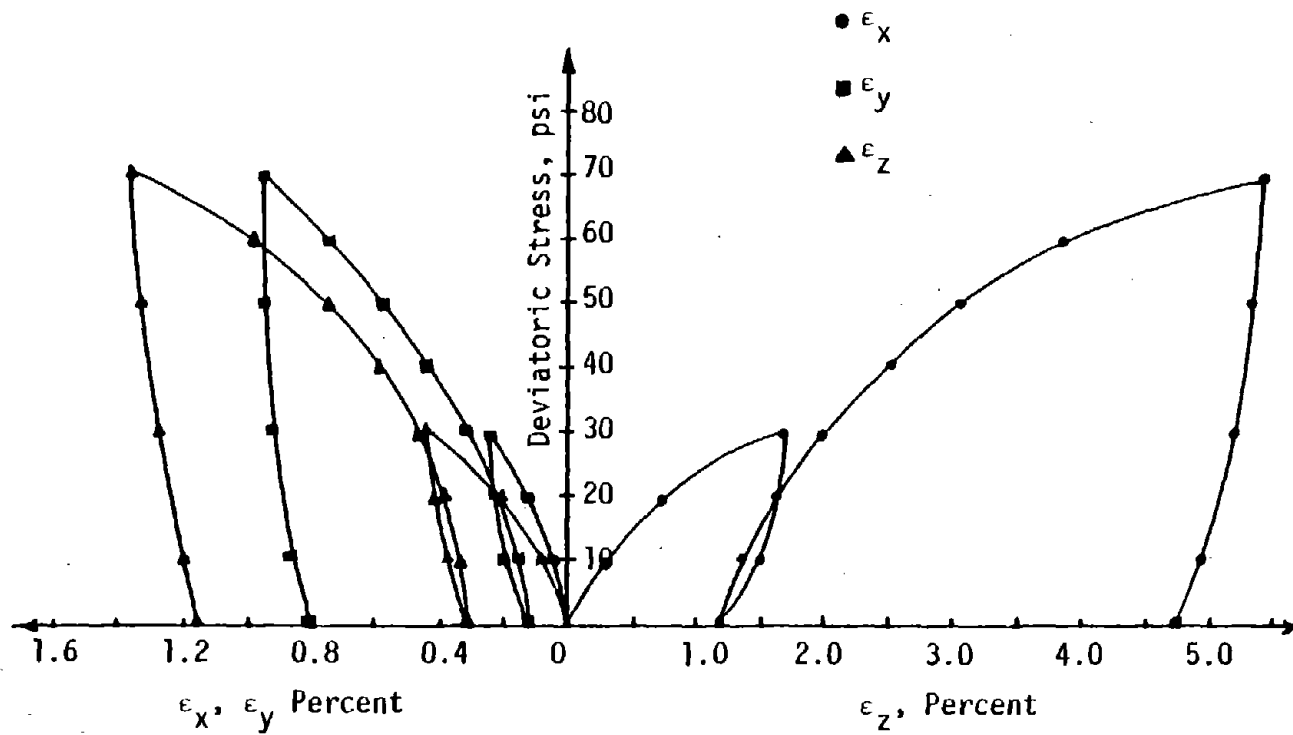
Figure 4.7   Stress-Strain Response Curves for Conventional Triaxial Compression
Test.   (σ_3 = 20.00 psi) Ballast III

Table 4.3

Comparison of Strain at Different Stress Levels
(Hydrostatic Compression)

Mean Pressure (psi)	Ballast II Mean Strain Percent	Ballast III Mean Strain Percent
15.0	0.26	0.19
25.0	0.44	0.41
35.0	0.56	0.56
45.0	0.67	0.70
55.0	0.75	0.82
65.0	0.88	0.95

Table 4.4

Comparison of Strain at Different Stress Levels
(Conventional Triaxial Compression)

Confining Pressure (psi)	Deviator Stress (psi)	Ballast II Axial Strain Percent	Ballast III Axial Strain Percent
	15.0	0.32	0.44
10.0	25.0	0.92	1.52
	35.0	2.58	2.96
	15.0	0.70	1.05
15.0	25.0	1.93	2.25
	35.0	3.02	3.10
	15.0	0.45	0.50
20.0	25.0	0.90	1.05
	35.0	1.875	2.12

diminished. This happens invariably in all the three cases, the cases being tests with confining pressures of 10.00 psi (69.00 kpa), 15.00 psi (1.03×10^2 kpa) and 20.00 psi (1.38×10^2 kpa).

Though it is seen that the total strains due to monotonic loading are not influenced significantly due to different grades in material, it is observed that there is significant difference in rebounding (elastic recovery) properties (strains). It is well documented in the next section.

4.5.4 Resilient Modulus

The variation of Resilient Modulus E_r with confining pressure for ballast III is shown in Fig. (4.8). The definition of Resilient Modulus is described in section 2.7.2. From the Fig. (4.8), the Resilient Modulus can be expressed as

$$E_r = 2600 \, \sigma_3^{0.27} \qquad \text{(psi)} \qquad\qquad (4.5)$$

where σ_3 is the confining pressure. The variation of $E_{z(x)}$ and $E_{y(x)}$ with confining pressure are shown in Fig. (4.9). The recovery of strain is more in the load applied direction in case of ballast III than that of ballast II. Probably because of this, the recovery of strain in Lateral directions are less for ballast III when compared to those for ballast II. The Resilient Modulus for ballast II as defined in the section 4.9 is $1300 \, \sigma_3^{0.87}$ (psi).

It can be seen that the maximum size of the particle in the ballast II is 20 mm and in ballast III, it is 10 mm. Both are
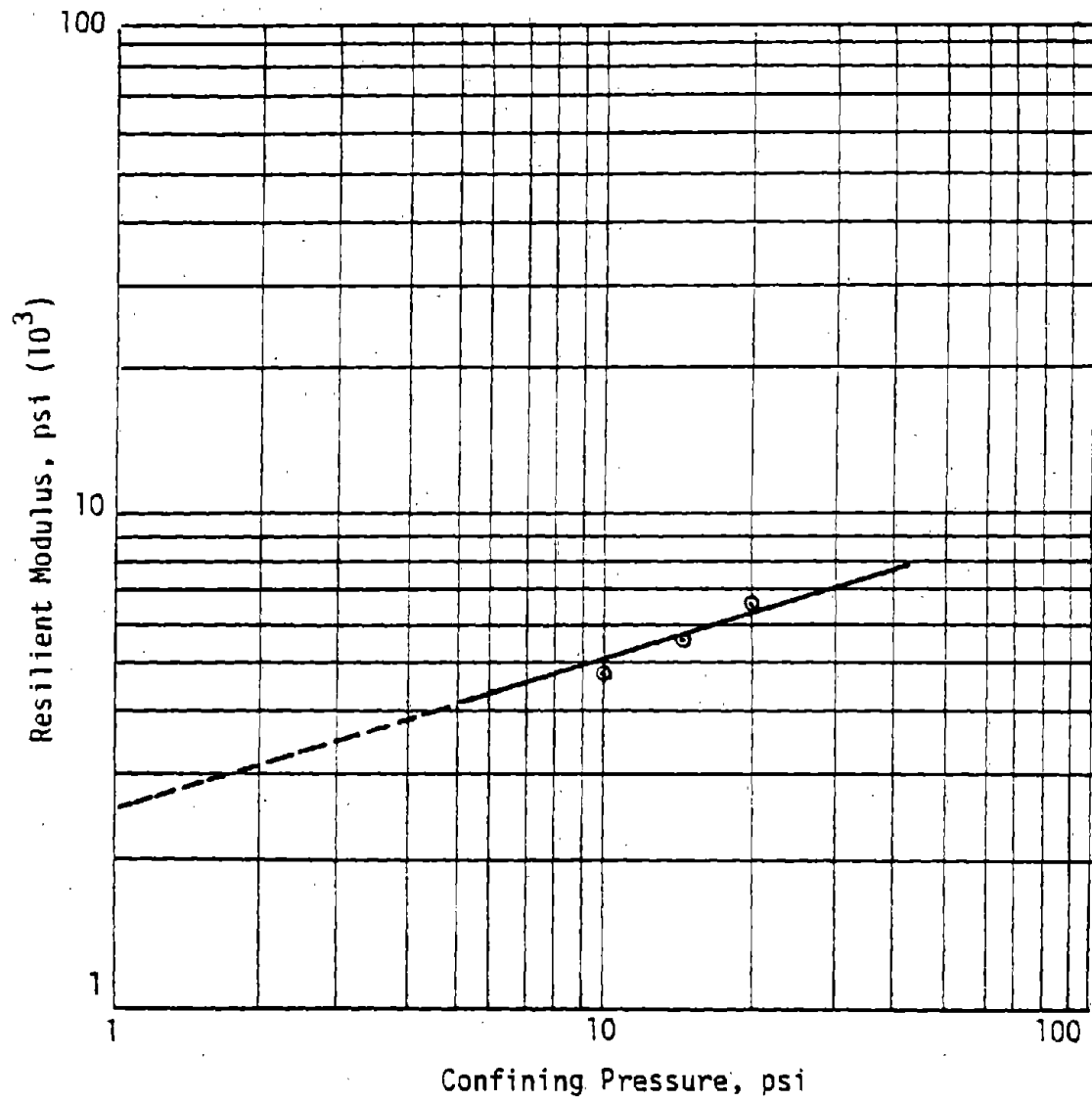
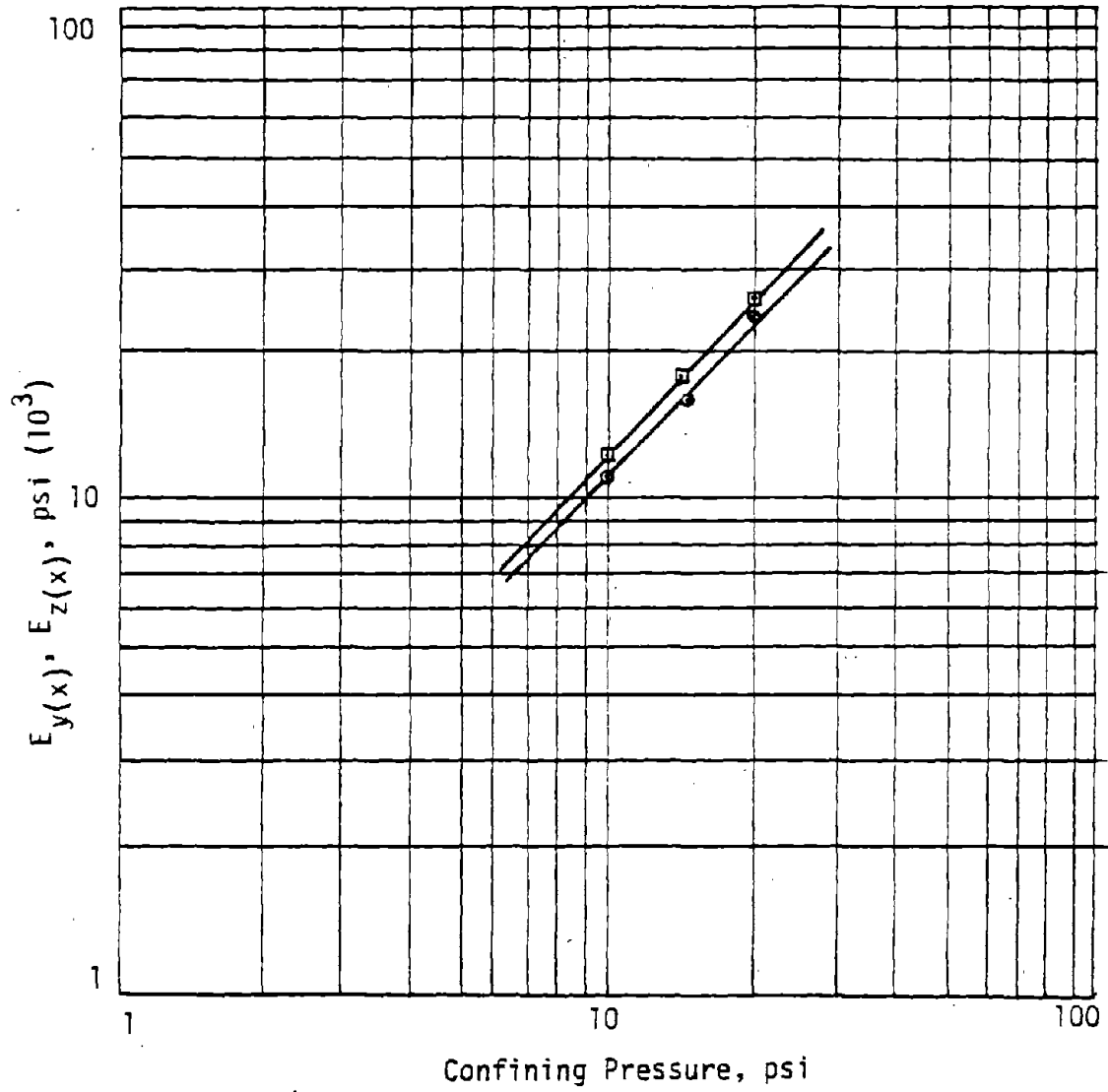Figure 4.8 Variation of Resilient Modulus with Confining
Pressure

Figure 4.9 Variation of $E_{y(x)}$ and $E_{z(x)}$ with Confining Pressure

granite gneiss. The parent material has particles of maximum size 40 mm. From the available data, [41], for granitic gneiss, AREA Grade 4 material of maximum particle size of 40 mm, the Resilient Modulus is found to be [41] 4800 $\sigma_3^{0.6}$ (psi).

The variation of the Resilient Modulus with the maximum particle size in the material, for a particular value of confining pressure (σ_3 = 10.00 psi, = 69.00 kpa) is shown in the Fig. (4.10). The Resilient Modulus has a direct linear relationship with the maximum particle size.

4.6.1 Load-Response Study

The apparatus performance has been investigated to ascertain how well the device fulfills the design criteria and how much signi-ficance can be attributed to test results. Details of the apparatus are given in reference 18.

4.6.2 Testing Procedure

When a specimen is tested in Conventional Triaxial Compression state in this device, for an example, if the stress levels are the same in all three directions (σ_1 = σ_2 = σ_3 = 100.00 psi, 690.0 kpa) and if σ_1 is to be increased to 150.00 psi (1035.0 kpa), fluid is pumped until the pressure gage shows 150.00 psi (1035.0 kpa). This operation is repeated until there is no further drop in pressure after the pumping is stopped. Once the load gets stabilized this way, the deformation readings are then taken. A study has been undertaken in order to check that in this process of stabilization
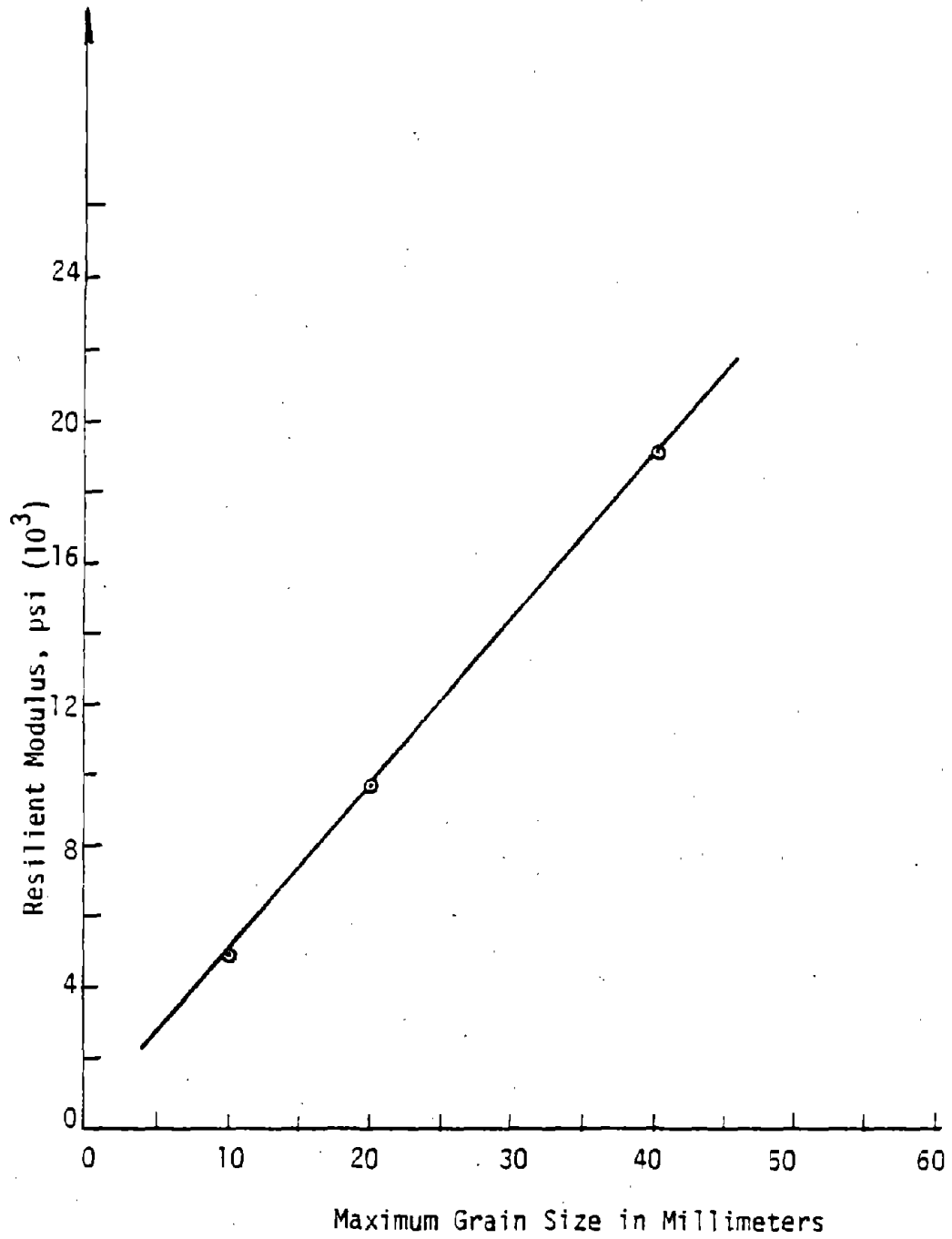
Figure 4.10 Variation of Resilient Modulus with Grain Size

of the applied load (increment), the creep of material is not included in the recorded deformations.

Two samples of ballast, prepared with an initial compacted density of 90 pcf (1.44 g/cm^3) are tested. The loading and deformation recording procedures are as follows.

In the first case, the sample is centered and the load is applied hydrostatically upto 100.00 psi (690.00 kpa). Then keeping the confining pressure the same, the deviator stress is increased in the z direction. The fluid is pumped until the pressure gage shows the predetermined stress level, and immediately the deformations are measured and recorded. Then pumping is continued to the next increment, and once the stress level is reached, the deformations are measured and the process is continued until a desired stress level is reached. The sample is then unloaded in the same way in stages and reloaded and this cycle is repeated. This stress-strain response of the material is plotted in Fig. (4.11).

In the second case, a similar sample with the same initial density is tested. This time, when each increment is applied, the fluid is pumped until the load gets stabilized. That is, the load does not drop from that level after pumping is stopped. The defomrations are read and recorded. Next the increment of load is then applied. The history of loading the same as in case I is followed. The stress-strain response is plotted in Fig. (4.12).
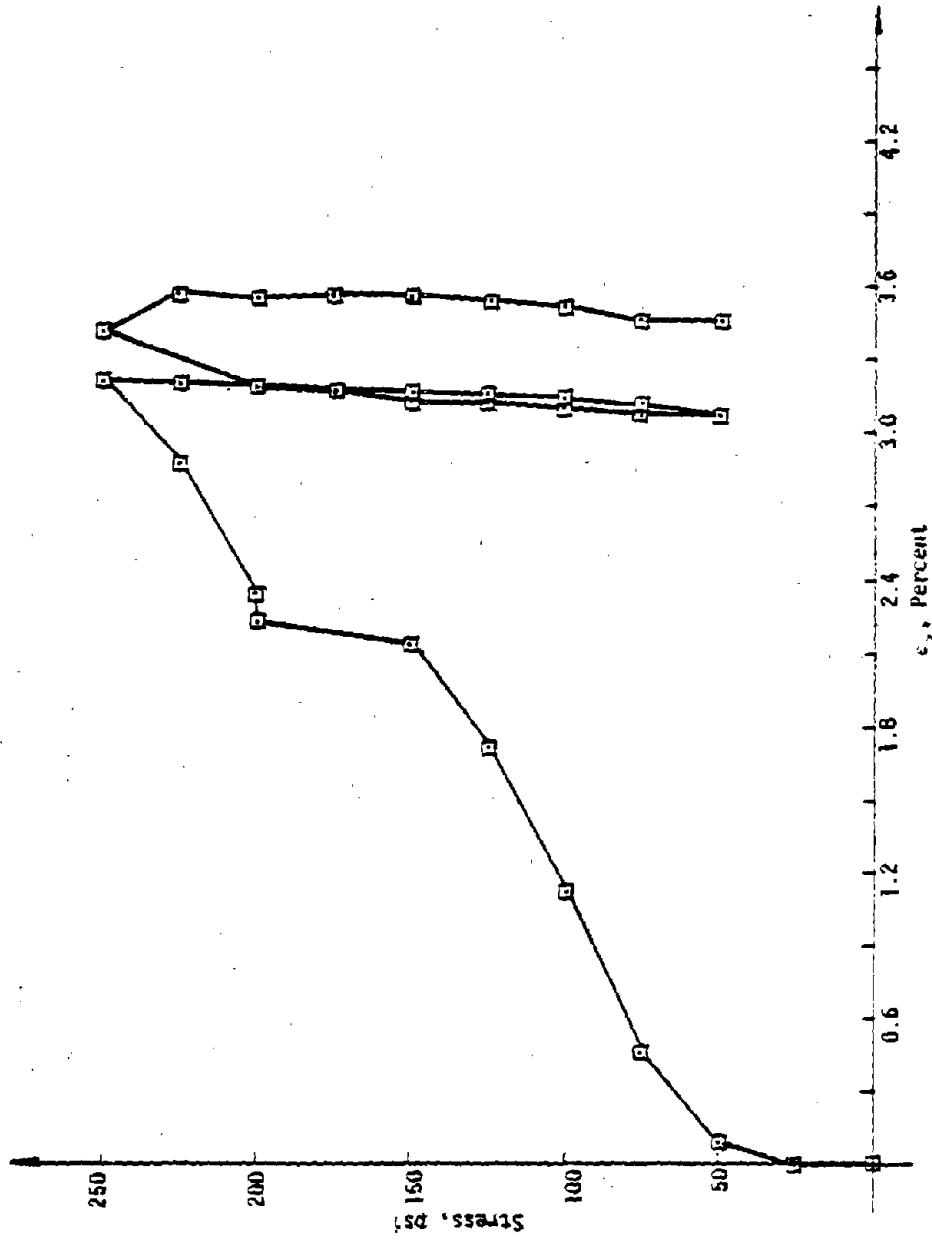
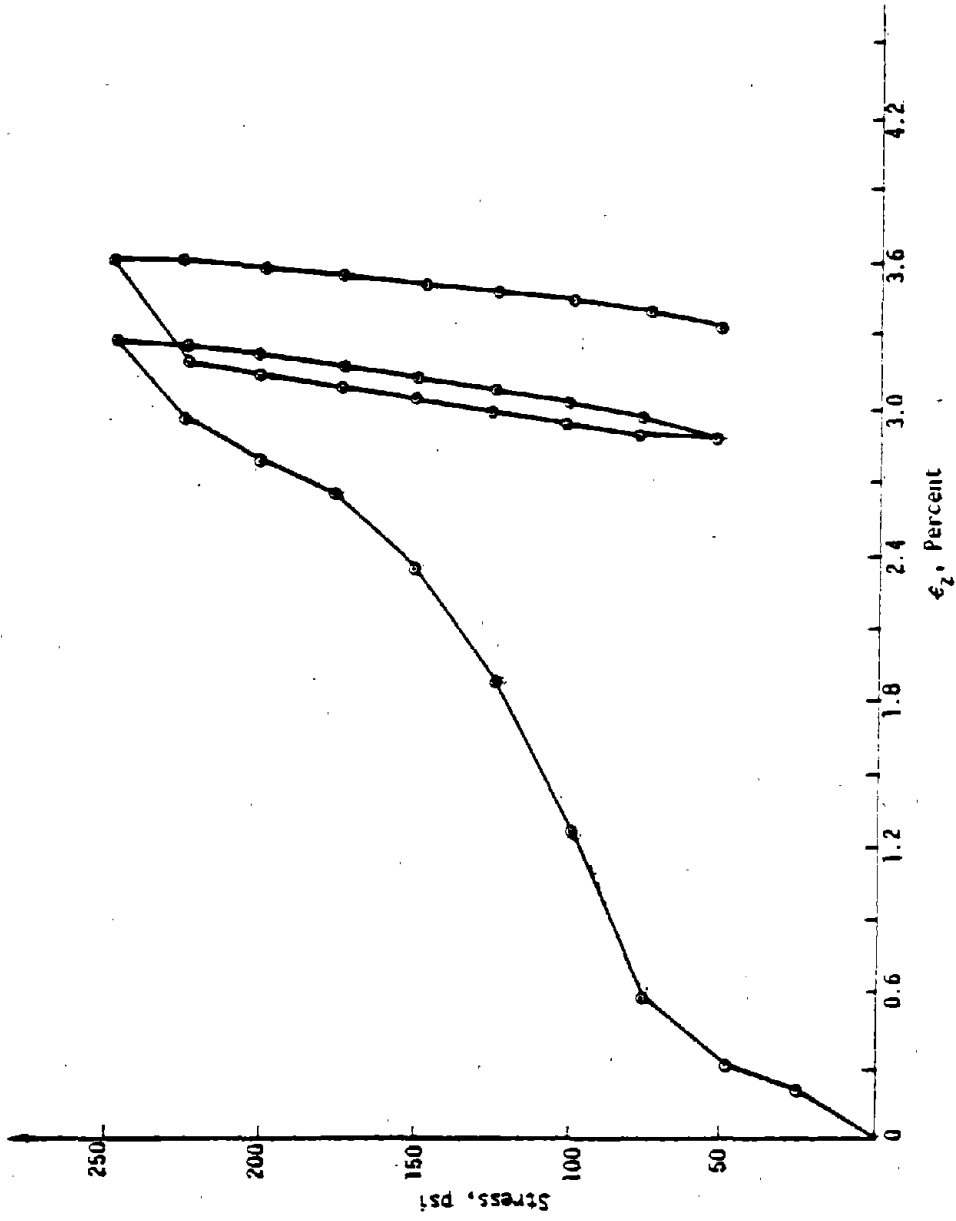Figure 4.11 Immediate Response of Strain Recorded

Figure 4.12 Strain Recorded after Load Stabilization

4.6.3 Test Results

When the two responses, Figs. (4.11) and (4.12) are compared, it is observed that the strains in both cases do not vary significantly at the maximum stress level of 250.00 psi (1.72 x 10^3 kpa), the difference being about 0.2 percent. Even at each load level, the difference between the two results is small except at the initial two load increments. The increase in strain after one unloading and reloading cycle is slightly more in the case 2. The recovery of strain after the first unloading cycle is slightly more about 0.3 percent in case II and it gets reduced as the second unloading cycle is completed to about 0.15 to 0.2 percent. This comparison implies that the procedure of loading such that measurements of strains are after the load stabilized would not involve significant amount of creep strain.

Pumping fluid till the load gets stabilized is probably necessiated due to the elastic response of the apparatus-pressure system and also due to cell reaction to the load applied. So the observed deformations are due to immediate response of the material, as it happens in the track-bed due to fast-moving load. Thus it can be concluded that though the apparatus does not possess dynamic loading system, yet its results can be considered to simulate quasi-static approximately a cyclic (repetitive) load.

Also, unlike cyclic cylindrical triaxial cell, in the truly triaxial device, it may be possible to derive stress-strain data from (static) loading-unloading-reloading response. The truly triaxial device can offer a number of advantages over the cylindrical

triaxial device. One such is, tests can be performed under a variety of realistic stress paths on the material.

4.7.1 DETAILS OF TESTS

Samples of ballast II are tested in the truly triaxial device. Specimens are prepared to an initial compacted density of 90.00 pcf (1.44 g/cm^3), as explained in section 2.5.3. The sample to be tested is slided into the cubical cavity of the multiaxial device. The remaining faces are then fixed and fluid pressure lines are connected to the respective side ports. An initial hydrostatic confining pressure is applied on the sample, equal to that of initial vacuum pressure. The vacuum pressure is now discontinued. The sample is ready for test under a desired stress path. The method of testing, recording the stresses and deformations are as explained in section 3.4.2. Tests are conducted on ballast in HC, CTC, CTE, RTE, RTC, SS, TC and TE states and the stress-strain responses together with the discussion of test results are presented here.

4.7.2 Hydrostatic Compression (HC or IC)

The specimen is compacted to an initial density of 1.47 g/cm^3. The initial hydrostatic confinement is held to be 5.00 psi (34.50 kpa). This is followed in all tests conducted on ballast II. Increments of load of the same magnitude are applied on all six faces of the specimen. Loading is applied by pumping silicon liquid into the flexible membranes. Deformation readings are recorded at each stress level only after the load gets stabilized

at that level. Three unloading - reloading cycles are followed. The stress-strain response of the material in hydrostatic compression is presented in Fig. (4.13).

It is observed from the figure that the unloading curve has a slope much greater than the loading slope. Reloading, except for a small hysteresis loop, generally follows the unloading curve upto a point close to the previous maximum stress. If stress is increased further, the stress-strain curve approaches the continuation of the original loading curve. The unloading slope increases as the stress level increases, indicating that the material stiffness as it gets compressed.

The curve for monotonically increased loading, that is, ignoring unloading and reloading part upto the previous maximum stress level, is used to find the model parameters. The initial bulk modulus is determined to be 4.0×10^3 psi (27.6×10^3 kpa).

4.7.3 Conventional Triaxial Compression (CTC)

The stress-strain response curves for three separate CTC tests at different confining pressures plotted in Figs. (4.14), (4.15) and (4.16). The stiffness increases with confining pressure. The slope of the unloading curve is the elastic modulus. As the number of unload-reload cycles increases, the size of hysteresis loop also increases. All the three tests reached an ultimate strength plateau indicating failure. The tests are terminated when they reach that level.

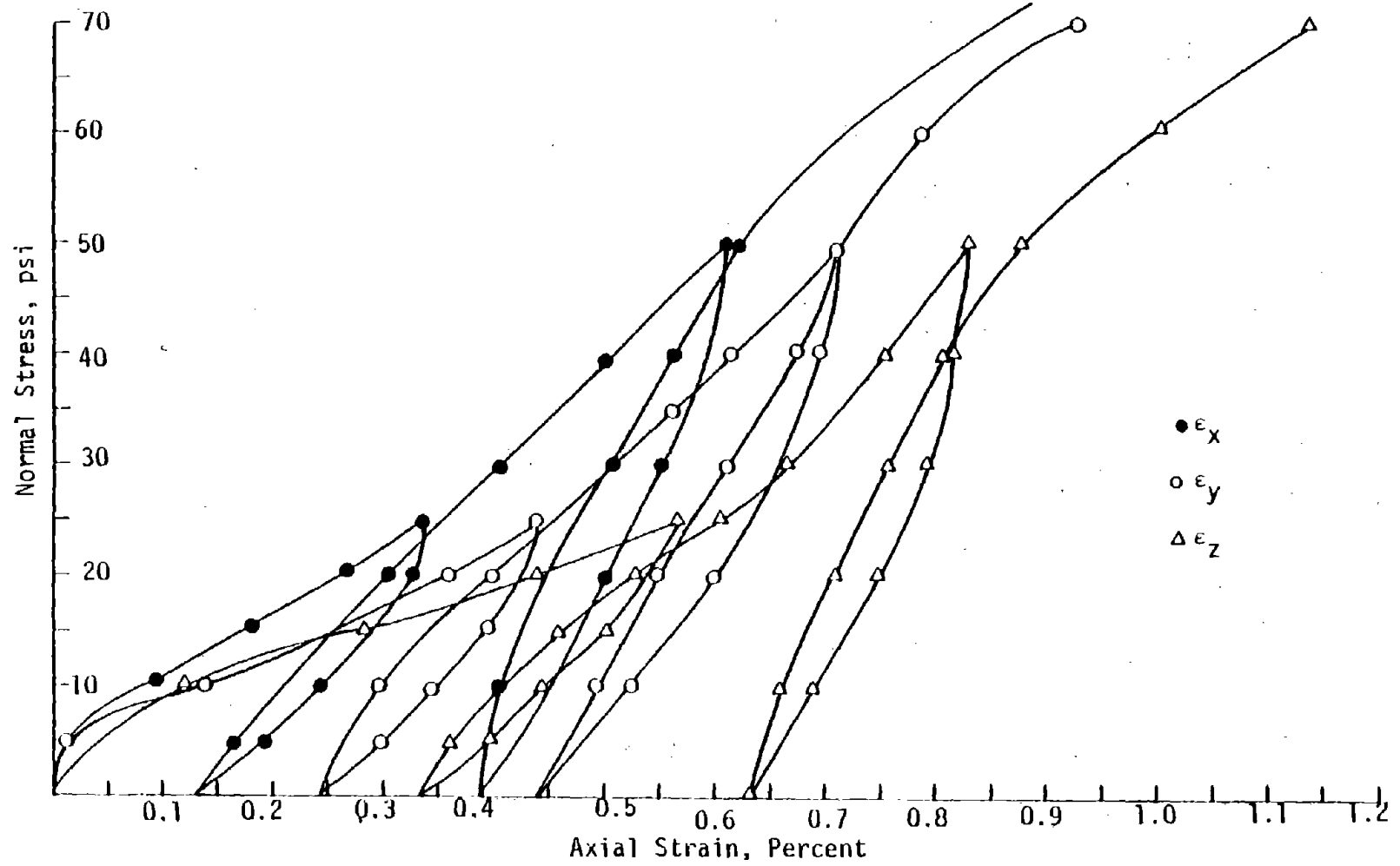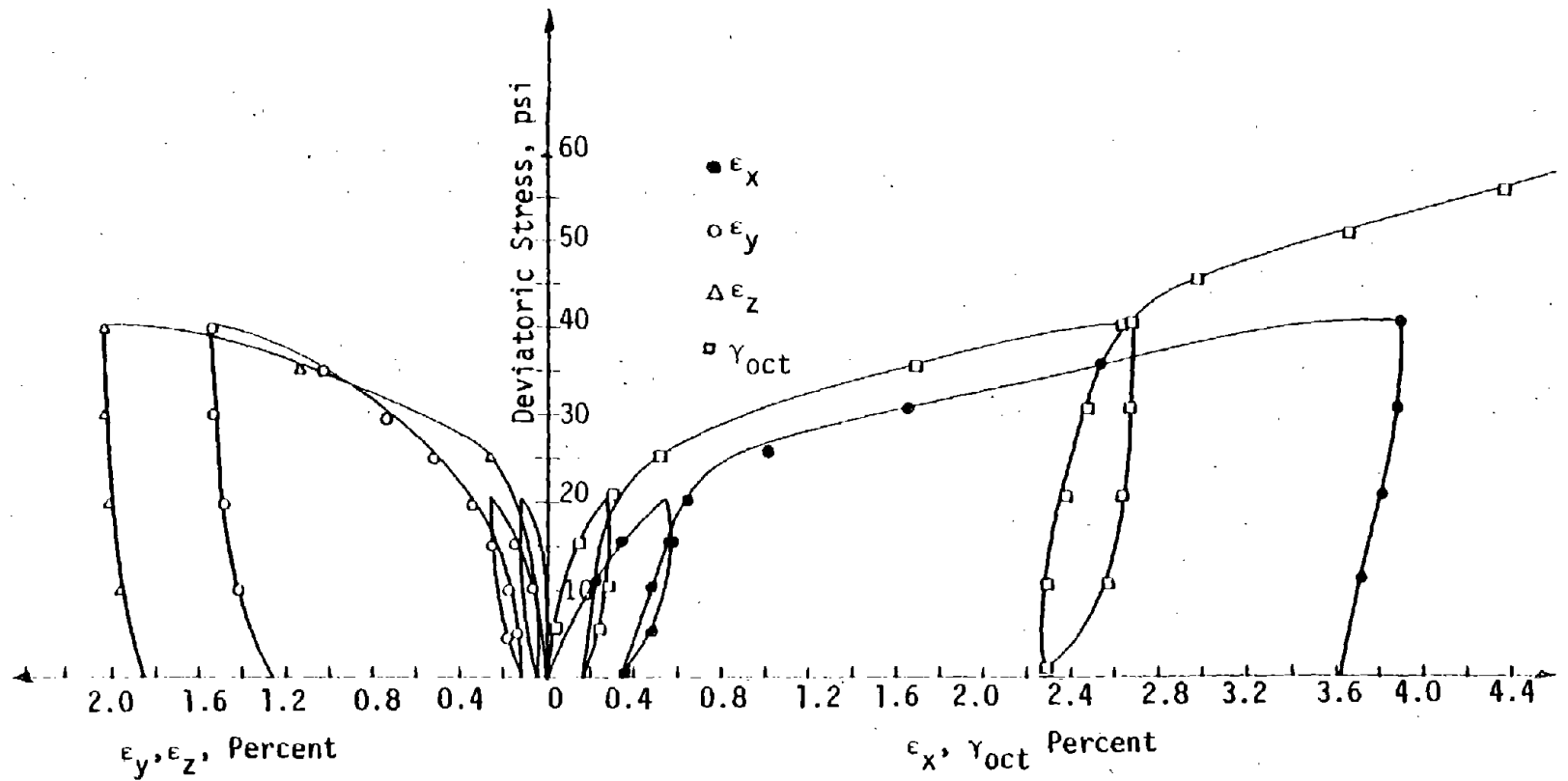Figure 4.13   Stress-Strain Response Curves for Hydrostatic Compression Test

Figure 4.14 Stress-Strain Response Curves for Conventional Triaxial Compression
          Test $(\sigma_2 = 10.00$ psi$)$
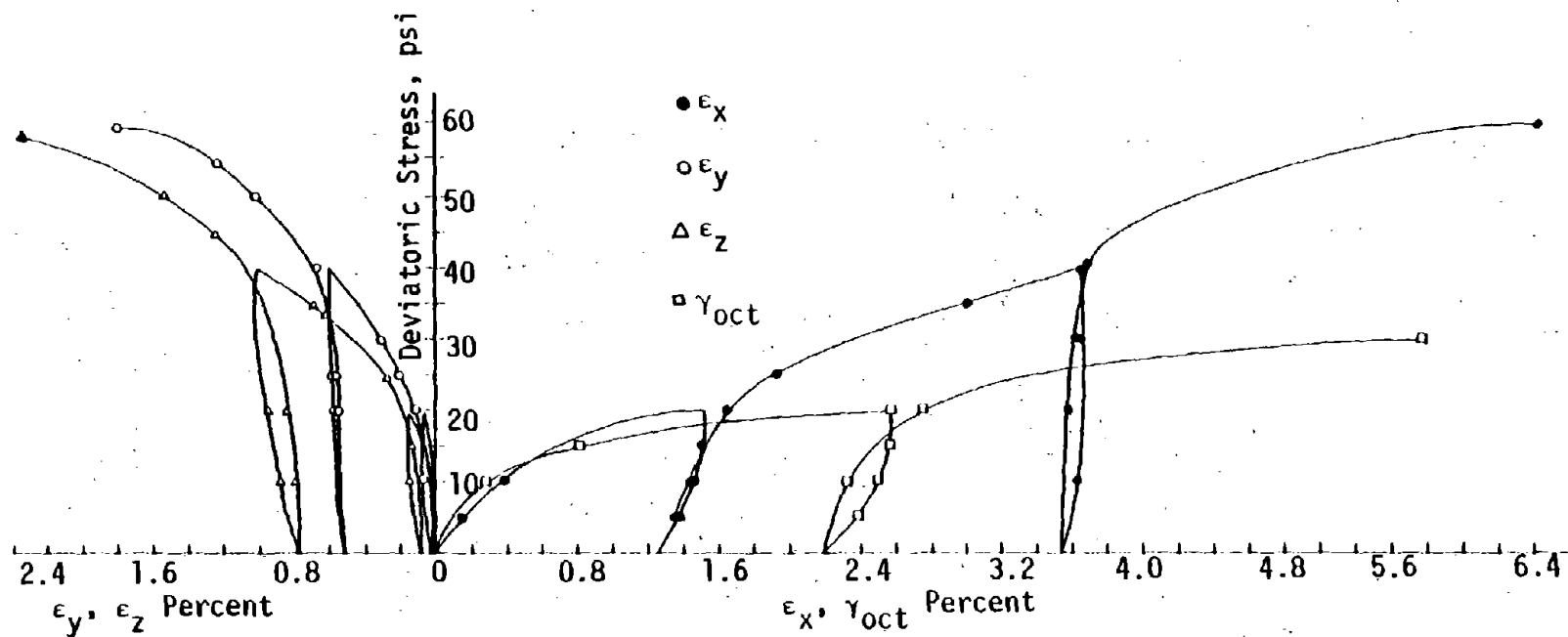
Figure 4.15 Stress-Strain Response Curves for Conventional Triaxial
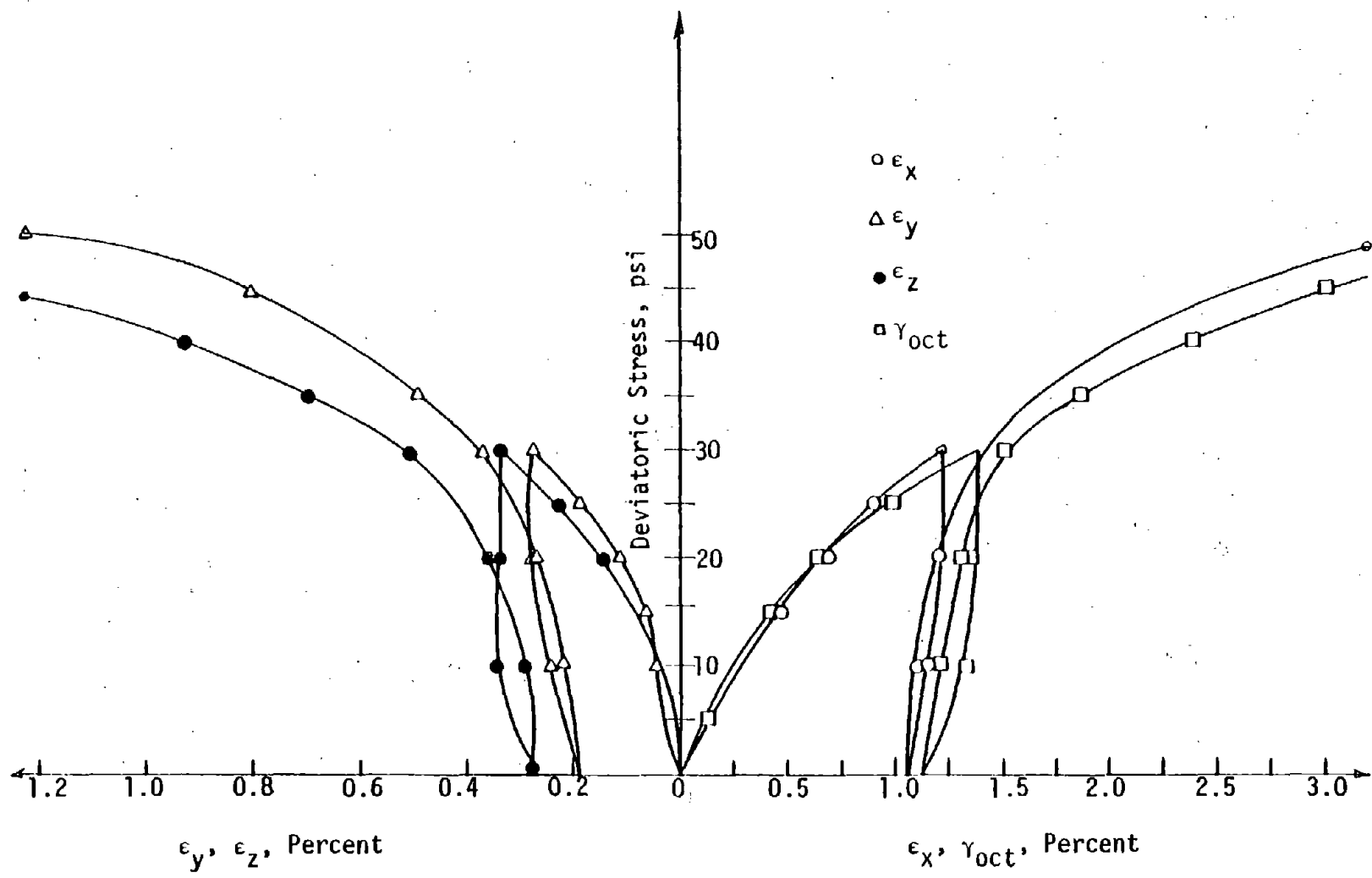Compression Test $(\sigma_2 = 15.00 \text{ psi})$

Figure 4.16   Stress-Strain Response Curves for Conventional Triaxial Compression
Test   (σ_2 = 20.00 psi)

4.7.4 Reduced Triaxial Compression (RTC)

Three RTC tests are conducted on ballast II. The hydrostatic stress levels at which RTC path is followed are 30.00, 40.00 and 50.00 psi (207.00, 276.00, 345.00 kpa). Keeping σ_1 constant, σ_2 and σ_3 (confining pressure) are reduced in stages with decrement $\Delta\sigma_2$ equal to the decrement $\Delta\sigma_3$. The stress-strain response curves observed in these tests are plotted in Figs. (4.17), (4.18) and (4.19). In all three tests, a well defined ultimate strength level at a relatively small strains is reached. The magnitude of the shear stress at which failure is observed is 11.20 psi (77.28 kpa) with σ_{oct} = 30.00 psi (207.00 kpa). In the other two cases, they are 15.80 psi (109.20 kpa) and 19.10 psi (131.79 kpa) with σ_{oct} = 40.00 psi (276.00 kpa) and 50.00 psi (345.00 kpa) respectively. This is more a linear relationship between J_1 and J_{2D}.

4.7.5 Simple Shear (SS)

Simple shear tests on ballast samples are run with σ_{oct} = 25.00 psi (172.50 kpa) and σ_{oct} = 35.00 psi (241.50 kpa). Intermediate principal stress (σ_2) is kept constant equal to the value of σ_{oct}. The major and minor principal stresses σ_1 and σ_3 are increased and decreased respectively by equal amounts so that σ_{oct} remains constant. The stress-strain responses obtained from these two tests are shown in Figs. (4.20) and (4.21). In both cases it is observed that the intermediate principal strain is slightly compressive. A well-defined ultimate strength level is reached in both tests. The initial slope

Figure 4.17   Stress-Strain Response Curves for Reduced Triaxial Compression Test
(σ_1 = 30.00 psi)

Figure 4.18   Stress-Strain Response Curves for Reduced Triaxial Compression Test $(\sigma_1 = 40.00 \text{ psi})$
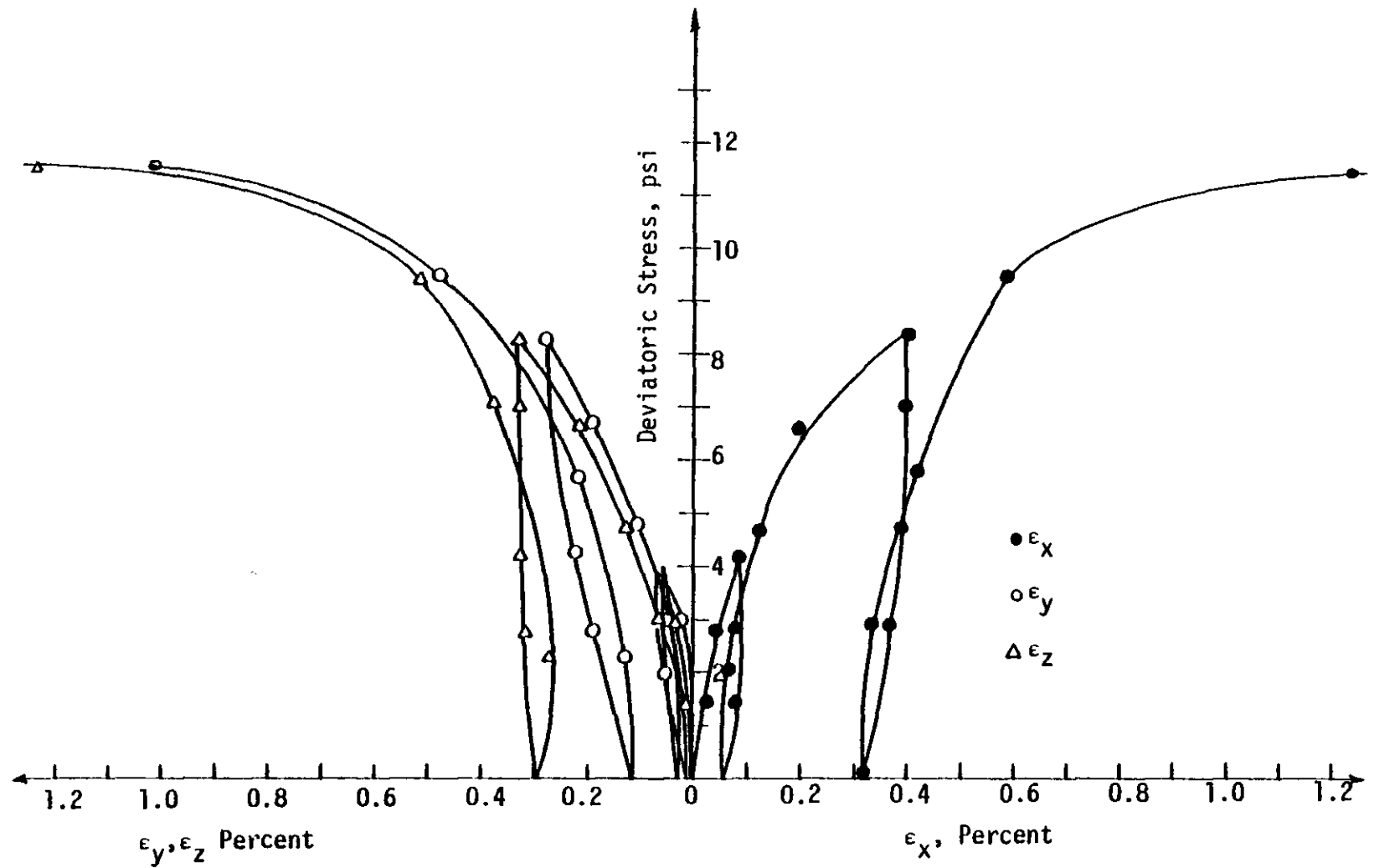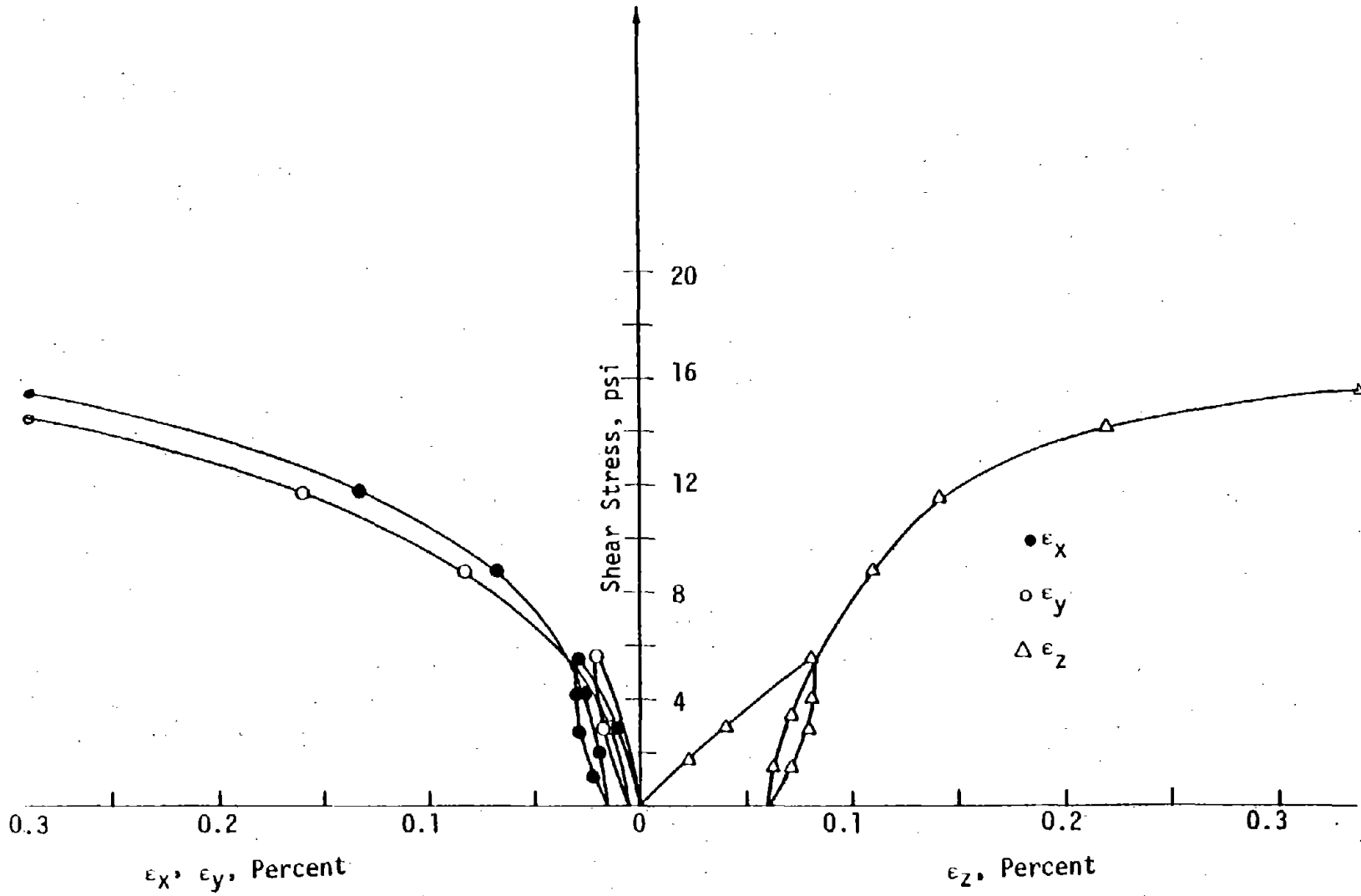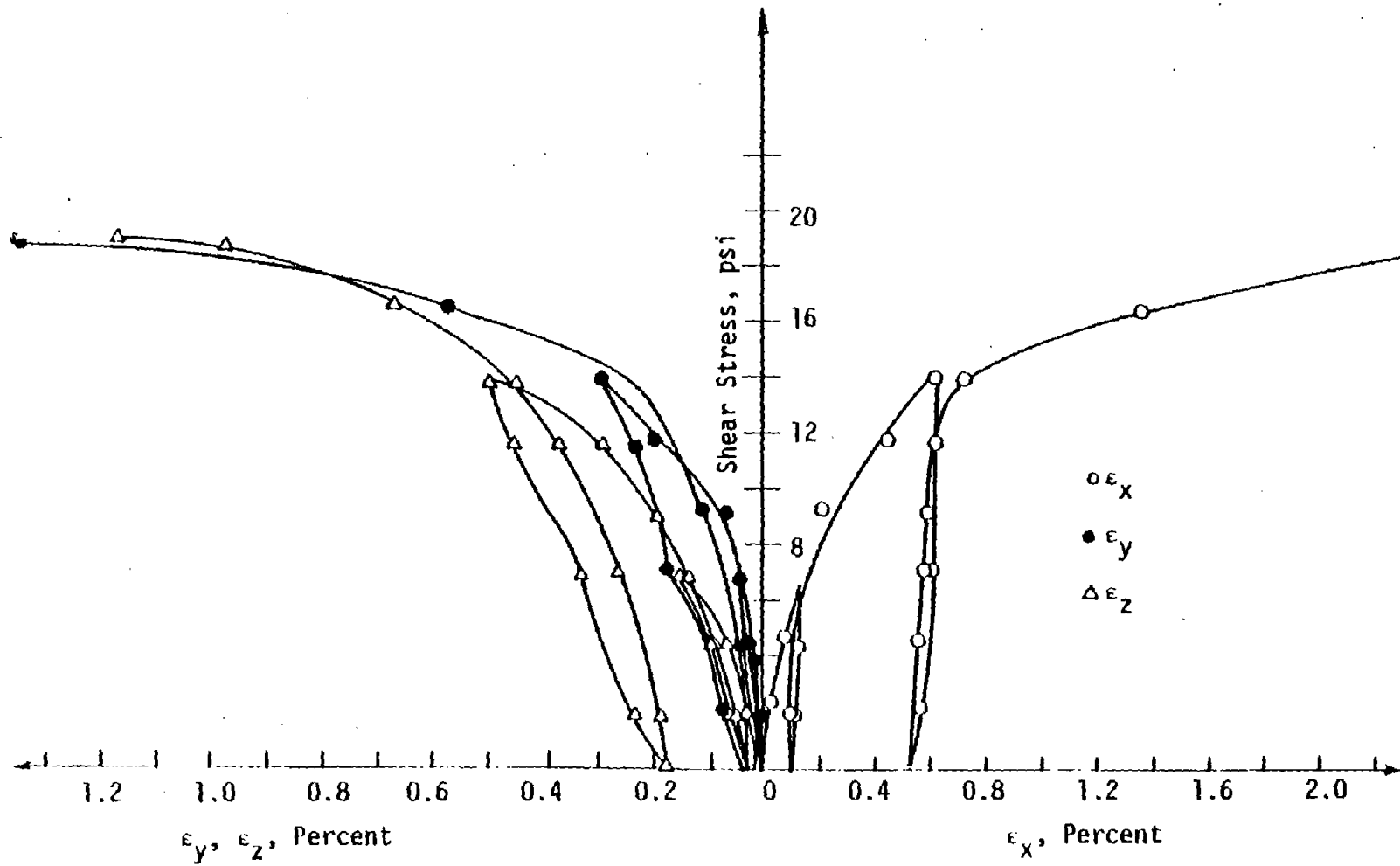
Figure 4.19 Stress-Strain Response Curves for Reduced Triaxial Compression Test
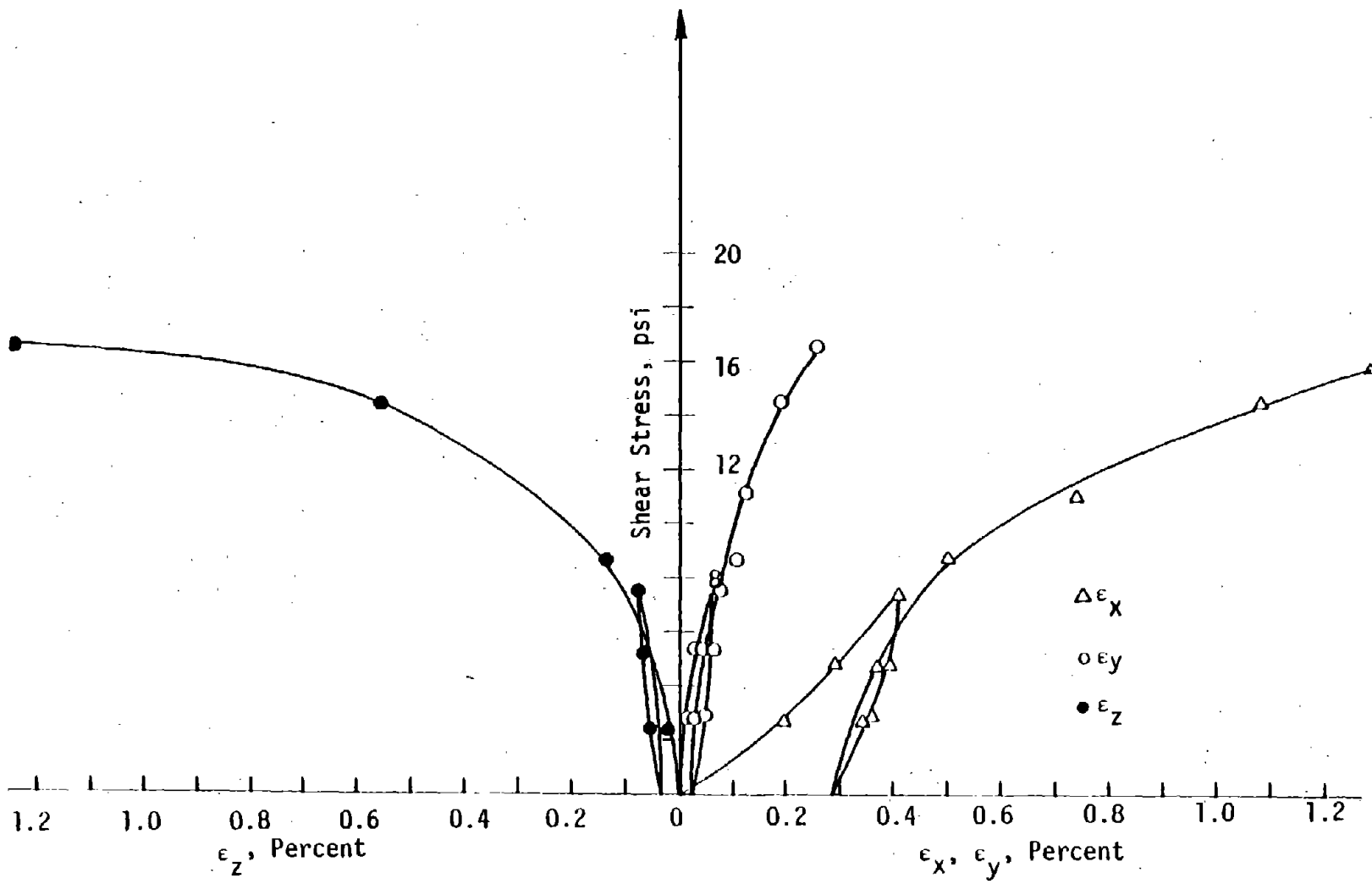($\sigma_1 = 50.00$ psi)

Figure 4.20 Stress-Strain Response Curves for Simple Shear Test (σ_{oct} = 25.00 psi)
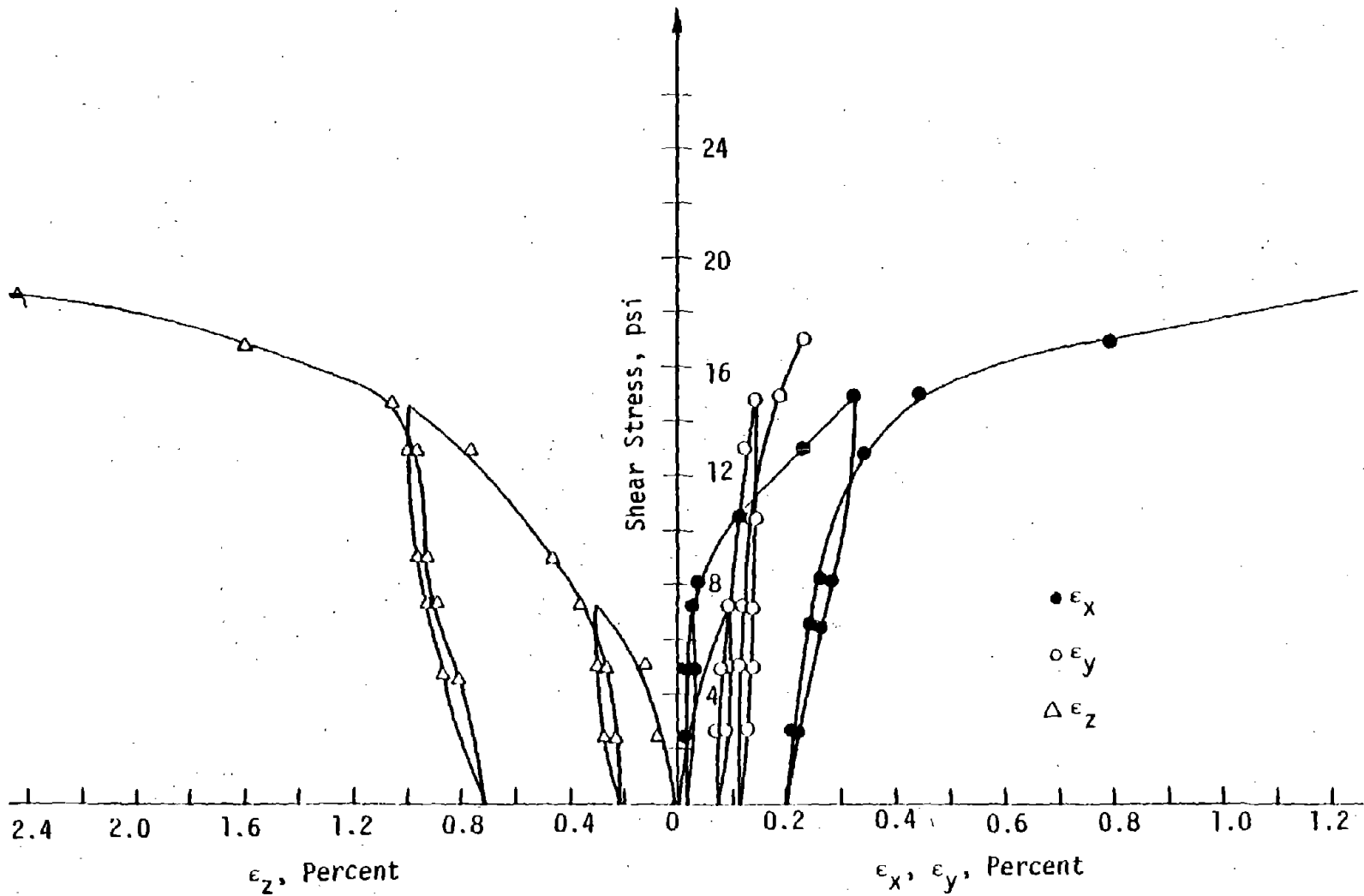
Figure 4.21 Stress-Strain Response Curves for Simple Shear Test (σ_{oct} = 35.00 psi)

of the curve is steeper in case of the test with σ_{oct} is 35.00 psi
(241.50 kpa) to that with σ_{oct} is 25.00 psi (172.50 kpa). This may
be due to the reason that the sample is more compressed with σ_{oct}
35.00 psi (241.50 kpa) and thus exhibits more shear stiffness. Large
shear strain increase is also noticed at ultimate strength levels
in this case.

4.7.6 Reduced Triaxial Extension (RTE)

The sample is loaded hydrostatically upto 40.00 psi (276.00 kpa).
The confining pressure σ_2 and σ_3 are kept constant at this level and
σ_1 is reduced in steps. The results of the test are plotted in
Fig. (4.22). A well-defined ultimate strength level is reached in
this test. The maximum shear stress is observed to be 16.40 psi
(113.16 kpa) as against 15.80 psi (109.02 kpa) recorded at failure
in RTC test with the same initial hydrostatic level of 40.00 psi
(276.00 kpa). The ratio of axial to lateral strain at failure
is about 2.00 as is also observed in that RTC test.

4.7.7 Permanent Deformation Behavior

From various investigations carried out on permanent deformation
behavior, it can be concluded that one of the important factors
influencing the repeated load plastic strain behavior of ballast are
the degree of compaction and the stress level. Also, unlike resilient
response, permanent deformation behavior of ballast is found to depend
on loading history. The increase in plastic strain in general is
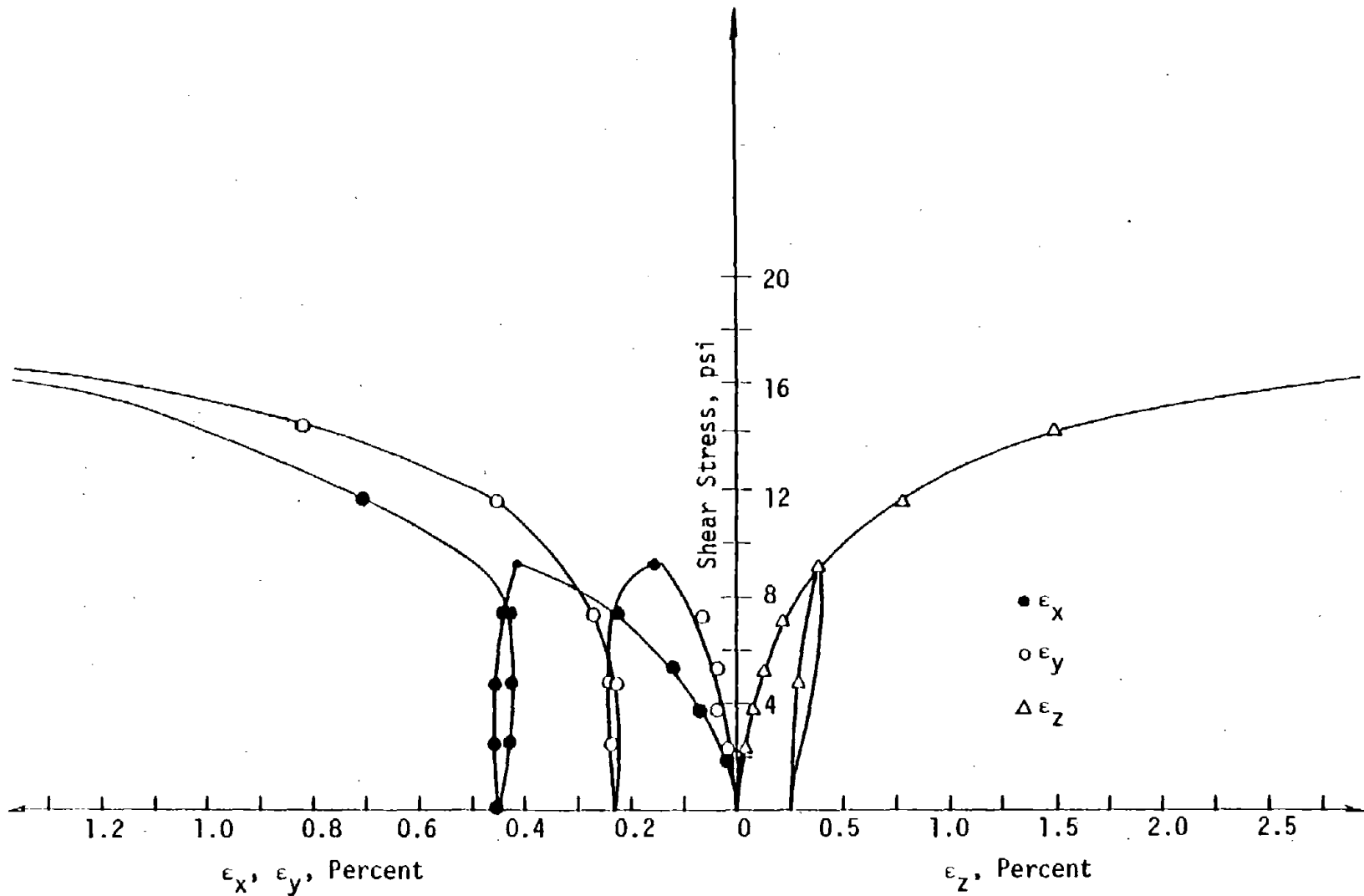
Figure 4.22 Stress-Strain Response Curves for Reduced Triaxial Extention Test (σ_2 = 40.00 psi)

seen to be inversely proportional to the number of loading cycles, for a constant stress ratio equal to repeated deviator stress divided by confining pressure.

Under heavily loaded trains considerable ballast resistance will be caused by high frictional resistance. Proper compaction of ballast bed during laying and maintenance, will avoid the possibility of large deformations occurring in the ballast due to a large number of repetitive loads. Most of the tests have been performed at low pressures only, since the height of ballast in track is small and the confining pressures are small. At low cell pressures, the density of placement has an immense effect on the ballast failure resistance.

In this investigation, the material is compacted to an initial density nearly equal to the field density of ballast at the track bed. The material is uniformly graded. The samples are subjected to few load - unload - reload cycles under different stress paths. Each time, when the sample is reloaded, it is taken beyond the previous stress level and then unloaded. Therefore, the stress ratio is not constant. Figure (4.15) shows the stress-strain responses for a CTC test with a confining pressure of 15.00 psi (103.5 kpa). The initial compacted density is 90.00 pcf (1.44 g/cm^3). The strain the sample has undergone for a deviator stress of 45.00 psi (310.5 kpa) is about 3.78 percent. These results are compared with available information [41] on the same type of material under the same state of stress and density.

Figure (4.23) shows the increase in strain with increase in number of cycles of load applications as reported by Knutson [41]. Ballast tested was granite gneiss, and the same kind was tested in this investigation. The results depicted in this figure is from a cyclic triaxial test where sample has been subjected to a deviator stress of 45.00 psi (310.5 kpa) a confining pressure of 15.00 psi (103.5 kpa). The increase in strain becomes very small as the number of cycles approaches to 5000. It can be regarded that the sample has undergone a maximum strain of 3.4 percent under a confining pressure of 15.00 psi (103.5 kpa) and a deviator stress of 45.00 psi (310.5 kpa). The initial density of the sample was 93.00 pcf (1.48 g/cm^3).

The difference in magnitude of strain observed in the two cases is about 8.0 percent. So the test results herein can be treated to be a good representation of the material behavior under the conditions as in a track bed.

4.7.8 Effects of Stress Paths

The shear moduli, determined from the test results CTC, SS, and RTC are plotted against the gradients, g, of the three stress paths in Fig. (4.24). The gradients from CTS, SS and RTC are 3.0, 0.0 and -1.50 respectively. The definition of the gradient is given in section 2.6.7 [24]. The shear modulus calculated from CTC test results is more than that obtained from SS test and that determined from RTC test is the least of the three.
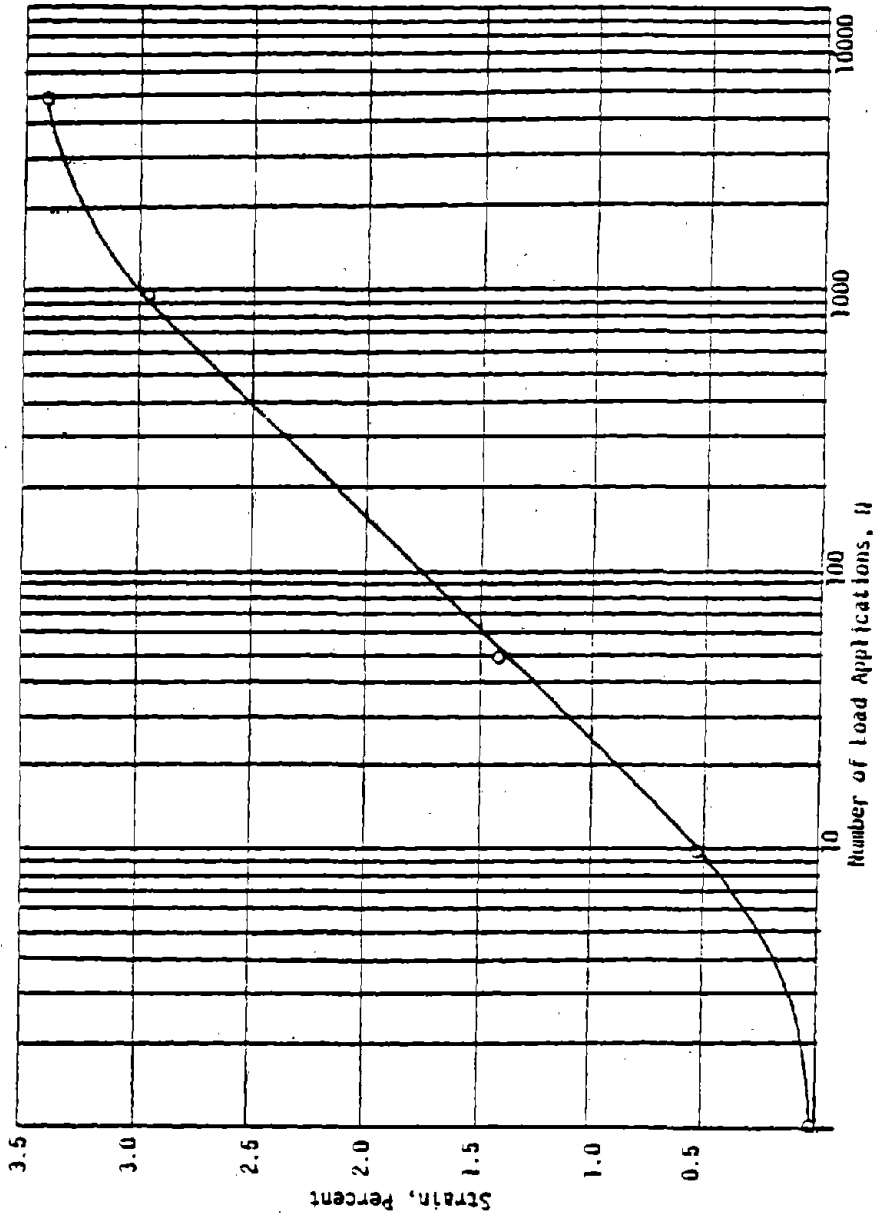
Figure 4.23 Effects of Gradation and Density on Plastic Strain Response for Granitic Gneiss
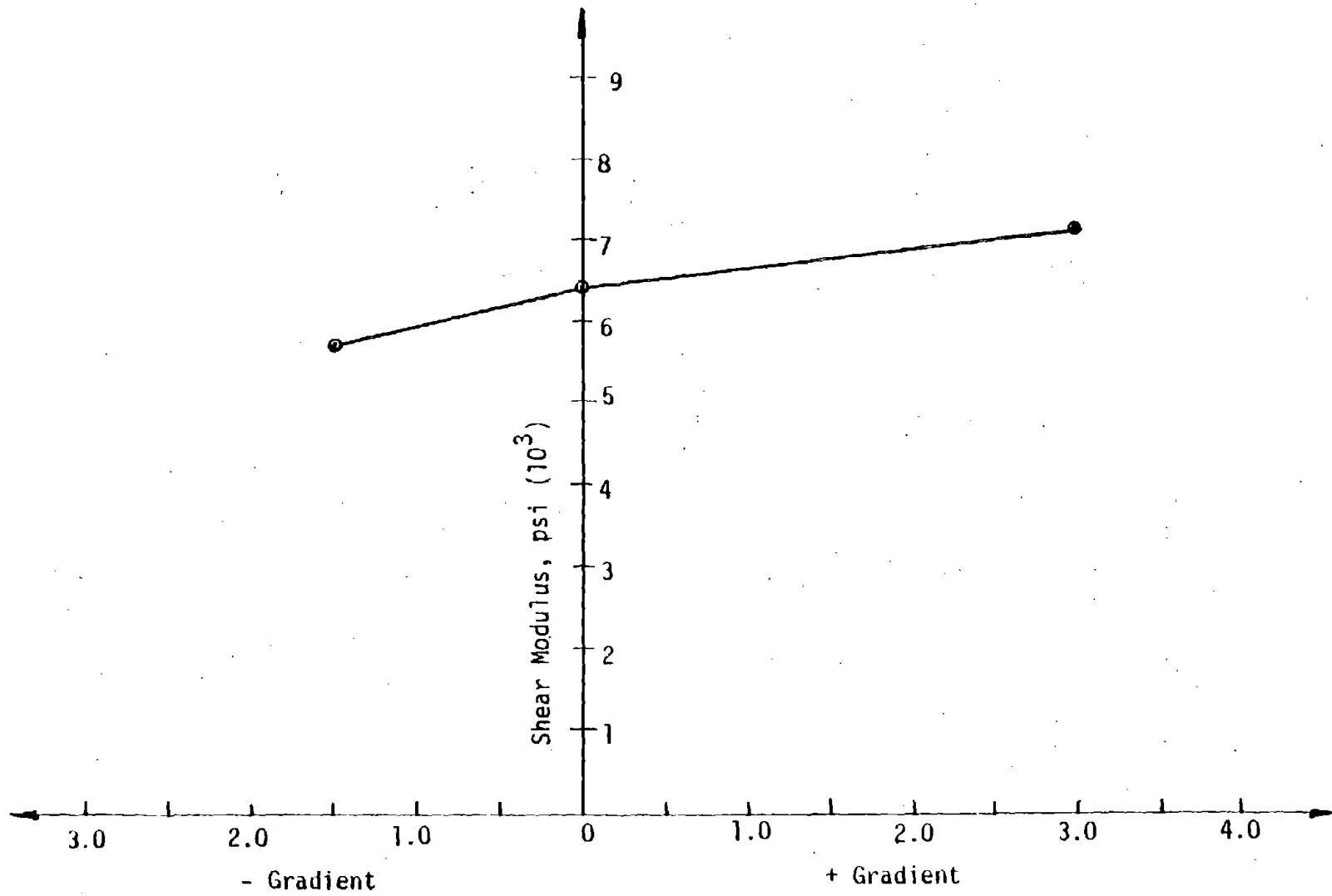
Figure 4.24   Variation of Shear Modulus with Different Stress Paths

4.8.1 ADVANCED CONSTITUTIVE MODELS

Early attempts to mathematically model the behavior of ballast under both static and/or dynamic loadings were based on the assumption that the ballast could be approximated as a linear elastic material. Of course such a model can be of extremely limited validity. They were subsequently replaced by simple elasto-plastic models of vonMises or Drucker-Prager type, in which a yield function was used to describe the material failure under specific combinations of the shear stresses and pressure. Recently, more advanced elasto-plastic models have been used to model the action of the ballast under a wide variation of applied pressure. In these models the yield condition depended upon the pressure in a general way. Different pressusre-volume relations were used for initial loading and for subsequent unloading and reloading.

Although these models reproduce actual ballast behavior quite adequately in both static and cyclic uniaxial strain tests, they do not do so in triaxial compression tests. But this mathematical material model, namely, variable moduli model in which the basic constitutive law is an isotropic relation between the increments of stress and strain reproduces adequately, the behavior both in static and dynamic uniaxial and triaxial tests. The model has no explicit yield condition. The bulk and shear moduli, however, are functions of the stress and/or strain invariants.

It is possible, from the test data, to develop advanced plasticity models, as in the case of subballast. However, in

view of the past experience and the test results herein, it is felt that a variable moduli model based on two parameters bulk modulus K, and shear modulus G, may be appropriate.

4.8.2 Details of Variable Moduli Model

The incremental form of the stress-strain relation in variable moduli model can be expressed as [15,17,47]

$$\Delta S_{ij} = 2G \; \Delta \varepsilon_{ij} \tag{4.6}$$

$$\Delta p = 3K \; \Delta \varepsilon_{ij} \tag{4.7}$$

where ΔS_{ij} and $\Delta \varepsilon_{ij}$ are the deviatoric stress and strain increments respectively, and Δp and $\Delta \varepsilon_{ij}$ are the mean stress and strain increments. In writing Eqs. (4.6) and (4.7) an implicit assumption is made that the material is isotropic, because the separation of the constitutive relation into deviatoric and volumetric parts precludes any coupling between them as is observed in granular media.

There have been three major models in vogue. They are:

1) Constant Poisson's Ratio Model,

2) Variable Moduli Model based on the Invariants of the strain tensor,

3) Combined stress-strain variable moduli model.

4.8.3 Constant Poisson Ratio Model

The ratio of the bulk modulus to shear modulus is assumed to be constant. The two moduli can be functions of mean pressure or volumetric strain or both. The model can be expressed as

$$\frac{K}{G} = \frac{2(1+\nu)}{3(1-2\nu)} = \text{constant} \qquad (4.8)$$

This model has been found to be satisfactory only for the uniaxial states of strain and it gives contradicting predictions in the triaxial conditions [47]

4.8.4 Variable Moduli Model with Invariants of Strain Tensor

The bulk modulus K and the shear modulus G are assumed to be functions of the first invariant of the strain tensor, I_1, and the second invariant of the deviatoric strain tensor, I_{2D} and can be expressed as [47]

$$K = K_0 + K_1 I_1 + K_2 I_1^2 \qquad (4.9)$$

$$G = G_0 + G_1 \sqrt{I_{2D}} + G_2 I_1 \qquad (4.10)$$

K_0 and G_0 are initial bulk and shear moduli respectively. K_1, K_2, G_1 and G_2 are material parameters.

This model fails to take into account unloading part. Another limitation is that, in many existing finite element procedures, stresses are stored rather than strains and hence the implementation of this model in an existing program can require additional difficulties.

4.8.5 Combined Stress-Strain Variable Moduli Model

Both the shear modulus and the bulk modulus are assumed to depend upon the stress and strain invariants. Different functions

G and K apply in initial loading and subsequent unloading and re-loading. For initial loading, the bulk modulus K which is expressed as a function of the mean strain and a shear modulus G which is as a function of first two stress invariants or more specifically the pressure p and the square root of the second invariant of the deviatoric stress tensor. They can be written as [47]

$$K = K_0 + K_1 I_1 + K_2 I_1^2 \qquad (4.11)$$

The bulk modulus is chosen to be a quadratic in I_1 where I_1 is the first invariant of strain tensor. The shear modulus, when expressed in terms of J_1 and J_{2D} where J_1 is the first invariant of stress tensor and J_{2D} is the second invariant of deviatoric stress tensor is

$$G = G_0 + \gamma_1 J_1 + \gamma_2 \sqrt{J_{2D}} \qquad (4.12)$$

All these models are based on experimental curves. Eqs. (4.11) and (4.12) are the first terms in the series expansions of more general analytic functions K and G of the stress and strain invariants. The quantity $\sqrt{J_{2D}}$ is preferred rather than J_{2D} itself, since it is of the same order as J_1 and the components of the stress tensor. At zero stress and strain the bulk and shear moduli reduce respectively to K_0 and G_0, the "linear elastic" values, which are related in terms of the "elastic" poisson's ratio ν_0 .

$$\frac{K_0}{G_0} = \frac{2(1+\nu_0)}{3(1-2\nu_0)} \qquad (4.13)$$

with γ_1 positive and γ_2 negative, the material hardens in shear with increasing pressure and softens with increasing shear stress.

By specializing the above relation for triaxial state of stress as

$$\sqrt{J_{2D}} = \frac{1}{\sqrt{3}} (\sigma_1 - \sigma_3) \qquad (4.14)$$

and

$$J_1 = p = \frac{\sigma_1 + 2\sigma_3}{3} \qquad (4.15)$$

G can be expressed as

$$G = G_0 + \frac{\gamma_1}{3} (\sigma_1 + 2\sigma_3) + \frac{\gamma_2}{3} (\sigma_1 - \sigma_3) \qquad (4.16)$$

So a necessary condition for G to decrease as σ_1 increases is that

$$\gamma_1 + 3 \gamma_2 < 0 \qquad (4.17)$$

In other words $\gamma_1 > 0$ and $\gamma_2 < 0$.

The five parameters to fully describe the model are

$$K_0, K_1, K_2, G_0, \gamma_1 \text{ and } \gamma_2 \qquad (4.18)$$

If the stress quantities are non-dimensionalized, they can be written as

$$\frac{G_0}{K_0}, \frac{K_1}{K_0}, \gamma_1, \gamma_2, \frac{K_2}{K_0} \qquad (4.19)$$

The ratio G_0/K_0 is positive and is related by the Eq. (4.13). The higher order terms K_1/K_0 and K_2/K_0 may be positive and negative. The values are restricted by the condition that $K > 0$.

The material behavior under loading is quite different from unloading conditions. In case of uniaxial state of stress, loading and unloading can easily be seen as the state is only one-dimensional. Under three-dimensional state of stresses it is not easily seen. Different relationships for G and K are to be assumed under unloading conditions, thus accounting for inelastic behavior in load-unload cycles [47]. In this investigation, it is assumed that the response under unloading and reloading upto the maximum past state of stress is essentially elastic.

In fact, this model differs with plasticity model by the way unloading is defined. In plasticity models, unloading is defined by a yield criterion which represent both deviatoric and hydrostatic states of stresses, whereas, in variable moduli model, behavior under deviatoric and hydrostatic states of stresses are decomposed and described independently.

Both G and K, vary continuously with the states of stress in this model. Therefore solution of boundary value problems have to be done using incremental procedures only. The incremental stress-strain relationship in terms of G and K can be expressed as

$$d\sigma_{ij} = Kd\varepsilon_{KK}\delta_{ij} + 2G(d\varepsilon_{ij} - \frac{d\varepsilon_{KK}}{3}\delta_{ij}) \qquad (4.20)$$

Under plane strain and axisymmetric idealizations, the incremental stress-strain relationship is

$$
\begin{Bmatrix} d\sigma_{11} \\ d\sigma_{22} \\ d\sigma_{12} \\ d\sigma_{33} \end{Bmatrix} = \begin{bmatrix} K + \frac{4G}{3} & K - \frac{2G}{3} & 0 & K - \frac{2G}{3} \\ K - \frac{2G}{3} & K + \frac{4G}{3} & 0 & K - \frac{2G}{3} \\ 0 & 0 & 2G & 0 \\ K - \frac{2G}{3} & K - \frac{2G}{3} & 0 & K + \frac{4G}{3} \end{bmatrix} \begin{Bmatrix} d\varepsilon_{11} \\ d\varepsilon_{22} \\ d\varepsilon_{12} \\ d\varepsilon_{33} \end{Bmatrix} \quad (4.21)
$$

The fourth row and column are meaningful for axisymmetric idealization; for the plane strain conditions, the constitutive matrix is (3 x 3).

4.8.6 Determination of Material Parameters

The problem of choosing material parameters to fit the data is greatly simplified when there are tests available in which as few of the independent variable as possible are varied simultaneously. The hydrostatic test, in which the pressure and volumetric strain are measured is the best test to offer data for computing the values of K which appear in Eq. (4.11). Shear tests like simple shear test or conventional triaxial compression test where shear stress and shear strain are measured would be desirable tests from which the values of γs in the shear moduli Eq. (4.12) can be determined.

4.8.7 Details of Material Model Developed

In the combined stress-strain variable moduli model, K, the bulk modulus is expressed in terms of the first invariant of the strain tensor and the shear modulus, G, is expressed in terms of the first invariant of the stress tensor and the second invariant of the deviatoric stress tnesor. They can be expressed as

$$K = K_0 + K_1 I_1 + K_2 I_2 \quad \text{and} \tag{4.22}$$

$$G = G_0 + \gamma_1 J_1 + \gamma_2 \sqrt{J_{2D}} \tag{4.23}$$

where K_0 and G_0 are initial values of bulk and shear moduli respectively and K_1, K_2, γ_1, γ_2 are other material parameters. These parameters are determined from the stress-strain responses of the material obtained from the experimental results. The following parameters are determined.

$$K_0 = 1000.00 \text{ psi } (8268.0 \text{ KN/m}^2)$$

$$G_0 = 462.00 \text{ psi } (3183.2 \text{ KN/m}^2)$$

$$\tag{4.24}$$

$$K_1 = -1.02 \times 10^5 \text{ psi } (-6.92 \times 10^5 \text{ KN/m}^2)$$

$$K_2 = 4 \times 10^6 \text{ psi } (27.56 \times 10^6 \text{ KN/m}^2)$$

$$\gamma_1 = 60.00$$

$$\gamma_2 = -133.00 \quad (\text{psi}^{-1})$$

These material parameters when substituted in the model results

$$K = 1000 - (1.02 \times 10^5) I_1 + (4 \times 10^6) I_1^2 \quad (psi) \qquad (4.25)$$

and

$$G = 462 + 60 J_1 - 133 \sqrt{J_{2D}} \quad (psi) \qquad (4.26)$$

4.9 RESILIENT MODULUS

The resilient behavior of ballast II is shown in Fig. (4.25), namely variation of resilient modulus, E_r with the confining pressure. The resilient modulus increases with increase in confining pressure. The relationship is linear on a log-log plot. The resilient modulus, E_r, the ratio of deviator stress to the recoverable axial strain can be expressed as

$$E_r = K\sigma_3^n \qquad (4.27)$$

From the Fig. (4.25), it is seen when $\sigma_3 = 1$, $K = E_r = 1300.00$ psi (8.97×10^3 kpa). The slope of the line is 0.87. Therefore the Eq. (4.27) can be rewritten as

$$E_r = 1300 \, \sigma_3^{0.87} \quad (psi) \qquad (4.28)$$

The values of $E_{z(x)}$ and $E_{y(x)}$ are plotted against the confining pressure in Fig. (4.26). The definitions of $E_{z(x)}$ and $E_{y(x)}$ are given in section 2.7.3. It can be seen that both are varying linearly with confining pressure in log-log plot. Furthermore, they are almost parallel to each other and also nearly parallel to E_x. The slope of $E_{z(x)}$ is 1 and that of $E_{y(x)}$ is 1.12.
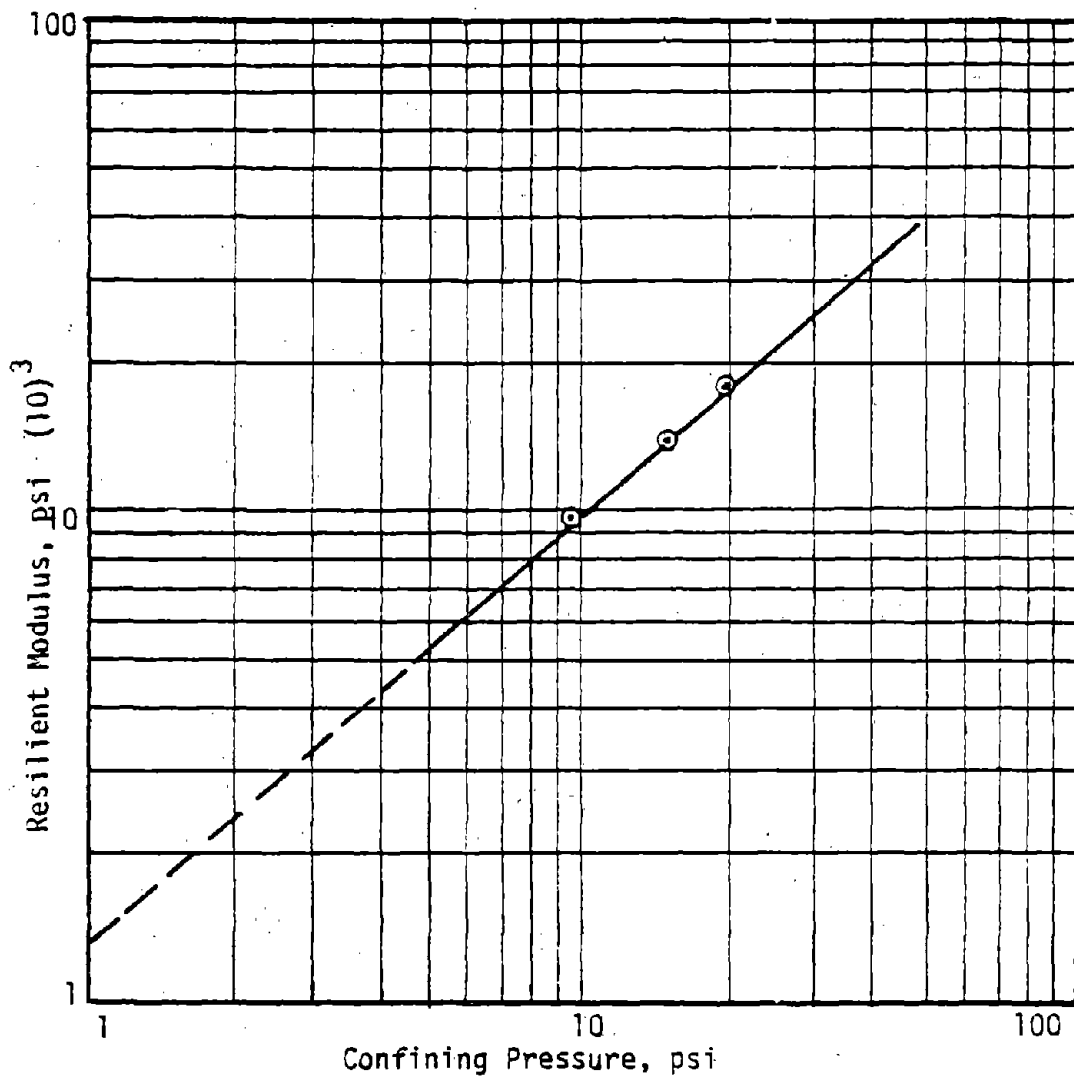
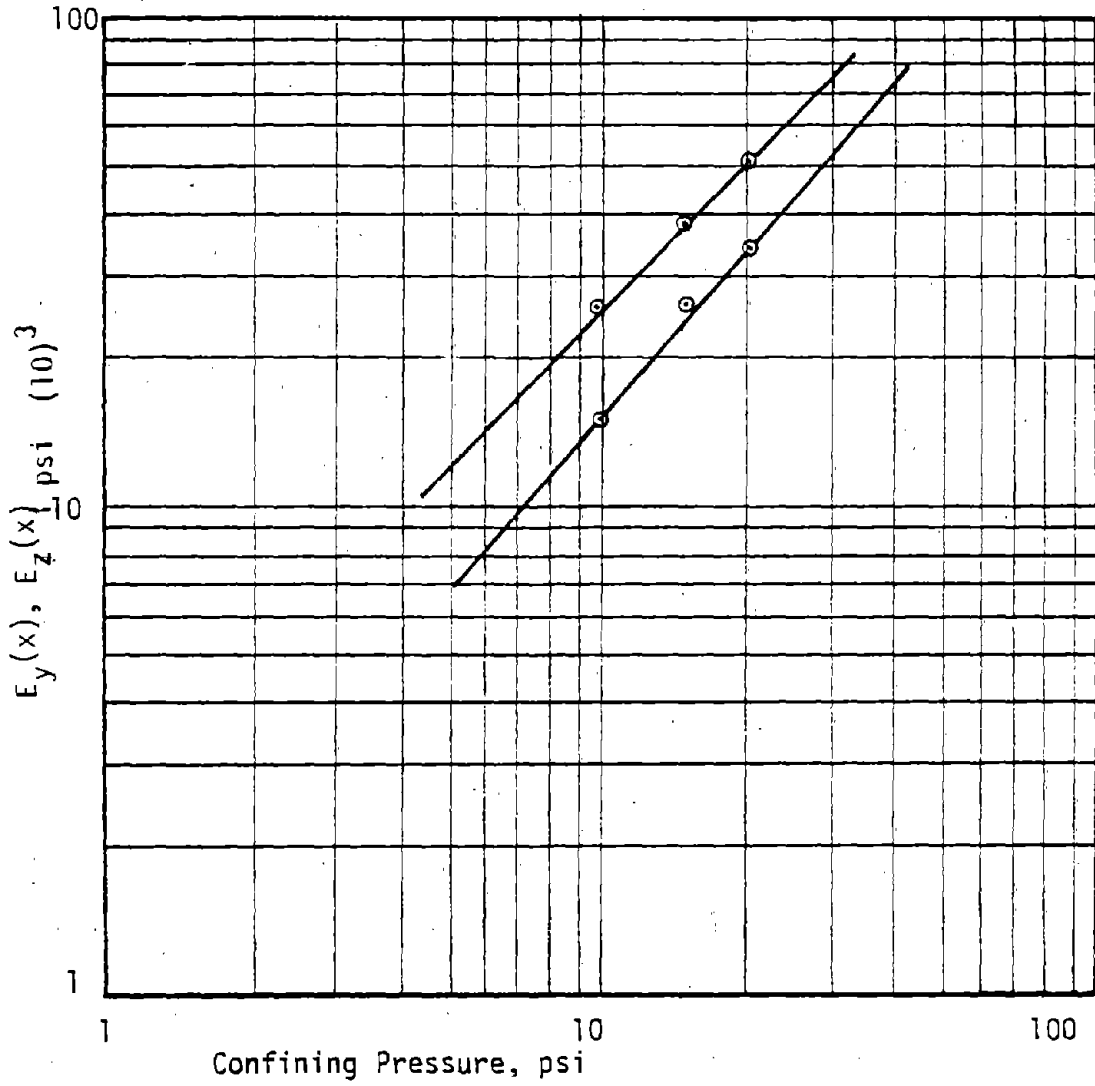Figure 4.25 Variation of Resilient Modulus with
Confining Pressure

Figure 4.26   Variation of $E_y(x)$ and $E_z(x)$ with
Confining Pressure

Chapter 5

MATERIAL MODEL FOR GRANULAR SOIL

5.1 INTRODUCTION

An engineer concerned with the design of geotechnical structures faces a variety of problems with complex boundary conditions that may change during construction, and other factors such as nonhomogeneous and nonlinear materials. The finite element method is a powerful analytical tool for such problems; however, the highly complex nature of the materials involved often limits the use of the method. The nonlinear nature of soil is an important property that makes its behavior difficult to formulate. But in recent years, many investigators have made efforts to develop more realistic mathematical models for soils, some of which will be referred to in this study.

5.2 PROBLEM STATEMENT

Highly idealized, simple linearly elastic stress-strain models or piecewise linear models, have been sometimes used to analyse soil behavior. However, the importance of use of realistic and proper constitutive laws has been felt for a meaningful numerical analysis. A general description and philosophy of various constitutive models and the methods of determination of constitutive parameters is available in Ref. 17. The objective of this research is to develop a methodology for the realistic prediction of the field and laboratory behavior of soils under quasi-static loads.

The response of a mass of granular material subjected to a load depends on the properties of the individual constituents and the arrangement and interaction of the particles as well as the nature of loading. The particulate nature of the soil and its multiphase nature makes it difficult to model its behavior in a general fashion. Hence certain assumptions have to be made regarding the material itself and the loading conditions. The present study does not include the effect of factors such as the speed of loading or long-term effects. Therefore, creep and other time-dependent behavior are not considered.

In this study, the remolded samples of the silty sand from the subgrade of the UMTA section, TTC, Peublo, Colorado [39] a water content of 9% which is the optimum moisture content is considered. Since at low degrees of saturation, the development of excess pore pressure is prevented, it is assumed that all tests conducted herein are fully drained and the stresses referred to in this section are effective stresses unless stated otherwise.

5.3.1 REVIEW OF PAST WORK

The term "failure" has been used in a broad sense in the literature on behavior of soils. It has been used to represent the beginning of inelastic state or to define the actual rupture of the material. Numerous failure criteria have been introduced by different investigators in the past to model the behavior of soil or to investigate the strength characteristics of soil under

different stress and/or strain conditions. Therefore, failure can be defined in general, as a point on the stress path where the corresponding stress, load, strain, displacement or a combination of these has passed a certain prescribed limiting value.

The criterion of a critical slope of the stress-strain curve has been used as a criterion for defining failure by some investigators. According to such a definition, failure is reached when the slope of the stress-strain curve has decreased to a limiting value. For instance, failure can be defined as the stress level on the stress-strain curve where there is an abrupt increase in deformation rate.

Some investigators have used the size of the maximum strains developed in the soil to indicate the strain of failure. Such a criterion may be a good solution for soil where limited amounts of deformation can be tolerated. A definition of failure more widely used is based on the stress level in the soil. In this definition, it is assumed that the soil fails when the stress level or certain combinations of the stresses reaches a limiting value. The main shortcoming of the stress limit failure criterion is the size of the strains at failure which depends not only on the stress level, but on the initial conditions of the soil and the confining pressure as well. In some of the classical failure criteria, such as the Mohr-Coulomb and Drucker-Prager, failure is based on the peak stress level. The definition of failure that will be adopted in this study is the critical condition for the soil is explained below.

5.3.2 Critical State Condition

In the course of shearing of a soil, the strains start to increase and the stresses reach the critical state at ultimate conditions. On such grounds, in 1936 Hvorslev [40] defined a critical condition to designate the failure of the soil. According to his definition, the critical condition is reached when a continued flow does not cause further changes in the shearing resistance and the void ratio. Later Roscoe [60] adopted similar concepts in critical state soil mechanics. The critical state has been defined as a condition that a specimen of soil undergoing shear stresses will reach under which further increments of shear stress will not affect the void ratio. Historical development of critical state concept can be found in several publications by Roscoe, Schofield and Wroth [60,63].

Four basic assumptions are made in the critical state theory: (1) The soil material is continuously disturbed over its whole volume, it is homogeneous and isotropic (2) The mechanical behavior of soil material depends only on effective stresses. The presence or absence of pore water pressure or moisture tensions has no effect except in so far as they alter the effective stresses. (3) The mechanical behavior of soil can be described by a macroscopic model. It is not necessary to relate behavior to the properties of an interaction between individual particles, and (4) There are no time dependent aspects of mechanical behavior and the soil is not viscous.

The assumption of isotropy immediately reduces the problem to one of relating three principal strains to three principal stresses. Further, simplification can be made by assuming the yield surfaces to be symmetrical about the space diagonal. For example, if the symmetrical cone of extended von Mises criterion is assumed, the stress system can be reduced in terms of only two variables, namely p (spherical pressure) and q (deviatoric stress). The corresponding straind are volumetric and distortion strains. These two strains have one important distinction in a plastic material volumetric strain is strictly limited in magnitude, whereas distortion strain is unlimited.

It can be difficult to develop a general relationship between four variables. Roscoe et al [60,63] have reduced the problem to a relationship between p,q and V(e). They have done this by relating distortion strain to volumetric strain by means of the normality principle of the theory of plasticity.

The experimental investigation carried out by Roscoe and his co-workers had been with a conventional cylindrical triaxial apparatus. With p as the mean pressure, q related to shear stress, $d\epsilon_v$ the incremental volumetric strain and $d\gamma$ the incremental shear strains, for axisymmetric triaxial conditions, these quantities can be defined as follows.

$$p = \frac{\sigma_1 + 2\sigma_3}{3} = \frac{J_1}{3} \tag{5.1}$$

$$q = (\sigma_1 - \sigma_3) = 3 J_{2D}^{1/2} \tag{5.2}$$

$$d\epsilon_v = (d\epsilon_1 + 2d\epsilon_3) \qquad (5.3)$$

and

$$d\gamma = \frac{2}{3}(d\epsilon_1 - d\epsilon_3) \qquad (5.4)$$

In a three-dimensional space with the coordinates being the mean pressure p, the shear stress q, and the void ratio e, Roscoe found that the critical states form a curve, Fig. (5.1), whose projections on the two planes e = 0 and q = 0 are given by the equation, Fig. (5.2)

$$q = M.p \qquad (5.5)$$

$$e - e_0 - \lambda \ln\left(\frac{p}{p_0}\right) \qquad (5.6)$$

respectively. λ and M are two soil constants, and e_0 is the void ratio at p = 1. Then

$$e = e_0 - \lambda \ln p \qquad (5.7)$$

Similarly, the swelling line can be described by

$$e = e_0 - \kappa \ln \frac{p}{p_0} \qquad (5.8)$$

These two parameters, λ and k, are basic soil constants used in the critical state theory.

This concept of critical state soil mechanics has led to the development of the Cam Clay model [60] for soft clays and eventually, to the modified Cam Clay model in 1968 [63]. A brief description of the basic principles of this model are given here.

The State Boundary Surface

When stress paths for triaxial compression tests on normally consolidated samples of remolded clay are plotted in p-q-e space, they fall on or within a unique surface called the "state boundary surface". The states in which the soil can exist in static equilibrium are inside the boundary surface. When the state of soil is beneath the state boundary surface, it is in the elastic state and when stress path reaches the boundary surface, yielding will occur which will result in elastic-plastic strains. So the intersection of the elastic wall, Fig. (5.1), and the state boundary surface is considered as a yield locus. These are illustrated in Fig. (5.2) which shows the intersection of the state boundary surface and the q = 0 plane. The curve VCL in this figure is the isotropic compression line given by

$$e = e_0 - \lambda \ln \left(\frac{p}{p_0}\right) \tag{5.9}$$

and the other curve is the critical state line.

Critical State Line (CSL)

Under free conditions of drainage, the loading of a saturated soil sample, is usually associated with some volume changes as well as distortions. It passes through progressive states of yielding before reaching a state of collapse. The yielding continues to occur until the material reaches a critical state, after which the void ratio remains constant during the subsequent deformation.
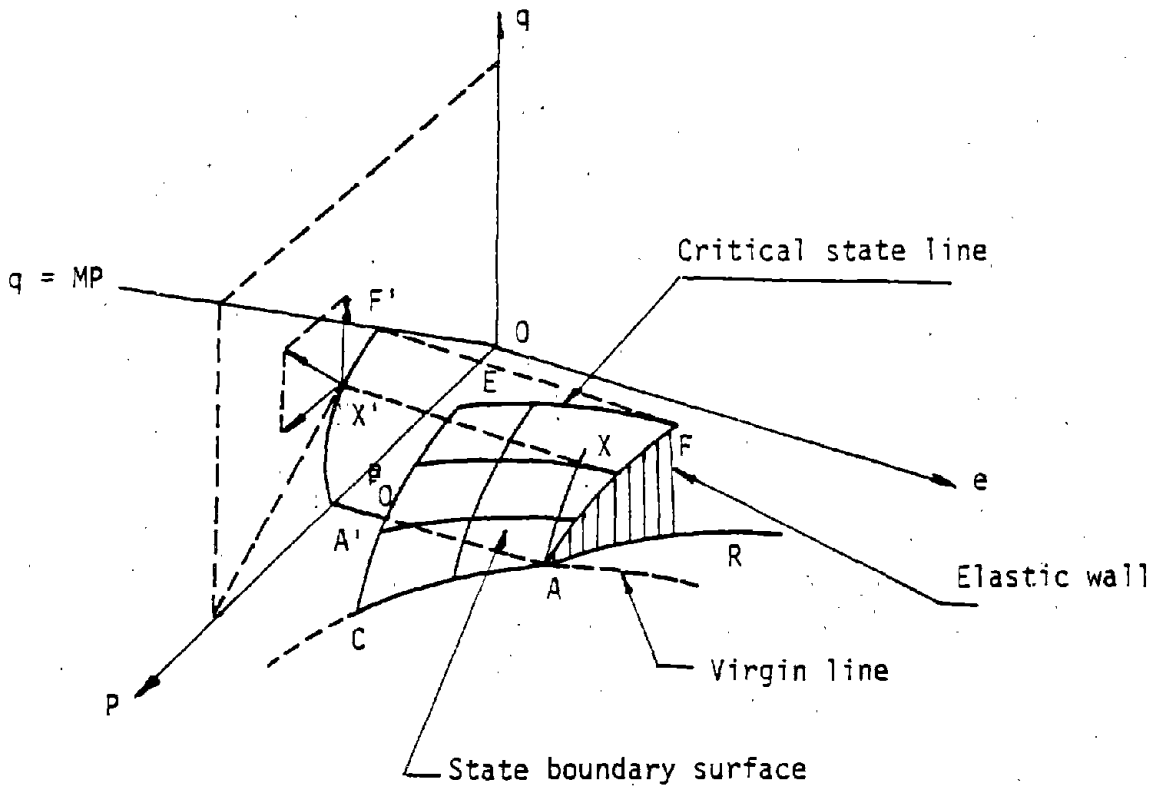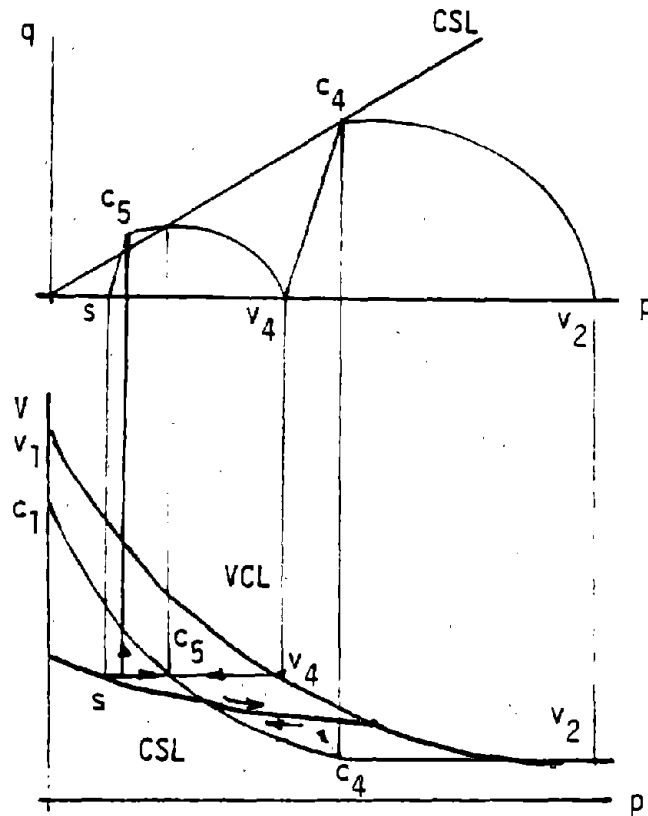
Figure 5.1   State Boundary Surface

Figure 5.2   Projections of Loading paths of Fig. 5.1 on
to (a) the p-q plane and (b) the p-V plane.

In other words, the material has attained the critical void ratio and the arrangement of the particles is such that no volume change takes place during shearing. This can be considered as the ultimate state of the material. The locus of the ultimate states has been observed to be a straight line on p-q space and this line is called the critical state line. The slope of this line on the p-q plot is denoted by M and it is a material parameter. The distortions that the soil undergoes may be partly recoverable and partly permanent. The plastic stress-strain behavior of soil can be seen from the e - lnp curve, Fig. (5.3).

A normally consolidated material, upon loading will follow the virgin curve AB. When the load on the sample is reduced, the un-loading path does not follow the loading path (virgin curve) because of its elastic-plastic nature. As the recovery of strain is not total, the material follows path BD upon unloading. When the material is reloaded, it follows the same path upto B and then the path BC, which is the extension of the virgin curve AB. The slope of the loading path is defined as λ, and the slope of the unloading path as k. The vertical intercept AD is the plastic component of volumetric strain and DD' the elastic component.

The strain tensor can be decomposed as

$$d\varepsilon_{ij} = d\varepsilon^e_{ij} + d\varepsilon^p_{ij} \tag{5.10}$$

where $d\varepsilon^e_{ij}$ and $d\varepsilon^p_{ij}$ are the elastic and plastic strain tensors, respectively. In the stress-strain theory based on the critical
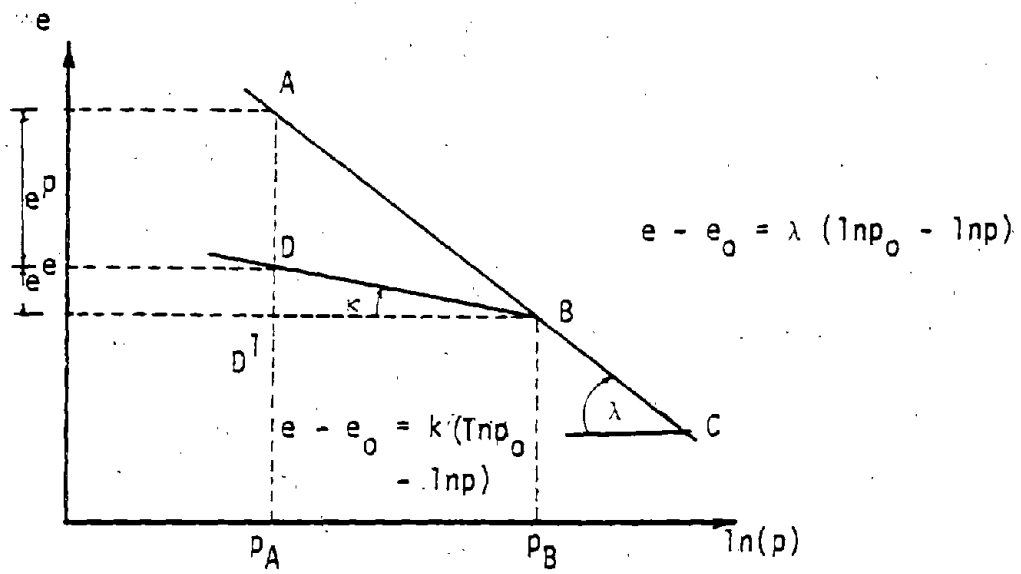
Figure 5.3   Void Ratio - ln(p) relationship for the
             Critical State model

state concept, it is assumed that at critical state there is no recoverable energy associated with shear distortions; therefore, $d\varepsilon^e_{ij} = 0$ and so $d\varepsilon_{ij} = d\varepsilon^p_{ij}$.

Within the three-dimensional space of p,q,e, there are two different types of behavior possible. These two regions are separated by the vertical wall beneath the critical state known as critical state wall, Fig. (5.4). On the side of this wall remote from the origin the material is initially relatively loose and under sufficient loading will compress and become stronger, that is, it must be treated as work hardening material. The strains will be uniformly distributed throughout the mass and calculations of deformations are therefore possible. This state is called wet because as the volume decreases the proportion of the pore space filled with water increases and the soil will appear wetter. On the origin side of the wall, the material is relatively dense and under sufficient loading will fail in a brittle manner and become weaker. It will dilate but the dialation only occurs on their failure planes, the rest of the soil tending to move as solid blocks. Under these circumstances, calculations of overall deformation are not possible.

In the p-q-e space, the yield locus for a particular specific volume is a curve running from the value of p_u at the critical state line down to p on the p axis. Any combination of stresses inside this curve does not cause yielding. If the loading path goes outside this curve then the material yields, its specific volume changes and a new yield locus is formed.
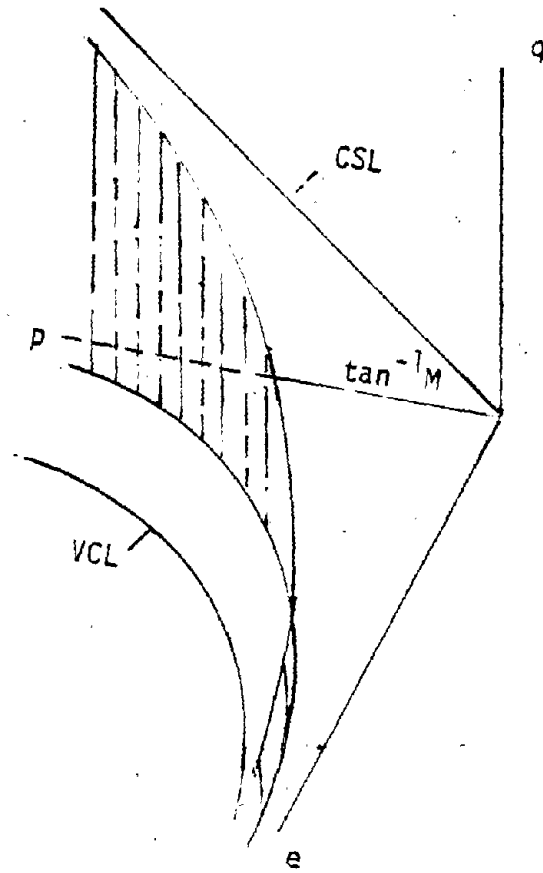
Figure 5.4   The Critical State Wall

In the early works of Drucker, Gibson and Henkel [30] the yield surfaces suggested are a family of expanding hemispheres. The cambridge group initially suggested that the yield surfaces be more nearly a family of bullet shaped curves; this shape was found to be inconsistent, particularly at its intersection with the p-axis.

An elliptical shape, mathematically a convenient curve, has been suggested subsequently and it has also been shown to fit certain soils. The successive elliptical yield surfaces lie with their major axis extending from virgin consolidation line to the specific volume axis and the minor diameter extending from the p_o-e plane to the critical state line.

The process of plastic yielding with decreasing specific volume is shown in Fig. (5.2). The elliptical yielding surface can be defined by an equation [63]:

$$\frac{q^2}{(Mp_u)^2} + \frac{(p-p_u)^2}{p_u^2} = 1 \qquad (5.11)$$

where p_u is the spherical pressure of state on the CSL and is the function of the specific volume V as

$$p_u = \exp\left(\frac{c_1-V}{\lambda}\right) \qquad (5.12)$$

where C_1 is specific volume at unit pressure on the CSL.

From the e-lnp relationship, Fig. (5.3), the plastic volumetric strains, $d\epsilon_v^p$ can be evaluated as

$$d\epsilon_v^p = \frac{(\lambda - \kappa)}{1 + e_0} \frac{dp_0}{p_0} \tag{5.13}$$

The incremental plastic strain vector will be normal to the yield surface at any point and can be written as

$$\frac{d\gamma^p}{d\epsilon_v^p} = -\frac{dp}{dq} \tag{5.14}$$

The values of shear and volumetric plastic strains can be derived in terms of p, q, and M from the energy considerations [63]. They are

$$d\epsilon_v^p = -\left[\frac{\lambda - \kappa}{Mp} (dq - \eta dp) + \frac{\lambda}{p} dp\right] \tag{5.15}$$

and

$$d\gamma^p = \frac{\lambda - k}{Mp(1+e)} \left(\frac{dq}{M - \eta} + dp\right) \tag{5.16}$$

Here η is the slope of the stress path line.

The left-hand-side of the normality equation can now be expressed in terms of p and q. Then this equation can be integrated to obtain the yield function. The yield function so obtained for the modified Cam Clay model is

$$F = q^2 - M^2 p_0 p - M^2 p^2 = 0 \tag{5.17}$$

5.4 TESTING PROGRAM

5.4.1 Description of Material Tested

The material used in this study is a granular material obtained from UMTA test section at Pueblo, Colorado. The grain size distribution of the material is shown in Fig. (5.5). It is a well graded material with an uniformity coefficient of 3.2. Its specific gravity is 2.59. The dry material brought from the site is tested for its optimum moisture content (OMC). The Procter compaction test results, namely the maximum dry density and the optimum moisture content are determined and plotted in Fig. (5.6). The maximum wet density of the material is 2.23 g/cm^3 for an optimum moisture content of 9%. It is worth mentioning here that the wet density of undisturbed soil sample reported by KO [43] is 2.23 g/cm^3; the same density is obtained in the remolded state, but at OMC.

5.4.2 Sample Preparation

The soil sample is prepared in a 4.00 inch (10.16 cm) cube mold Fig. (5.7). The procedure is very similar to that explained in section 2.5.3 in this study. A known amount of dry soil is mixed with water to obtain a water content of 9%; that is, OMC. This wet soil is filled into the mold in three layers. Each layer is tamped 20 times by a tamping mechanism where a falling weight of 1.00 lb (453 g) has a free fall of 6 inches (15 cm). This compaction procedure is established by trial and error to obtain an initial compaction density of 2.04 g/cm^3. The density of test samples,
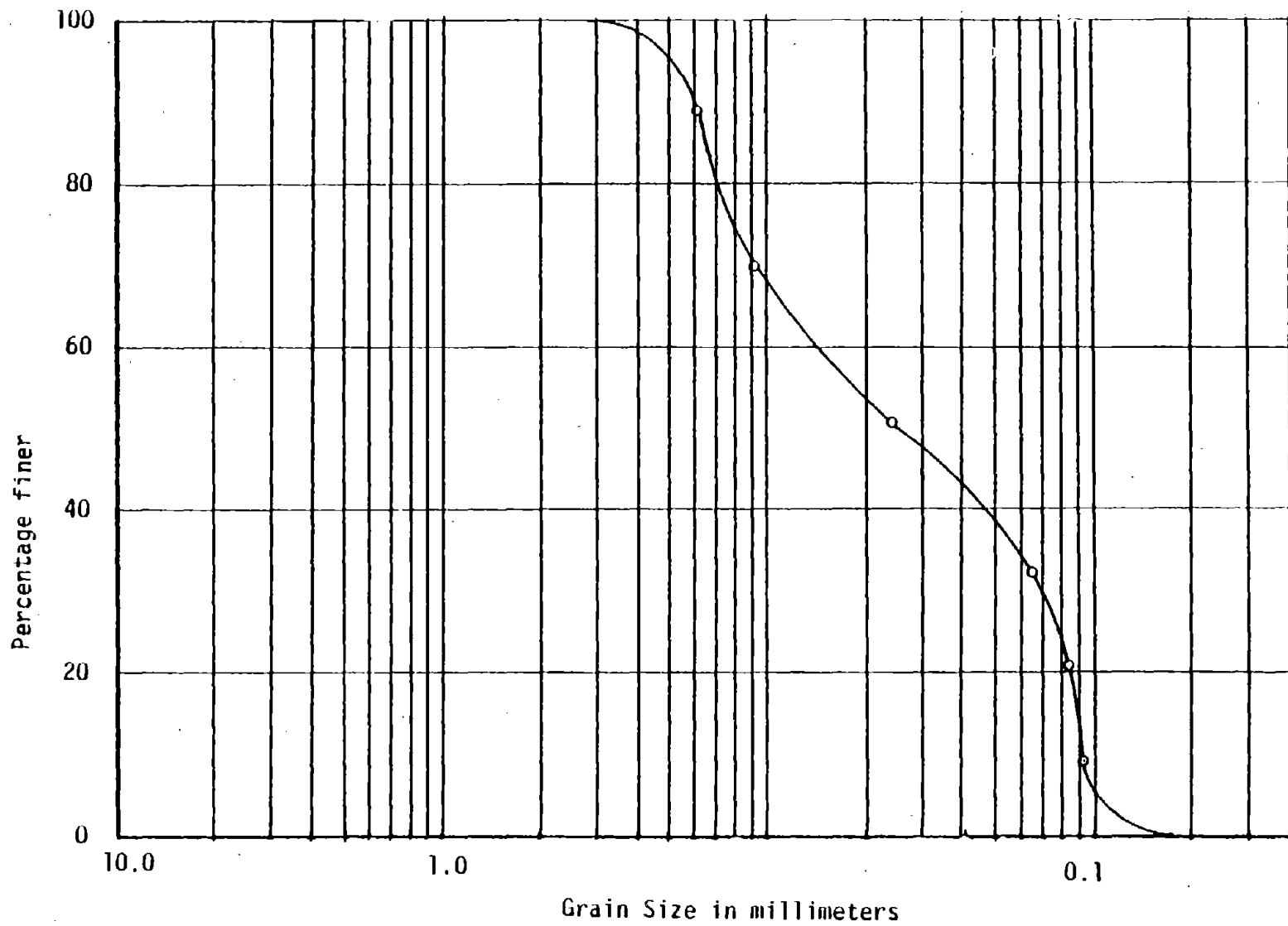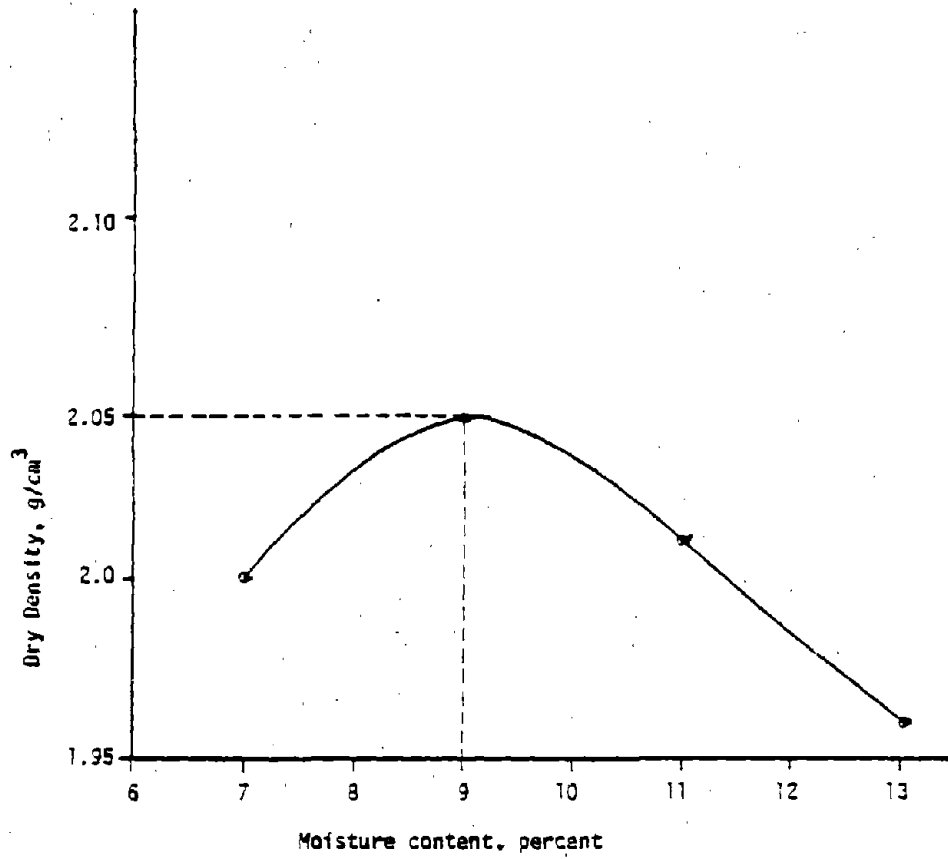
Figure 5.5 Grain Size Distribution Curve For Pueblo Soil

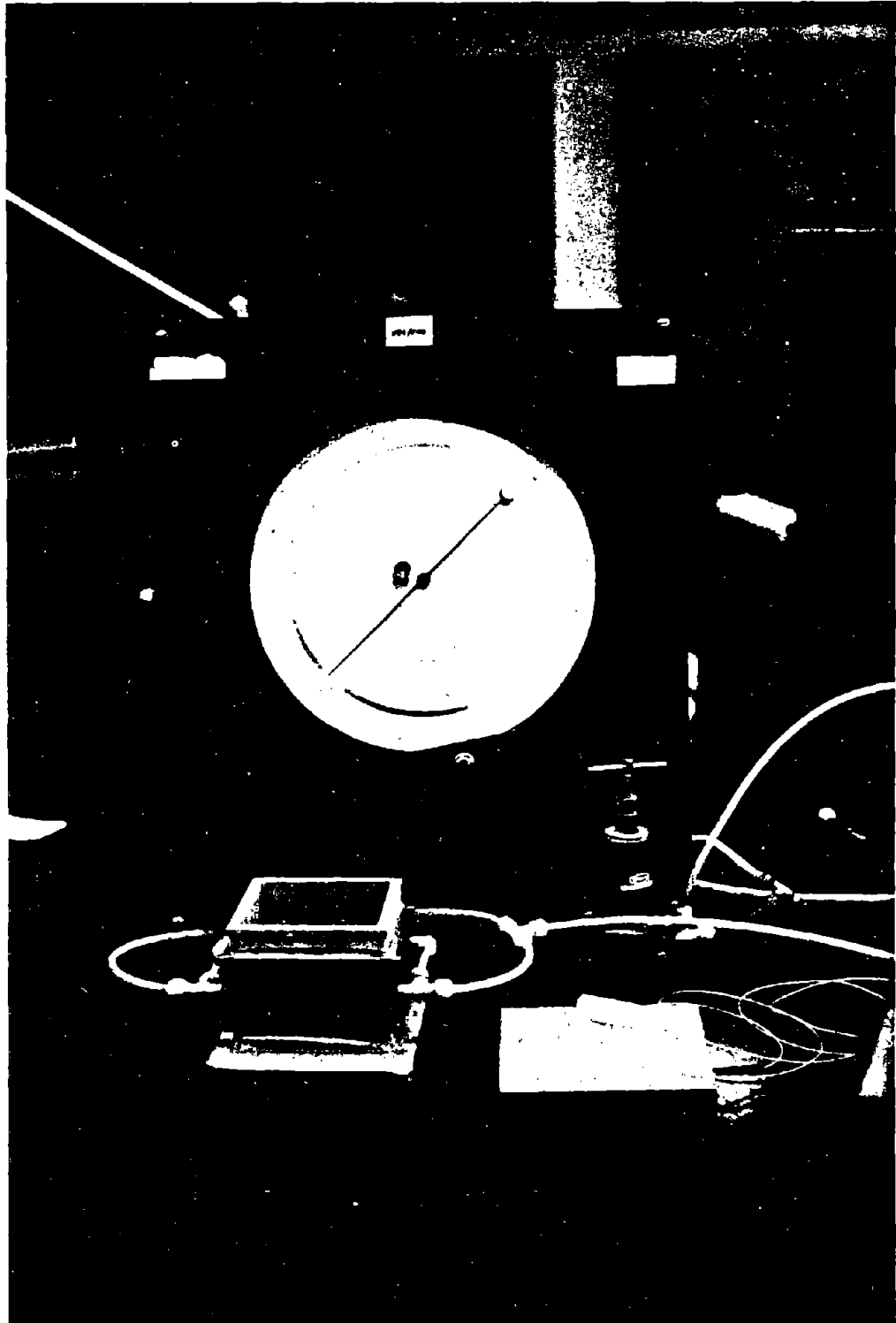Figure 5.6 Moisture Content - Density Relationship

Figure 5.7   Sample Mold - With Vacuum Fixtures

however, varied from 1.86 g/cm^3 to 2.08 g/cm^3 with an average value of 1.99 g/cm^3.

After levelling off the sample in the mold, the top cover plate is placed over the mold with the dental dam sheath glued on it. Now the external vacuum is released. A vacuum commensurate with the initial confining pressure is applied and any leaks in the sample are sealed; specimens have been prepared by using as little as 1.00 psi (6.9 kap) vacuum confinement. Finally, the mold is carefully removed and excess sheath material is trimmed away. The sample is loaded in the truly triaxial device in the same manner as the subballast samples, Chap. 2.

5.4.3 Testing Equipment

The multiaxial testing device used in this investigation is explained in detail in section 2.5.2; equipment preparation before testing is explained in section 2.5.4.

5.4.4 Test Details and Results

Various stress paths and their abbreviations used in the testing program are shown in Fig. (2.7). These include Hydrostatic or Isotropic Compression (HC), Conventional Triaxial Compression (CTC), Conventional Triaxial Extension (CTE), Reduced Triaxial Compression (RTC), Reduced Triaxial Extension (RTE), Triaxial Compression (TC), Triaxial Extension (TE) and Simple Shear (SS) stress paths. Siriwardane [67] performed and assisted in a part of the tests conducted on the subgrade material from the UMTA site, TTC, Peublo, Colorado.

In addition for comparison of material behavior in the undisturbed and remolded states, the stress path followed by Ko [43] in testing undisturbed samples is followed in testing the remolded specimens here; the details of the stress path are shown in Fig. (5.17). The water content of undisturbed sample is 9.4% and its density is 2.23 g/cm^3.

5.4.5 Hydrostatic Compression (HC)

Figure (5.8) presents hydrostatic compression curves for the soil used in this study. The initial confining pressure is 3.00 psi (20.70 kpa). The initial density of the material is 1.86 g/cm^3. The sample is loaded upto 25.00 psi (1.74 x 10^2 kpa) in hydrostatic compression in increments of 5.00 psi (34.8 kpa) and unloaded. Each increment is given only after the deformation is stabilized at that level. The reloading is continued up to 50.00 psi (3.48 x 10^2 kpa), and then unloaded. Again it is loaded up to 75.00 psi (5.22 x 10^2 kpa) three times that of the maximum expected pressure on the soil due to the track load.

From the Fig. (5.8) it is seen that the normal strains in the z direction are lower than the normal strains in the other two directions. This may be due to the fact that the sample is compacted in the z direction during sample preparation. The mean pressure and volumetric strain relationship from this test is shown in Fig. (5.9). It is evident from the trend of the loading curve, which tends to bend upward as the mean pressure increases, that the material is hardening with an increase of pressure.
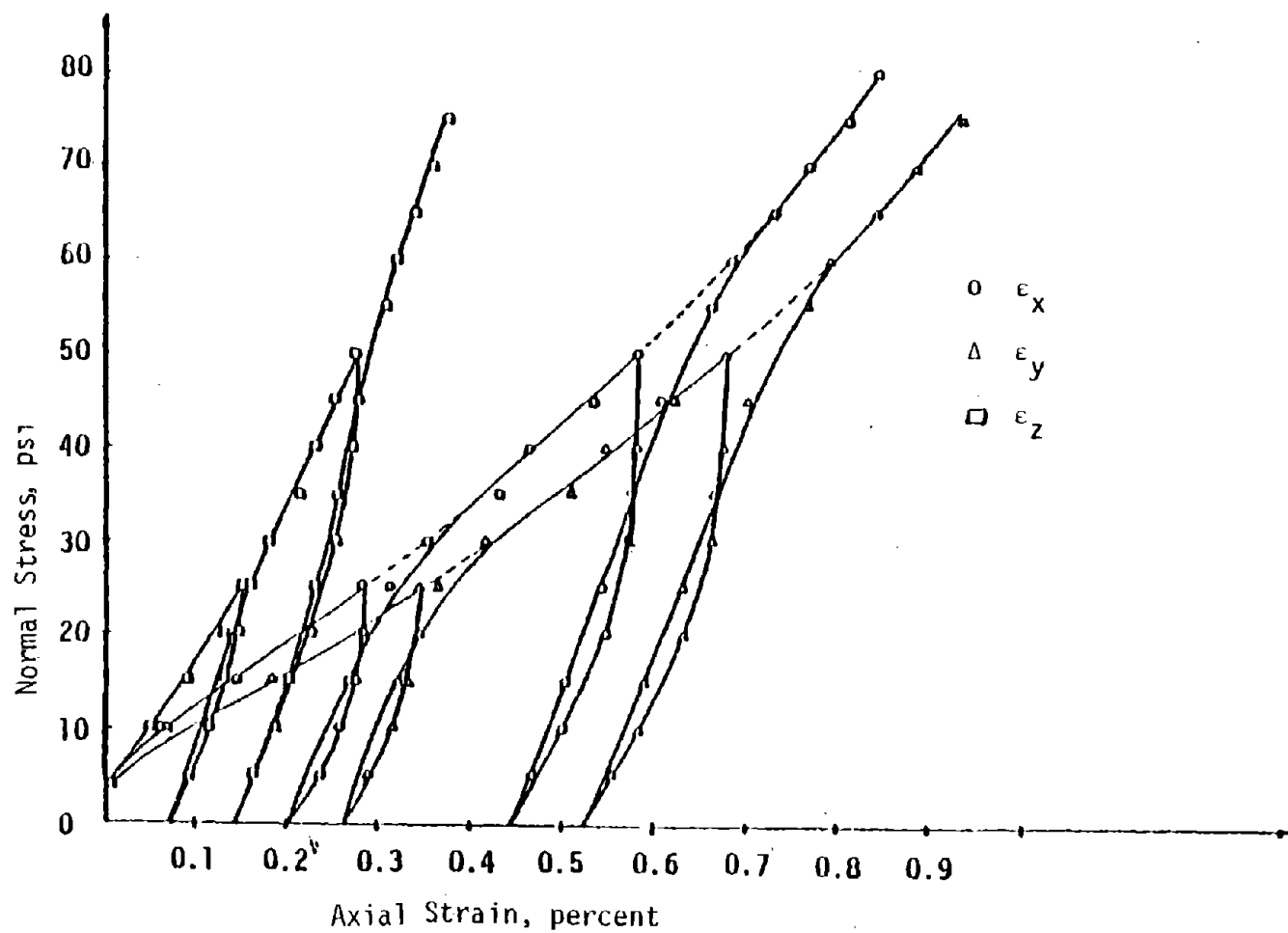
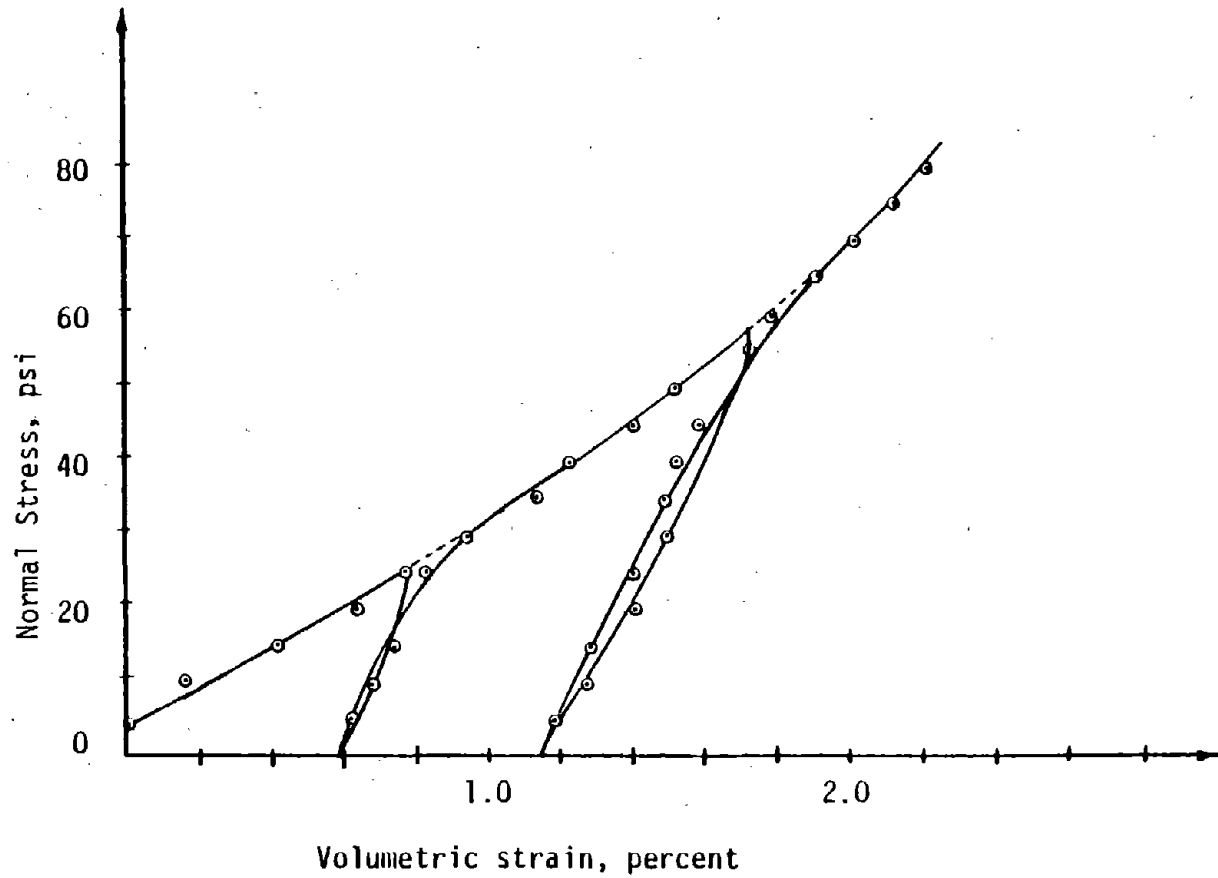Figure 5.8   Stress-Strain Response Curves for Hydrostatic Compression Test

Figure 5.9   Mean Pressure - Volumetric Strain Response for Hydrostatic
Compression Test

5.4.6 Conventional Triaxial Compression (CTC)

Results from CTC tests on the soil are shown in Figs. (5.10) and (5.11). By keeping σ_2 and σ_3 the same and constant, σ_1 is increased in this test. Tests are conducted on samples with different confining pressures 10.00 and 20.00 psi (69.00 and 138.00 kpa). The sample is initially loaded to a hydrostatic (isotropic) pressure equal to the desired confining pressure and then the CTC stress path is followed.

The normal (lateral) strains in the y and x directions are essentially the same at the stress level considered. The steep unloading and reloading curves show that shear deformations are primarily plastic. The unloading-reloading cycles reveal that hysteresis seems to increase with increasing stresses. It is noted from the figures that the compressive strains show a net increase over an unloading/reloading cycle, while extension strains exhibit a net decrease.

Failure is well defined in these tests by a large increase in strain; the ultimate strength reaches at a strain of about 9% or higher.

5.4.7 Reduced Triaxial Compression (RTC)

The stress-strain curve for an RTC test on the soil specimen with σ_{oct} = 20.00 psi (138.00 kpa) is shown in Fig. (5.12). The initial density of the sample is 2.01 g/cm^3. Here σ_1 is held constant and the minor and intermediate principal stresses, in other words the confining pressures are decreased in equal amounts.
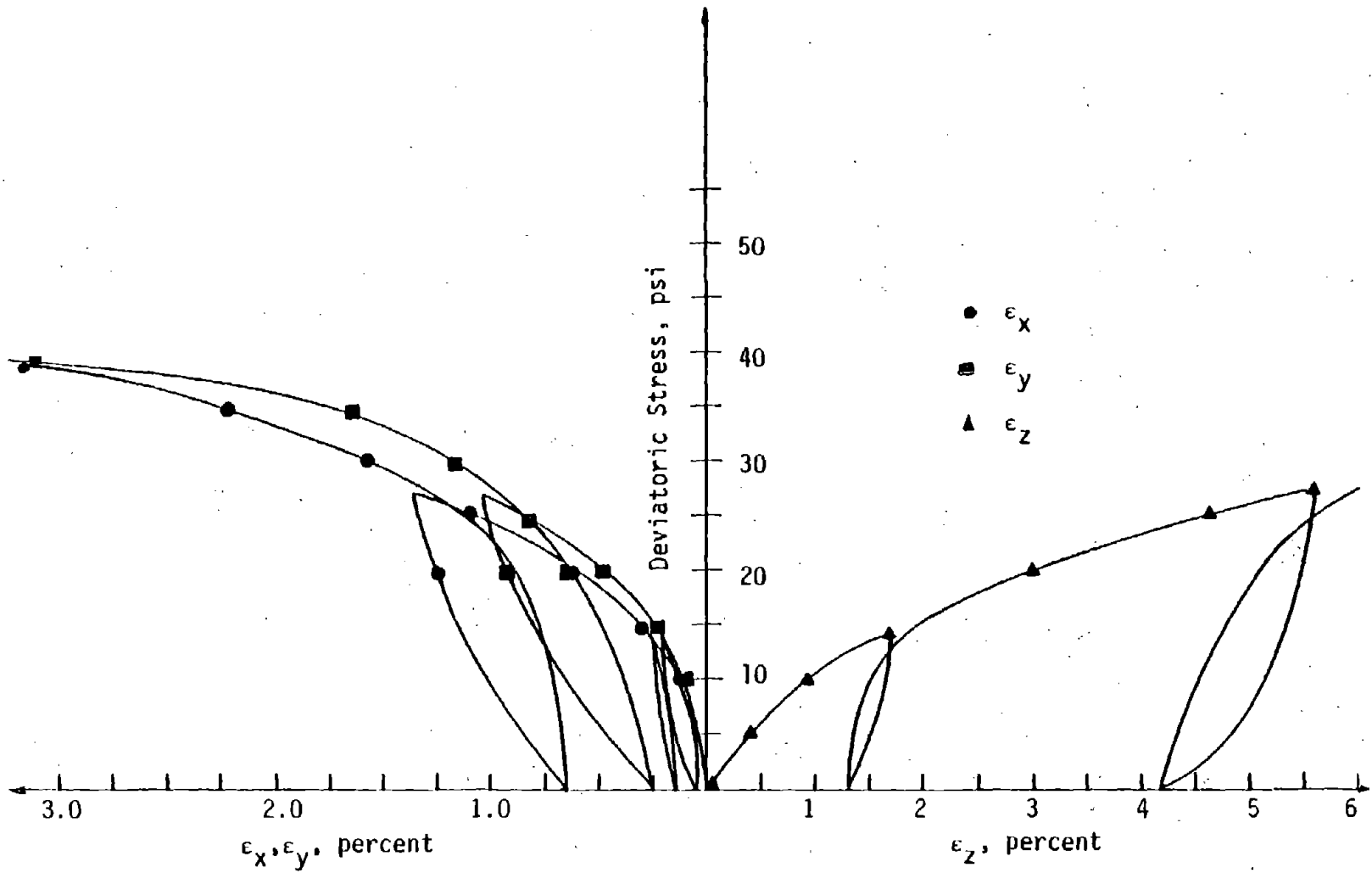
Figure 5.10 Stress-Strain Response Curves for Conventional Triaxial Compression
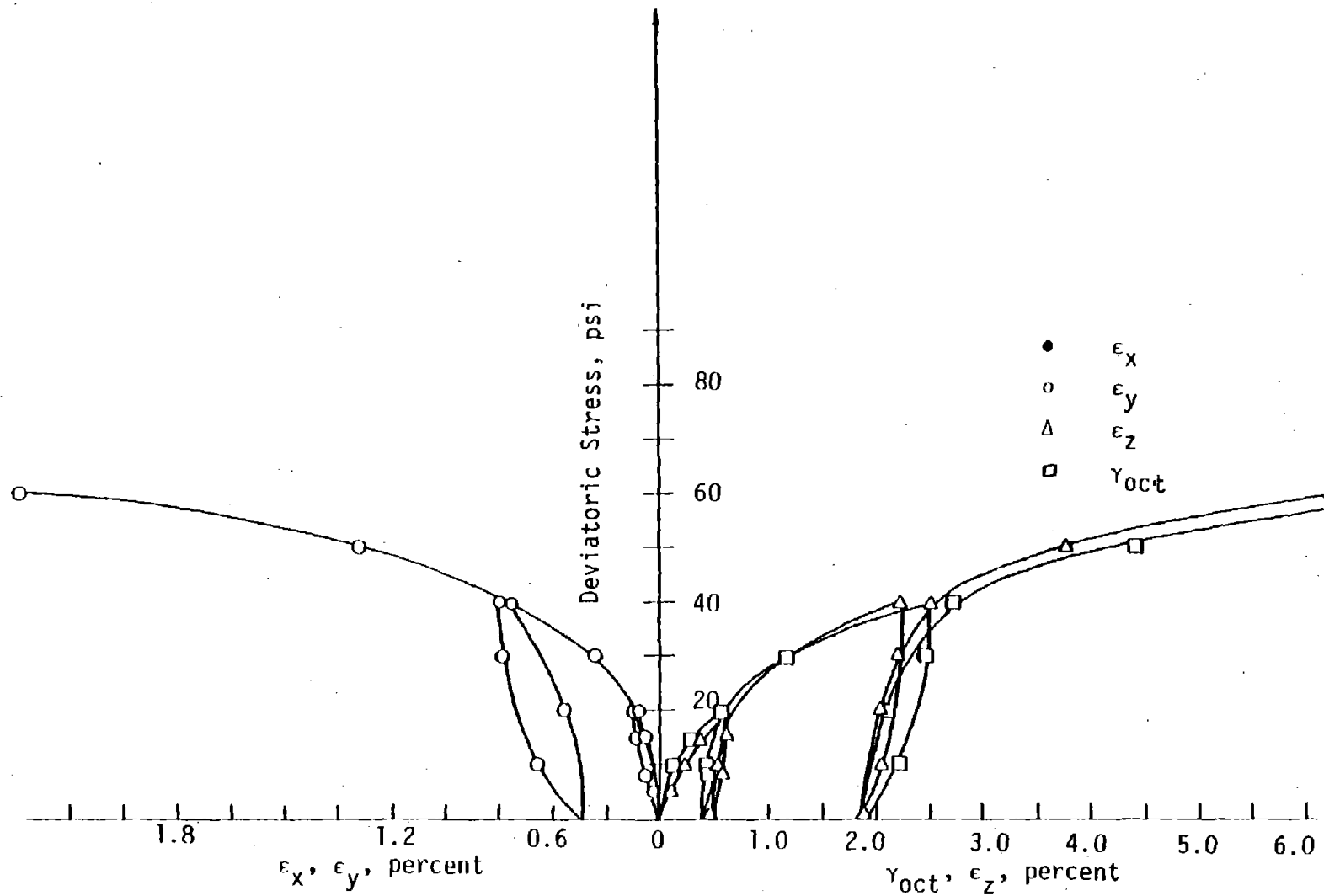Test (σ_2 = 10.00 psi)

Figure 5.11 Stress-Strain Response Curves for Conventional Triaxial Compression Test ($\sigma_2 = 20.00$ psi)
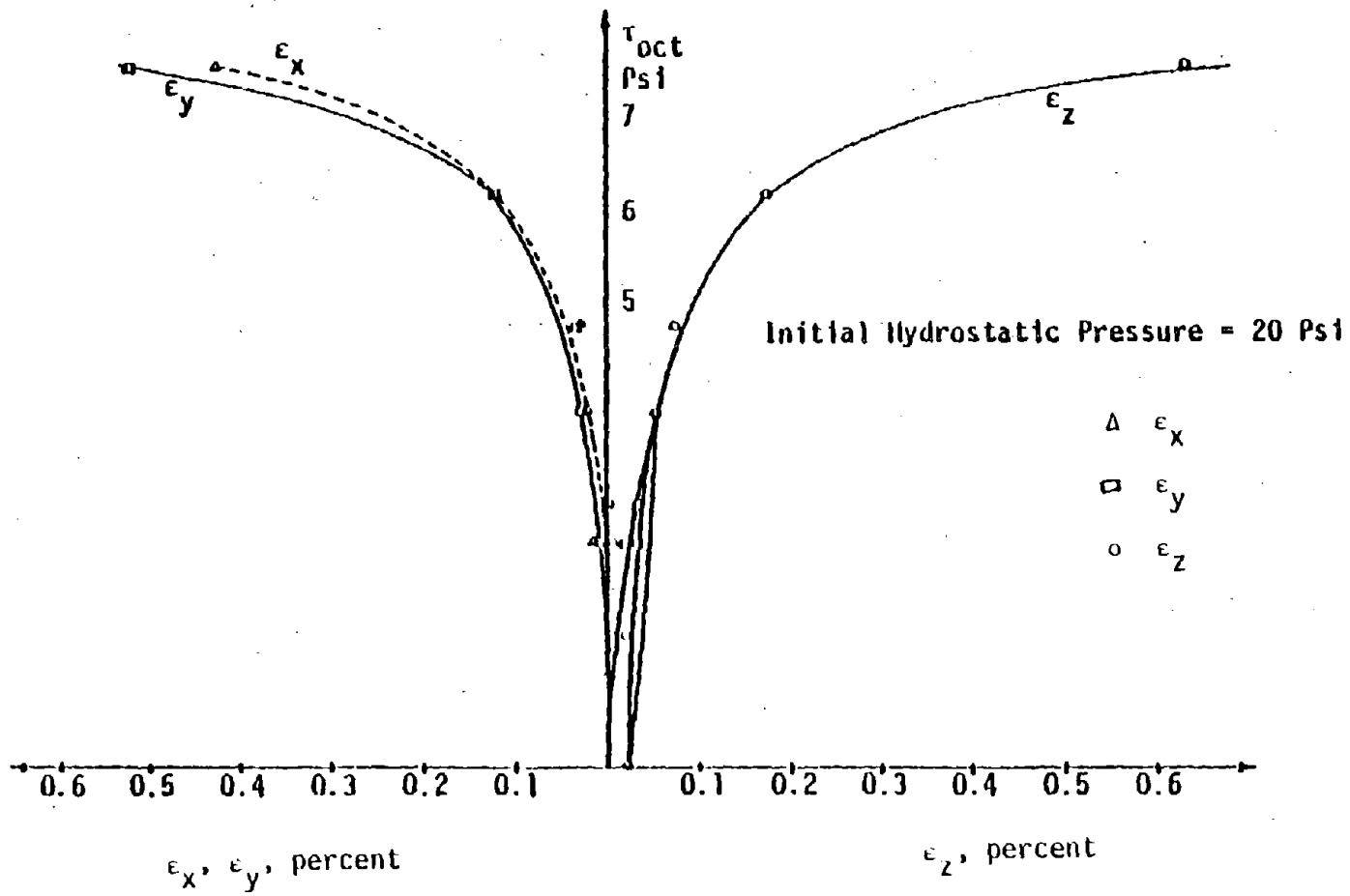
Figure 5.12   Stress-Strain Response Curves for Reduced Triaxial Compression Test

The failure is clearly defined for this stress path. But this well defined ultimate state occurs at relatively small values of strains.

5.4.8 Simple Shear (SS)

The stress-strain curves for SS tests with σ_{oct} = 20.00 psi (138.00 kpa) is shown in Fig. (5.13). The test is conducted by increasing σ_1 and decreasing σ_3 by the same amount from an initial hydrostatic state of stress while σ_2 is held constant. The normal strains in the intermediate principal stress direction is very low about 1.00 percent even at ultimate stress. The normal strain ε_z at the ultimate conditions is about 7.00 percent, while the lateral strains are about 6.00 percent.

5.4.9 Triaxial Compression (TC)

The stress-strain curves for TC tests with σ_{oct} = 25.00 psi (175.85 kpa) is shown in Fig. (5.14). The TC test is conducted by increasing σ_1 and decreasing both σ_2 and σ_3 by equal amounts such that the value of σ_{oct} remains constant. The sample is initially loaded to a hydrostatic pressure of the desired value of σ_{oct}, and and then TC path is followed. The initial density of the sample is 2.03 g/cm^3. The normal strains ε_z at failure (ultimate condition) is about 8.00 percent. The ultimate state is well-defined in these tests.

5.4.10 Triaxial Extension (TE)

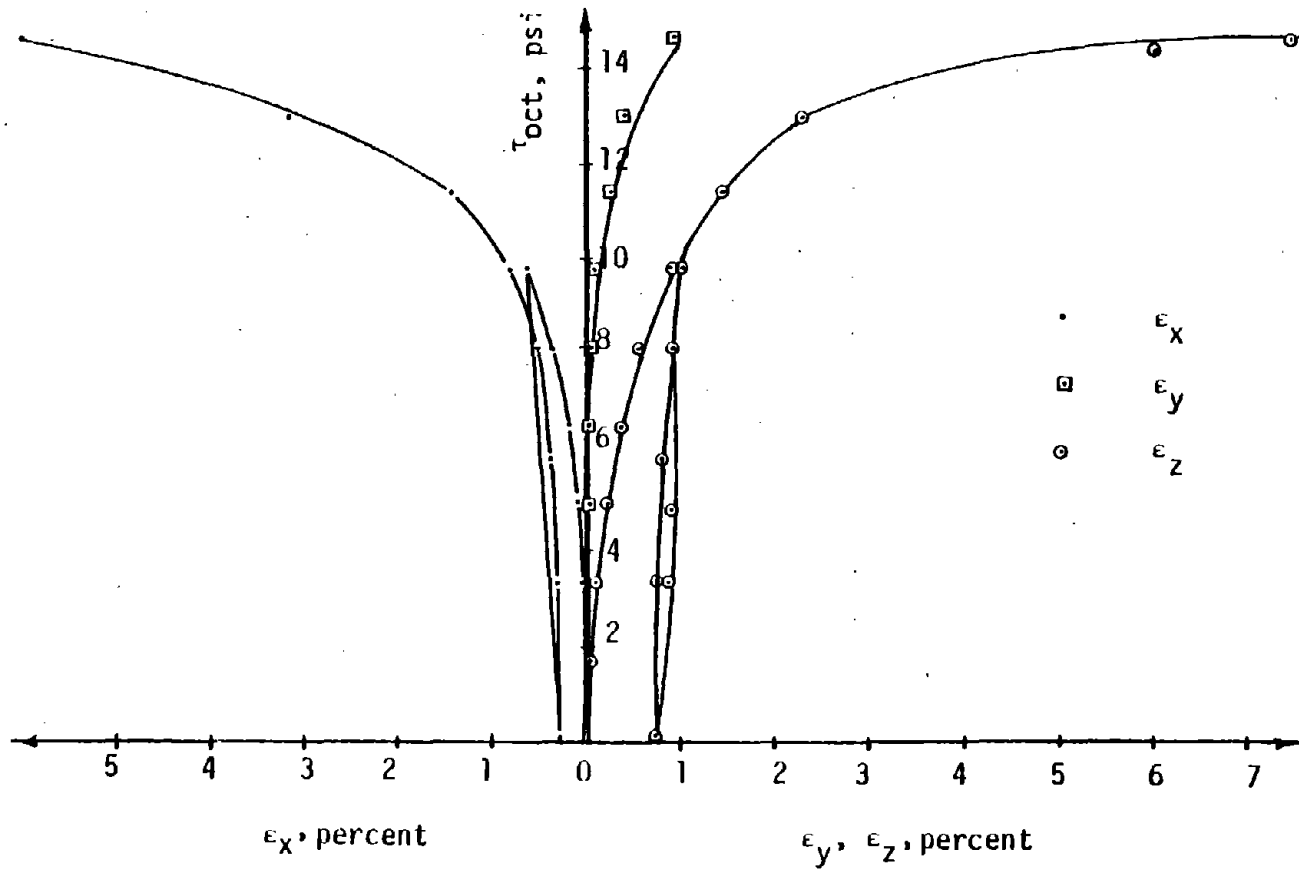In TE test, σ_3 and σ_2 are increased while σ_1 is reduced to

Figure 5.13 Stress-Strain Response Curves for Simple Shear Test

245

T_{oct}
Psi

● ϵ_z

▲ ϵ_x

◪ ϵ_y

20

Initial Hydrostatic Pressure = 25 Psi

10

5 4 3 2 1 1 2 3 4 5 6 7 8

ϵ_x, ϵ_y, percent
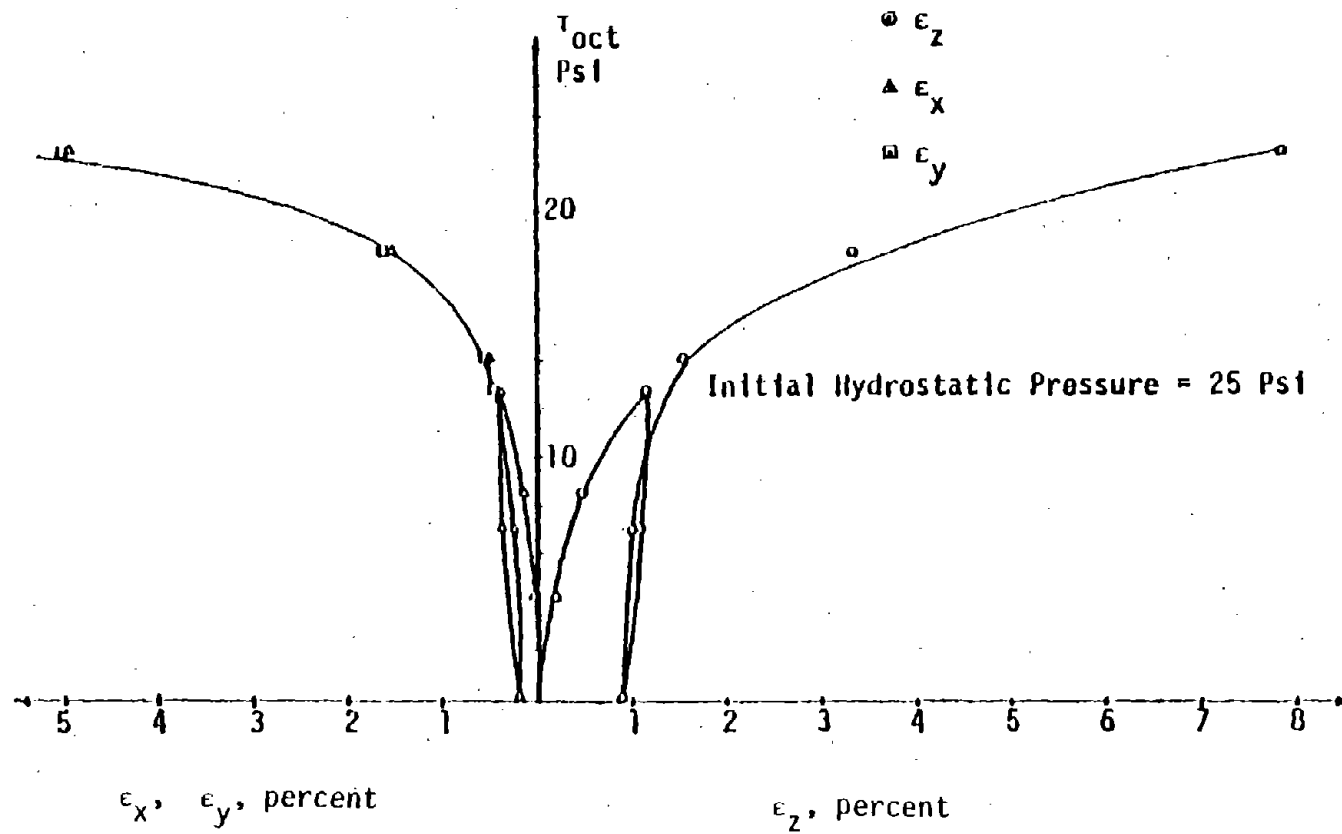
ϵ_z, percent

Figure 5.14   Stress-Strain Response Curves for Triaxial Compression Test

maintain σ_{oct} at a constant level. Figure (5.15) presents results

from a TE test at σ_{oct} = 20.00 psi (138.54 kpa) on a specimen compacted

to an initial density of 2.04 g/cm^3. The normal strains ε_x and ε_y

at ultimate condition are about 6.0 percent.

5.4.11 <u>Conventional Triaxial Extension</u> (CTE)

The stress-strain curves for CTE test is shown in Fig. (5.16).

In CTE, σ_2 and σ_3 are increased in equal amounts while keeping

σ_1 constant. The sample with an initial compacted density of 2.02

g/cm^3 is subjected to an hydrostatic pressure of 20.00 psi (138.00

kpa), from where the CTE path is followed. An ultimate state of

stress is reached with the normal strain at a relatively low level.

5.5.1 <u>Comparison of Results with Conventional Cylindrical Triaxial</u>

    <u>Tests</u>

Ko et al. [43] tested soil samples collected from the test site

at Pueblo, Colorado. The stress-strain relationships obtained by

them are for undisturbed samples with 9.4 percent water content and

unit weight of 2.33 g/cm^3 [39]. The specimens were extruded directly

from the sampling tubes into the flexible membrane test container to

minimize disturbance to the soil; the test apparatus used was the

conventional triaxial device. The apparatus was capable to measure

vertical deformation (ε_1) and volumetric strains. The output from a

minimum of six equally spaced transducers were averaged to measure

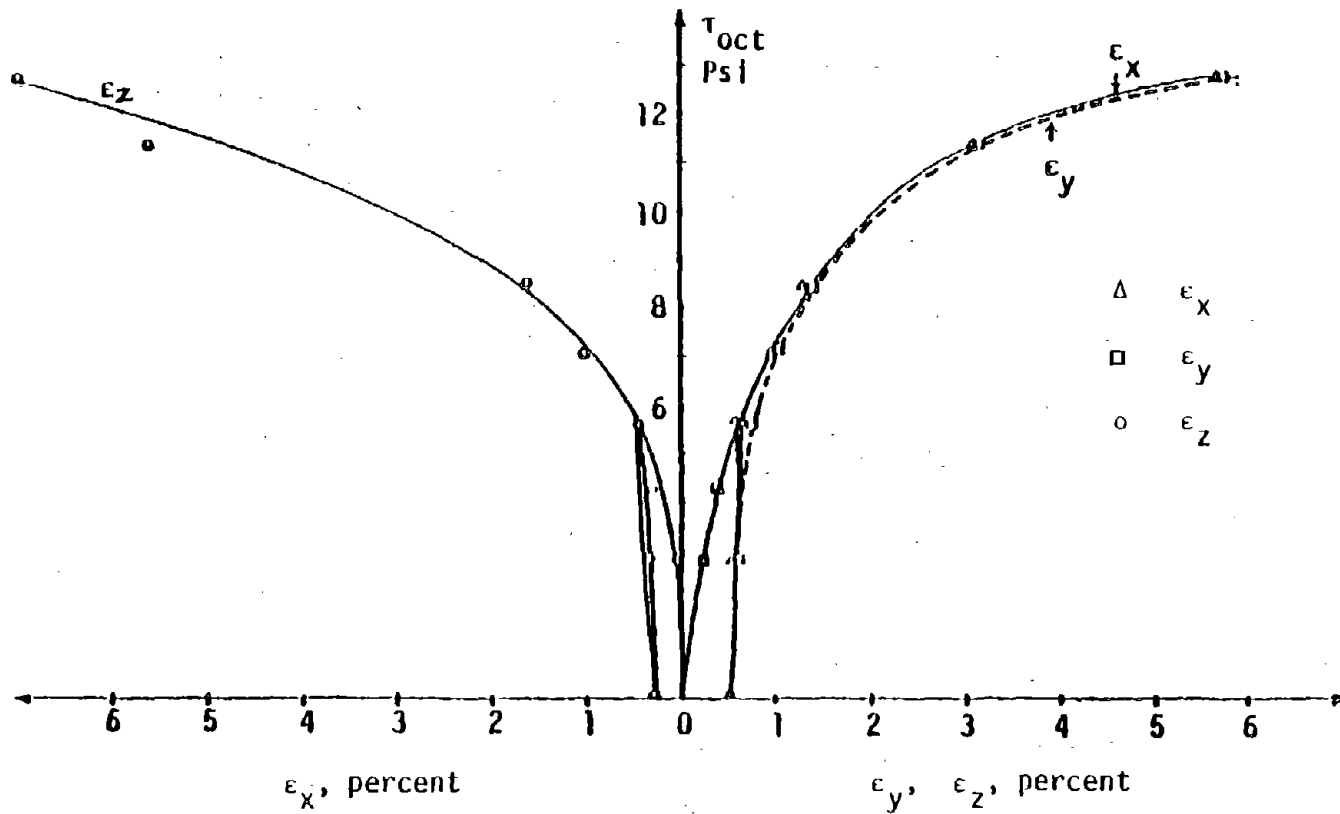the mid-height horizontal strain (ε_3) [43].

Figure 5.15   Stress-Strain Response Curves for Triaxial Extension Test
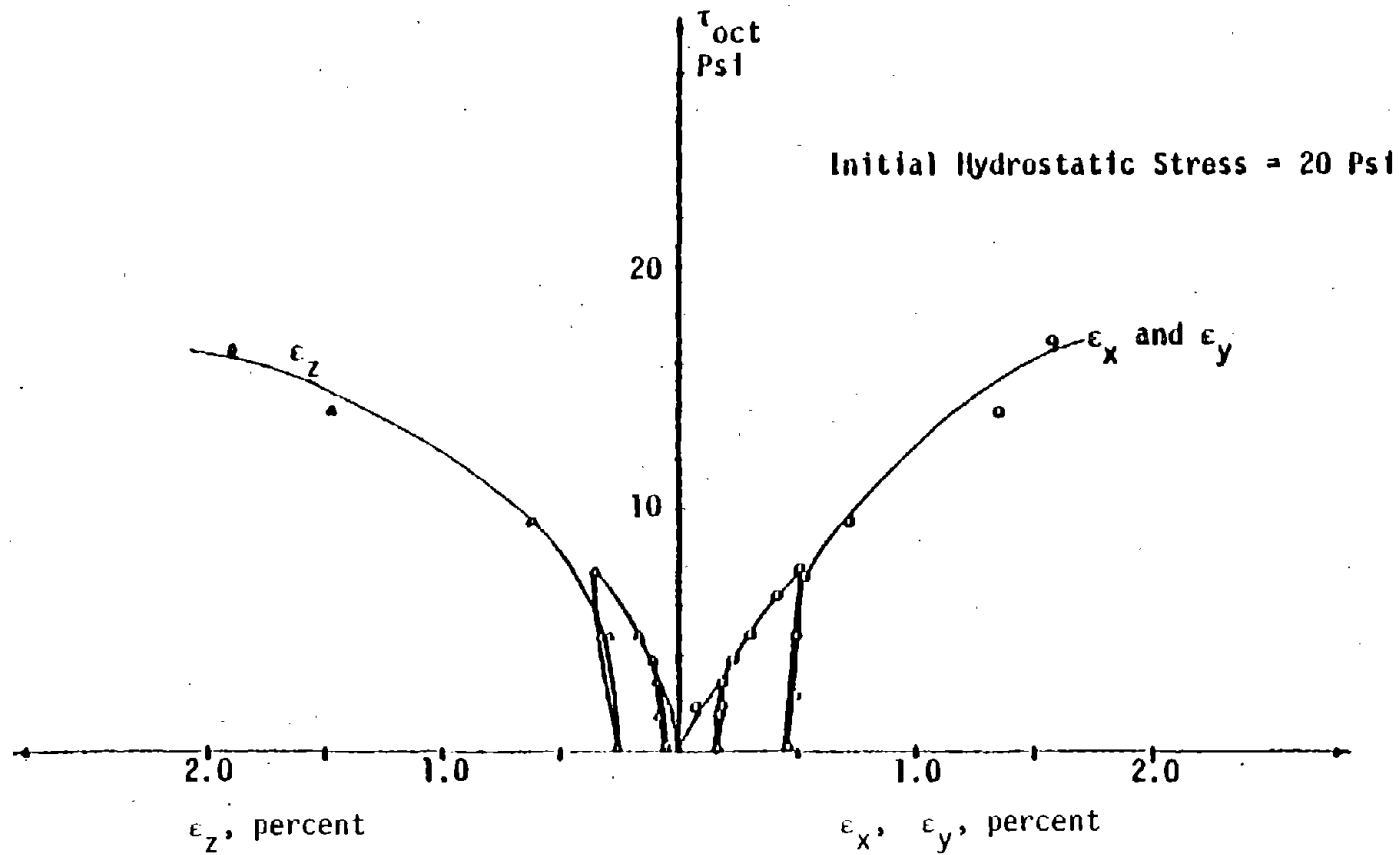
Figure 5.16 Stress-Strain Response Curves for Conventional Triaxial Extension Test

The specimen were subjected to the loading sequence as shown in Fig. (5.17). The direction of the arrows shows the loading sequence ($\phi \to A \to B \to A \to C \to E \to D \to C \to A \to \phi$). In this sequence of loading, either σ_1 or σ_3 is held constant while the other is varied or both σ_1 and σ_3 are varied simultaneously by equal amounts. The stress-strain relation obtained by Ko et al [43] is shown in Fig. (5.18).

In this investigation, remolded samples are tested for obtaining their stress-strain relationship. However, it is interesting to note that at its optimum moisture content (OMC) of 9 percent, the soil from the same test site has the denisty of 2.23 g/cm^3 exactly the same as that of the unit weight of the undisturbed soil with moisture content of 9.4 percent. One inferrence that can be drawn from this observation is that both samples have been taken from a well stabilized made-up subgrade. Samples of soil compacted at its OMC to an initial compaction density of about 2.23 g/cm^3 are tested in a truly triaxially device (stress controlled type). For comparison of the response of soil in the two kinds, namely undisturbed and remolded, the sample is loaded in this device by following the same stress path followed by Ko, et al and the stress-strain response is shown in Fig. (5.19).

From the comparison of the two responses, it can be concluded that there is no significant difference between the two. However, small variations like increased percentage of strains at low stress levels in case of specimens tested in conventional triaxial apparatus are noticed. Similar deviations have been observed while studying
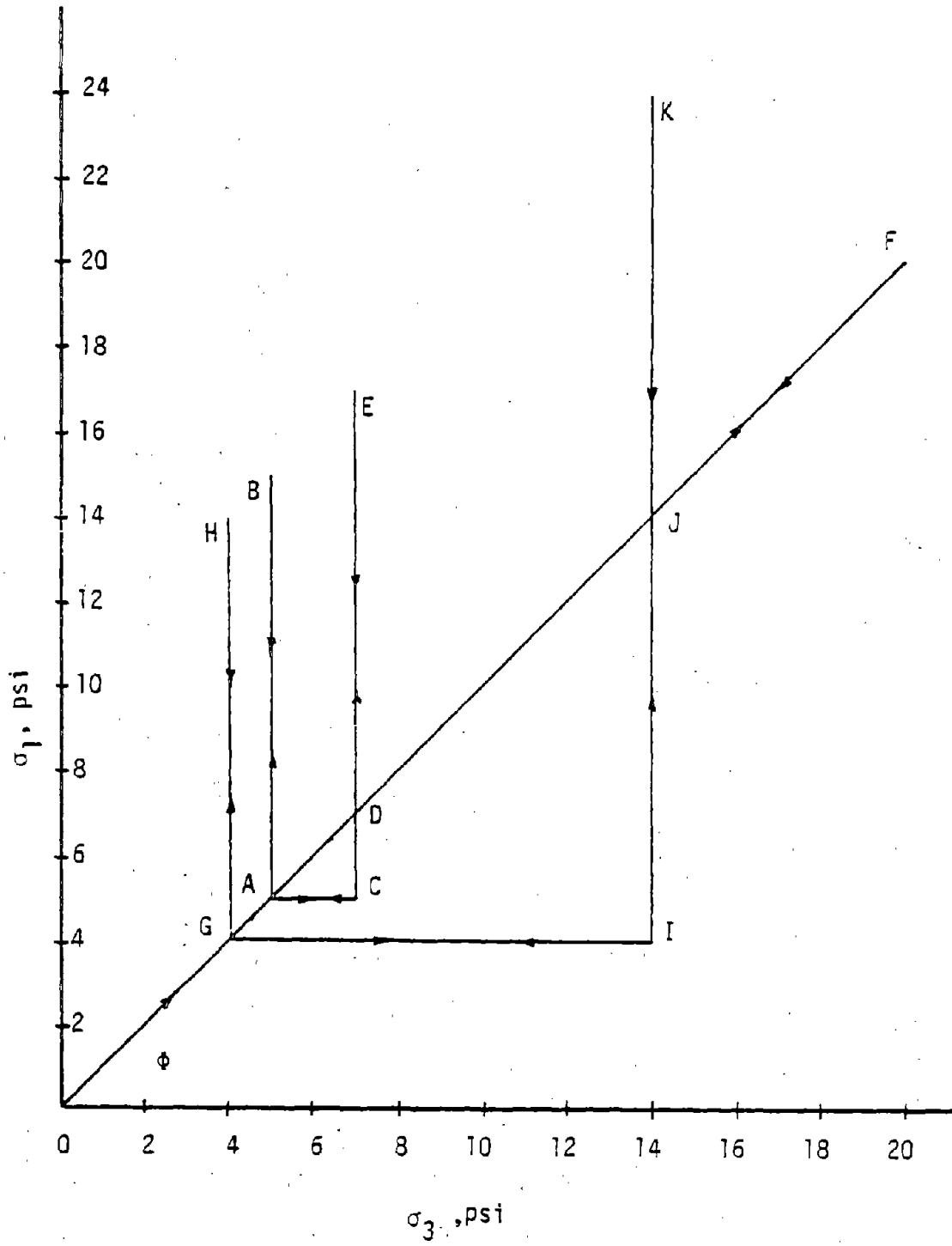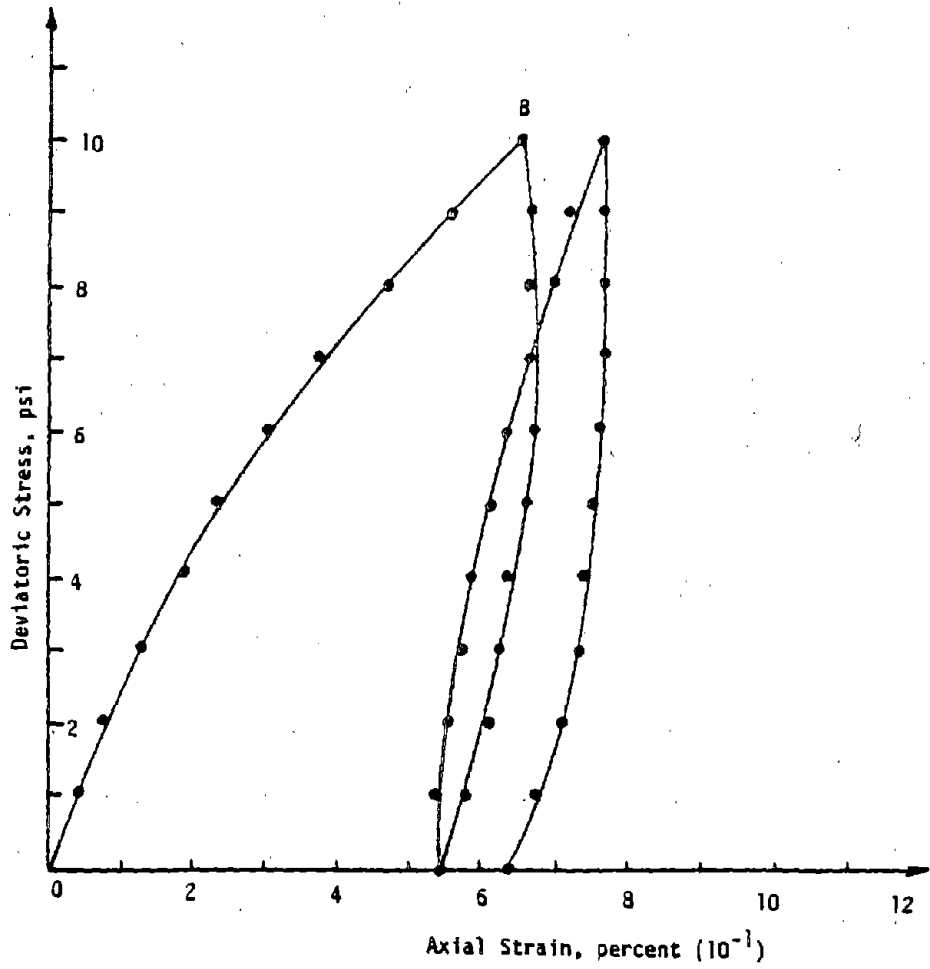
Figure 5.17 Stress Path (Ko)

Figure 5.18 Axial Strain Vs Deviatoric Stress (Ko)

Figure 5.19 Axial Strain Vs Deviatoric Stress (Remolded Soil)

the performance study of the truly triaxial device comparing with results obtained in the conventional triaxial apparatus. The maximum strains at the end of loading sequence $\phi \to A \to B$ are about 0.59 and 0.64 percent for remolded and undisturbed samples, respectively. The elastic recovery at the end of sequence $B \to A$, is 0.13 percent in case of remolded sample and is 0.11 percent for undisturbed sample.

Therefore, it is considered justifiable that the stress-strain response obtained for the soil in this investigation, though on remolded samples, to be regarded as on essentially the same as that from undisturbed samples.

5.6.1 MATERIAL MODELING

The material model used here to characterize the constitutive behavior of the soil is based on the critical state concept. The material parameters λ and k are determined from the e-lnp relationship obtained from the hydrostatic compression test data; their values, $\lambda = 0.017$ and $k = 0.0028$, are determined from Fig. (5.20). These values appear to be low; this may probably be because the sample tested is remolded well compacted dense sample with initial compacted average density of 2.23 g/cm^3.

5.6.2 Failure Surface

The failure envelop [68] for this soil is drawn in Fig. (5.21). For the tests are conducted with various stress paths, as explained in section 5.4, it is proposed to draw failure surface on $J_1 \sqrt{J}_{2D}$
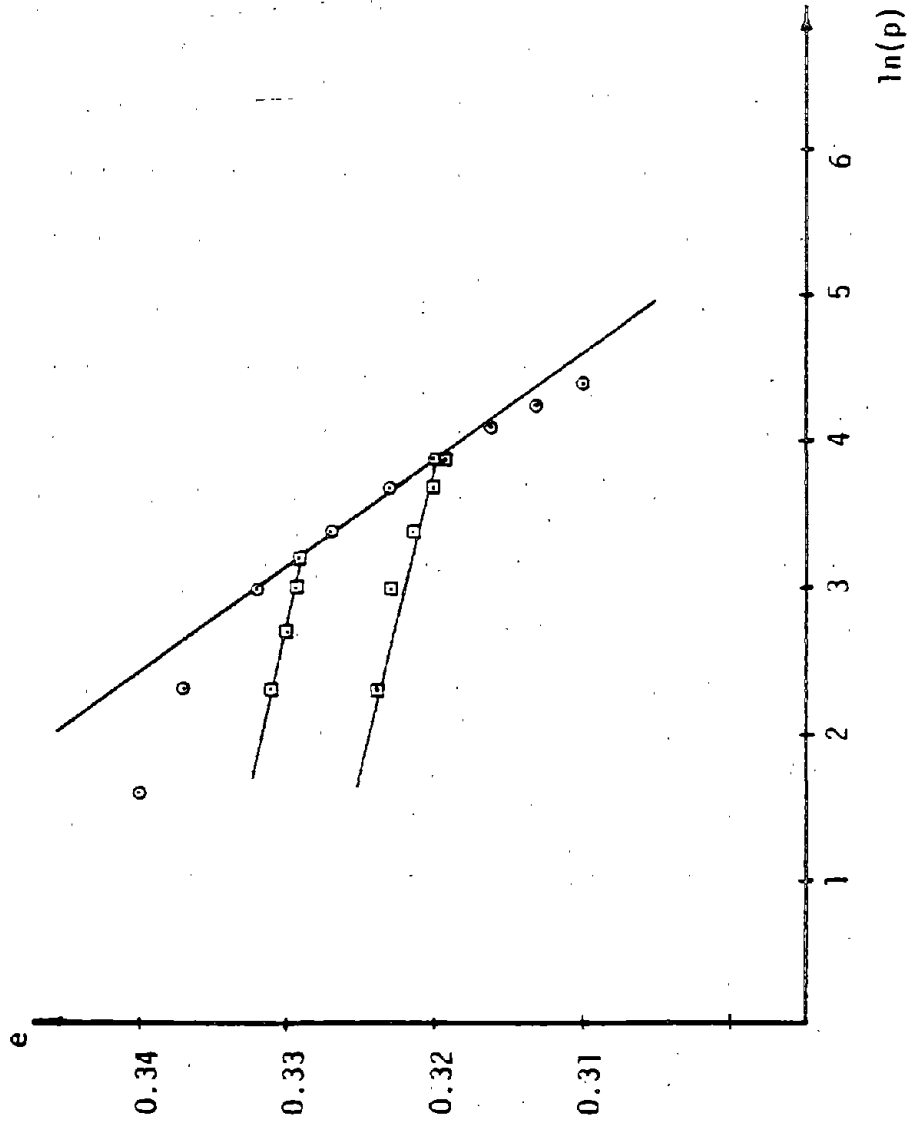
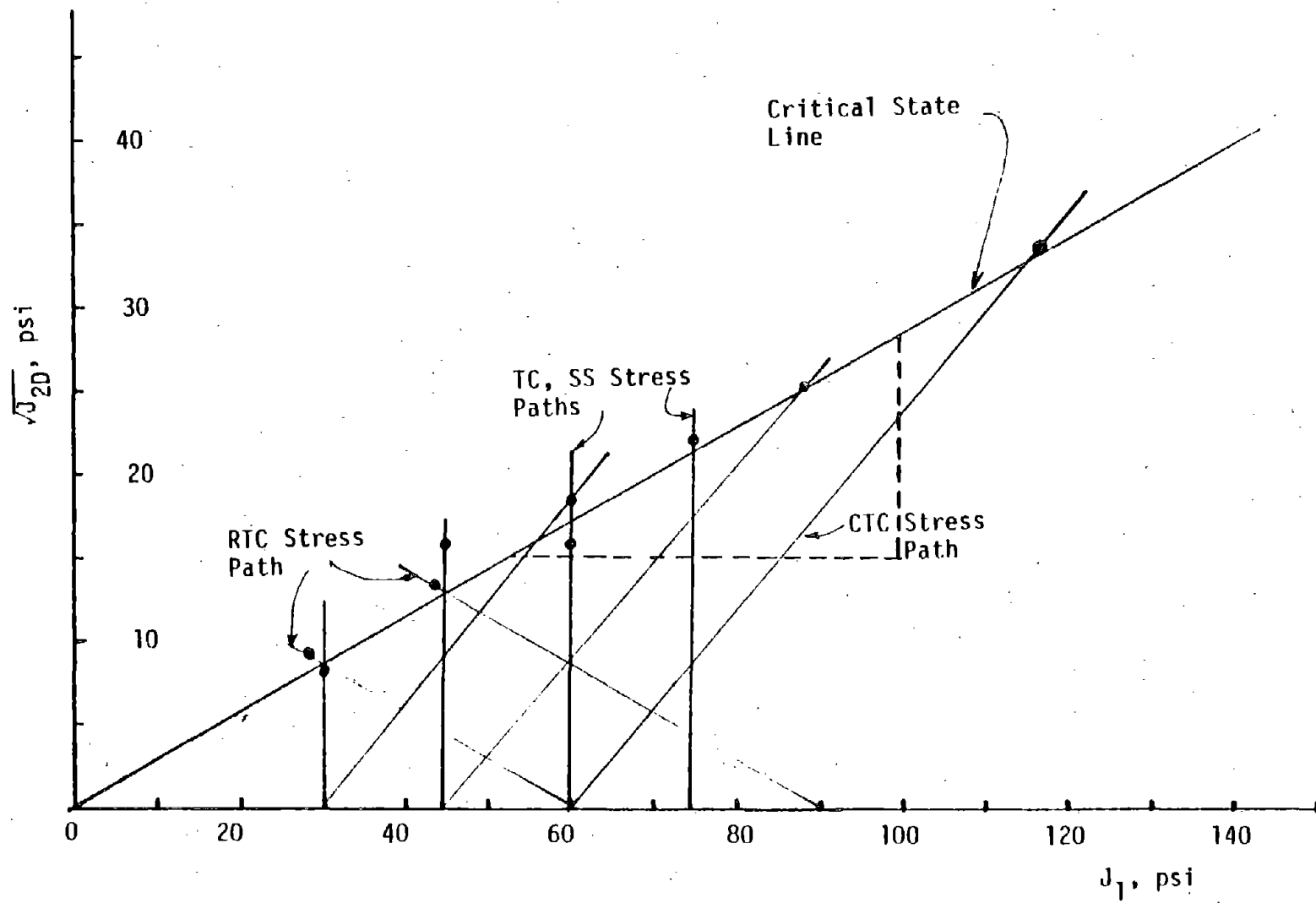Figure 5.20 Void Ratio – ln p Relationship

Figure 5.21 Failure Envelop for Peublo Soil

space so that all test results can be well represented. The ultimate
stress levels are marked along the respective stress paths and an
average curve is drawn passing through the origin. This is essen-
tially the critical state line. The scatter of failure points is not
significant. The slope of the curve in Fig. 5.21 is found to be
0.286. The value of M, Fig. (5.1), in the critical state model
is then found as

$$\sqrt{J_{2D}} = 0.286 \ J_1$$

since $\quad q = \sqrt{3J_{2D}}; \ p = \dfrac{J_1}{3}$ $\qquad\qquad$ (5.18)

$$q = 1.48 \ p$$

Therefore, M = 1.48.

The initial void ratio is 0.34. As the sample is a well com-
pacted, this e_0 is probably on the minimum side. The soil here has
been brought to the condition as it exists at the site, and then
tested. Therefore, even before the commencement of the test, the
sample is comparitively dense. As no test has been run on the same
soil in different states like loose and medium dense, results from
such tests are not accounted here in establishing the critical state
line, it is suggested to consider the critical state parameter M
obtained as an approximate value.

5.6.3 Plastic Potential Surface

Plastic strain increment vectors are computed at several
selected points along the various stress paths from the available

stress-strain curves. The plastic strain increments correspond to J_1 and $\sqrt{J_{2D}}$ are 1/3 (dI_1^p) and $2(dI_{2D}^p)^{1/2}$ respectively. The sets of plastic strain increment vectors represent discrete segments of continuous plastic flow field. The shape of the plastic potential surfaces are established such that the strain increment vectors are orthogonal to them, Fig. (5.22).

5.6.4 Yield Surface

Moreover, the yielding (surface) cap interests the J_1 axis at right angles and intersects the critical state line at a slope parallel to the J_1 axis. The accumulated volumetric strain, ε_v^p is calculated at number of points along the J_1 axis and along the other stress paths, and the points are marked along the paths. Then contours of equal ε_v^p are drawn, Fig. (5.23). These contours are obtained by joining the points so that ε_v^p is constant along the surface.

The yield and potential surfaces appear to be the same, hence the material can be assumed to follow the associated law of plasticity. If they are approximated as elliptical, they can be expressed as

$$R^2 J_{2D} + (J_1 - L) - R^2 b^2 = 0 \qquad (5.19)$$

The value of R, the ratio of semi major and minor axes of the ellipse is found to be 1.12. This equation will then define the moving yield surface.

The yield loci or caps in the critical state and cap models are
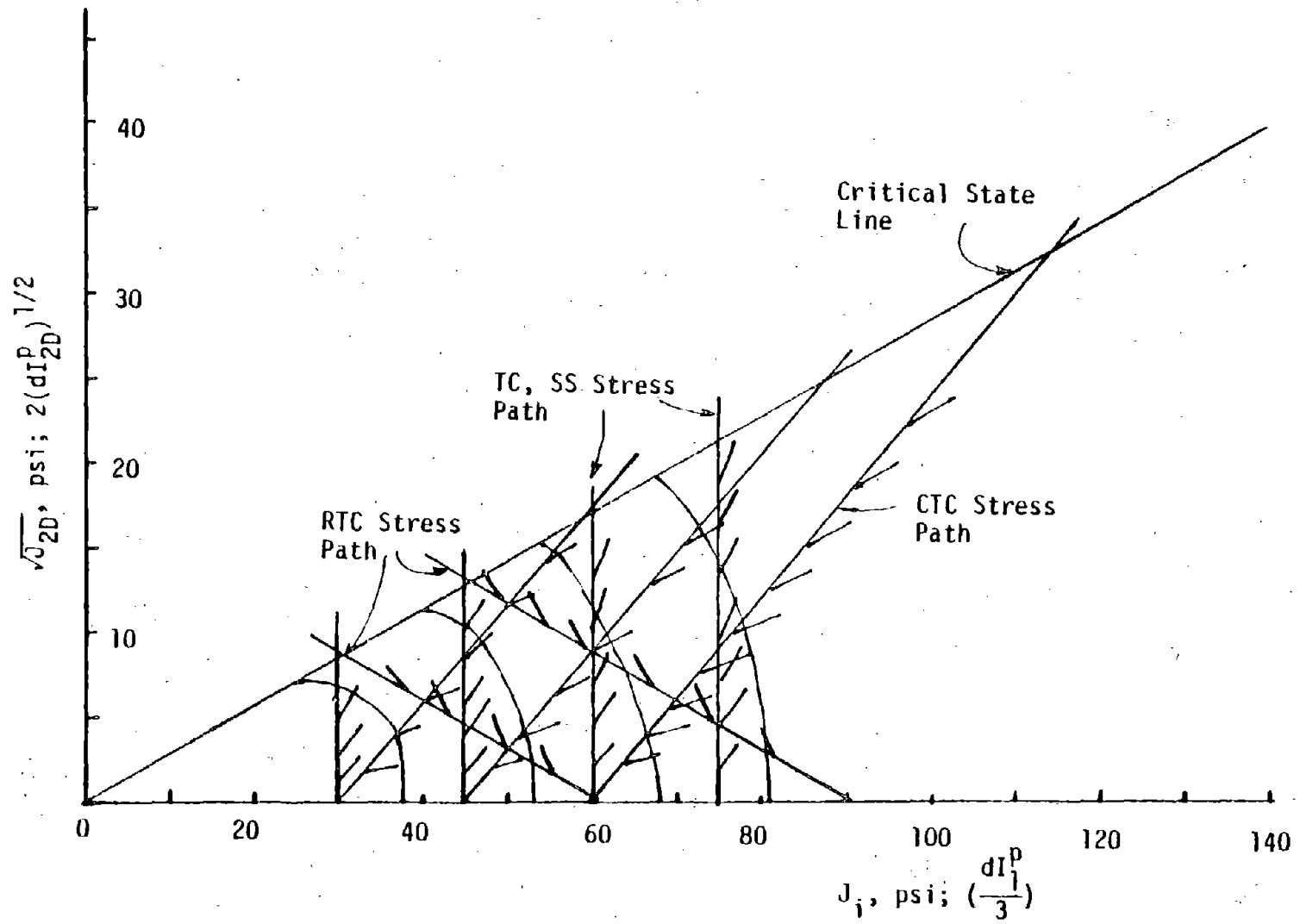
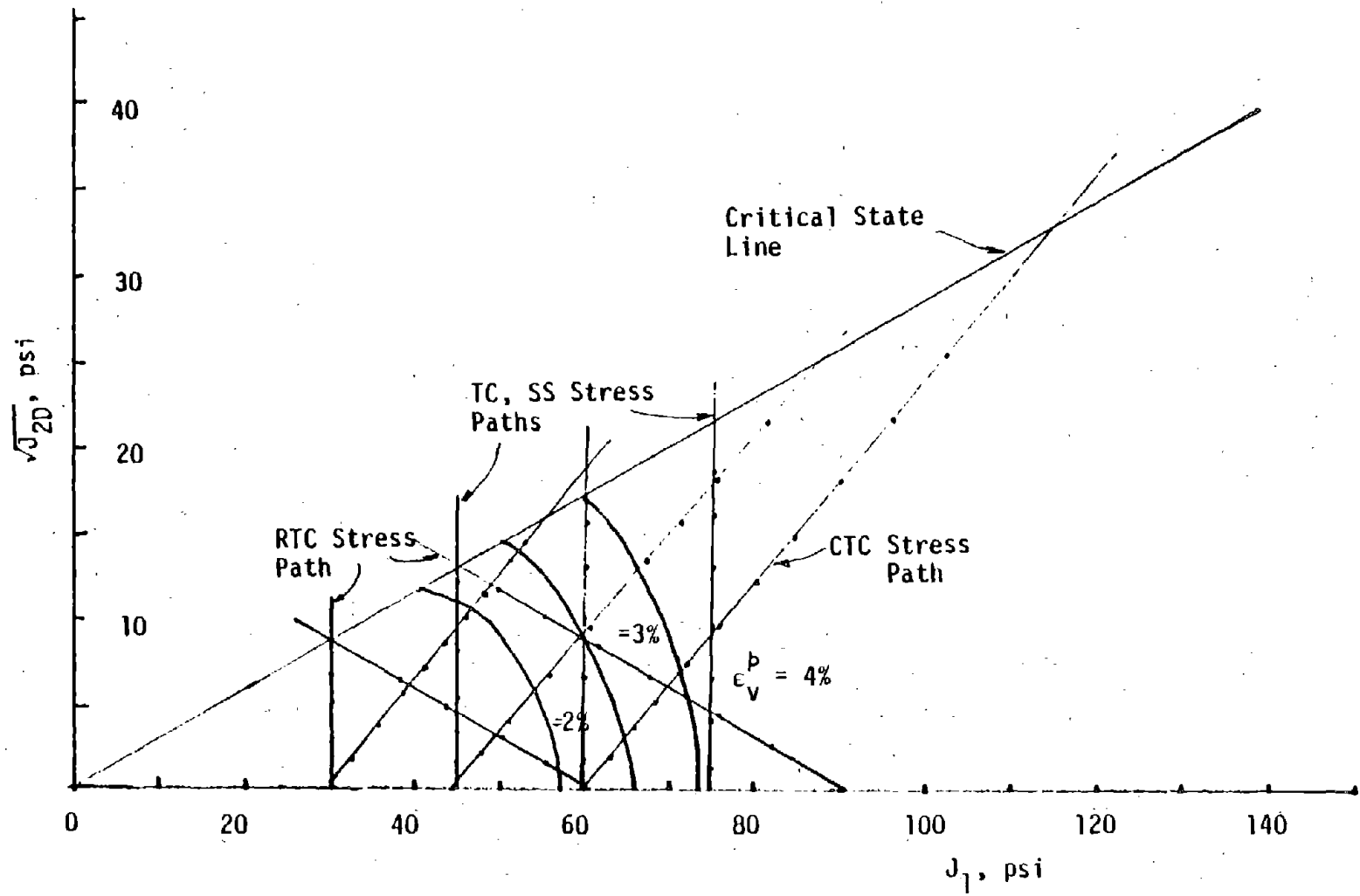Figure 5.22   Plastic Strain Increment Vectors and Potential Surfaces

Figure 5.23   Yield Surfaces for Peublo Soil

found as to surfaces on which the total volumetric plastic strain, ϵ_v^p, is invariant.

Chapter 6

BEHAVIOR OF INTERFACES

6.1 INTRODUCTION

The analysis of a track bed should include influence of the interface between various components. Due to the heavy moving load, tractive forces can be introduced in all the directions. If the loading is such that significant amount of relative slip does not occur between the two layers, it may be admissible to assume compatibility between the two. However, in many cases it is necessary to consider the relative slip, loss of contact and rebounding at the interfaces. In order to account for this behavior special finite elements have been proposed [25]. The stiffness properties of such interface elements are derived from tests that can simulate the transfer of shear stress.

6.2 PROBLEM STATEMENT

It has been observed that there are hardly any rational procedures, analytical or experimental, available for obtaining stress-strain behavior of interfaces such as tie-ballast. The direct shear test consisting of one medium in the bottom half and the other in the upper half has been often used to determine the material parameters. This test suffers from certain limitations. A new dynamic multi-degree of freedom of freedom shear device has been developed for determining the behavior of interfaces. This device permits determination of shear and normal stiffnesses for the interfaces.

6.3.1 Normal Stiffness

The shear and normal stiffness of an interface can be defined
as

$$[K] = \begin{bmatrix} K_{nn} & 0 \\ 0 & K_{ss} \end{bmatrix} \tag{6.1}$$

where K_{nn} and K_{ss} are the normal and shear stiffness of the interface
element. This scheme assumes that the shear and normal nodes are
uncoupled. Symbolic curves showing normal and shear behavior of an
interface are shown in Fig. (6.1).

6.3.2 Shear Stiffness

It can be defined as the magnitude of the shear stress to
unit shear displacement. The main factor influencing this phenomenon
is friction. Friction is defined as the resisting force or resistance,
which one body offers to the sliding or rolling of another body over
it. This sliding friction is due to the interlocking of the asper-
ities of two surfaces. Even highly polished surfaces show these
irregularities, when greatly magnified. If the friction is sufficient
to prevent relative motion of the bodies, it is said to be static
friction, but if the bodies move with respect to each other, it is
called kinetic friction.

The sliding friction between two media depends upon (1) the
nature of the substances, (2) condition of the surfaces and (3) the
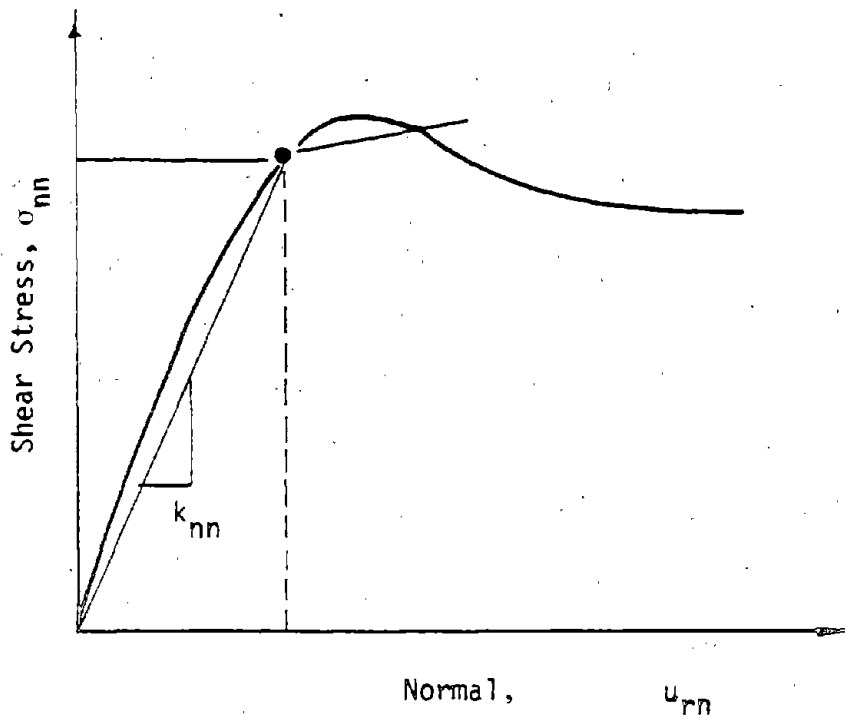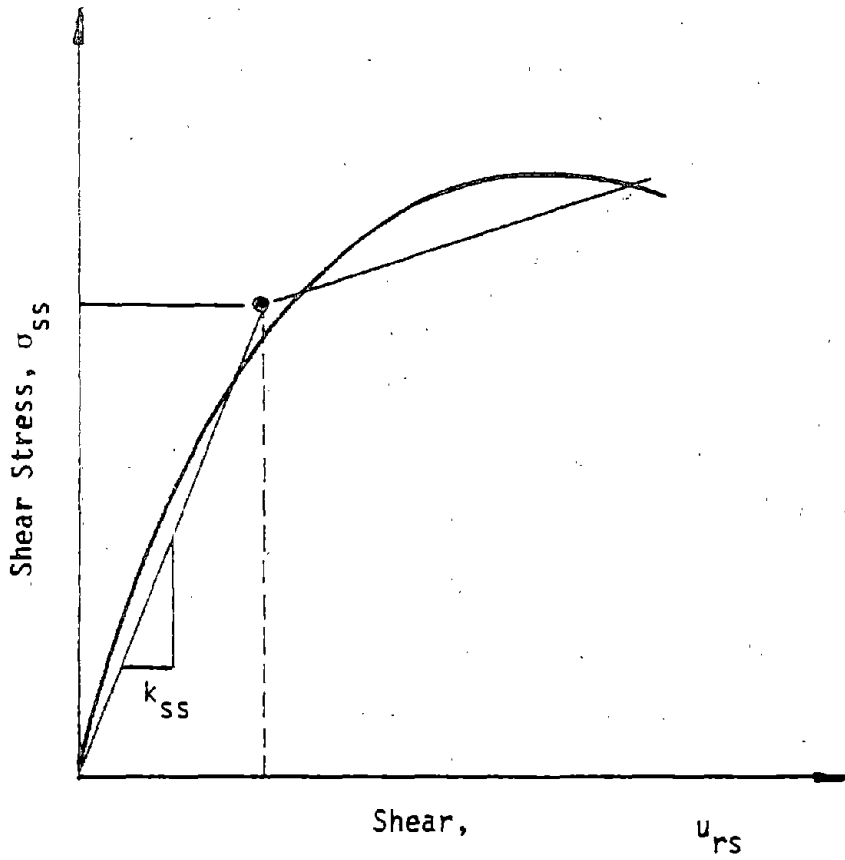normal force pressing the surfaces together. It is proportional

Figure 6.1 Bi-Linear Relationship

to that force. However, it is essentially independent of the area of surfaces in contact and the speed, except at starting.

6.4 REVIEW OF LABORATORY TESTS

A review of laboratory tests for determination of interface behavior is given here. Though direct shear test has been widely used, the test suffers from certain limitations. The direction of critical stress can be inclined to be the direction of shearing and the maximum shear stress can be greater than the measured shear stress parallel to the axis of the shear box. Further, the distribution of shear stresses may not be uniform. Reviews of various devices are presented by Desai [22,23].

A schematic diagram of the apparatus proposed by Brumund and Leonards [10] is shown in the Fig. (6.2). Here interface is introduced as the circumference of a circular rod which is inserted co-axially into a cylinder of soil. The soil is surrounded by a light membrane. Shearing stress, static or dynamic, is applied through an axial load to the rod. Values of coefficients of friction are obtained for both static and dynamic conditions for smooth and rough concrete interfaces. However, it is not certain whether uniform state of stress is achieved in the interface. Also any ecentricity in the introduction of the annular shear ring will cause complexity in stress distribution across the interface.

Huck, 35 al [38] developed a ring shear device, Fig. (6.3). This ring shear device can apply static or dynamic loading and can
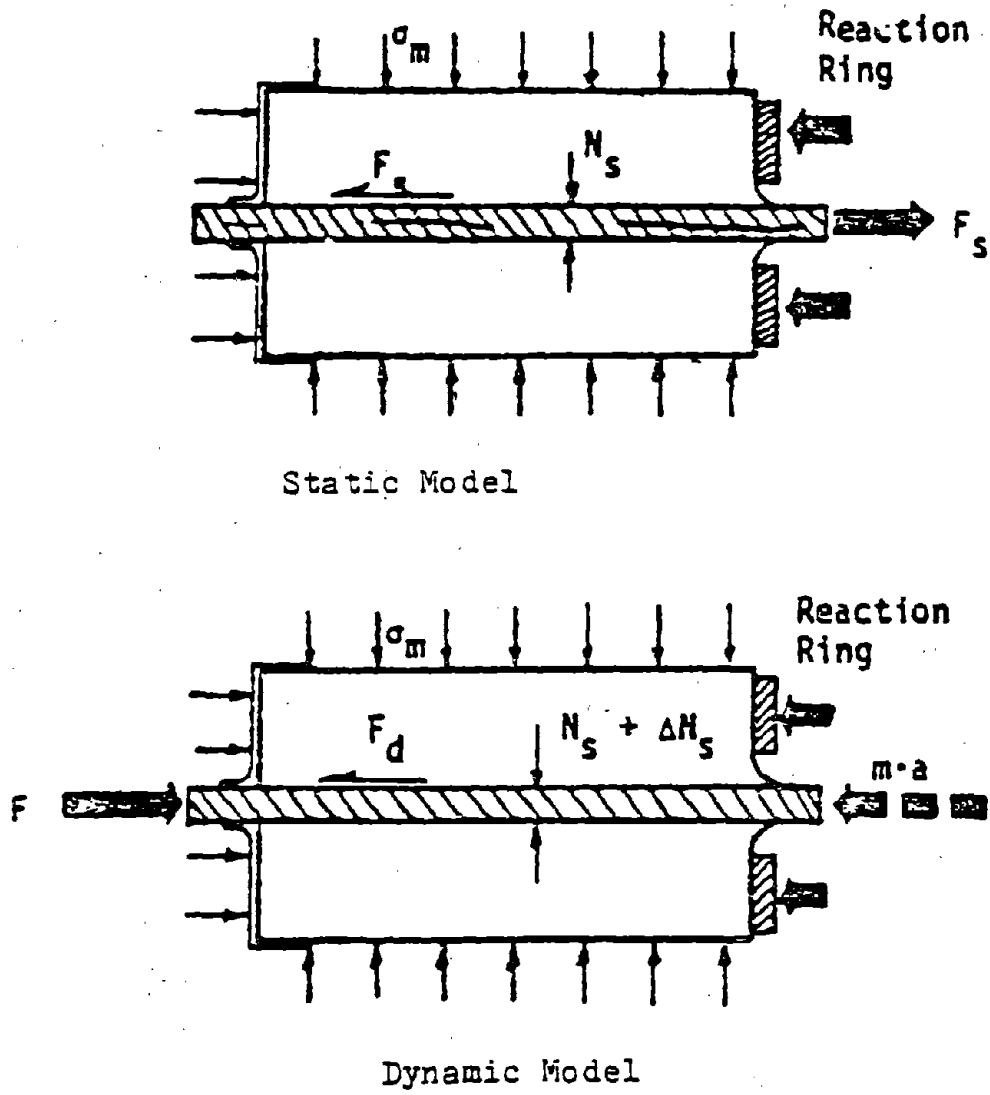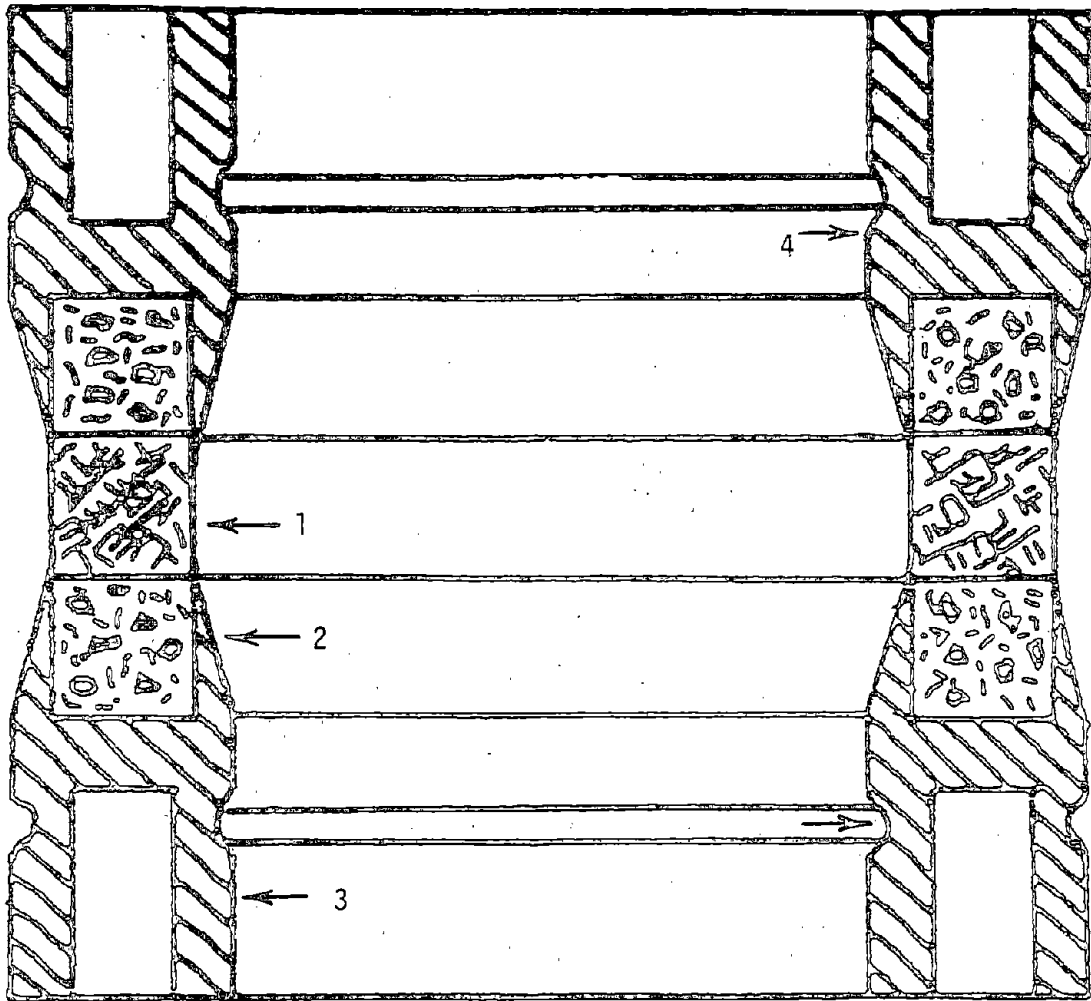
Figure 6.2 Annular Shear Device

1. Soil Specimen   4. Upper Loading Platen

2. Concrete   5. Lower Loading Platen

3. Steel Holder

Figure 6.3 Ring Shear Device

induce uniform states of stress. This device can well define the interface behavior under dynamic conditions at high normal stresses. The specimen of soil is an annulus of diameter of 17.7 cm with inside diameter of 12.7 cm and height upto 2.5 cm. The specimen is confined by membranes and is loaded at top and bottom by concrete surfaces. An analytical model for interface behavior was also proposed by Huck, et al.; it allows for various modes such as adhesion, friction, ploughing and lifting and accounts for existance of asperities, actual contact area, obliqueness of contact forces and time effects. It also involves both deterministic and statistical approaches. Yet the derivations are very lengthy and require a number of parameters for defining the interface behavior.

For practical use, it is necessary that the test device be simple and the mateial parameters be as few as possible consistent with required accuracy. The newly developed Cyclic Multi-Degree of Freedom Shear Device can provide such a device [23].

6.5 CYCLIC MULTI-DEGREE-OF-FREEDOM SHEAR DEVICE (CYMDOFS)

The details of design, development and construction of this device are given by Desai [23]; salient details are reporduced herein for the sake of completeness. The CYMDOFS, Fig. (6.4), essentially consists of a large shear box, the bottom half is fixed to a frame which is designed to withstand a (vertical or horizontal) load up to 30.0 tons and a frequency of 2.0 Hz, and the top box is connected to a horizontal cylinder of 7.0 tons capacity. Both stress controlled
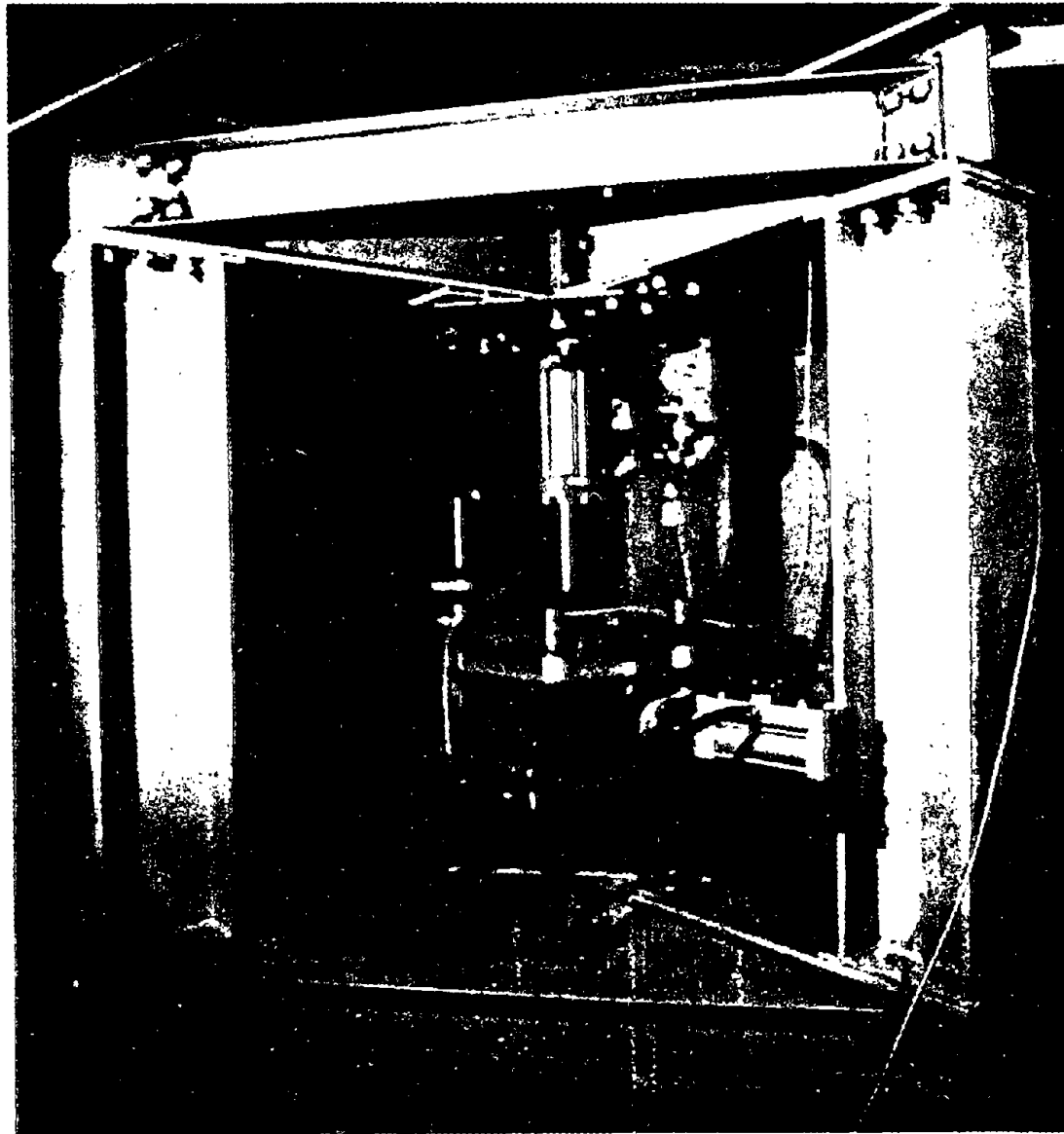
Figure 6.4   Assembly of CYMDOFS

and strain controlled tests can be conducted in this device. A hydraulic pump, 3000.00 psi (2.07 x 10^4 kpa) and 30.00 gpm capacity, supplies the required pressure input. A normal load is applied through a vertical hydraulic cylinder of 7.0 tons capacity. Load cells, to monitor horizontal and vertical loads, LVDTs, to record horizontal and vertical displacements are controlled by MTS electronic control units. A function generator allows load application in any form of a repetitive loading.

Loading

The loading frame is designed to withstand a load of 30.00 tons (vertical or horizontal) and a frequency of 2.0 Hz. The horizontal hydraulic cylinder is fixed to the vertical member of the frame. So also the vertical hydraulic cylinder is fixed to the junction point of upper diagonal members of the frame through a pin joint.

Test Box

Figure (6.5) shows a photograph of the test box. The bottom part of the test box is 16.00 x 16.00 inches (40.00 x 40.00 cm) and the top part is 12.00 x 12.00 inch (30.00 x 30.00 cm). Thus, at this time, samples of size 12.00 x 12.00 inch (30.00 x 30.00 cm) can be tested. The box is designed such that the top half can be subjected to:

1. Cyclic load in the vertical mode,

2. Cyclic load in the horizontal mode with a static (constant) vertical load, and
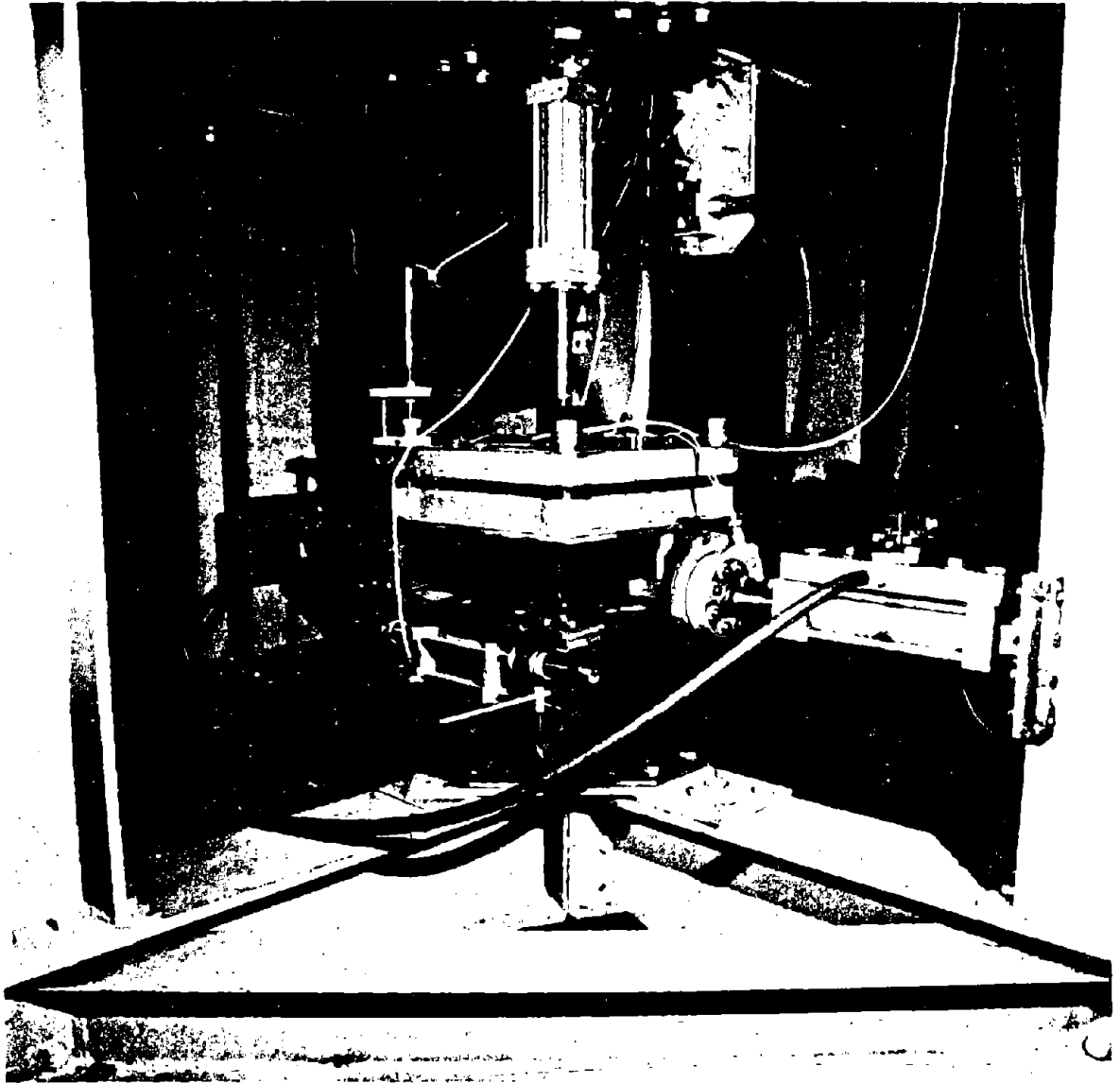
Figure 6.5   Shear Box

3. Cyclic load in both the vertical mode and horizontal mode.

The forces and displacements are measured in the vertical and horizontal directions by using load cells and LVDTS in the respective directions.

The load cell used is a fatigue rated universal falt load cell. It is electrical resistance type. It is calibrated to give a load of $\pm$ 12,000.00 lbs ($\pm$ 5454.5 Kg).

Linear Variable Differential Transformer (LVDT) essentially consists of a thin rod sliding in a vented casing. The movement of the rod into the casing directly provides a highly linear, hysteresis - free relationship between voltage output and displacement. The LVDTs used in this test set up are calibrated to have a displacement of 1.00 inch (2.54 cm) for an excitation voltage of $\pm$ 10.00.

Control System

A schematic diagram of the hydraulic-electronic control system is shown in Fig. (6.6). The hydraulic parts consists of two cylinders, one in the vertical direction and the other in the horizontal direction. The cylinders are connected to an electronic servo controller system through servo-valves. A hydraulic pump of 30000.00 psi (2.07×10^4 kpa) (variable discharge type) 30.00 gpm maximum capacity, supplies the required pressure input. The readouts of the load cells and LVDTS are fed to an automatic data acquisition system. The servo-control system is essentially controlled by the MTS control unit in the respective direction.
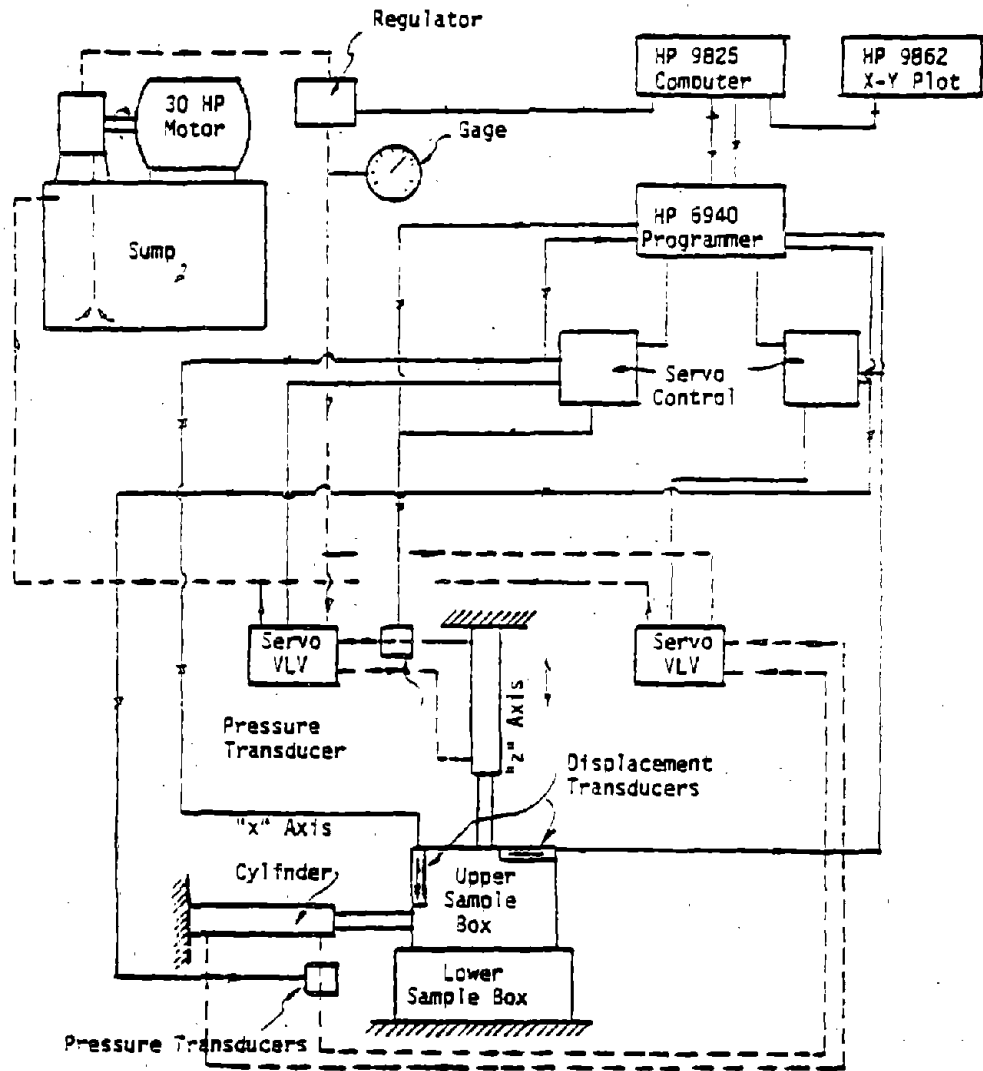
Figure 6.6 Flow Diagram for Cyclic-Multi-Degree-of-Freedom
            Shear Device

A function generator allows load application in various forms at desired frequency. A counter in the control unit directly shows the number of cycles of application.

A photograph of the complete assembly of electronic control unit is shown in Fig. (6.7). It consists of a function generator, two MTS 406 control units, (one each for each direction), a voltmeter, an ossiloscope and a main MTS 436 control unit.

Further details and instruction for the use of the device are given by Desai [23], and Desai and Janarthanam [22].

6.6 TESTING PROGRAM

6.6.1 Vertical Vibration TEst

A column of ballast, Fig. (6.8), confined laterally is subjected to a cyclic load. The resulting deformations over a wide range of number of cycles of load application are measured. The details of testing and the test results are presented here. Full sized ballast from the UMTA test site at TTC, Peublo, Colorado is tested. Properties of ballast have been given in section 4.5.2.

Equipment Preparation

The MTS control unit is switched on. The hydraulic pump is started and a pressure of 50.00 psi (345.00 kpa) is set in the gage. The valve for the cooling system is open for the flow of cold water. In both control units, the "feed back selects" are set to the transducer 1, namely LVDT. The top box can be moved
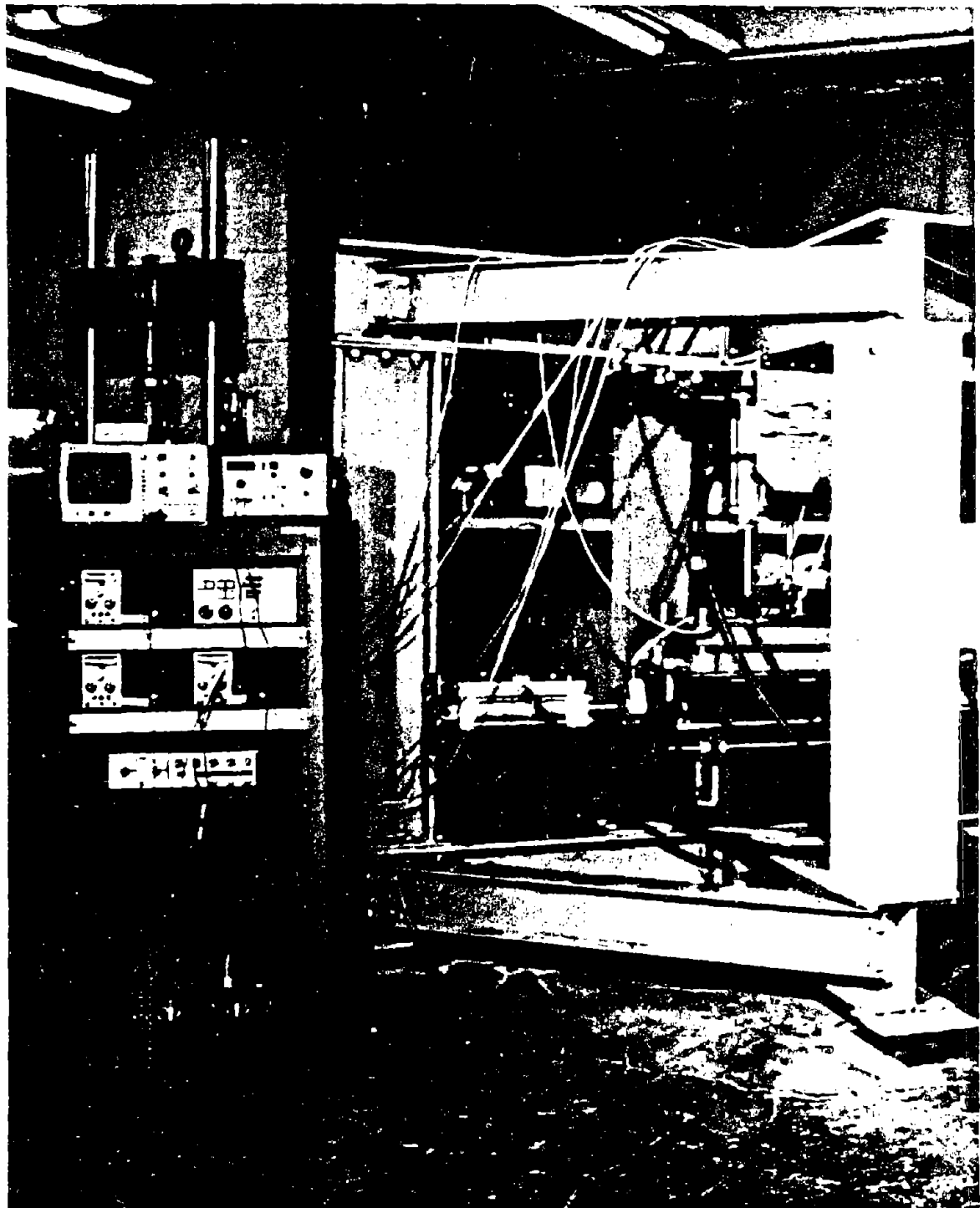
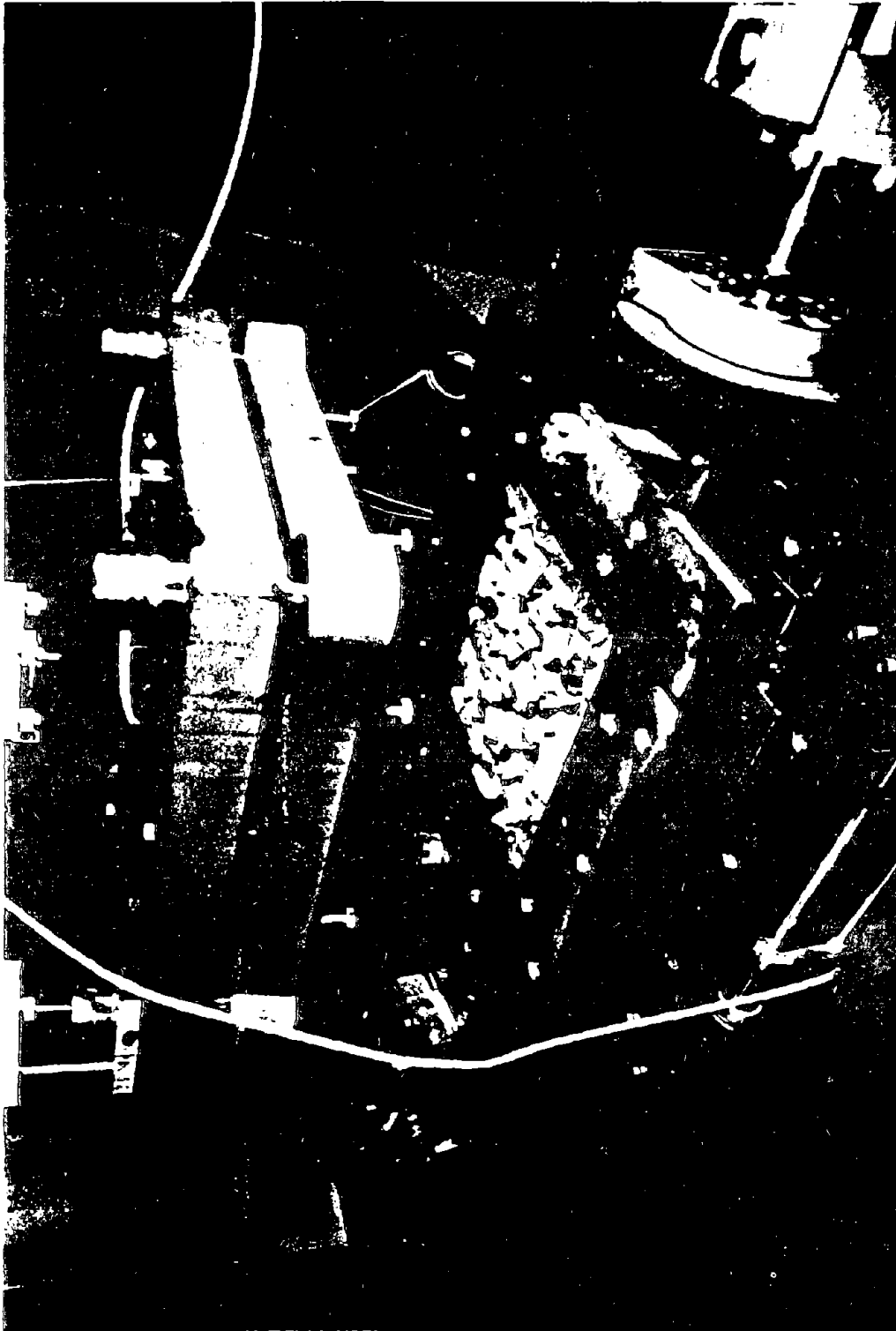Figure 6.7   Control Panel for CYNDOFS

Figure 6.3 Column of Ballast in Shear Box for Vertical Vibration Test

back and forth by operating horizontal cylinder and the top cover plates by the vertical cylinder. The self weight of the cover plate is 240.00 lbs (109.09 Kg).

The top box is centered over the bottom box carefully. Any further, horizontal motion of the top box is now locked. The cover plate is then moved away so that enough room is available for sample preparation.

After the ballast is placed in and compacted to an initial density of 112.00 pcf (1.79 g/cm^3), the top cover plates are moved into position. They are lowered very slowly. Precaution is taken that the plate does not rest on ballast but just touches the surface. The "feed-back" select is now set to transducer 2, namely the vertical load cell. The vertical motion is now stress controlled.

The function generator is set to a frequency of 0.50 Hz and a sine function of loading. Positive loading of the sample is only possible in this set up. So a positive sine function is set as shown in Fig. (6.9). Now the sample is ready for test.

Testing

In this test, a vertical repetitive load with an amplitude of 3000.00 lbs (1364.00 Kg) is applied. The set point knob is adjusted to apply 3000.00 lbs (1364.00 Kg), the desired dynamic load, as a static load. The "RUN" button in MTS 436 control unit is pressed and SPAN knob is now adjusted to apply the load. LVDT and load cell readings are taken at various intervals: N = 100, 500, 1000, 2000,
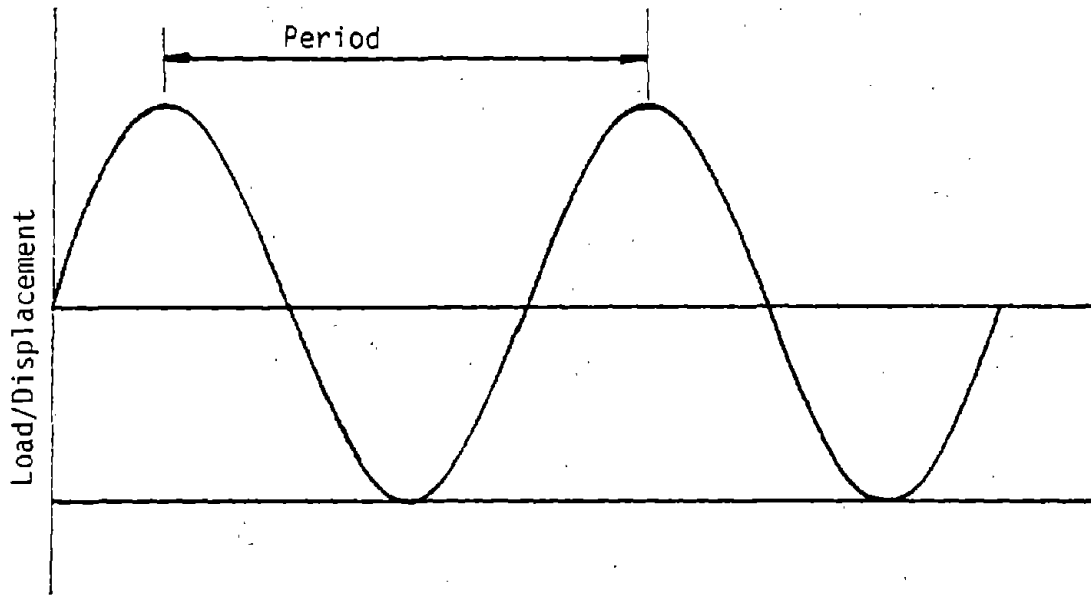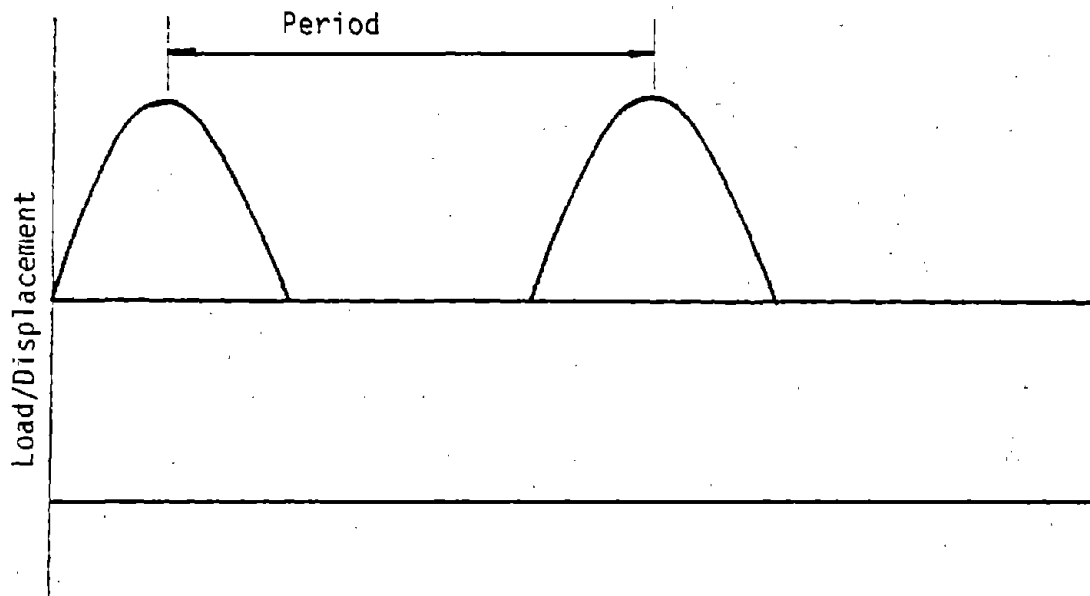
Figure 6.9 Loading Function - Positive Sine Function

3000 and 5000 cycles. The accumulated vertical strain is measured and plotted against number of cycles in Fig. (6.10).

Test Results

It is seen that the cummulative axial strain increases steadily in the beginning. With increasing number of cycles, the rate of increase of cummulative strain decreases. That is, the magnitude of additional strain decreases and becomes small thus making cummulative strain almost stationary after about N = 5000.

The initial deformations may be due to particles readjustment. As loading cycles increases, this densification for the given load becomes nearly complete and the material undergoes elasto-plastic deformation, then the material reaches a stable state; no more significant amount of deformation occurs thereafter.

6.6.2 Interface Behavior Study

The main objective of this study is to understand the physical behavior of the interfaces between tie (concrete) ballast. A comprehensive series of tests was run at a frequency of 0.5 Hz with different normal and horizontal loads. Details of the tests run, responses of the interface and the discussion of test results are given here.

Materials Used

The ballast used in this study is from the UMTA test site at Pueblo, Colorado [39]. Its physical properties and grain size
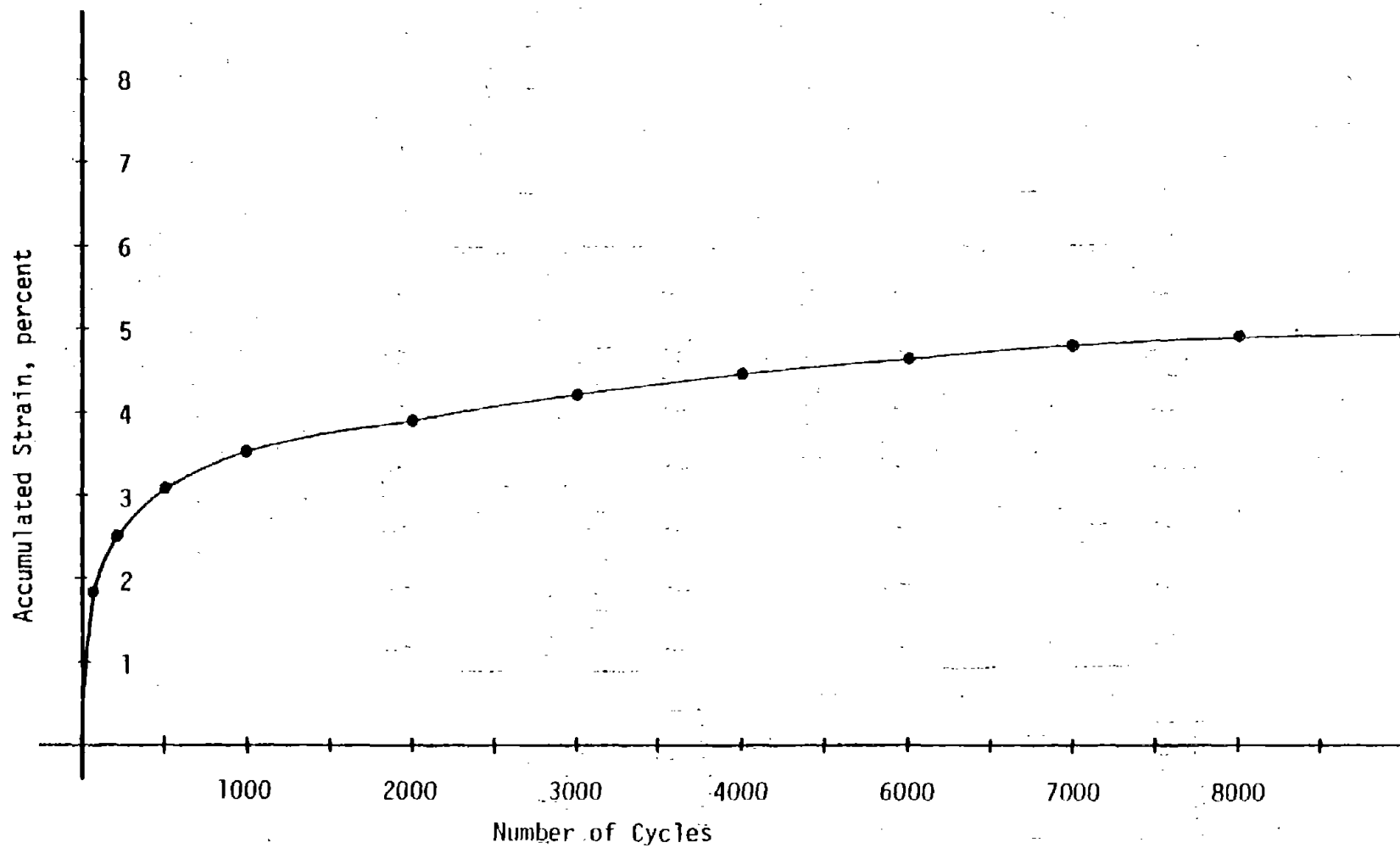
Figure 6.10 Accumulated Strain in Vertical Vibration Test

distribution are given in section 4.5.2. The concrete block is made to simulate the strength and frictional characteristics similar to the concrete ties used at the test site.

Concrete-Tie Block

Concrete blocks 15.00 x 15.00 x 7.00 inch (38.10 x 38.10 x 17.78 cm) are cast in wooden molds. The concrete mix is made of broken granite chips, stone sand and cement. The water/cement ratio of the mix is 0.5. Mechanical concrete mixer is used for unform mixing. The concrete mix is poured into the mold and vibrated with a needle vibrator for 3 minutes. The top surface of the mold is leveled with a trowel. The concrete mix is allowed to granually get set. After one hour, a hard brush is floated on the surface to make the surface corrugated as the surface of the ties at test site. After 24 hours, the wooden mold is removed and the block is cured for 28 days. Curing of concrete is done by pooling water.

Cured concrete block, Fig. (6.11) is left to dry for 28 days. This block is then placed in the bottom box of shear device and centered. The gap between the concrete block and the bottom box is 0.50 inch (1.25 cm) all around. Wooden wedges are driven in between to prevent any movement of the sample, Fig. (6.12). The elastic constants E and ν are 4.2 x 10^6 and 0.2 respectively.

Equipment Preparation

The initial operations on MTS control unit to be carried out are explained in section 5.6.1. With the top box centered over the
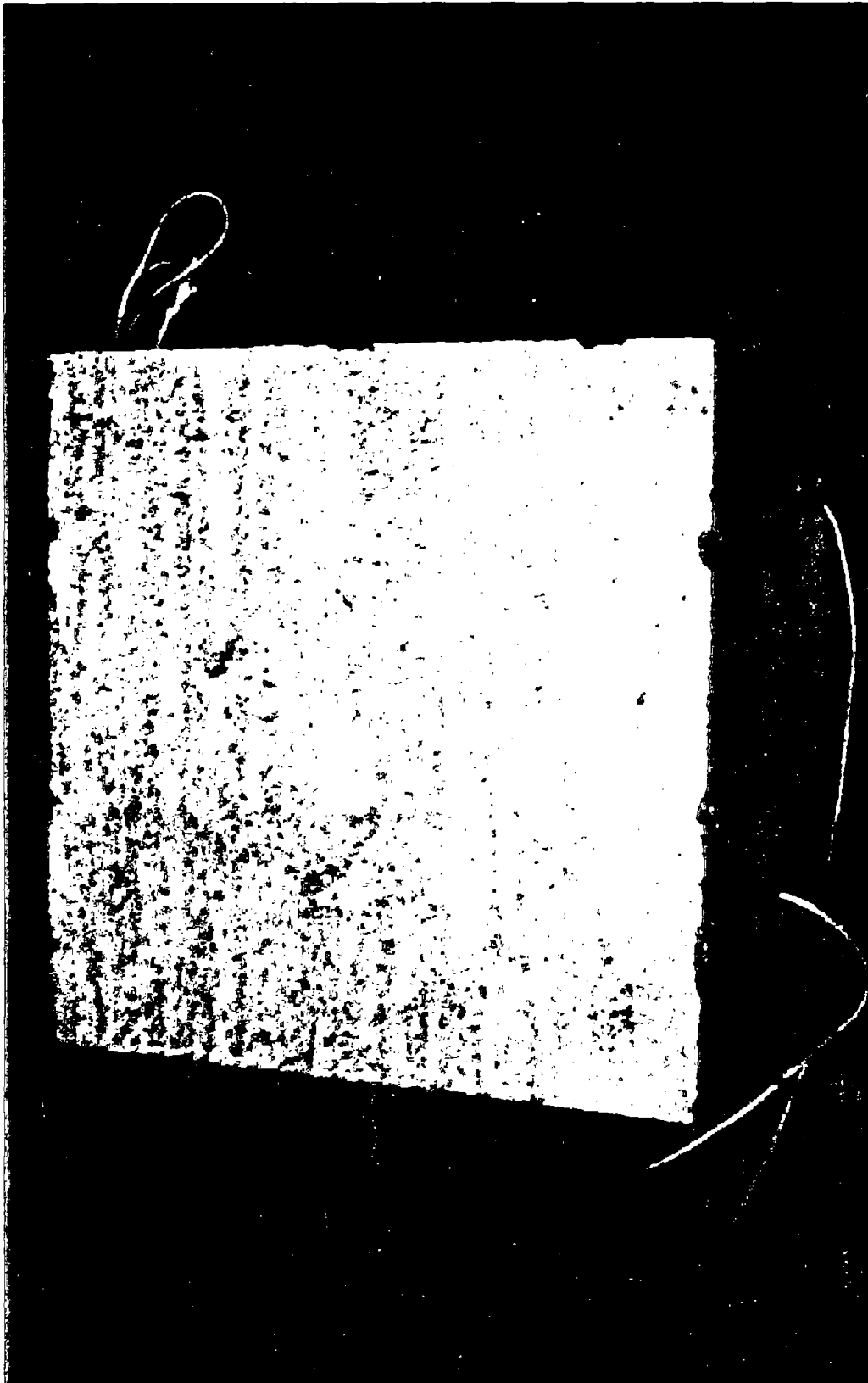
Figure 6.11 Concrete Block After Curing

Figure 6.12 Concrete Block in the Shear Box - Before Test

bottom box, the concrete block is adjusted to move up or down so that there is a gap of 0.10 inch (0.25 cm) between the top surface of concrete block and the bottom rim of the top box. This avoids any physical contact between the concrete block and steel rim of the top box.

With the top box centered over the bottom box, weighed ballast is spooned into the top box and compacted with proctor compaction. The cover plates are then fixed as explained in Section 5.6.1.

Testing

Both FEED BACK selects are set to transducer 2, namely the load cell. Both directions are now stress controlled. Function generator is set to a frequency of 0.5 Hz and a sine function loading. With no load in both vertical and horizontal directions, initial readings of the four transducers are taken.

If the vertical load to be applied is 3000.00 lbs (1364.00 Kg), it is applied incrementally and after applying each increment of load, readings are taken. The vertical LVDT records the deformation at each increment of loading.

Before the application of time-dependent horizontal load, again the four transducers are read and recorded. Both LVDT and load cell of horizontal direction will show zero reading. Before applying the horizontal load, the RUN button is pushed and SPAN knob of the MTS control unit for horizontal direction is operated to set the desired

magnitude of horizontal load. The readings on four transducers are taken at intervals like at Hz 100, 1000, 2000, 3000, and 5000 cycles. From the observations of pilot test results, it is seen that there is no further significant change in horizontal relative displacement after about 5000 cycles. So the tests are run upto 5000 cycles. For each normal load, the variation of relative displacement to horizontal shear at different cycles are plotted. The vertical deformation observed for different horizontal shear states over number of cycles are plotted for each normal load.

Test Results

The ratio of horizontal shear stress to the relative displacement is the shear stiffness. Figures (6.13-6.18) show the variation of relative horizontal displacement over number of cycles with respect to a horizontal shear with a given normal load. The initial shear stiffness (at shear stress equal to zero) is then calculated at 100, 1000, 2000, 3000 and 5000 cycles for each normal load (stress) and plotted in Fig. (6.19). At a constant number of cycles, shear stiffness is seen to increase with normal stress. On application of horizontal shear ver number of cycles, the shear stiffness decreases for the same normal load. The shear stiffness decreases for the same normal load. The shear stiffness degradation, for each normal load (stress) over number of cycles are presented in Fig. (6.20). Shear stiffness K_s decays as the number of cycles increases and then becomes near constant. The variation of K_s
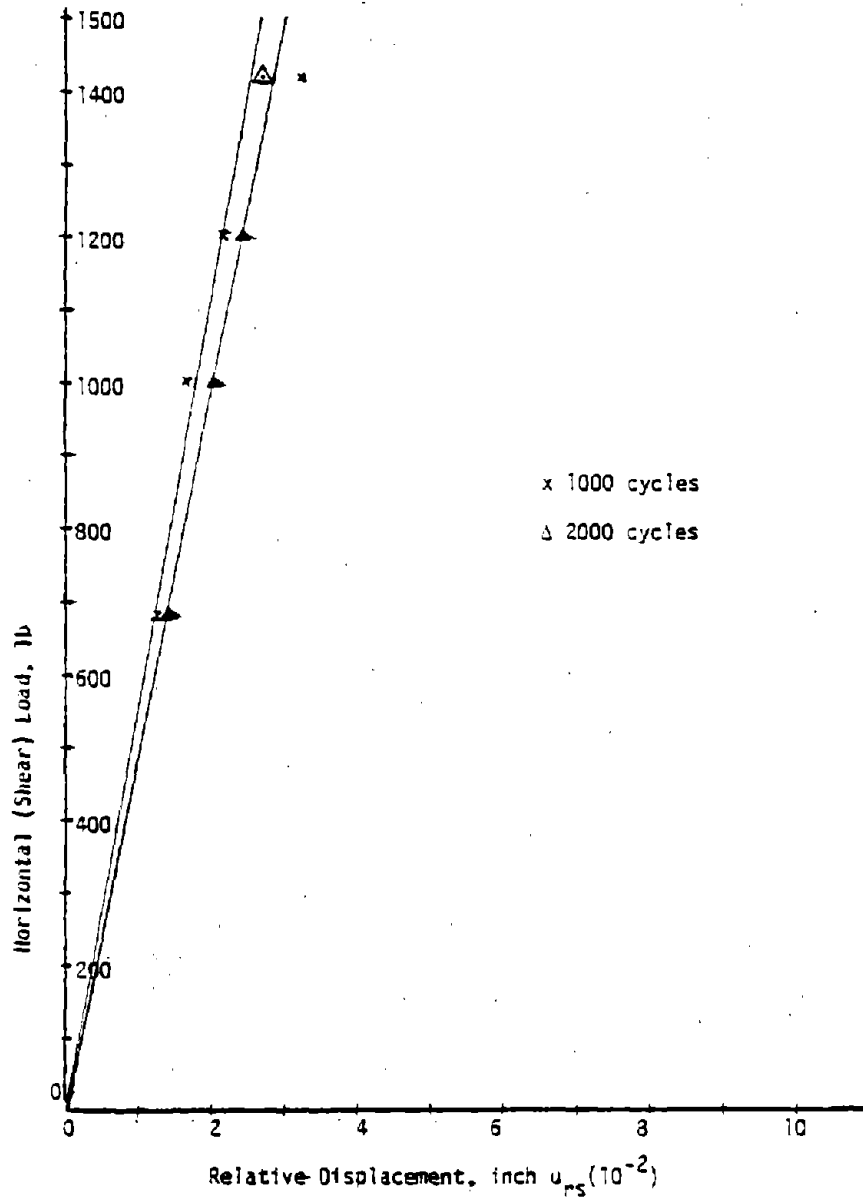
Figure 6.13 Variation of Relative (Horizontal) Desplacement with Shear Load (σ_{nn} = 6.94 psi)
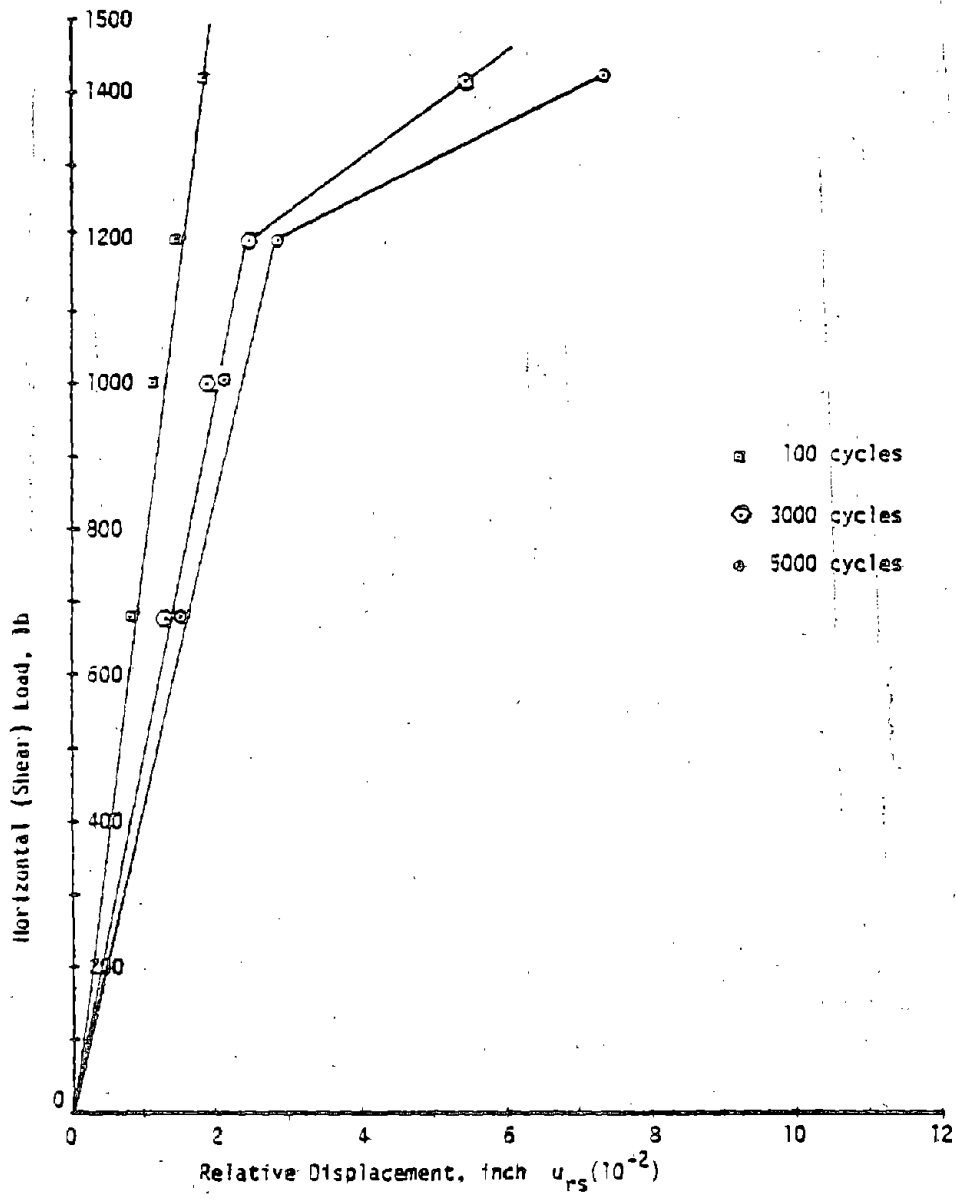
Figure 6.14 Variation of Relative (Horizontal) Displacement with Shear Load (σ_{nn} = 6.94 psi)
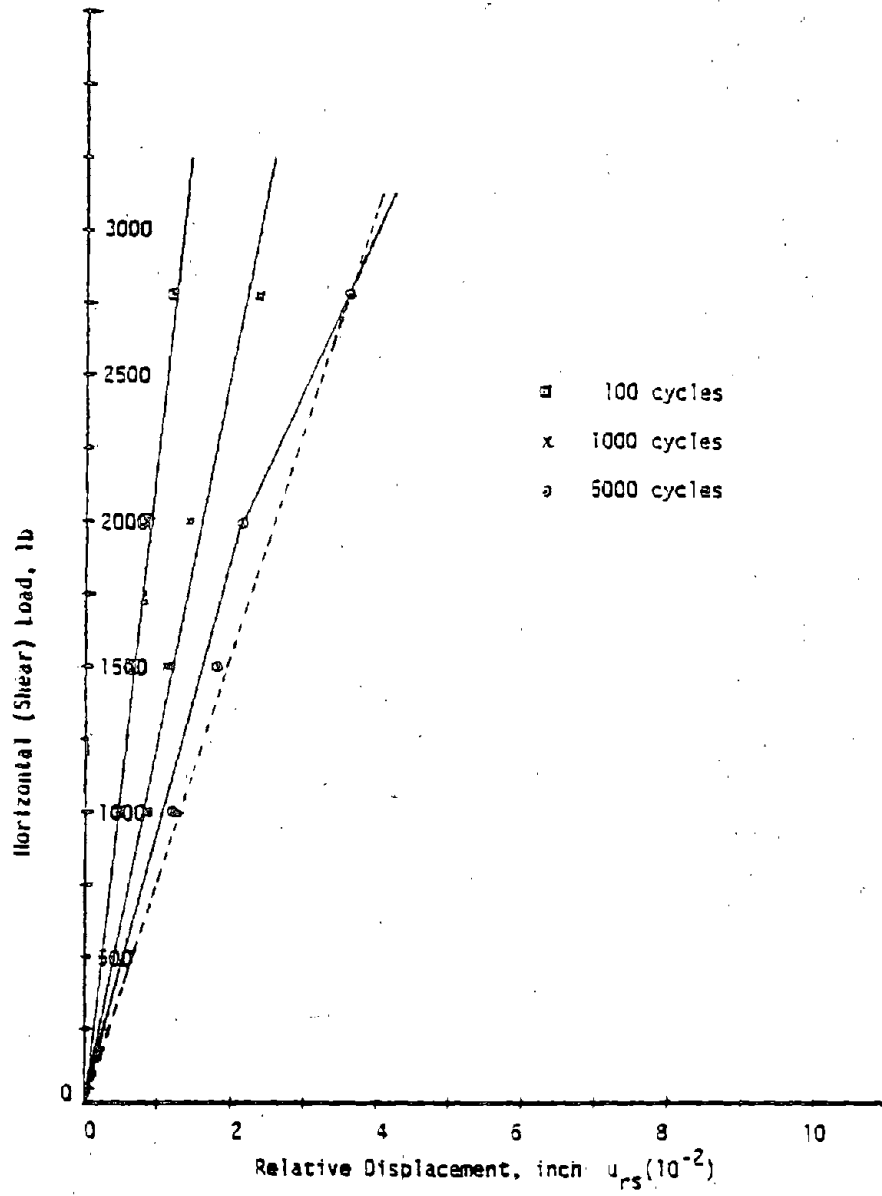
Figure 6.15 Variation of Relative (Horizontal) Displacement with Shear Load ($\sigma_{nn} = 20.83$ psi)
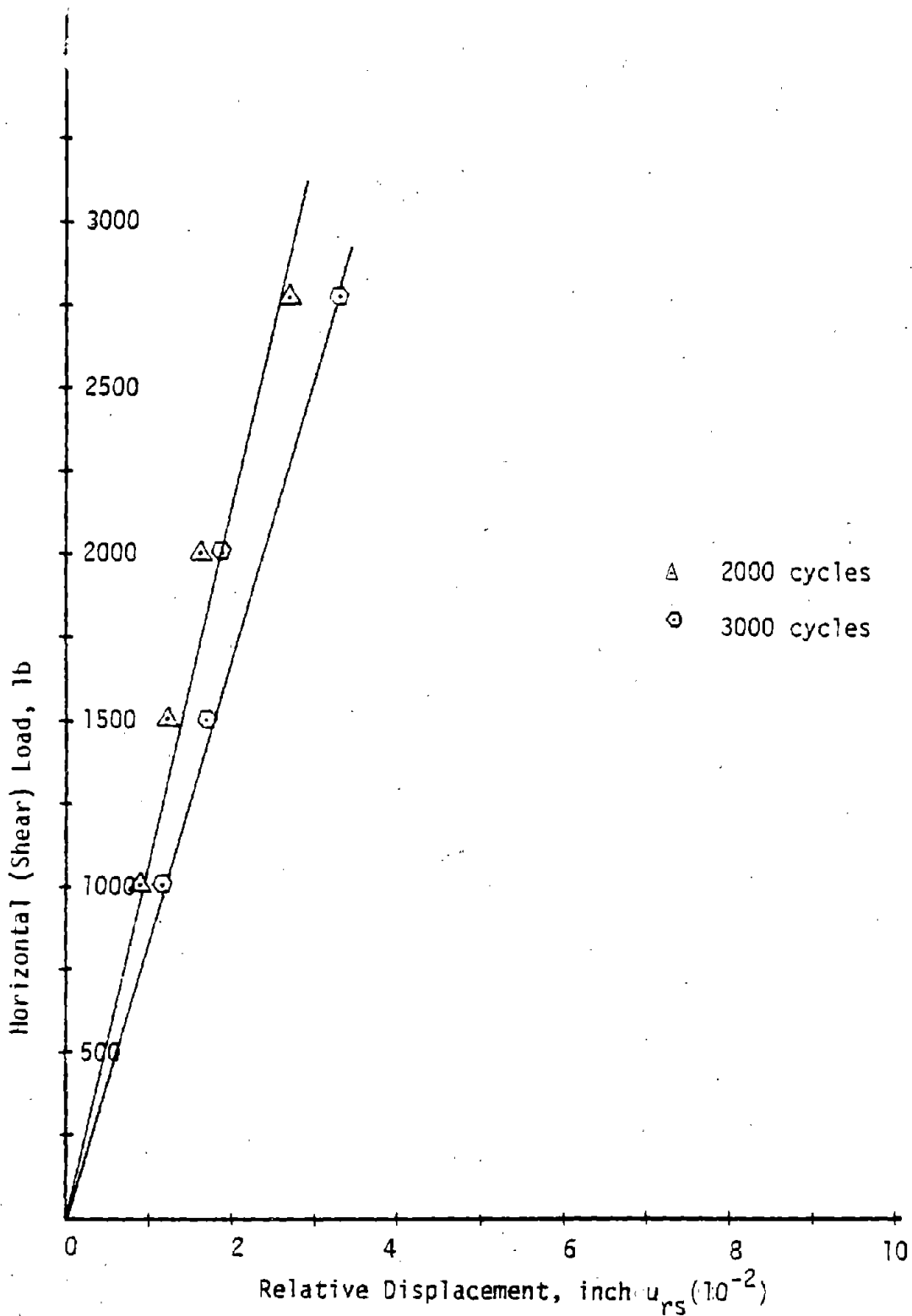
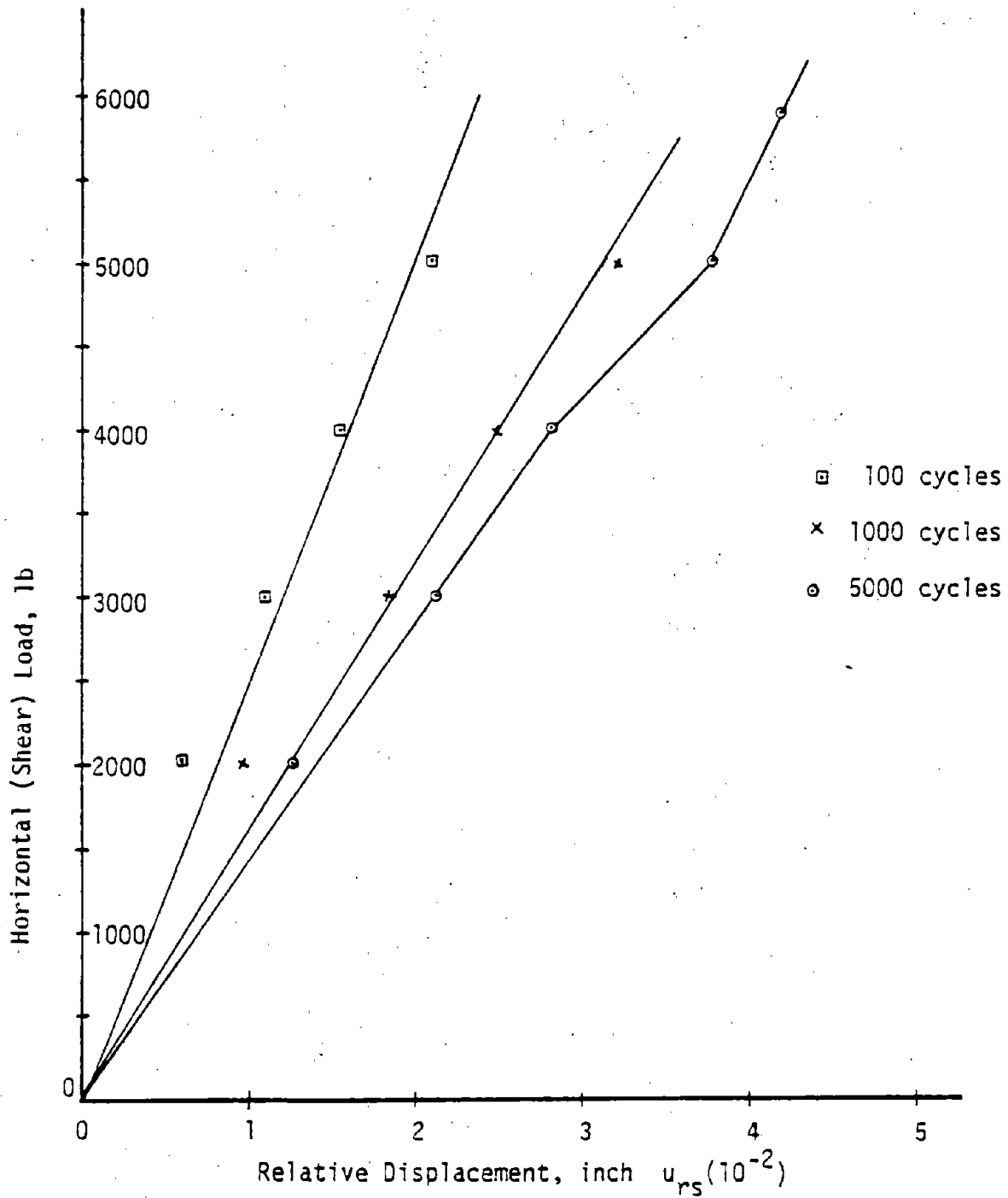Figure 6.16 Variation of Relative (Horizontal) Displacement with Shear Load (σ_{nn} = 20.83 psi)

Figure 6.17 Variation of Relative (Horizontal) Displacement
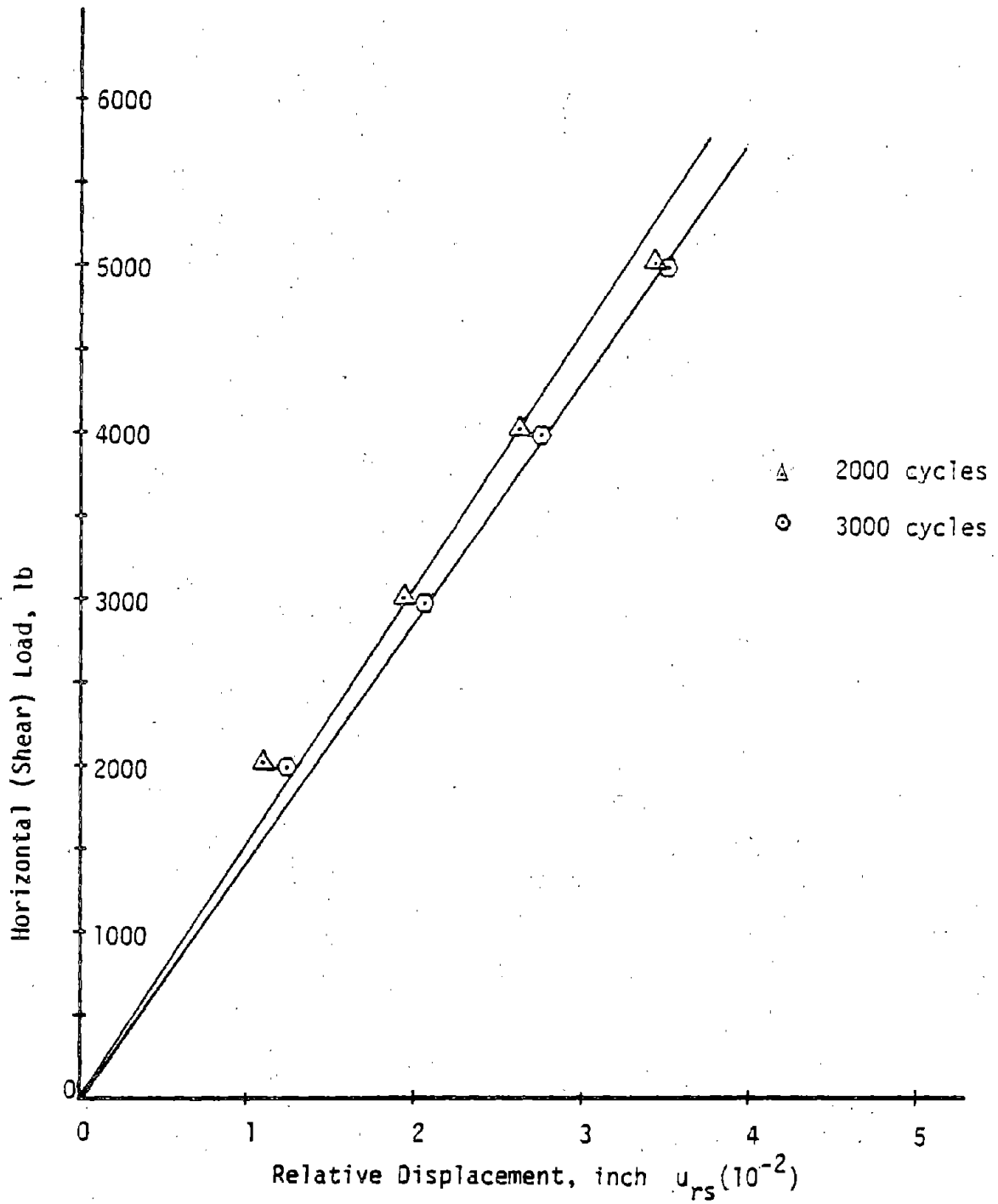with Shear Load (σ_{nn} = 48.6 psi)

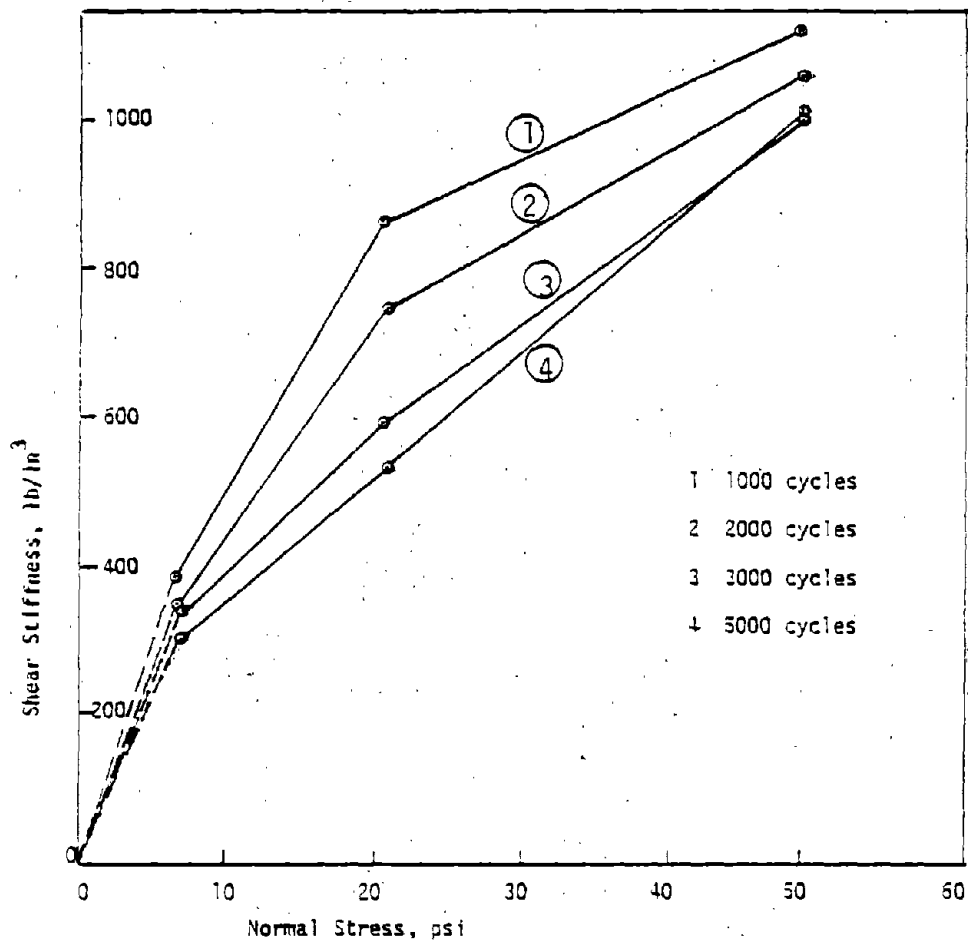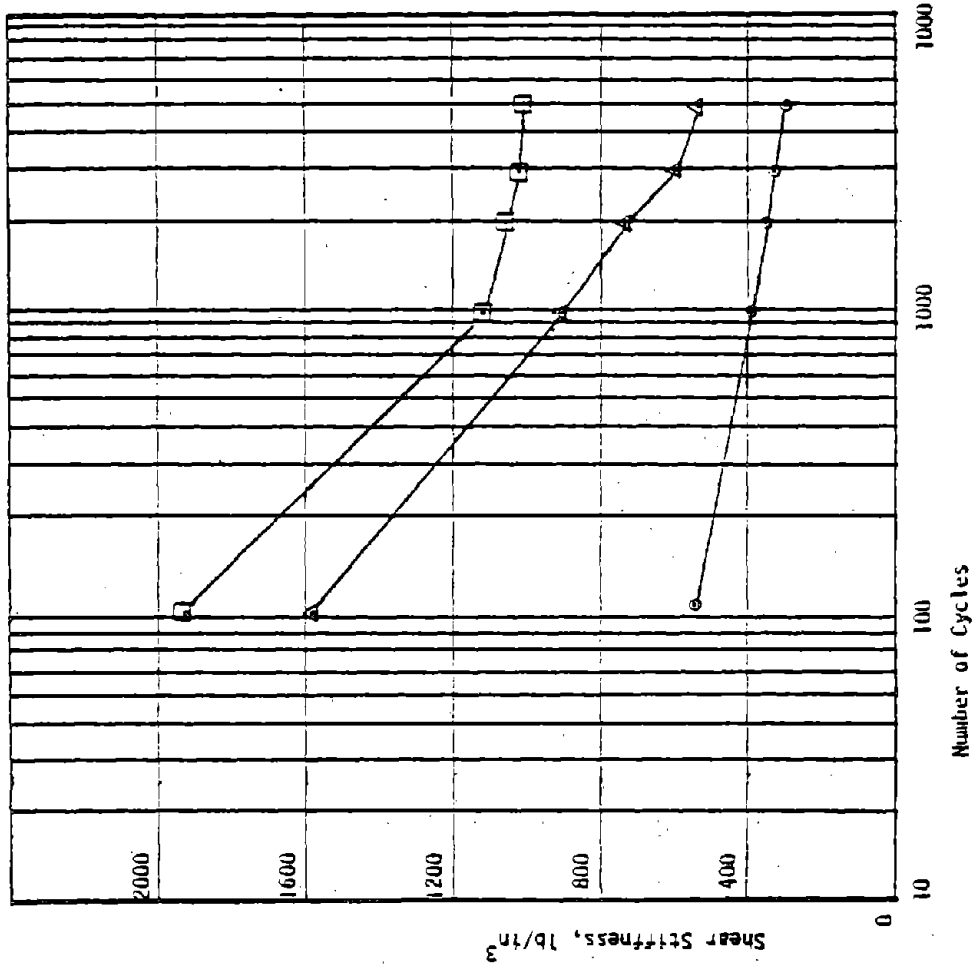Figure 6.18 Variation of Relative (Horizontal) Displacement with Shear Load (σ_{nn} = 48.6 psi)

Figure 6.19   Variation of Shear Stiffness of the
Interface with Normal Stress

Figure 6.20 Variation of Shear Stiffness of the Interface with Number of Cycles

with number of cycles is seen to be nonlinear. It is evident that K_s is a function of normal load and number of cycles.

Figure (6.21) shows the top surface of concrete block after the test, in which the initial contact area, a square of 12.00 x 12.00 inch (30.48 x 30.48 cm), is marked. It can be seen that the asperities are worn out due to abrasion by ballast. The distinction between the initial corrugated surface and the final worn out surface was found to be significant. The decay of K_s over a number of cycles can also be due to decrease in frictional resistance caused by gradual wearing of the asperities.

Figures (6.22, 6.24 and 6.26) show the variation of normal deformation over number of cycles for each horizontal shear state. The normal stiffness at 100, 1000, 2000, 3000 and 5000 cycles are determined for each horizontal shear state. The normal stiffness is K_{nn} is plotted for each ratio of σ_{nn}/σ_{ss} over the number of cycles. Figures (6.23, 6.25, and 6.27) show these variations for normal stresses 6.94, 20.83, 48.6 psi (47.88, 143.72 and 335.34 kpa) respectively. As the ratio σ_{nn}/σ_{ss} decreases, for a constant number of cycles, for a particular case of normal stress, K_{nn} decreases. As the number of cycles increases, for a constant σ_{nn}/σ_{ss}, K_{nn} decreases. The variation in most of the cases is nonlinear. As σ_{nn} increases, for a constant N values, and approximately constant value of the ratio σ_{nn}/σ_{ss}, K_{nn} increases significantly. Nevertheless this K_{nn} may not be regarded as the normal
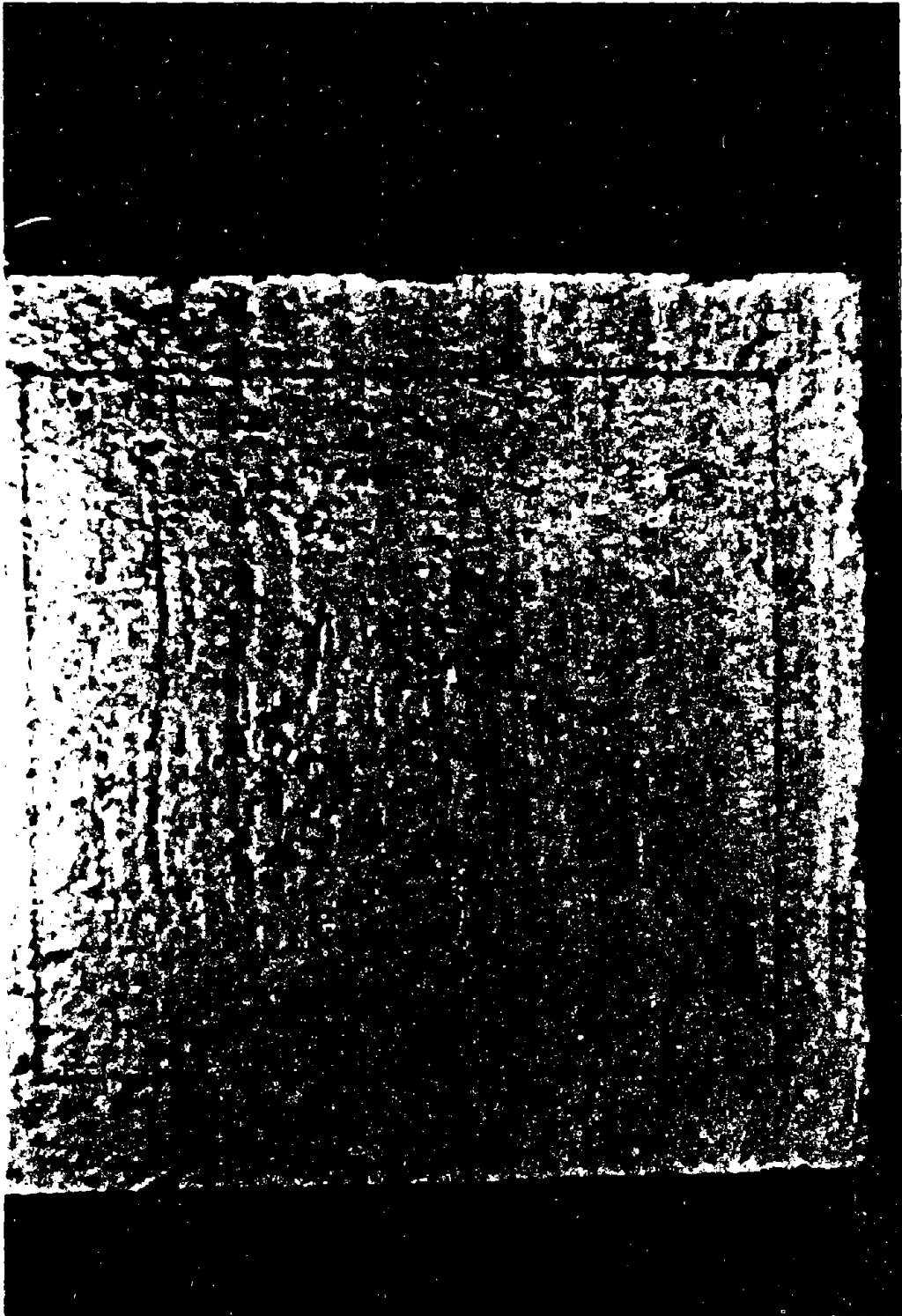
Figure 6.21 Concrete Block Surface - After Test

Figure 2.22 Variation of Vertical Deformation with Number of Cycles (σ_{un} = 6.94 psi)

Figure 6.23   Variation of Normal Stiffness with N (σ_{nn} = 6.94 psi)

Figure 6.24 Variation of Vertical Deformation with Number of Cycles (σ_{mn} = 20.83 psi)

Figure 6.25 Variation of Normal Stiffness with N (σ_n = 20.83 psi)
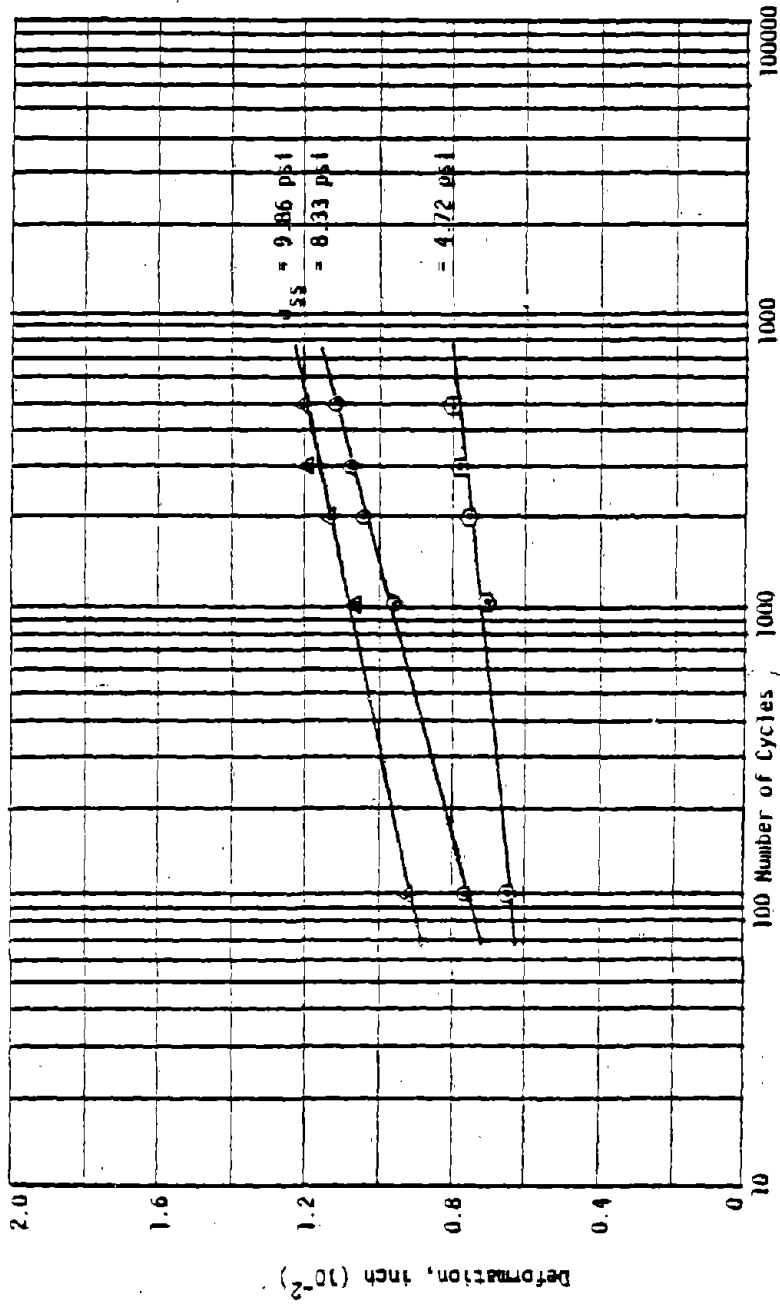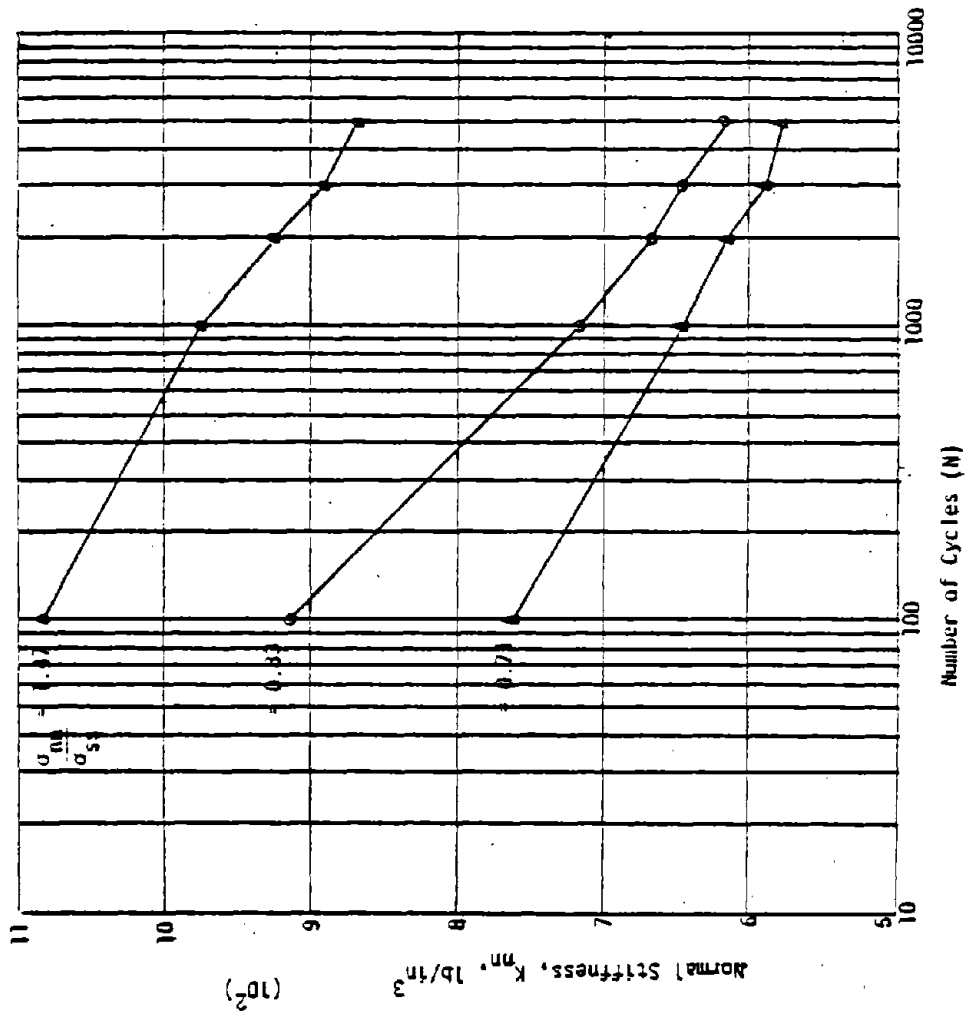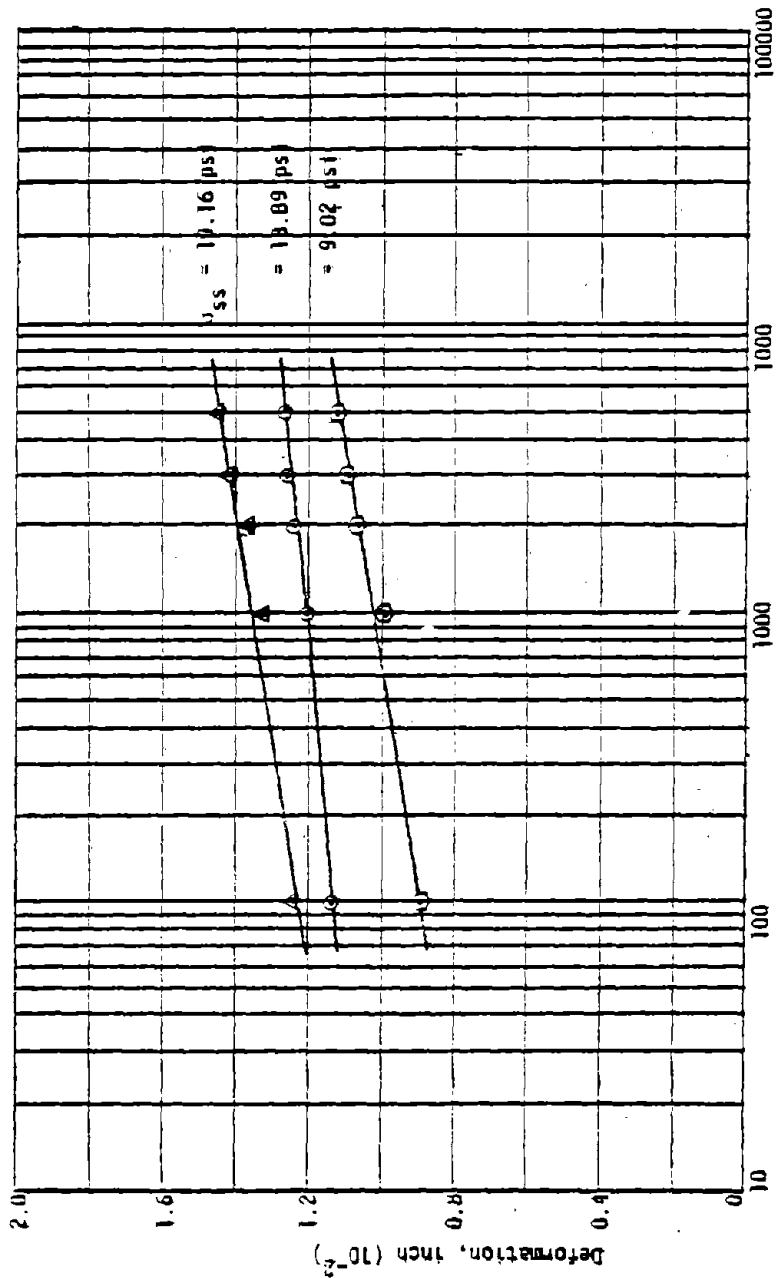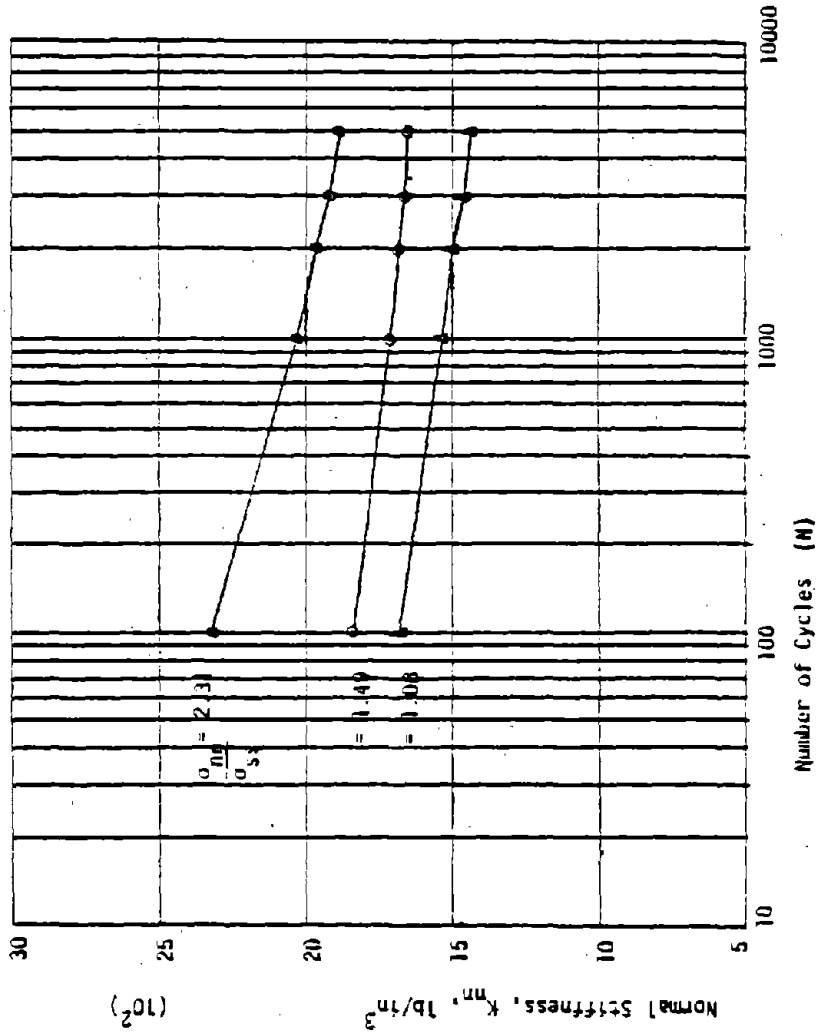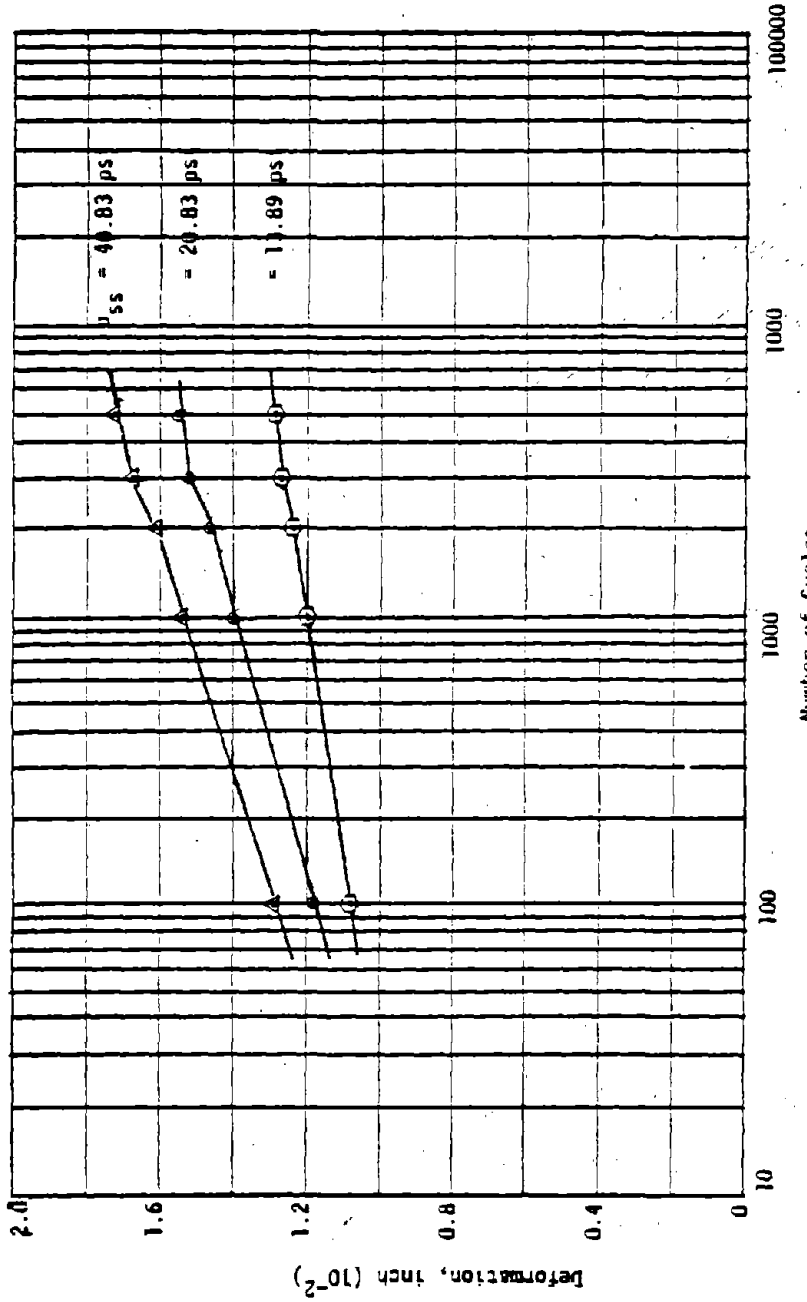
Figure 6.26 Variation of Vertical Deformation with Number of Cycles (σ_{DD} = 48.60 psi)
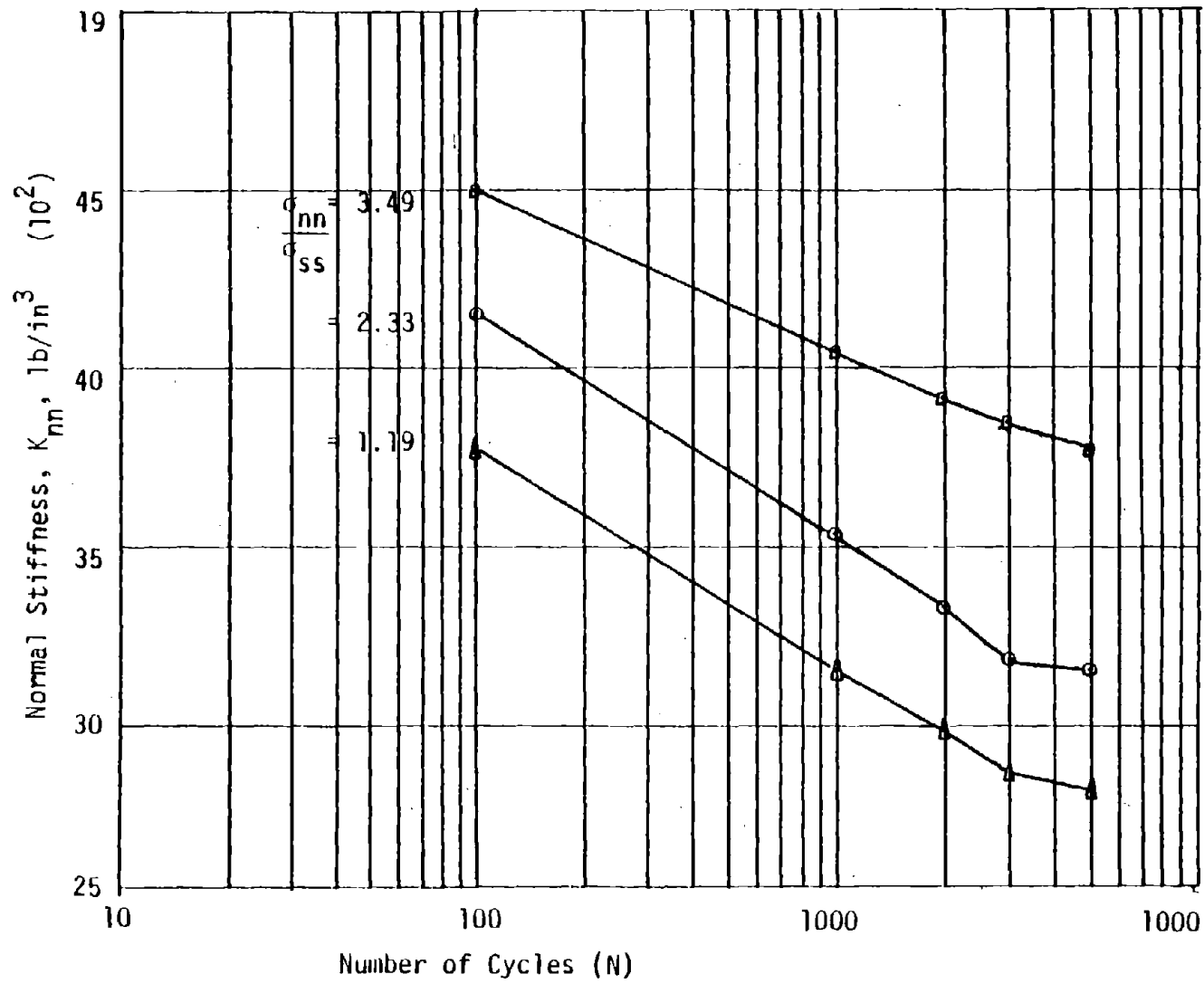
Figure 6.27   Variation of Normal Stiffness with N   (σ_{nn} = 48.60 psi)

stiffness at the interface. The stiffness of the column of ballast
also contributes to K_{nn} now determined and discussed.

6.6.3   Testing of Ballast - Subballast Interface

Ballast is placed on a bed of compacted subballast during the
formation of the track bed. Then ballast bed is tamped to attain
the desired field density. These two beds placed one over the other
transfer the load from the track to the subgrade soil. The ballast
just above subballast gets burried in the surface subballast and both
layers become almost an integral unit. Over number of passes of
moving load namely vehicle, these two beds get consolidated. The
normal stiffness increases during the period of consolidation. Once
these two beds get stabilized, the normal stiffness almost remains
constant thereafter.

A vertical vibration test is conducted on a column of subballast-
ballast. Both subballast and ballast used in this test are from the
UMTA test site at Pueblo, Colorado. The properties of subballast
and ballast are given in sections 2.5.1 and 4.5.2 respectively.

Testing Program

The subballast is spooned into the bottom box of the shear
device. It is compacted by Proctor compacting device to the field
density. The height of filling is 7.00 inches (17.78 cm).

The top box is then centered over the bottom box carefully.
The horizontal motion, any further, of the top box is now locked.
Ballast is placed in and compacted to an initial compacted density

of 112.00 pcf (1.79 g/cm^3). The final adjustments and equipment preparations are carried out as explained in section 6.6.1. Tests are planned to carry out at different normal loads like 500.00 lbs (227.20 Kg) 1000.00 lbs (454.40 Kg), 2000.00 lbs (908.80 Kg) and 3000.00 lbs (1363.20 Kg).

The vertical load is a repetitive load. Often, it is like a pulse type of loading as shown in Fig. (6.9). The function generator is set to a sine function of loading. The "set point" know is adjusted to apply 500.00 lbs (227.20 Kg), the desired dynamic load, as a static load. The RUN button in MTS 436 control unit is pressed and SPAN knob is not adjusted to apply 500.00 lbs (227.20 Kg), dynamic load. Total dynamic load is 500.00 lbs (227.20 Kg). As the FEEDBACK select is set for STRESS CONTROLLED, the load will be maintained and the vertical LVDT records the deformations. The accumulated vertical strain is calculated at the end of 5000 cycles and plotted. Figure (6.28) shows the variation of normal stiffness of the two beds together with σ_{nn}. Fig. (6.29) shows the surface of the subballast bed after the test. Ballast is removed very carefully without disturbing the subballast. The indendations made by ballast penetration on the subballast surface is clearly seen.
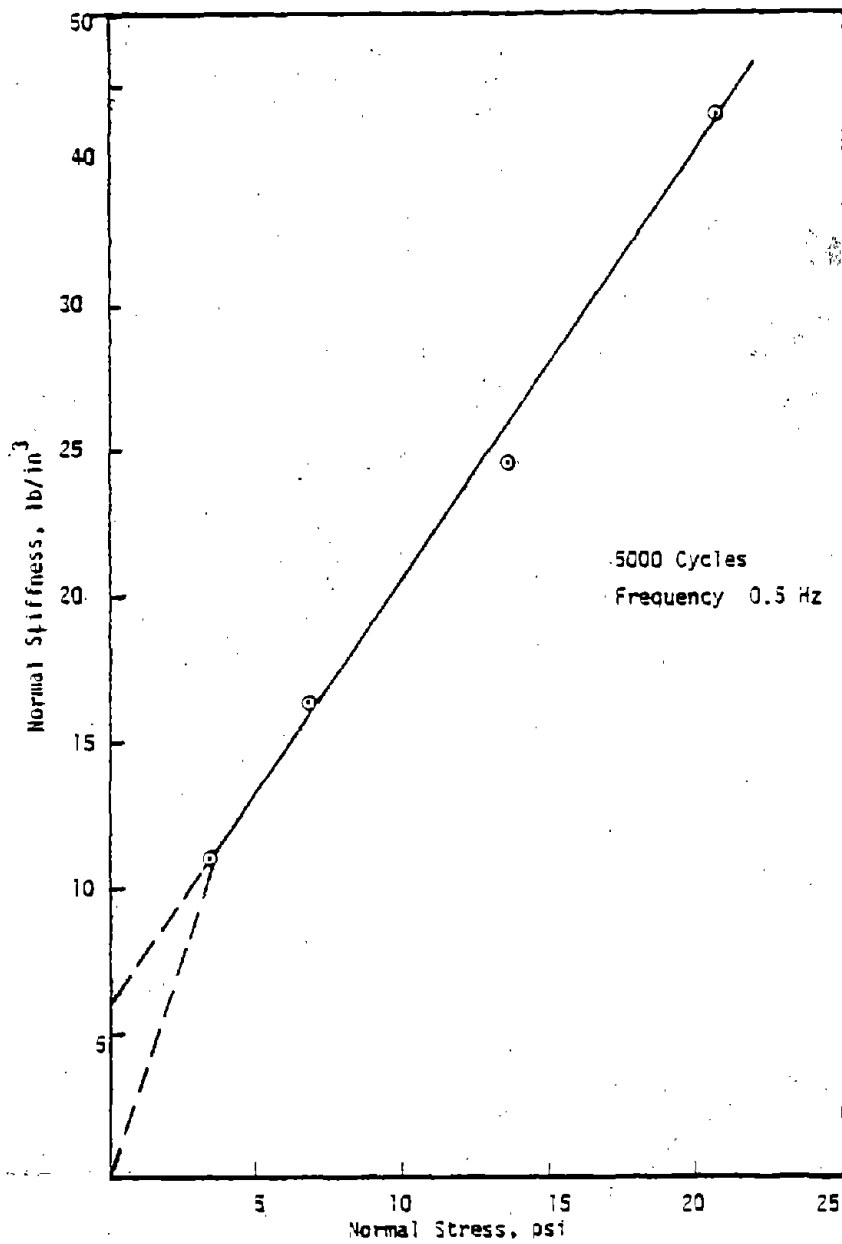
Figure 6.28   Variation of Normal Stiffness with Normal Stress
for Ballast - Subballast

Figure 6.29 Surface of Subballast Bed – After Test

6.6.4 Tests at Higher Loading and Different Frequencies

Two additional tests were performed to study the behavior of ballast-subballast interface subjected to higher values of vertical repetitive loading and two frequencies 0.5 and 1.0 Hz. Table 6.1 shows details of the dimensions of ballast and subballast, densities of each, initial or insitu pressure p_0, and amplitude of applied sinusoidal load for the two tests with frequencies of 0.5 and 1 Hz. Figure 6.30 shows shows a schematic of the specimen showing ballast-subballast interface.

The tests were conducted up to number of cycles of loading N = 10,000. Figure 6.31 shows typical results in terms of total normal stress σ_n (which is the sum of the initial pressure p_0 and the function F (t) = A sinωt) and accumulated vertical strain. The data points do not yield a smooth curve; this can be due to the continuing reorientation of the particles of ballast during the repetitive loading. It can be seen that as the number of loading cycles increase, the strain increases. However, the rate of increase diminishes at greater number of loading cycles. Figure 6.32 shows observed relations between accumulated strain and number of cycles of loading, N, for tests with the two frequencies. The trend of reduced rate of increase in the strain or stabilization of strain at greater number of cycles is illustrated in this figure. It may be noted that the trends for both frequencies in this figure are similar, although there is a difference in the magnitudes of strain for a given N.

In the above tests, the initial load p_0 was first applied 'slowly' in four increments; then the cyclic load was applied. The relation between

Table 6.1   Details of Tests Under Higher Loading

Test Number	Frequency Hz	Height of the Subballast (inch)	Height of the Ballast (lb/cft)	Unit Weight of Subballast (lb/cft)	Unit Weight of Ballast (lb/cft)	Initial Pressure (psi)	Amplitude of Cyclic Load (psi)
1	0.5	5.75	7.500	133	112.0	20.0	11.875
2	1.0	5.75	7.875	135	112.5	20.0	11.875

1 psi = 6.89 kPa

1 inch = 2.54 cm

$F(t) = A \sin\omega t$

Ballast

16"
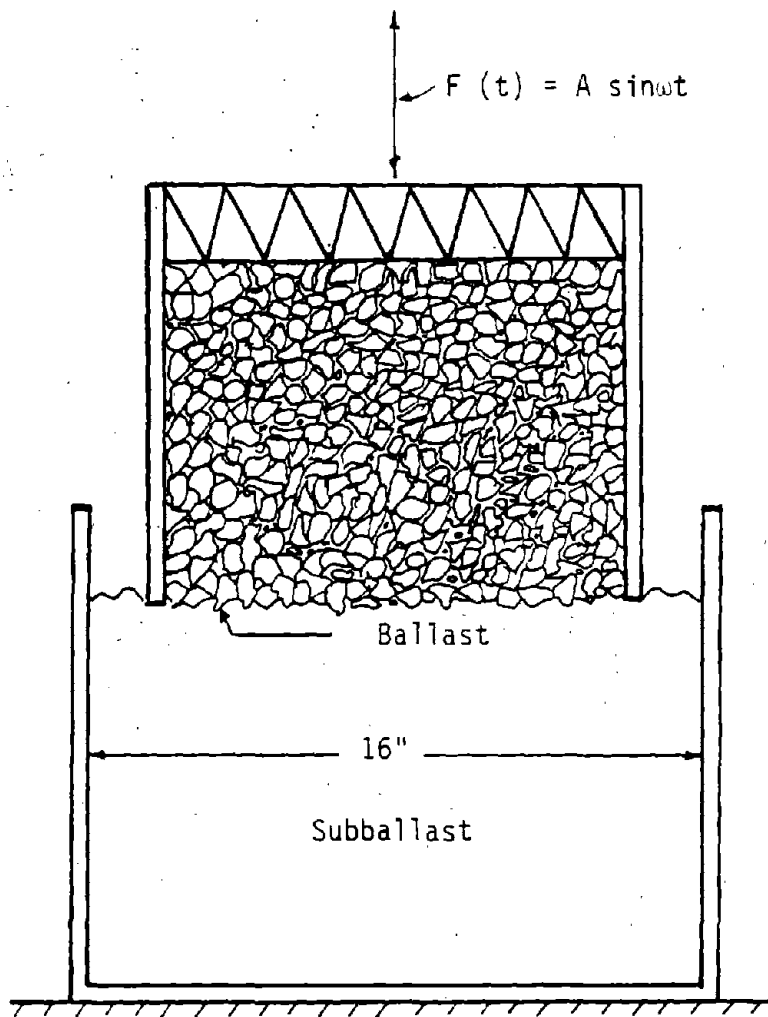
Subballast

1 inch = 2.54 cm

Figure 6.30   Schematic of Ballast-Subballast Interface

Initial Pressure p_0 = 20 psi
Amplitude of Loading A = 11.875 psi
Frequency = 0.50 Hz
(ω)

F (t) = A sinωt

Load

p_0

Time

Normal stress, σ_n, psi

40

30

11.875

20

10

N = 1   2   3   9,10   49,50   299,300   1999,2000   4999, 5000

6999,7000   10,00

Assume zero at the end of p_0 (Fig. 6.33)

0   20   40   60
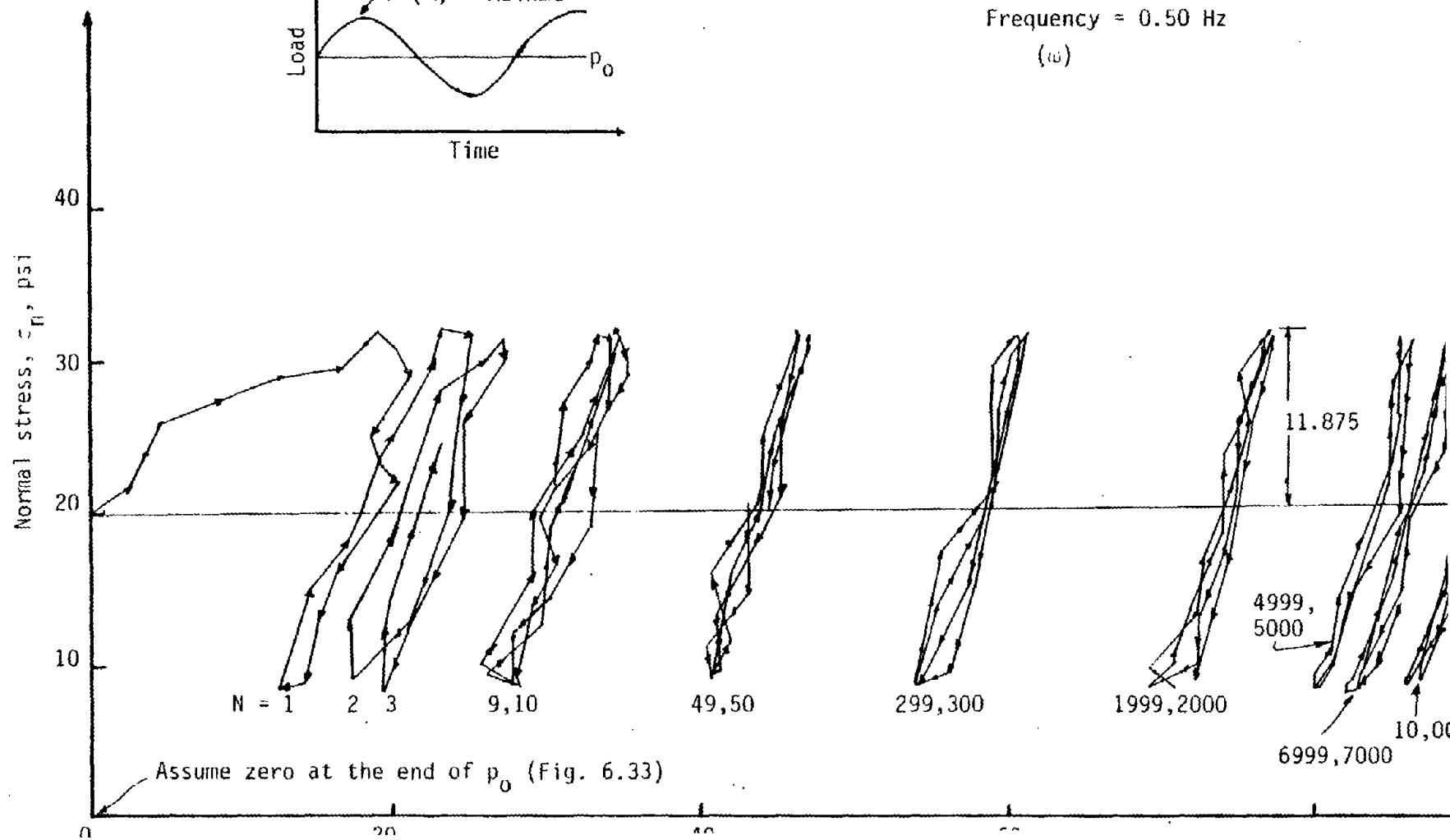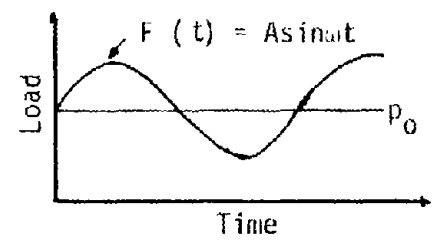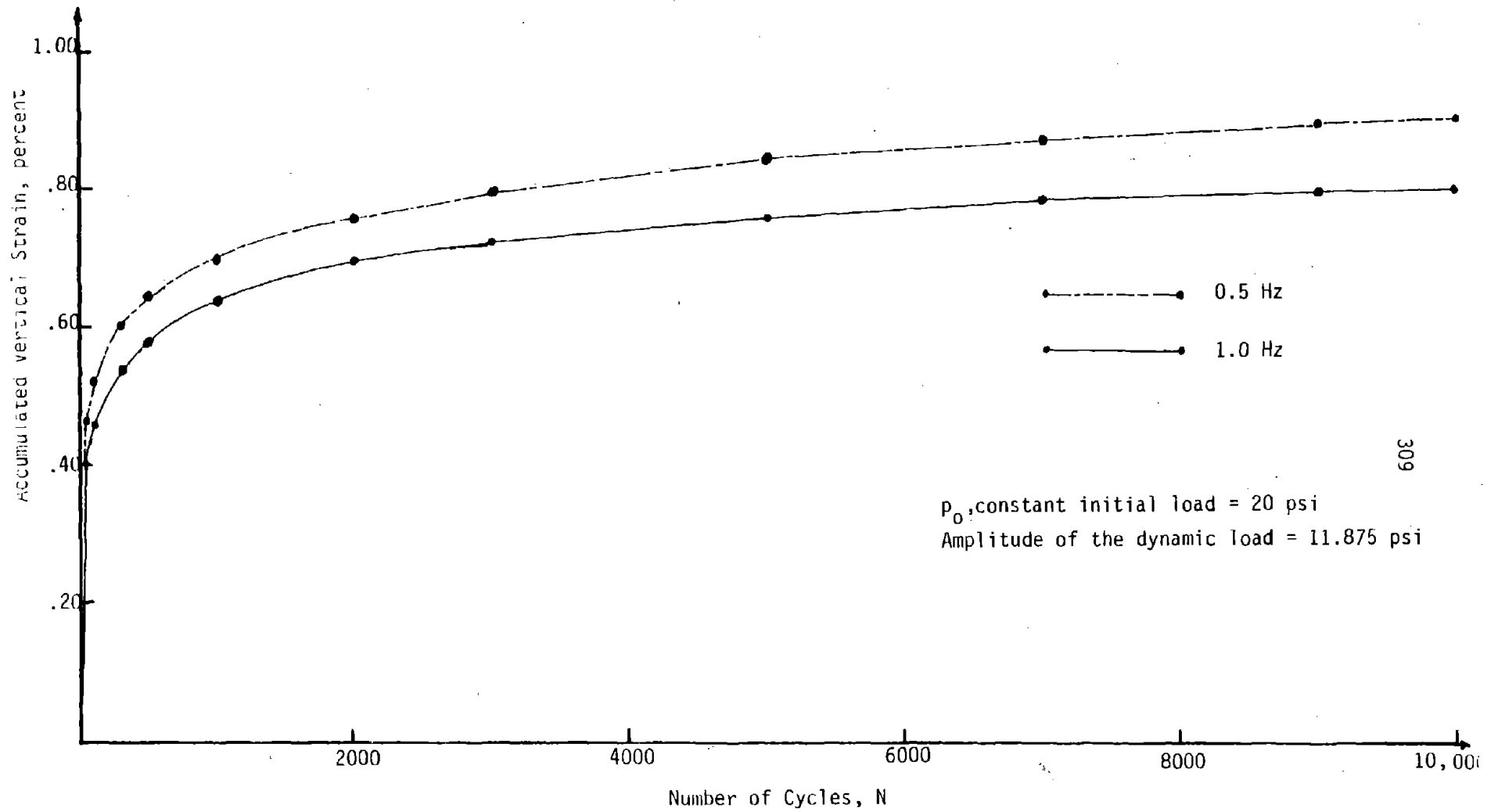
Figure 6.32   Relations Between Accumulated Strain vs Number of Cycles

normal stress σ_n and vertical strain for the slow loading is shown in Fig. 6.33. The average slope of the curve, which is a measure of the constrained 'static' modulus, is about 4400 psi (30 MPa).

Figure 6.34 shows variation of constrained cyclic modulus with number of cycles; it represents average slope of the unloading-reloading loops in Fig. 6.31. The value of this modulus is low for the first 1 to 3 cycles, then it increases at a faster rate and after about 2000 cycles, it stabilizes.

Comment

In view of limitations on time and resources, only a limited number of tests have been possible with the CYMDOF device. However, these tests have indicated that the device is capable of providing satisfactory and realistic results. Further research can be carried out for studying behavior of interfaces under vertical and horizontal motions and of track materials under vertical motions by using the device.

Figure 6.33   Normal Stress vs Strain Under Initial Loading

311

Figure 6.34 Variation of Constrained Cyclic Modulus
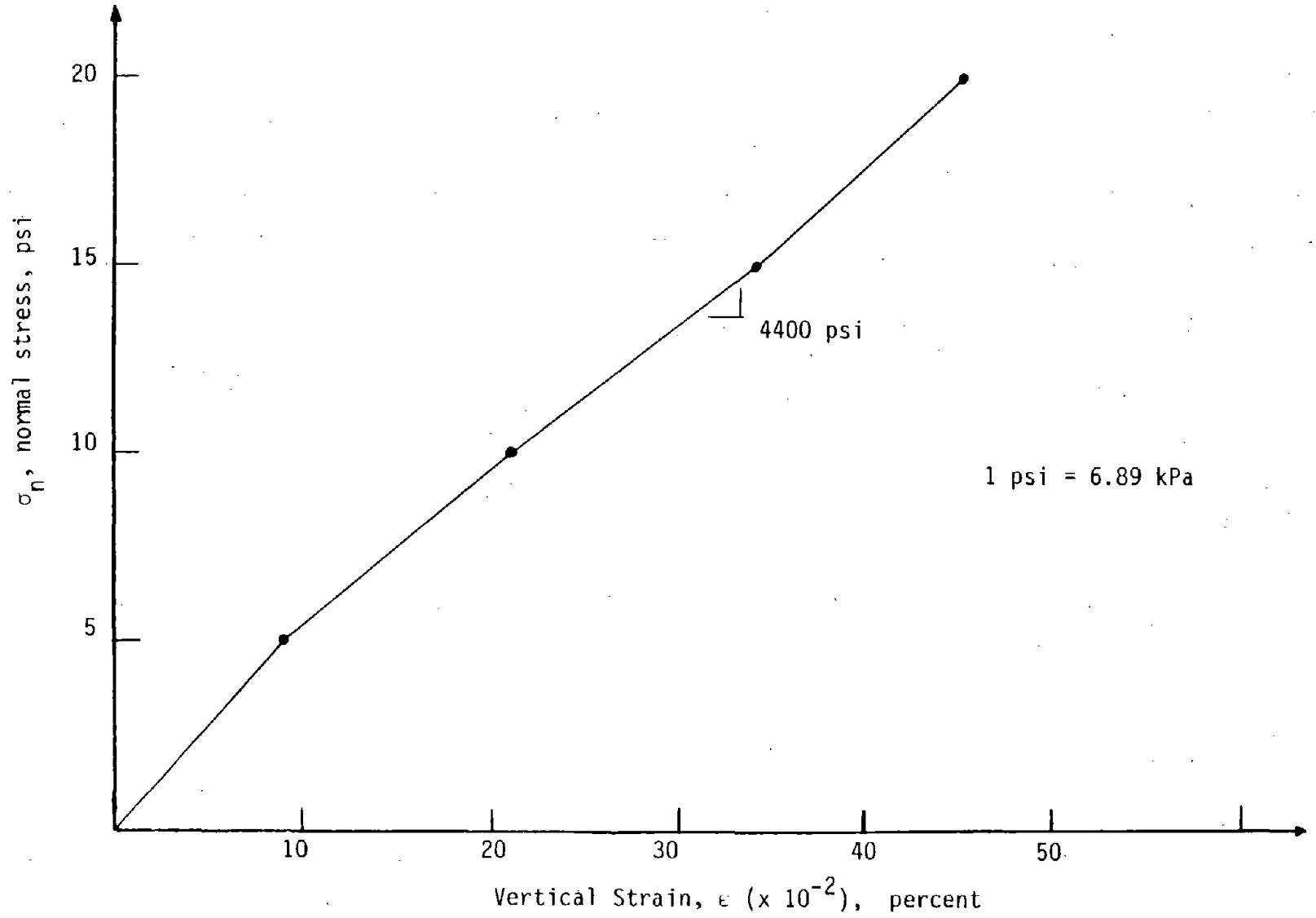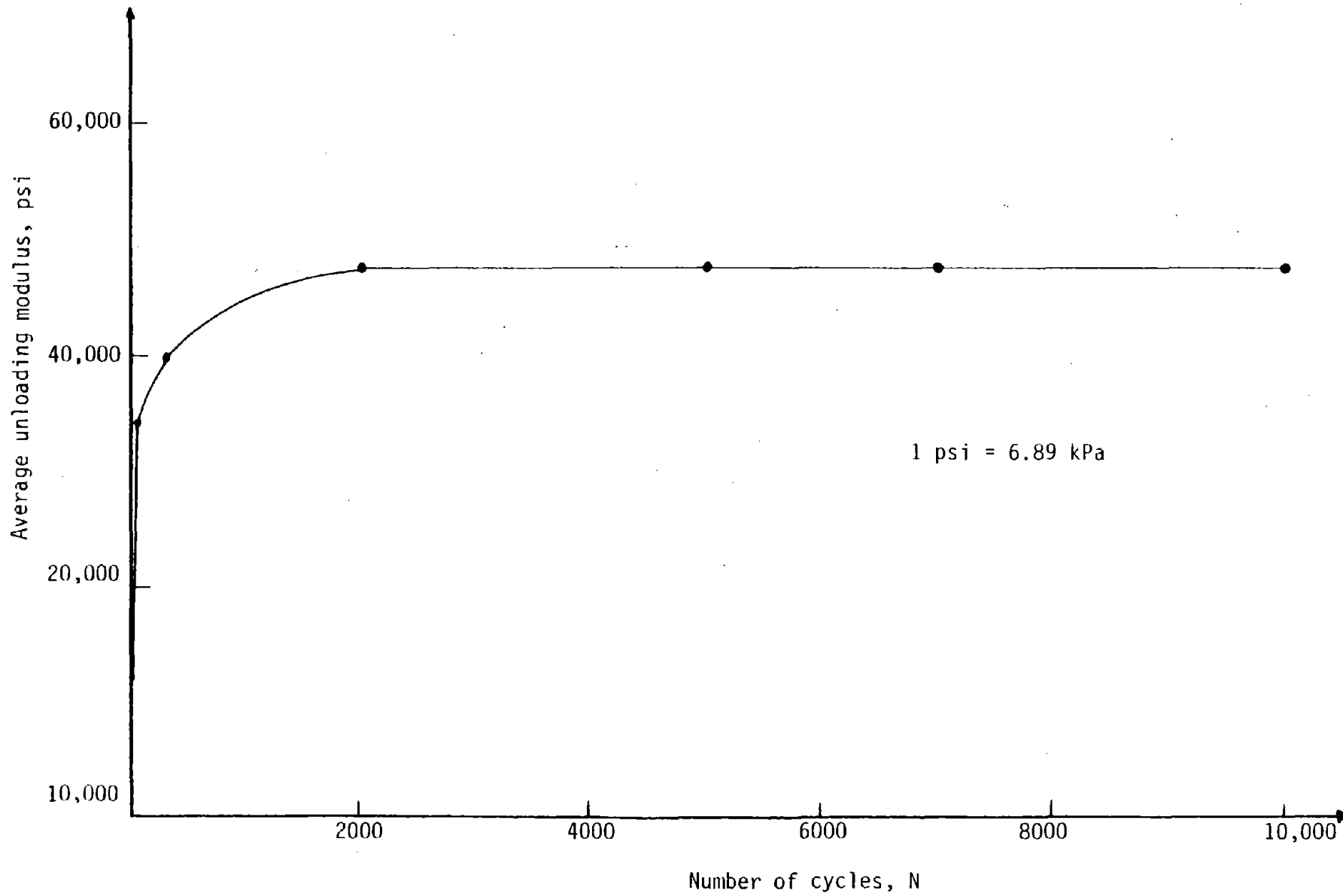
312

CHAPTER 7

SUMMARY

The materials in Track beds and interfaces between them exhibit complex stress-strain response. In order to obtain satisfactory predictions of the actual behavior of track support structures from any solution procedure such as closed-form and computer based, it is essential that the stress-strain response is determined from appropriate laboratory tests.

In order to characterize three-dimensional behavior of wood in ties, ballast, subballast and subgrade soils, this study uses truly triaxial or multiaxial devices. These materials are tested under a variety of realistic stress paths that can occur in the track beds under loadings from the vehicles. Based on the test results, it is possible to determine appropriate stress-strain or constitutive models for different materials affected by factors such as anisotropy, state of stress, stress path, plastic behavior, hardening and volume change behavior under shear.

A new cyclic device, called CYMDOF, is developed and used for testing interfaces between wood and ballast, concrete and ballast and ballast and subballast. It is possible to develop various elastic and plastic stress-strain models for interfaces as affected by factors such as state of stress, accumulated strain, frequency and number of loading cycles. Only limited number of interface tests have been

conducted. This is a unique device and it has significant potential for studying interface behavior as well as uniaxial behavior of track materials for design, maintenance and safety analysis.

In the past, most investigations have studied laboratory behavior of track materials under uniaxial or cylindrical triaxial tests. Hardly any previous studies have considered the important question of behavior at interfaces. The research herein goes a step forward in testing for three-dimensional behavior of track materials, and it opens a rather new direction in testing for behavior of interfaces.

REFERENCES

1. AAR Research and Test Department report on "Comparitive Study of Physical Properties of various Types of Wood", in Rail Road Cross Ties, July 1977.

2. Allen, J. J., "The Effects of Non-Constant Lateral Pressures on the Resilient Properties of Granular Materials," Ph.D Thesis University of Illinois, 1973.

3. Allen, J. J., and Thompson, M.R., "Resilient Response of Granular Materials Subjected to Time Dependent Lateral Stress," Transportation Research Report No. 5 0, pp. 1-13, 1973.

4. American Railway Engineering Association, Manual of Recommended Practice, American Railway Engineering Association, 59, East Van Buren St, Chicago, 1969.

5. American Society for Testing and Materials - Standared Methods of Testing Small Clear Specimens of Timber ASTM D, 969, pp. 43-52.

6. Barksdale, R. D., "Repeated Load Test Evaluation of Base Course Materials," Ph.D Thesis, Georgia Institute of Technology, Atlanta, 1972.

7. Bodig, J., and Goodman, J. R., "Prediction of Elastic Parameters for Wood," Wood Science Vol. 5, No. 4, pp. 249-264, April 1973.

8. Boyce, J. R., et al, The Resilient Behavior of a Granular Material under Repeated Loading, ARRB Proceedings, Vol. 8, 1976.

9. Brown, S F., "Repeated Loading Tests on a Granular Material," J. Geo. Tech. Engg. Dvn, ASCE, Vol. 00, No. GT 7, July 1974 pp. 825-84 .

10. Brumund, W. E., and Leonards, G. A., "Experimental Study of static and Dynamic Friction between Sand and Typical Construction Materials," J. of Testing and Evaluation, ASTM, 1.2, 1973, pp. 162-165.

11. Burdell, C .A., " State-of-the-Art of U.S.A, Rail Road Cross Ties," Report to the Railway Tie ASSn, Aug 1977.

12. Chamberlin, W. P., and Yoder, E. J., "Effect of Base Coarse Gradation on Results of Laboratory Pumping Tests," Proceedings of the Highway Research Board, Washington, Bulletin 202, 1958, pp. 59-79.

13. Dean Marachi, N., et al, " Evaluation of Properties of Rockfill Materials," J. of Geo. Tech. Engg, Dvn. ASCE, Vol. 98, No. SM 1, Jan 1972, pp. 95-113.

14. Desai, C.S., et al, "Procedure, Selection and Application of Plasticity Models for a Soil", International J. for Numerical and Analytical Methods in Geomechanics, Feb 1980

15. Desai, C. S., and Christian, J. T., (Eds), Numerical Methods in Geotechnical Engineering, McGraw-Hill Book Co, 1977.

16. Desai, C. S., "Some Aspects of Constitutive Models for Geologic Media," Proc. 3rd. Int. Conf. Num. Meth. in Geomech., Aachen, W. Germany, 1979.

17. Desai, C. S., and Srivardane, H. J., "Constitutive Laws for Engineering Media., Prentice-Hall, Under Publication

18. Desai, C. S., and Janardhanam, R., " A High Capacity Truly Triaxial Device and Applications, " Submitted to J. Geotech. Testing, ASTM.

19. Desai, C. S., Siriwardane, H. J., and Janardhanam, R., "Load Transfer and Interaction in Track Guide-way System, " Report Sumitted to D.O.T. Univ. Research, 1980.

20. Desai, C. S., "A General Basis for Yield, Failure and Potential Functions in Plasticity," International J. For Numerical and Analytical Methods in Geomechanics. Vol. 4, 1980, pp. 361-375.

21. Desai, C. S., and Siriwardane, H. J., "A concept of Correction Functions to Account for Non-Associative Characterestics of Geologic Media, International J. for Vol. 4, 1980, pp. 377-387.

22. Desai, C. S., and Janardhanam, R., "User's Manual for Dynamic Multi-Degree of Freedom Shear Device", - Report, Department of Civil Engineering, Va Tech, 1981.

23. Desai, C. S., "A Dynamic Multi-Degree of Freedom Shear Device," Report No. 80. 36, Department of Civil Engg, Va.Tech, Aug 1980, Submitted to J. Geotech. Testing, ASTM.

24. Desai, C. S., and Wu, T. H., "A General Function For Stress-Strain Curves," 2nd International Conference on Numerical Methods in Geomechanics 1976, VPI & SU.

25. Desai, C. S., "Soil-Structure Interaction and Simulation Problems," Finite Elements in Geomechanics, Ed. by Gudehus, G., John Wiley, N.Y, 1977.

26. DiMaggio, F. L., and Sandler, I. S., "Material Model for Granular Soil", J. of Engg. Mech. Dvn. ASCE, Vol. 197, No. 3, 1971.

27. Donaghe, R. T., et al, "Strength and Deformation Properties of Rock Fill, " Technical Report. 8, U.S. ARmy Expt. Stn. Vicksburg, Jan 1978.

28. Drucker, D. C., "On Uniqueness in the Theory of Plasticity," Quarterly of Appl. Math., Vol. 14, 1956.

29. Drucker, D. C., "Some Implications of Work-Hardening and Ideal Elasticity," Quarterly of Appl. Math., V. 7, No. 4, 1950, pp. 411-418.

30. Drucker, D. C., "A More fundamental approach to Plastic Stress-Strain Solutions," Pro. 1st U.S National Congress of Applied Mechanics (487-491).

31. Gaskin, P. N., and Raymond, G. P., "Response of Rail-Road Ballast to Vertical Vibration," Transportation Engg. J. ASCE, Vol. 104, No. TE 1, Jan 1978, pp. 75-87.

32. Gaskin, P. N., and Raymond, G. P., "Constribution to Selection pf Rail Road Ballast," Proc. ASCE., Vol. TE 2, 1976, pp. 377-394.

33. Goodman, J. R., "Structural Design With Wood an Over Review, " Wood Science, 1973.

34. Goodman, J. R., and Bodig, J., "Orthotropic Elastic Properties in Wood in Compression," pp. 2301-2319. J. of Structural Dvn. ASCE Vol. 96, No. ST 11, 1970, Proc. Paper 7682.

35. Goodman, J. R., and Bodig, J., "Orthotropic Strength of Wood in Compression," - Wood Science, Vol. 4, No. 2, Oct 1971, pp. 83-94.

36. Hicks, R. G., and Monismith, C. L., "Factors Influencing the Resilence Response of Granular Materials," Highway Research Record 345, TRB. 1971, pp. 15-31.

37. Hill, R., "The Mathematical Theory of Plasticity - Oxford - Clarendon Press, England, 1950.

38. Huck, P. J., et al, "Dynamic Response of Soil/Concrete Inter- faces at High Pressure," Report. AFWL-TR-73-264, IIT Research Institute, Chicago.

39. Kaman Sciences Corporation, Report to D.O.T 1979, Oct. Deter- mination of Vehicle Induced Forces on Transit Track Structure.

40. Kirkpatric, W. M., "Effects of Grain Size and Grading on the Shearing Behavior of Granular Materials," Proceedings of 6th International Conference on SM & FE, Vol. 1, 1965, pp. 273-277.

41. Knutson Reid Merry, "Factors Influencing the Repeated Load Behavior of Railway Ballast," Ph.D. Thesis 1976. University of Illinois.

42. Knutson, R., Thompson, M., Mullin, T., and Tayabji, S., "Materials Evaluation Study-Ballast and Foundation Materials Research Program," Report No. FRA - OR & D - 77-02, Jan 1977, To D.O.T.

43. Ko, H. Y., and Kim, M. M., "Soil Properties at Pueblo Test Center," Report to Kaman Sciences Corporation, 1979.

44. Laras Back, "Non-linear Mechanical Behavior of Wood," - Ph.D Thesis. 1966. Syracuse University.

45. Lowe, J., "Shear Strength of Coarse Embankment Dam Materials," Proceedings, 8th Congress of Large Dams, 1964, pp. 745-761.

46. Mould, J., "Constitutive Characterization of Granular Materials at Low Effective Stress Levels," M.S. Thesis. Va. Tech, 1979.

47. Nelson, I., and Baron, M. L., "Investigation of Ground Shock Effects in Nonlinear Hysteretic Media," Reports I and II. 1969, DAA Report.

48. Norris, C. S., "Strength of Orthotropic Materials Subjected to Combined Stresses. *U.S. Forest Prod. Lab, Report*, No. 1816, 1971.

49. Office for Research and Experiments of the International Union of Railways (O.R.E.), 1970. "Stresses and Strains in Rails, Ballast and in the Formation Resulting from Traffic Loads," Question D 71, *Report No.* 10, (Vol. 1, p. 39, Vol. 2, Tables and Figures).

50. Office of Research and Experiments of the International Union of Railways, "Deformation of Railway Ballast under repeated Loading," *Report D*, 117/RP 5, 1974.

51. Prager, W., *An Introduction to Plasticity*, Addison - Wesly, 1951.

52. Prevost, J. H., "Soil Stress-Strain Strength Models Based on Plasticity Theory," *Ph.D. Dissertation*, Stanford University, 1974.

53. Raymond, G. P., "A Study of Stress and Deformations Under Dynamic and Static Load Systems in Track Structure & Support," *Report* No. 75-10-, *Queen's* Univ., Kingston, Canada, 1975.

54. Raymond, G. P., et al., "Railroad Ballast Load Ranking Classification," *J. of Geotechnical Eng. Dvn.* Vol. 105, No. GT2, Feb. 1979, pp. 305-322.

56. Raymond, G. P., et al., "Repeated Load Triaxial Tests on a Dolomite Ballast," *J. of Geo. Tech. Eng. Dvn.*, ASCE, No. GT 7, July 1978, pp. 1013-1029.

57. Raymond, G. P., "Research on Rail Support Improvement", Paper Presented to Transportation Research Board, Jan., 1977.

58. Robnett, Q. L., et al., "Structural Model and Material Evaluation Procedures," Ballast and Foundation Material Research Program, Report No. FRA - OR&D-76-255, July, 1976.

59. Robnett, Q. L., et al., "Ballast and Foundation Materials Research Program," Technical Data Bases Report, Department of Civil Eng., University of Illinois, 1975.

60. Roscoe, K. H., and Burland, J. B., On the Generalized Stress-Strain Behavior of a Set Clay, Cambridge University Press, Cambridge, 1968.

61. Salem, M. T., "Vertical Pressure Distribution in the Ballast Section and on the Subgrade Beneath Statically Loaded Ties," Ph.D. Thesis, University of Illinois, 1966.

62. Saxena, C. S., and Arora, S., A Text-Book of Railway Engineering, Dhanpat Rai Publishers, Delhi, 1977.

63. Schofield, A. N., and Wroth, C. P., Critical State Soil Mechanics, McGraw Hill, 1968.

64. Selig, E. T., "Apparatus and Procedures for a Railroad Ballast Plate Index Test," Geotechnical Testing J. GTJODJ, Vol. I. No. 4, Dec., 1978, pp. 233-227.

65. Selig, E. T., et al., "Railroad Ballast Density Measurement," Geotechnical Testing J., GTJODJ, Vol. 1, No. 1, Mar., 1978, pp. 41-54.

66. Selig, E. T., et al., "Ballast and Subgrade Response to Train Loads," <u>Report to Transportation Research Board</u>, Jan., 1978.

67. Siriwardane, H. J., Nonlinear Soil-Structure Interaction Analysis of One-, Two-, and Three-Dimensional Problems Using Finite Element Method, <u>Ph.D. Thesis</u>, 1980. Virginia Tech.

68. SokolniKoff, I. S., <u>Mathematical Theory of Elasticity</u>," McGraw-Hill, N.Y., 1956.

69. Sture, S., Desai, C. S., and Janardhanam, R., "Development of a Constitutive Law for an Artificial Soil," <u>Proc. 3rd. Int. Conf. on Num. Meth. in Geomech.</u>, Aachen, 1979.

70. Sture, S., and Desai, C. S., "Fluid Cushion Truly Triaxial or Multiaxial Testing Device," <u>J. of Geotech. Testing</u>, ASTM, Vol. 2, No. 1, 1979.

REQUEST FOR FEEDBACK TO
The DOT Program Of University Research

This booklet is intended to serve as a reference source for transportation analysts, planners and operators. Your comments will be reviewed by the persons responsible for writing and publishing this material. Feedback is extremely important in improving the quality of research results, the transfer of research information, and the communication link between the researcher and the user.

YES NO

☐ ☐ Did you find the report useful for your particular needs? If so, how?

☐ ☐ Did you find the research to be of high quality?

☐ ☐ Were the results of the research communicated effectively by this report?

☐ ☐ Do you think this report will be valuable to workers in the field of transportation represented by the subject area of the research?

☐ ☐ Are there one or more areas of the report which need strengthening? Which areas?

☐ ☐ Would you be interested in receiving further reports in this area of research? If so, fill out form on other side.

Please furnish in the space below any comments you may have concerning the report. We are particularly interested in further elaboration of the above questions.

COMMENTS

Thank you for your cooperation. No postage necessary if mailed in the U.S.A.